Project No. 09-814

Bulk Nanostructured FCC Steels With Enhanced Radiation Tolerance

Fuel Cycle R&D

Dr. Xinghang Zhang
Texas A&M University

In collaboration with:
University of Wisconsin-Madison
Texas A&M University
University of Florida
Los Alamos National Laboratory
Argonne National Laboratory

Stu Maloy, Technical POC
Sue Lesica, Federal POC

NEUP Nuclear Energy University Programs
U.S. Department of Energy

FINAL PROGRESS REPORT

Project title: Bulk nanostructured austenitic stainless steels with enhanced radiation tolerance

Covering period: Oct. 1, 2009 through Sep. 30, 2012

Date of Report: October 27, 2012

Recipient: Texas Engineering Experiment Station

Address: Texas Engineering Experiment Station
TEES Research Services
006 WERC, Mail Stop 3406 TAMU
College Station, TX 77843-3406
Tel: 979-845-1264
Fax: 979-845-9643
URL: trsweb.tamu.edu

Award Number: DE-AC07-05ID14517

Project Number (Subcontract no.): 00088120

Subcontractors: University of Wisconsin, Madison; University of Florida

Other Partners: Dr. Stuart Maloy, Email: maloy@lanl.gov, Los Alamos National Laboratory

Contact(s):

Principal Investigator: Xinghang Zhang, 979-845-2143 (O), zhangx@tamu.edu

Co-PI: K. Ted Hartwig, 979-845-1585 (O), thartwig@tamu.edu

Co-PI: Todd Allen, 608-265-4083 (O), allen@engr.wisc.edu

Co-PI: Yong Yang, 352-846-3791 (O) yongyang@ufl.edu

1. Project Objective

The **objective** of this project is to increase radiation tolerance in austenitic steels through optimization of grain size and **grain boundary (GB)** characteristics. The focus will be on nanocrystalline austenitic Fe-Cr-Ni alloys with an fcc crystal structure. The long-term goal is to design and develop bulk nanostructured austenitic steels with enhanced void swelling resistance and substantial ductility, and to enhance their creep resistance at elevated temperatures via GB engineering. The combination of grain refinement and grain boundary engineering approaches allows us to tailor the material strength, ductility, and resistance to swelling by 1) changing the sink strength for point defects, 2) by increasing the nucleation barriers for bubble formation at GBs, and 3) by changing the precipitate distributions at boundaries.

Compared to ferritic/martensitic steels, austenitic stainless steels (SS) possess good creep and fatigue resistance at elevated temperatures, and better toughness at low temperature. However, a major disadvantage of austenitic SS is that they are vulnerable to significant void swelling in nuclear reactors, especially at the temperatures and doses anticipated in the Advanced Burner Reactor. The lack of resistance to void swelling in austenitic alloys led to the switch to ferritic/martensitic steels as the preferred material for the fast reactor cladding application. Recently a type of austenitic stainless steel, HT-UPS, was developed at ORNL, and is expected to show enhanced void swelling resistance through the trapping of point defects at nanometer-sized carbides. Reducing the grain size and increasing the fraction of low energy grain boundaries should reduce the available radiation-produced point defects (due to the increased sink area of the grain boundaries), should make bubble nucleation at the boundaries less likely (by reducing the fraction of high-energy boundaries), and improve the strength and ductility under radiation by producing a higher density of nanometer sized carbides on the boundaries. This project will focus on void swelling but advances in processing of austenitic steels are likely to also improve the radiation response of the mechanical properties.

2. Brief summary of major accomplishment - milestones

This is a very fruitful project. In collaboration with Dr. Jinsung Jang (KAERI, South Korea), we have made the following major progress.

(1) We examined the deformation mechanisms in ECAPed Fe-14Cr-16Ni alloys. The average grain size has been refined from 700 microns down to ~ 400 nanometers. The yield strength of ECAP alloys is 5-6 times greater than coarse-grained alloys, and the ductility remain very high, ~ 15% uniform elongation. What is more, these ultra fine grained alloys retain strong work hardening capacity. This is rare as most ECAPed alloys have very little work hardening capability. The strain rate sensitivity of the alloys is lower than bulk alloys.

(2) Ex situ isothermal annealing experiments showed the fine microstructure was thermally stable up to 673 K, and abnormal grain growth occurred at ~ 873 K. In situ annealing studies in a transmission electron microscope revealed the coarsening of grains. Analysis of grain growth kinetics from 873 to 1073 K yielded activation energy of grain growth to be ~ 207 kJ/mol. The grain growth mechanisms and annealing induced evolution of mechanical properties were discussed.

(3) He ion irradiation resistance of ultra fine grained Fe-14Cr-16Ni alloys. At a peak fluence level of 5.5 displacement per atom (dpa), helium bubbles, 0.5-2 nm in diameter, were observed in both coarse-grained (CG) and ultrafine grained (UFG) alloy. The density of He bubbles, dislocation loops, as well as radiation hardening were significantly reduced in the UFG Fe-Cr-Ni alloy comparing to those in its CG counterpart. The results imply that radiation tolerance in bulk metals can be effectively enhanced by refinement of microstructures.

(4) Significant microstructural damage, in the form of defect clusters, typically occurs in metals subjected to heavy ion irradiation. High angle grain boundaries have long been postulated as sinks for defect clusters, such as dislocation loops. Here we provide direct evidence, via in situ Kr ion irradiation under a transmission electron microscope, that high angle grain boundaries in nanocrystalline Ni, with an average grain size of ~ 55 nm, can effectively absorb radiation induced dislocation loops. These high angle grain boundaries significantly reduce the density and size of radiation induced dislocation loops in nanocrystalline Ni compared to their bulk counterparts, and thus nanocrystalline Ni achieves significant enhancement of radiation tolerance.

(5) Multiscale microstructure refinement of a 12Cr-ODS steel by equal channel angular extrusion (ECAE) is investigated by numerous microscopy techniques. The as-HIPped material showed a bimodal microstructure. Three types of second phase particles, including Y_2O_3, $(Cr, Fe)_{23}C_6$ and Cr oxide, were observed. The orientation correlation between Y_2O_3 and the matrix were found to be $(020)_\alpha$ // $(00\bar{4})_{Y2O3}$ and $[001]_\alpha$ // $[110]_{Y2O3}$. After ECAE, the large grains were refined and a homogeneous grain size was achieved. The Cr rich phases (Cr oxide and Cr carbide) were effectively refined. Yttrium oxide particles around the prior ultrafine grain boundaries were redistributed. Geometry change of large yttrium oxide particles from round or facet to triangular or elliptic shaped was observed. Hardening by ~ 35 % is hypothesized through the dislocation pile-ups mechanism against grain boundaries.

(6) During the annealing of 12 Cr ODS steel, the core-shell structure of the oxide particles was formed, which can be understood as the original growth of the Y_2O_3 particles where transition chromium oxides were formed as a case of low oxygen content in the matrix.

(7) The microstructure feature, mechanical properties and their response to heat treatment of cold ECAEed and hot ECAEed T91 alloys were studied. Cold ECAE was more effective in grain refinement, while hot ECAE was more effective in particle refinement. The refining mechanism of precipitates is due to the chemical elimination of prior austenite grain boundaries during hot ECAE, where is a potential preference nucleation site for carbides.

(8) In situ Kr radiation was performed on ECAPed Fe-14Cr-16Ni alloys. Studies show that the dislocation loop density in ECAPed alloys is much lower than that in coarse grained (as-received) alloys. Furthermore, no defect denuded zone was observed along grain boundaries in UFG specimens. This may be related to the fact that grain size (~ 400 nm) is greater than TEM foil thickness (~ 100 nm), and thus foil surfaces act as defect sinks as well.

(9) DSC experiments show that the the ECAPed Fe-14Cr-16Ni alloys should be thermally stable at a temperature below ~600°C, the materials display a radiation induced growth behavior even at the temperature as low as 300°C possible due to the irradiation assisted grain boundary migration and coalesce of subgrains from annihilation of dislocations (grains portioned by

dislocation walls). Nevertheless, the processed materials demonstrate a good radiation swelling resistance and no voids were observed up to a dose of 50 dpa.

(10) 304L and 316L stainless were processed by ECAP. The final products have an average grain size of ~ 100nm and grains are mostly equiaxed. The microstructure and tensile behavior of these alloys are studied. ECAP induces significant strengthening in these alloys.

(11) The microstructure and texture evolution of oxide dispersion strengthened ferritic steel during stepwise uniaxial tensile deformation were observed by high-resolution electron backscattered diffraction with a newly designed deformation device. The rotation behavior of individual ferrite grains as well as overall preferred orientation were traced and analyzed. The tendency describes that the grains rotate towards the stable orientation of 〈1 0 0〉//ND and 〈1 1 1〉//ND. The degree of rotation was dependent on their initial orientation. Vickers hardness test and transmission electron microscope analysis were performed before and after uniaxial tensile deformation to correlate the microstructure with its mechanical properties.

(12) Fe ion irradiation of ECAPed Fe-17Cr-12Ni-2.5Mo alloys indicated that the crystal structure of irradiated sample surface has changed from FCC to BCC phase. The sizes of the newly developed BCC grains were consistent with the ion irradiation depth, which could be estimated by molecular dynamics simulations.

Project Organization:

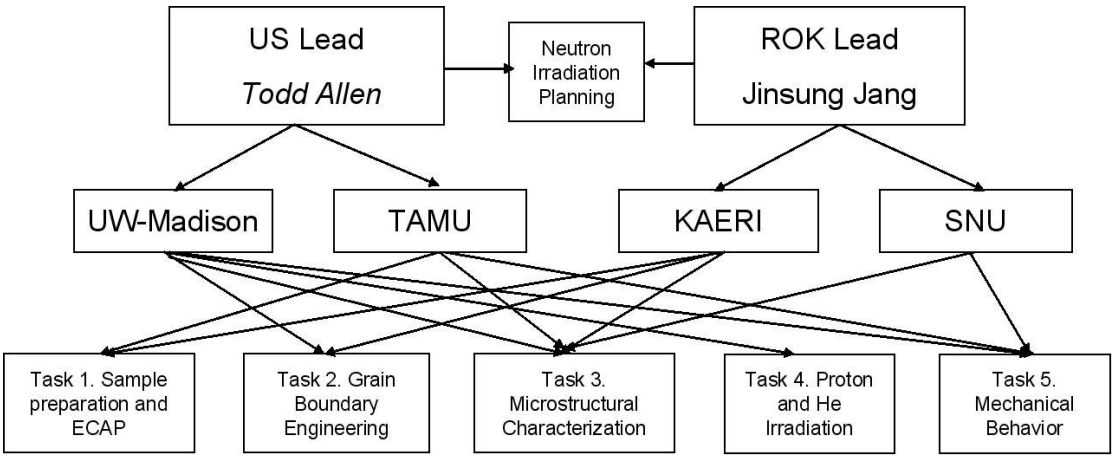

3. Project status - major progress

Major progress

Several projects have been running in parallel at each institution and through intimate collaborations. As each project contains several tasks listed in the above schematics, it is natural to group the projects based on their focus (rather tasks). For the sake of clarity, we summarized below the major progress of 12 projects, each led by an institution with mutual collaborations.

Section A. US contribution

A1. Deformation mechanisms of ultrafine grained Fe-Cr-Ni alloy processed by ECAP

Lead organization (Texas A&M, Xinghang Zhang, K. Ted Hartwig)

In the previous annual report, we have presented preliminary studies on mechanical properties of ECAPed Fe-Cr-Ni alloys. In this report, we present the complete studies of deformation mechanisms in Fe-Cr-Ni alloys.

The material used in the ECAP experiments was Fe-14Cr-16Ni (wt.%) ternary alloy, fabricated by vacuum cast and subsequent hot isostatic pressing, the initial average grain size is ~ 700 µm. ECAP experiments were performed in a split die with channels intersecting at a contact angle of 90°, which yield an effective strain of ~1.15 per single pass. The billet was machined to be 19 × 19 × 152 mm, and eight passes ECAE were carried out on the sample at 500°C using route Bc, which means that between subsequent passes, the sample was rotated by 90° continuously around its longitudinal axes.

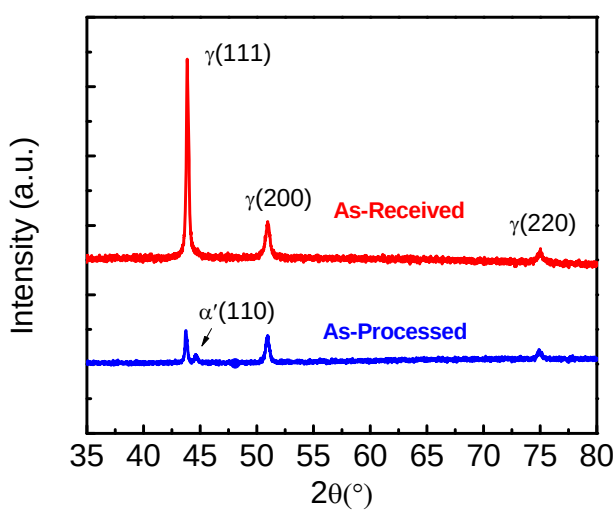

Fig.1.1. XRD profile of the as-received CG and as-processed UFG Fe-Cr-Ni alloy. The as-received sample is fully austenitic, and there is a small α′ (110) peak appears in the as-processed sample, which was taken from the longitudinal plane.

Fig.1.1 shows the XRD profiles of as-received coarse grained (CG) and as-processed ultra fine grained (UFG) Fe-Cr-Ni alloy. The as-received sample is fully austenitic. The as-processed sample was taken from the longitudinal plane of the ECAPed billet. As shown in Fig. 1.1, a small α′ (110) martensite peak appears. The peak intensity of austenite phase reduces and the full width half maximum (FWHM) increases after ECAP experiments due to grain refinement.

Fig.1.2 (a) shows the TEM micrograph of the UFG specimen. The inserted selective area diffraction (SAD) pattern has a ring pattern, indicating the formation of fine grains with high angle grain boundaries. Also SAD pattern suggests that austenite is the dominant phase. The statistical analysis of grain size distribution shows an average grain size of ~ 400 nm, as shown in Fig. 1.2 (b).

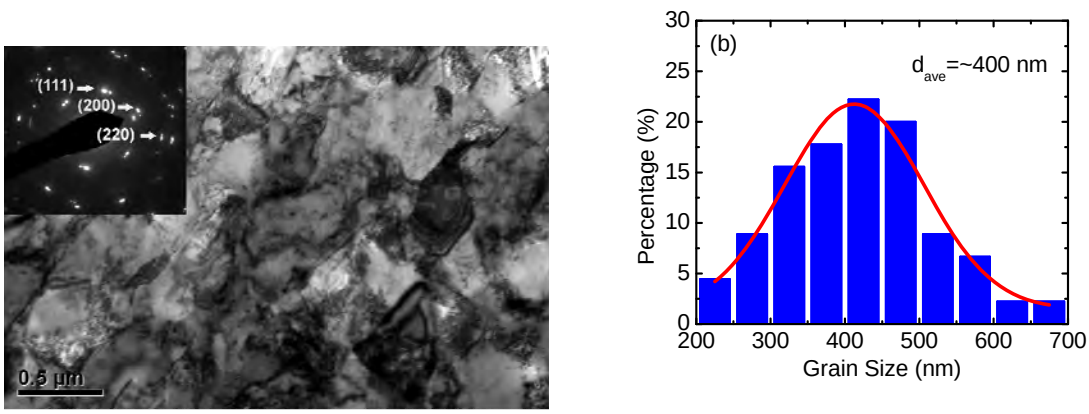

Fig.1.2 (a) TEM micrograph of UFG Fe-14Cr-16Ni. The inserted selected area diffraction (SAD) pattern shows ring pattern, indicating the formation of fine grains with high angle grain boundaries. (b) Statistical distribution of grains shows the average grain size is ~ 400 nm.

Fig. 1.3 shows the true stress- true strain curves of CG and UFG specimens tested at 20, 100 and 200°C using a constant strain rate of 10^{-3} s^{-1}. The yield strength of the sample after ECAP significantly increases from 100 (CG specimen) to 660 MPa (UFG specimen) tested at 20°C. The yield strength of the UFG specimen slightly decreases with increasing temperature from 20 to 200°C, whereas the ductility shows strong temperature dependence. The elongation-to-failure dramatically decreases by a factor of ~ 3 as the test temperature increases up to 200°C. Furthermore both CG and ECAPed UFG specimens possess significant work hardening

capability when tested at 20°C. Work hardening capacity in UFG specimen quickly degrades when tested at elevated temperatures.

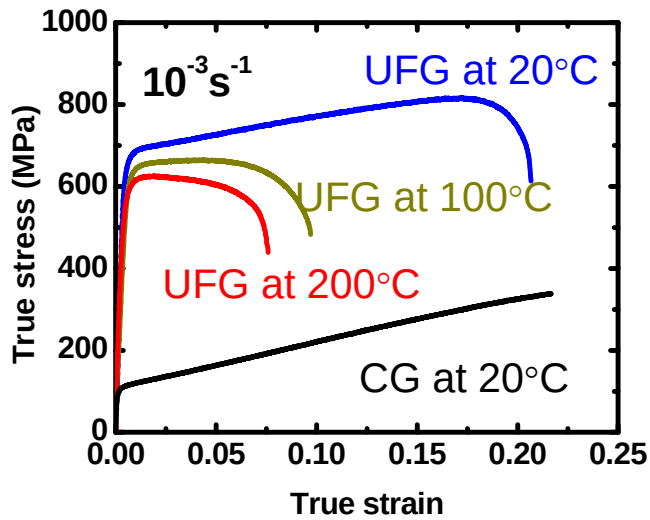

Fig. 1.3. True stress-true strain curves of CG (as-received) and UFG (as-processed) Fe-14Cr-16Ni alloy tested at a strain rate of 10^{-3} s^{-1} and at a temperature 20, 100 and 200°C.The yield strength of the alloy increases by a factor of ~ 6 after ECAP while work hardening capability retains. The ductility of the UFG sample decreases as testing temperature increases from 20 to 200°C.

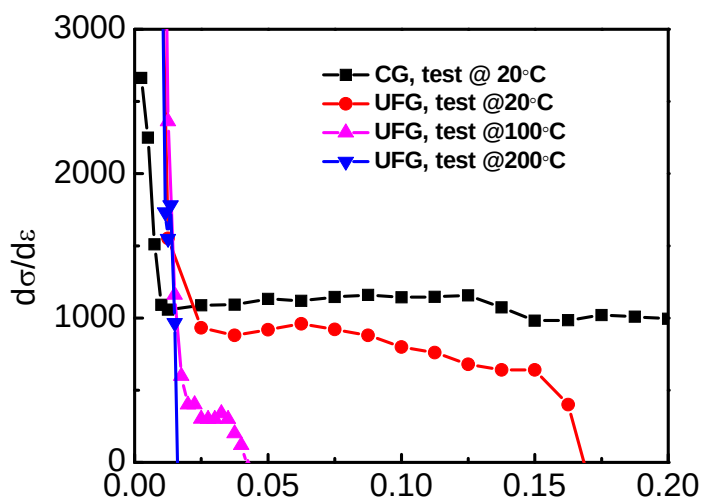

Fig. 1.4 Strain hardening rate (dσ/dε) vs. true strain (ε) at temperature from 20°C to 200°C for CG and UFG specimen. The average strain hardening rate of UFG sample reduces slightly at 20°C, compared with that of CG sample. As the test temperature increases from 20 to 200°C, the strain hardening rate decreases dramatically.

Fig. 1.4 shows strain hardening rate (dσ/dε) as a function of a true strain (ε). Comparing to CG specimen, the uniform strain hardening rate is slightly lower in UFG specimen tested at 20°C. As the testing temperature increases, the strain hardening rate of UFG specimen decreases dramatically.

The SEM micrograph in Fig. 1.5 shows the fracture surface of the UFG specimen tested at 20°C and 200°C. The dimple-like morphology dominates the fracture pattern after test temperature of 20°C, implying that the failure mode is ductile rupture, while more area on fracture surface tested at 200°C shows cleavage feature, as shown in Fig. 1.5 (b), although a few dimples still can be observed.

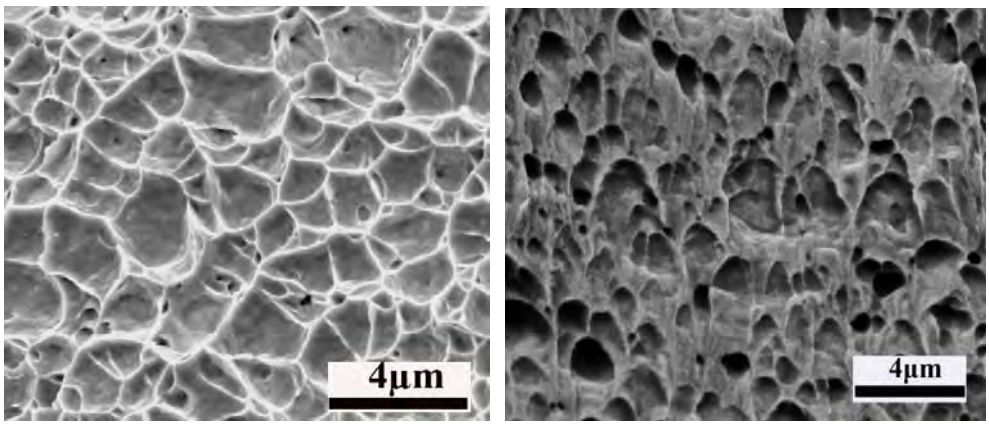

Fig. 1.5 (a) The fracture surface of UFG sample after testing at 20°C shows the dimple-like morphology. (b) The fracture surface of UFG sample subjected to the tensile test at 200°C shows dominated cleavage feature.

Microstructure of the UFG sample after tensile test at 20°C was examined by TEM. As shown in Fig. 1.6, the bright filed TEM image suggests that grains remain equiaxed, yet a higher density of dislocations together with deformation twins are observed. The SAD pattern suggests that austenite is still the dominant phase even though the samples were strained to a true strain of more than 15%.

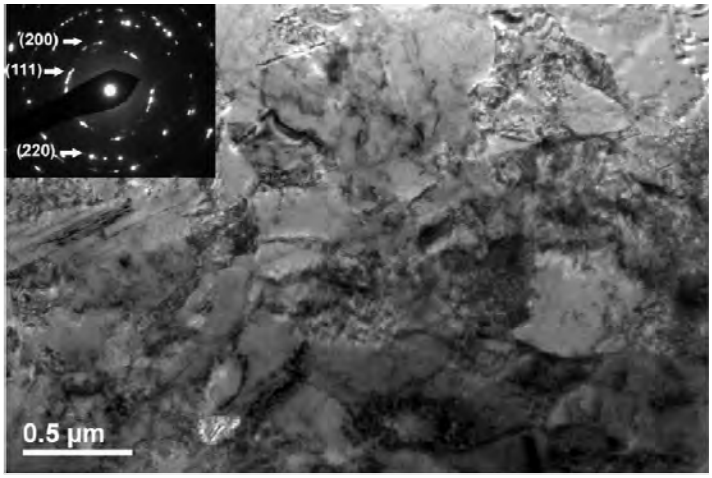

Fig. 1.6. TEM micrograph of UFG specimen after tensile test at 20°C shows the retention of UFG grains with a few deformation twins. SAD pattern indicates the major phase remains austenite.

Tensile jump tests at strain rates varying from 10^{-5} to 10^{-2} s^{-1} were performed to determine the strain rate sensitivity. Fig. 1.7 (a) shows the jump test results of CG and UFG samples at 20°C. Fig. 1.7 (b) presents the jump test results for the UFG samples at 100 and 200°C up to ~ 5% true strain. The numbers in Fig. 1.7 stand for the applied strain rates. For instance "-3" represents a strain rate of 1×10^{-3} s^{-1}.

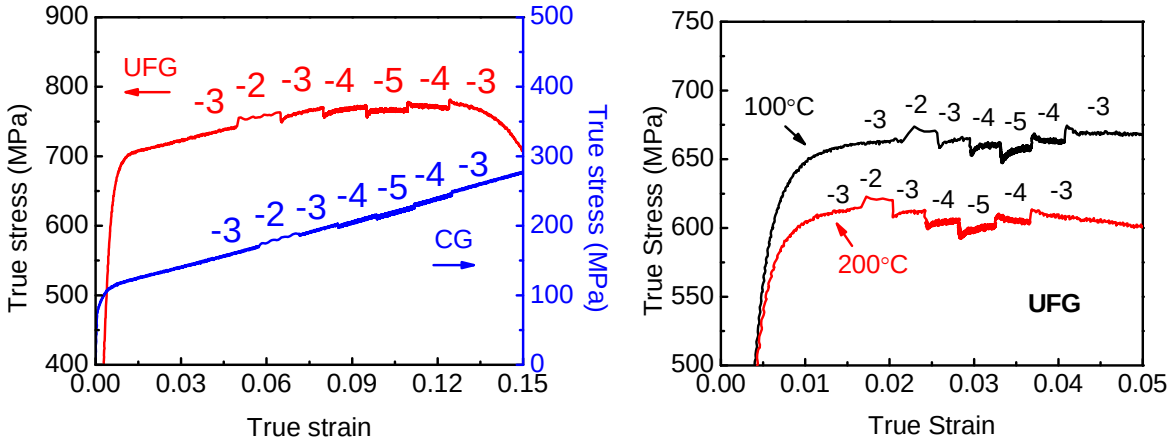

Fig. 1.7 (a) True stress-true strain curves of CG and UFG Fe-Cr-Ni alloy at 20°C, the strain rate varies between 10^{-5} s^{-1} to 10^{-2} s^{-1}. (b) True stress-true strain curves of UFG specimen during jump tests at 100°C and 200°C in the first 5% plastic strain.

The strain rate sensitivity exponent (m) can be calculated by

$$m = \left(\frac{\partial \log \sigma}{\partial \log \dot{\varepsilon}}\right)_{\varepsilon,T} = \left(\frac{1}{\sigma}\right)\left(\frac{\partial \sigma}{\partial \log \dot{\varepsilon}}\right)_{\varepsilon,T} \qquad (1),$$

where σ is true stress and $\dot{\varepsilon}$ is strain rate. The values of m can be calculated from the slope in the plot of $\log \sigma$ vs. $\log(\dot{\varepsilon})$, as shown in Fig. 1.8. At 20°C, the average value of m is estimated to be ~ 0.014 for CG specimen (the m value of bulk 304 SS at 30°C is ~ 0.012), By refining the gains, the average m value of the UFG sample at 20°C is calculated to be ~ 0.007, and as test temperature increases to 100 and 200°C, the m value rises to 0.009 and 0.012 respectively. The relationship between strain rate sensitivity and activation volume v is

$$m = \frac{\sqrt{3}kT}{\sigma v} \qquad (2),$$

where k is Boltzmann constant. By using the slope of $\sqrt{3}kT \log(\dot{\varepsilon})$ vs. σ, we derive the activation volume is ~ 130b^3 (where b is the Burgers vector) for CG sample and ~ 38b^3 for UFG sample at 20°C. At elevated temperature, the activation volume of the UFG specimen is reduced further to be ~30b^3 at 100°C and ~26b^3 at 200°C.

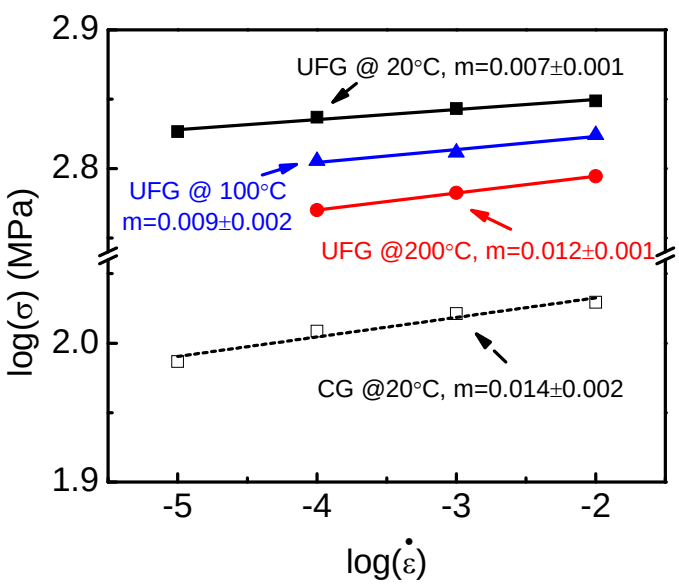

Fig. 1.8 Plot of log(σ) vs. log($\dot{\varepsilon}$), the strain rate sensitivity (m) is estimated by the slop of the curves. Average m value of CG and UFG specimen at 20C is calculated to be ~ 0.014 and ~ 0.007, respectively. For the UFG specimen, at elevated temperature, average value of m is ~ 0.009 at 100°C, and ~ 0.012 at 200°C.

Strain hardening

The microstructure of Fe-Cr-Ni alloy is successfully refined by three orders of magnitude, from 700 μm for as-received material down to 400 nm by ECAP processing at 500°C. The microstructure refinement is achieved by continuous accumulation of dislocations during severe plastic deformation. The increase of yield strength in UFG specimen at 20°C mainly originates from the grain refinement. The contribution of martensite to hardening is negligible as the predominant phase remains austenite after deformation. For most NC/UFG metals and alloys produced by using severe plastic deformation (SPD), dislocation saturation is achieved very quickly, resulting in the lack of strain hardening and diminished dislocation activity during deformation. However, under hot working conditions, some NC/UFG metals and alloys undergo dynamic recovery during SPD. The annihilation and rearrangement of dislocations due to the dynamic recovery lower the average stain energy associated with the dislocations and reduce the dislocation density inside the grains. The total dislocation density evolution rate ($\frac{d\rho}{d\varepsilon}$) can be expressed as

$$\frac{d\rho}{d\varepsilon} = \frac{d\rho_{store}}{d\varepsilon} - \frac{d\rho_{reco}}{d\varepsilon} \qquad (3),$$

where $d\rho_{store}/d\varepsilon$ stands for dislocation storage rate, which is an athermal component, and $d\rho_{reco}/d\varepsilon$ describes the dislocation density evolution due to dynamic recovery, which is influenced by thermal activation. In this current study, the strain hardening rate of UFG specimen at room temperature in the uniform deformation region is only slightly less than that of CG specimen and the true uniform strain exceeds 15%. During ECAP processing at 500°C, the dislocations produced by severe plastic deformation evolved into the grain boundaries and/or annihilated by dislocations with opposite Burgers vector. Both processes lower the overall dislocation density in grains. Dynamic recovery occurs during ECAP at elevated deformation temperature, and consequently renders the UFG specimen strain hardening capacity when tested at room temperature.

The effect of dynamic recovery on strain hardening rate becomes stronger with increasing temperature due to the increased mobility of dislocations. The strain hardening rate ($\frac{d\sigma}{d\varepsilon}$) can be described as

$$\frac{d\sigma}{d\varepsilon} = [\Theta_h - \Theta_r(\dot{\varepsilon}, T, \sigma)] \quad (4),$$

where Θ_h is an athermal hardening component due to dislocation storage, Θ_r is dynamic recovery term related to the temperature, strain rate and flow stress. As shown in Fig.4, during the uniaxial tensile tests, the strain hardening rate decreases quickly when temperature increases to 200°C. It is likely dislocation density rapidly reduces through annihilation of dislocations or grain boundary absorption. Both processes assist dynamic recovery and hence the strain hardening rate is reduced. Although the strain hardening rate dramatically reduces when the temperature rises to 200°C, the flow stresses only slight decreases. The retention of yield strength at elevated temperature indicates that the equiaxed fine grains are thermally stable at the testing temperature. The thermal stability of these UFG specimens will be reported elsewhere. The moderate reduction of yield strength is a result of temperature assisted activation of dislocations activities during the onset of plastic yielding.

Based on the Considere's criterion, the plastic instability (necking) occurs when

$$(\frac{\partial\sigma}{\partial\varepsilon})_{\dot{\varepsilon}} \leq \sigma \quad (5)$$

where σ and ε are true stress and true strain, respectively. The rapid reduction of strain hardening rate ($\frac{d\sigma}{d\varepsilon}$) leads to the onset of necking at smaller strain, and thus reduces uniform plastic strain during tensile tests.

Strain rate sensitivity of flow stress

The strain rate sensitivity of the Fe-Cr-Ni alloy reduces by a factor of 2 when the average grain size is refined from 700 μm to 400 nm. Although the absolute flow stress increase per strain rate of UFG specimen is larger than that of CG specimen, the m value still drops for the smaller grain size due to the inversely proportional relationship with flow stress, in Eq.(1). A

large activation volume estimated for CG specimen is related to the dislocations cutting through the forest dislocations, while the reduced activation volume in UFG sample might be attributed to the enhanced effect of grain boundary diffusion process. With the consideration of strain rate sensitivity, the Hart's instability criterion is

$$\frac{1}{\sigma}\left(\frac{d\sigma}{d\varepsilon}\right)_{\dot{\varepsilon}} - 1 + m \leq 0 \qquad (6),$$

It is clearly seen from the above equation that given the flow stress (σ), large strain hardening rate ($\frac{d\sigma}{d\varepsilon}$) and/or strain rate sensitivity (m) helps to sustain the homogeneous deformation before the onset of necking. Although the average strain rate sensitivity of UFG specimen increases from 0.007 to 0.012 by increasing the temperature from 20°C to 200°C, the rapid drop of the strain hardening rate results in the reduction of uniform plastic strain at 200°C. In other words, the strain rate sensitivity increase by temperature cannot compensate the decrease of strain hardening rate, and the improvement of strain hardening would offer more resistance to the onset of localized deformation.

A2. Thermal stability of ultra fine grains in ECAP processed Fe-14Cr-16Ni (wt.%) alloys

Lead organization (Texas A&M, Xinghang Zhang)

As-received Fe-14Cr-16Ni (wt.%) alloy had an average grain size of 700 μm. ECAP experiments up to 8 passes at 773K were performed to refine its microstructure by using route Bc, which means that between each subsequent pass, the sample was rotated by 90° around its longitudinal axes. The grain boundary characteristics and phases identification of the ECAPed sample were performed by using a LEO-1530 field emission scanning electron microscope equipped with capability to perform electron backscattering diffraction (EBSD) analysis. Ex situ annealing experiments were performed by using a vacuum furnace. The microstructure evolution of the ECAPed specimen after annealing was examined with a Quanta 600 field emission scanning electron microscope. In-situ annealing experiment was performed on a JEOL 2010 transmission electron microscope, operated at 200 kV and equipped with a Gatan SC1000 ORIUS CCD camera, at 973 K to study grain growth process. Samples for transmission electron

microscopy (TEM) studies were prepared by electropolishing using a mixture of perchloric acid and methanol solution. The microhardness of alloys was measured by using a Vickers microhardness tester under a loading force of 200 gf for 13 seconds. The average hardness values were determined from a minimum of 12 indentation experiments.

Fig.2.1 a shows the EBSD micrograph of ECAPed Fe-Cr-Ni alloy. The equiaxed microstructure with high angle grain boundaries was formed after ECAP process. Statistics of grain size distribution shown in Fig. 2.1b revealed an average grain size of ~ 0.4 µm. Fig.2.1c shows the retention of predominant austenite matrix (red) with ~ 12% (area fraction) martensite (green) dispersed along austenite grain boundaries. Martensite grains, as large as 0.3 µm, were occasionally distributed at triple junctions of austenite grains. A TEM micrograph (Fig. 2.2a) shows the existence of a large martensite grain at a triple junction of austenite grains. The martensite phase appeared to have a very high density of dislocations and the inserted selected area diffraction (SAD) pattern in Fig.2b confirmed the existence of α' martensite with body centered cubic (bcc) structure oriented along [211] zone axis.

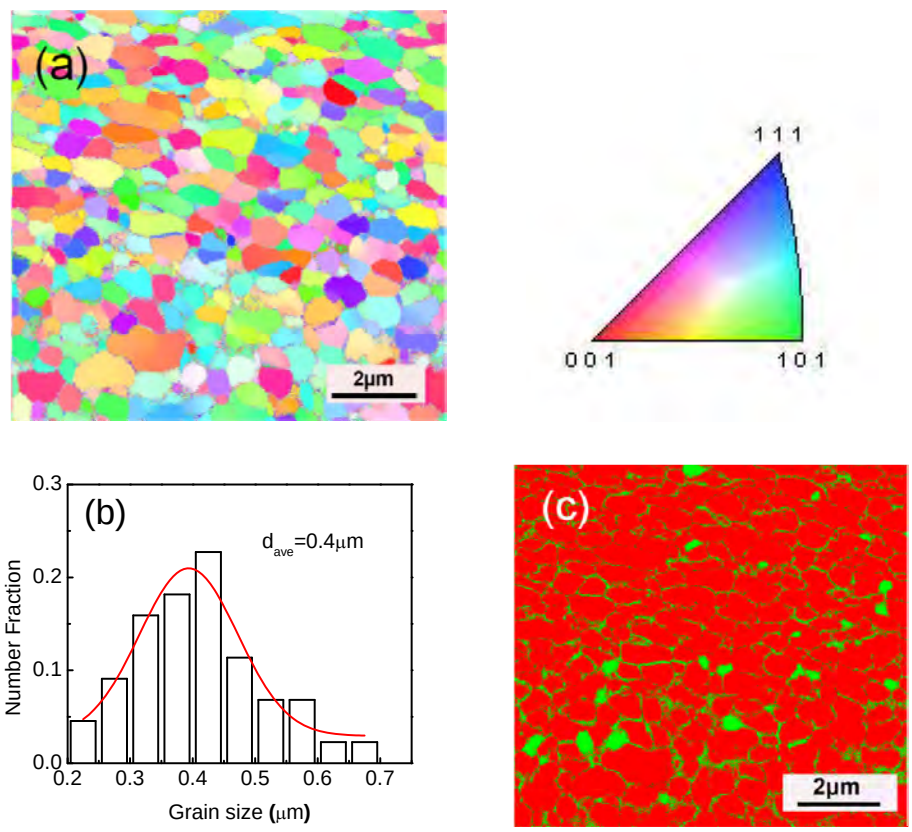

Figure 2.1. (a) Electron backscattered diffraction pattern (EBSD) of ECAPed Fe-Cr-Ni alloy. A majority of grains have high angle grain boundaries (b) Statistics of grain size distributions shows the average grain is ~ 0.4 µm. (c) The phase map of ECAPed sample by EBSD, in which the red matrix represents the austenite and the martensite grains are labeled in green.

Ex situ isothermal annealing studies show that the ultrafine grains were thermally stable up to 673 K. After annealing at 873 K, abnormal grain growth was observed as shown in Fig.2.3a. As presented in Fig. 2.3b, a bimodal distribution of grain sizes was identified with a lower bound average grain size of 0.86 µm and an upper bound average of 3.5 µm. TEM micrograph in Fig.2.3c also revealed the occurrence of abnormal grain growth at 873 K. At higher annealing temperature, 973 and 1073 K, unimodal distributions of grain size were observed by SEM, as shown in Fig.2.4a-c. In addition, abundant annealing twins were introduced. The evolution of grain sizes as a function of annealing temperature is illustrated in Fig.2.5. The average grain size remained constant up to 673 K, and slightly increased at 773 K. Due to the existence of bimodal distribution of grain sizes at 873 K, both the upper and lower bound average grain sizes were shown. Annealing at higher temperature led to the removal of the small grains, and the average grain size increased monotonically with temperature.

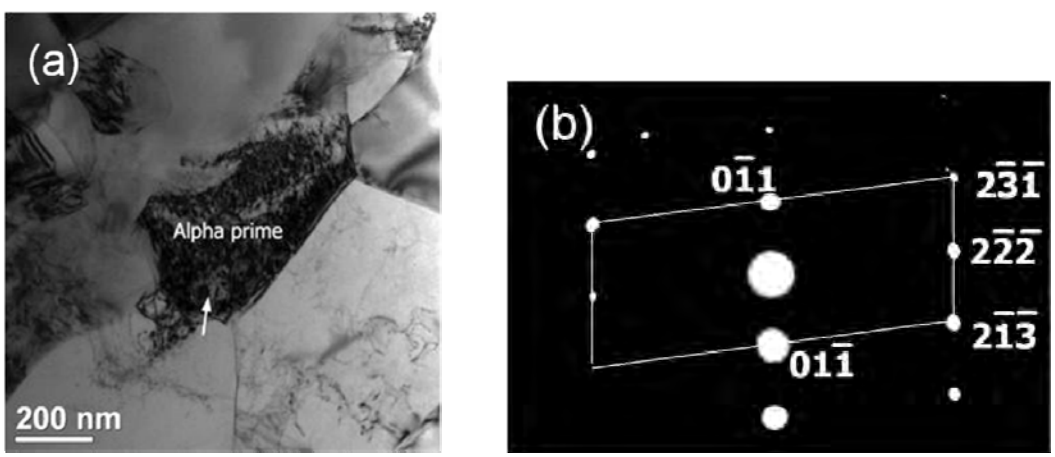

Figure 2.2. (a) A TEM micrograph of the ECAPed alloy shows the existence of a dark martensite grain at the triple junction of austenite grains. (b) Selective area diffraction pattern of the dark grain confirm that it has martensite phase, examined along the [211] zone axis.

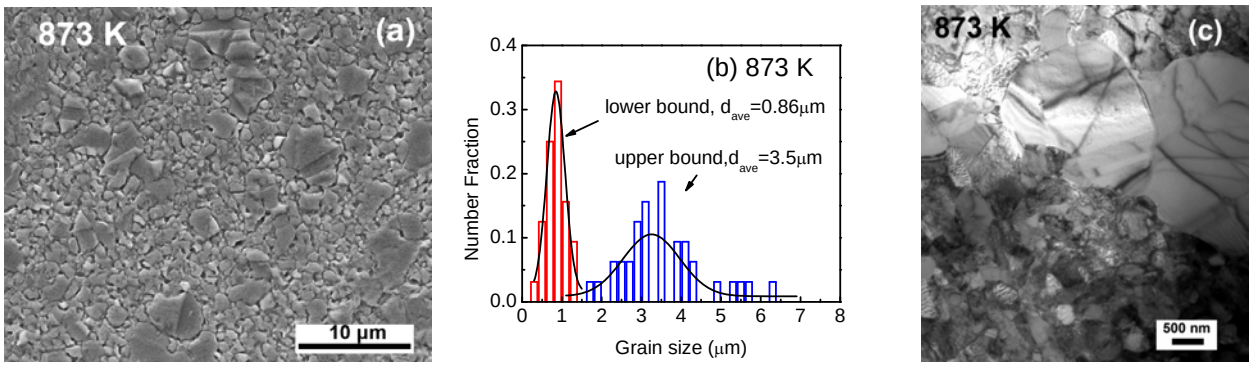

Figure 2.3. (a) An SEM micrograph of UFG Fe-14Cr-16Ni after annealing at 873 K/1h shows abnormal grain growth. (b) Statistics of grain sizes shows a bimodal distribution. The average grain size of lower bound and upper bound is 0.86 and 3.5 µm respectively. (c) A TEM micrograph of the alloy annealed at the same condition also shows the coexistence of small and large grains.

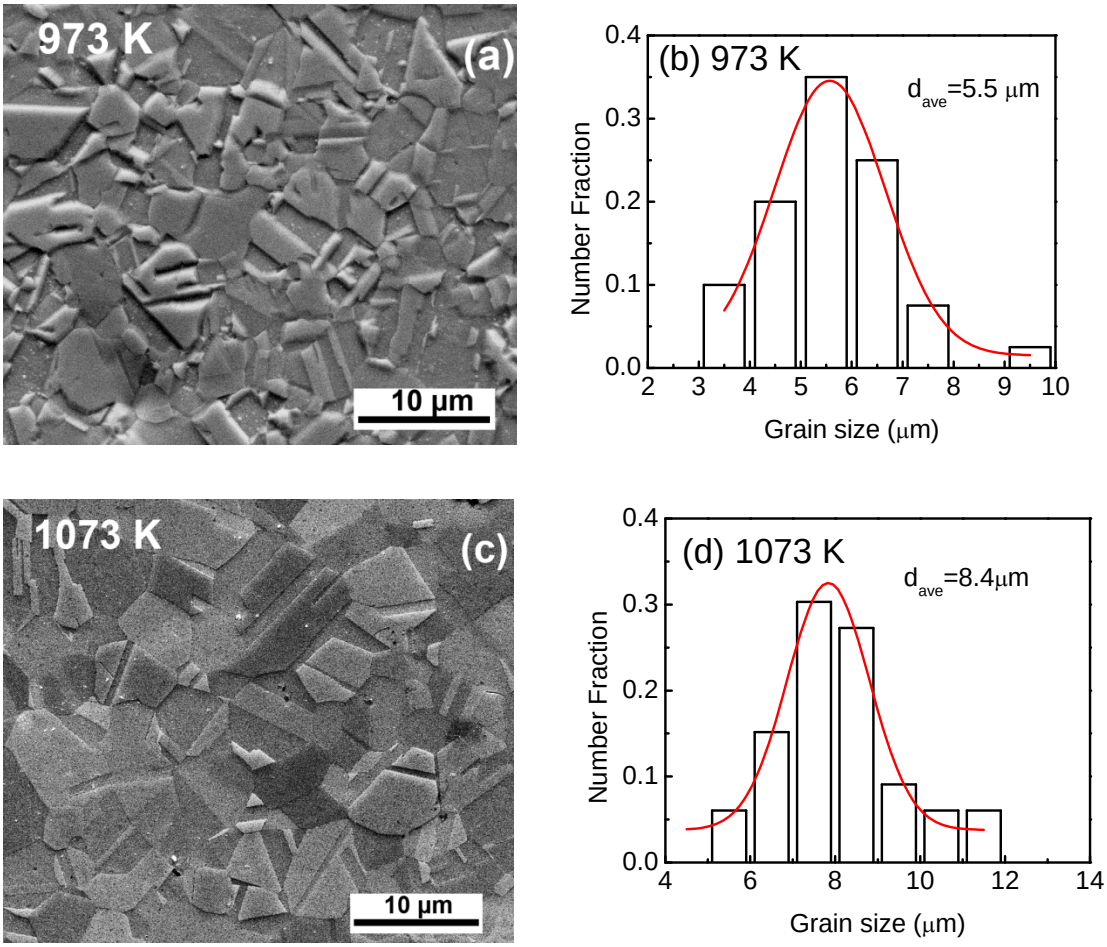

Figure 2.4. (a) An SEM micrograph of UFG Fe-14Cr-16Ni after annealing at 973 K/1h shows normal grain growth. Annealing twins were observed within grain. (b) Statistics of grain sizes of the alloy annealed at 973K shows unimodal distribution with an average grain size of ~5.5 µm. (c) An SEM micrograph of the alloy annealed at 1073 K/1h shows continuous grain growth and the generation of annealing twins. (d) Corresponding grain size distribution is again unimodal with an average grain size of ~ 8.4 µm.

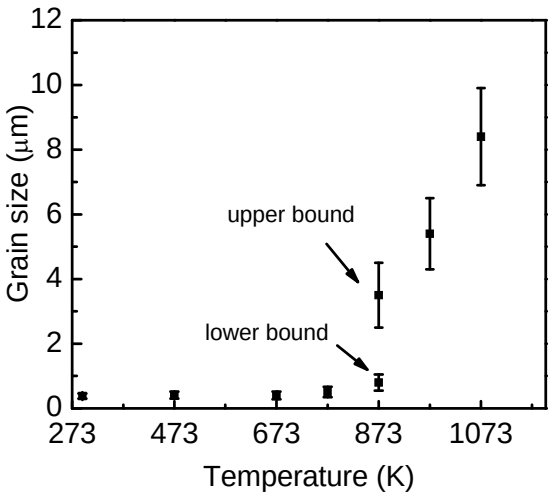

Figure 2.5. Grain size evolution upon annealing shows that grains are rather stable up to 773 K, followed by rapid grain growth thereafter. Both the upper and lower bound average grain size are shown at 873 K, at which abnormal grain growth was observed.

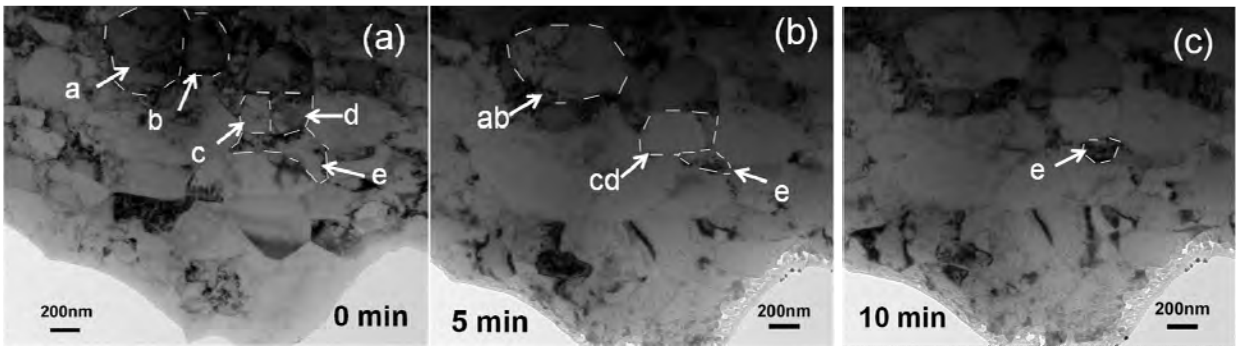

Figure 2.6. The microstructure evolution of UFG sample subjected to *in situ* annealing at 973 K inside a transmission electron microscope for various time. (a) At the onset of annealing. Five grains are labeled as a - e. (b) Annealing for 5 minutes leads to the coalescence of grains a and b, and c and d. Notice that grain e remains but becomes smaller. (c) After annealing for 10 minutes, the morphology of grain e changes by presumably grain rotation.

Microstructure evolution and grain growth in the UFG Fe-Cr-Ni alloy were observed by *in situ* annealing in a transmission electron microscope. Fig.2.6 shows the bright field TEM micrographs of the sample captured during annealing at 973 K for 0, 5, and 10 minutes. The microstructure was manifested by several notable features. (a) At the beginning of annealing studies, subgrains grew via rapid migration of grain boundaries, as evidenced by the coalescence of subgrains labeled as a-d. (b) Meanwhile large grains grew by consuming small grains, which is considered as the Ostwald ripening process, as shown by the evolution of grain e. (c) Dislocation density inside grains and near grain boundaries was reduced and grain boundaries became sharper and well-defined.

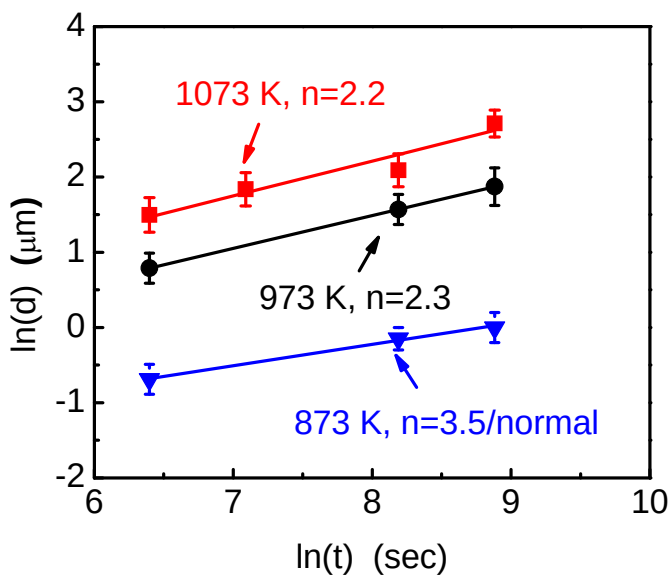

Figure 2.7. Plot of ln(d) vs.ln(t) at different temperatures, where d and t are grain size and annealing time, respectively. For the normal grain growth, the grain growth exponent value (n) are determined to be 3.5, 2.3, 2.2 at 873 K, 973 K and 1073 K, respectivly. At 873 K, the n value for normal grain growth is determined by excluding abnormal grain growth.

Ex situ annealing experiments were performed at 873, 973 and 1073 K, for various annealing time to investigate grain growth kinetics. The grain growth kinetics, correlating grain size (d) to annealing time (t) is described as:

$$d^n - d_0^n = kt \quad (1),$$

where d_0 is the initial grain size, n is grain growth exponent, and k is a rate constant, which is temperature dependent and related to the grain boundary mobility. The evolution of grain size (ln(d)) with annealing time (ln (t)) at 873-1073 K is shown in Fig.2.7. The values of n and k can be determined from the slopes and interceptions of the linear fit lines with the vertical axis. The normal grain growth exponent (n) decreased from 3.5 to 2.2 when temperature increased from 873 K to 1073 K. Due to the bimodal distribution of the grain sizes at 873 K, the n value was estimated to be 3.5 for normal grain growth excluding abnormal grain growth. The activation energy (Q) for grain growth can be obtained from the following expression:

$$k = k_0 \exp(\frac{-Q}{RT}) \qquad (2),$$

where k_0 is a constant, R and T are gas constant and annealing temperature, respectively. The average activation energy (Q_{ave}) estimated from the slope of the linear fit of the ln (k) vs. 1/T plot was ~207 kJ/mol, as shown in Fig.2.8. The activation energy for normal grain growth (Q_{normal}) excluding the contribution from abnormal grain growth was ~215 kJ/mol.

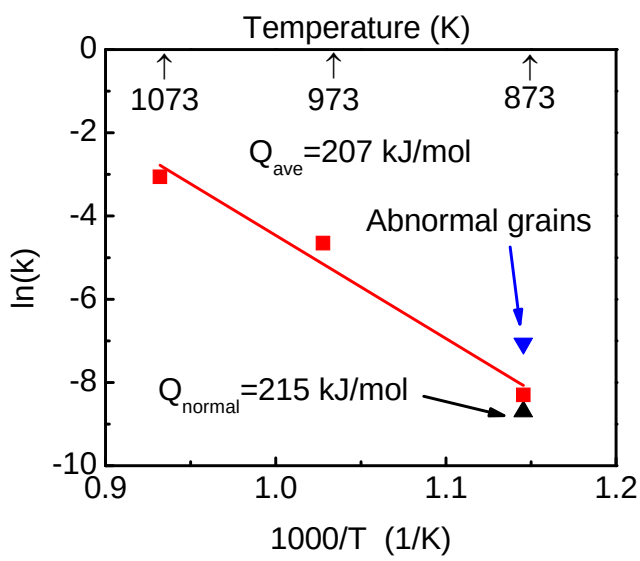

Figure 2.8. Based on the Arrhenius plot of ln(k) vs. 1/T, the average activation energy (Q_{ave}) is calculated to be ~ 207 kJ/mol. The activation energy for normal grain growth (Q_{normal}) excluding contribution from abnormal grain growth is ~215 kJ/mol.

Fig.2.9 illustrates the evolution of microhardness with the annealing temperature. Hardness remained the same, ~ 2.8 GPa, after annealing up to 673 K, started to decline at 773 K, and decreased rapidly thereafter at higher temperature. By 1073 K, the average microhardness decreased from the initial value of ~ 2.8 to ~1.6 GPa. Fig.2.10 summarizes the effect of grain size (d) on the variation of hardness. The linear relationship of H_v vs. $d^{-1/2}$ suggests the evolution of hardness followed the Hall-Petch relationship: $H_V = K_h(d^{-1/2}) + H_0$, where K_h and H_0 are constants, related to locking parameter and lattice friction stress respectively. The Hall-Petch curve of 304 SS was also provided in Fig.2.10 for comparison. The slope of the curve (K_h) for the present Fe-Cr-Ni alloy and 304 SS is 1.13 and 1.73 GPa•μm$^{1/2}$, respectively.

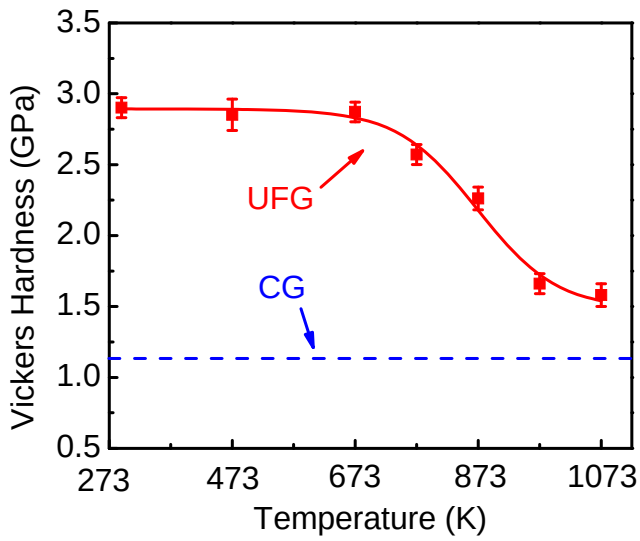

Figure 2.9. The variation of Vickers hardness with the annealing temperature. Hardness barely changes up to 673 K. Softening occurs at 773 K, followed by rapid reduction of hardness down to 1.5 GPa. The hardness of coarse-grained (CG) steel is shown as the horizontal dash line.

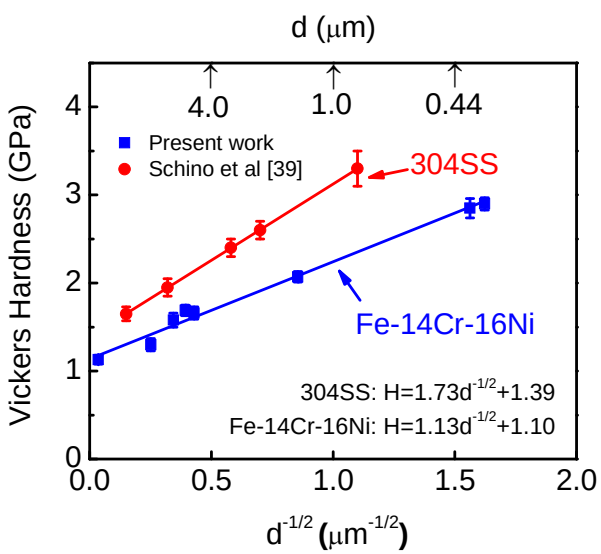

Figure 2.10. Plot of Vickers hardness vs. $d^{-1/2}$, where d is the average grain size. The linear fit of UFG Fe-14Cr-16Ni hardness data follows Hall-Petch relationship. In the same plot, the data for 304 SS are also shown for comparison. The slope of Hall-Petch plot for 304 SS is slightly greater.

Heavily deformed metals with a large fraction of high angle grain boundaries can continuously recrystallize during annealing. Humphreys *et al* have shown that a cellular structure will become resistant to discontinuous growth once ~ 70% of boundaries are high angle grain boundaries, because on average the cell boundaries will approach the conditions where they have similar grain boundary energy and mobility. However, the UFG Fe-Cr-Ni alloy, with ~ 90% of high angle grain boundaries (based on EBSD results that are not shown here), still show the abnormal grain growth at ~ 873 K. There are two possible mechanisms that lead to the abnormal grain growth in the current study. First, during ECAP process there is inhomogeneous accumulation of dislocations within grains and coexistence of high-angle and less mobile low-angle grain boundaries, thus there may be a large difference in the stored energy both within the grains and at different type of grain boundaries. The difference in stored energy provides the driving force for grain boundary migration. It is likely that recrystallization occurs preferentially in the regions with greater stored energy, leading to rapid growth of grains locally and thus the bimodal distribution of grain size. Second, the martensite particles might also contribute to the abnormal grain growth. At the early annealing stage at 873K, the martensite grains, acting as second phase particles, may generate pinning pressure on the grain boundaries. The competition between the pinning pressure and driving force for grain growth determines whether the grains should be stabilized or coarsen. Meanwhile, the inhomogeneous distribution of the martensite particles may also result in the non-uniform coarsening of grains. Fig.2.11 predicts the influence of the particle pinning pressure (F_v/d_p) and the matrix grain size on the mode of grain growth, where F_v and d_p are the volume fraction and average size of second phase particles. In the current case at 873K, the ratio (F_v/d_p) is 0.3μm^{-1} for the martensite phase, and an average austenite grain size of 0.4μm, shown as the solid square point in the abnormal grain growth region in Fig 2.11, we would anticipate the abnormal grain growth of austenite matrix. During longer annealing treatment at 873K, the martensite particles became unstable and partially transform to austenite, which resulted in the gradual removal of the pinning effect in some regions and thus even more inhomogeneous distribution of the martensite particles. At higher annealing temperature, the microstructure became uniform as defects, including martensites and high density dislocations were consumed. The two-phase alloy turned into single-phase, and a full recrystallized homogeneous grain structure was formed.

The activation energy for grain boundary and volume diffusion of iron in α-iron is 164 and 280 kJ/mol, respectively. Smith and Gibbs reported activation energy for grain boundary diffusion (180 kJ/mol) and volume diffusion of iron (284 kJ/mol) in Fe-Cr-Ni-Nb stainless steel. Our measured average activation energy for normal grain growth, ~207 kJ/mol, is somewhere between these values, but closer to the activation energy for grain boundary diffusion. In the ECAPed Fe-Cr-Ni alloy, there are several important factors that dictate the activation energy of grain growth. First, high density of dislocations in grain interiors and near grain boundaries leads to an increase in stored energy and driving force for grain growth. Second, a large volume fraction of high-angle grain boundaries increases atomic mobility and enhances the possibility of grain boundary migration. Third, phase boundary (between austenite and martensite) also assists the migration of grain boundaries. Finally, solutes (Cr and Ni) in the alloy increase the bond strength and thus lower the atomic mobility and increase the activation energy for grain coarsening. The first three factors can reduce the activation energy of grain growth in comparison to lattice diffusions, and may play dominant roles in determining the relatively low activation energy of grain growth in the current study.

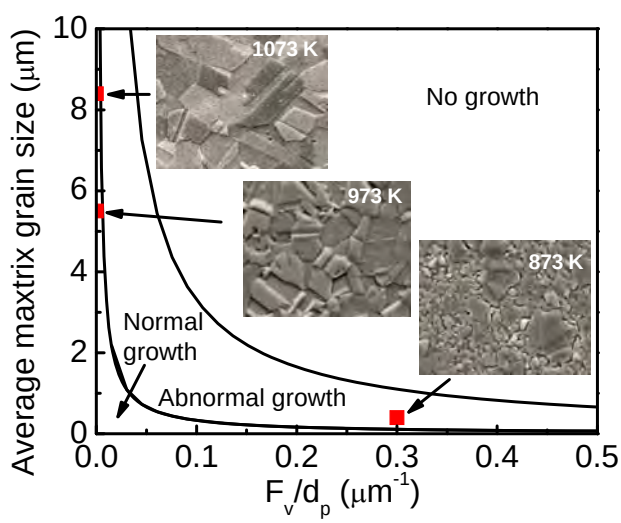

Figure 2.11. Map for abnormal and normal grain growth as a function of average matrix grain size (d) and second phase dispersion level (F_v/d_p), where F_v and d_p are the volume fraction and average size of second phase particles [40]. In the present study, d = 0.4 μm, F_v/d_p=0.3, the abnormal grain growth is predicted at 873 K. Without second phase particles after annealing at

973 K and 1073 K, the normal grain growth occurs. The corresponding microstructures of alloys are shown on the same plot.

The microhardness of UFG alloys decreased when annealed at 773 K. However microscopy studies did not reveal noticeable grain growth in this specimen. The softening at 773 K may be a consequence of reduction of dislocation density due to static recovery, and relaxation of internal residual stress resulting from the annihilation and rearrangement of dislocations. The softening at higher temperatures (≥ 873 K) is mainly attributed to recrystallization and grain growth. In addition, the temperature for martensite-to-austenite phase transformation is ~ 900 K for stainless steel, and for the current UFG alloy, no martensite phase was detected after annealing at 973 K for 1 hour, based on the EBSD result. Thus, the removal of martensite may also contribute to softening at higher temperatures. The slope of the Hall-Petch plot of the present Fe-14Cr-16Ni alloy is less than that in 304SS, indicating a lower resistance of grain boundaries to the transmission of dislocations. This phenomenon can be understood from several aspects. First, the average shear modulus of the current alloy is smaller than that of 304 SS due to a lower Cr concentration. The shear modulus of iron (82 GPa) and nickel (76 GPa) is close to each other. But Cr has a much greater shear modulus, 115 GPa. Second, impurity and precipitates such as carbides and sulphides in 304 SS, may exist along grain boundaries, and hence lead to the enhanced grain boundary resistance to the transmission of dislocations.

In the CG and UFG Fe-Cr-Ni alloy, the grain sizes are submicron or greater, and hence strengthening follows a typical Hall-Petch type of dislocation pile-up model, i.e. H_v increases linearly with the increase of $d^{-1/2}$. When grain size reduces to nanoscale, typically 50 nm or less, dislocation pile-ups become increasingly difficult, and hence the dislocation bowing mechanism may govern the hardening behaviors. A different model proposed for nanocrystalline materials can be used here to predict the peak hardness of the Fe-Cr-Ni alloy. The critical shear stress (τ) for bowing of dislocations is expressed by:

$$\tau = \frac{Gb}{2\pi L(1-v)}[(1-\frac{3v}{2})\ln(\frac{L}{b})-1+\frac{v}{2}] \quad (3)$$

where G is the shear modulus, b is the magnitude of Burgers vector, v is the Possion's ratio. L is the average length of dislocations, assumed to be $cd^{1/2}$, where c is 1.25 in nanoscale regime. To convert the shear stress to hardness, the estimations of $\sigma \approx 3\tau$ and $H_v \approx 3\sigma$ are used in the present study. By using G = 78 GPa, b = 0.254 nm, and v = 0.33, the peak hardness is

calculated to be ~ 6 GPa when the grain size is reduced to ~ 10 nm. This value is similar to what has been observed in sputtered nanotwinned 330 SS, where the hardness is ~ 6.5 GPa with average twin density is ~ 5 nm.

As a model alloy, the microstructure and microhardness of the Fe-Cr-Ni alloy are thermally stable up to 673K. To meet the requirement of future advanced nuclear reactors, methods, like alloying and addition of oxide particles, will be used to improve thermal stability and develop radiation resistant structural materials for higher temperature applications.

A3. He ion radiation damage of ultra fine grains in ECAPed Fe-14Cr-16Ni (wt.%) alloys

Lead organization (Texas A&M, Xinghang Zhang)

The Fe-14%Cr-16%Ni ternary alloy, with initial average grain size of 700 μm, was fabricated by vacuum cast and subsequent hot isostatic pressing. ECAP process was used to refine the grain size of the Fe-Cr-Ni alloy down to ~ 400 nm. Helium ions at an energy of 100 keV were implanted to coarse grained and ultrafine grained Fe-Cr-Ni alloy at room temperature to a fluence of $6 \times 10^{16}/cm^2$. Transmission electron microscopy (TEM) experiment was performed on a JEOL 2010 transmission electron microscope operated at 200 keV. Cross-sectional TEM (XTEM) samples were prepared by dimpling and low energy (3.5 keV) Ar ion milling. The artifacts induced by Ar ion milling were removed by low energy ion polishing process. Hardness and elastic modulus were measured at room temperature by Fischerscope HM 2000XYp instrument with a Vickers diamond indenter, using instrumented nanoindentation technique.

SRIM, based on Monte Carlo method, was used to calculate the defect and ion distribution in Fe-14Cr-16Ni compound irradiated by He ions at 100 keV with a fluence of 6×10^{16} ions/cm^2. The simulation, as shown in Fig.3.1, predicts that the peak damage induced by He collisions in the compound is ~ 5.5 dpa at a depth of ~ 250 nm, and the radiation damage extends to a maximum depth of ~ 480 nm. The peak He concentration, with a value of ~ 4.0 at.%, occurs at a depth of ~ 320 nm.

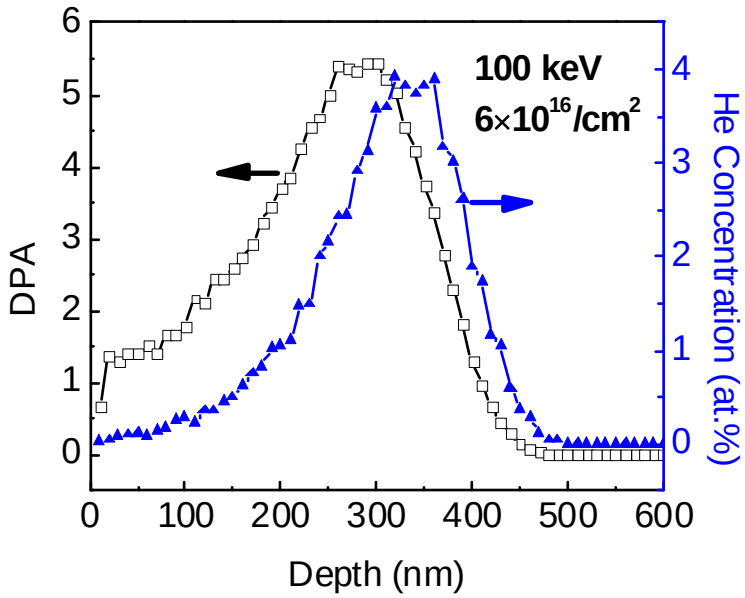

Figure 3.1. Depth profile of radiation damage (displacement per atom (DPA)) and Helium concentration obtained from SRIM simulation for Fe-14Cr-16Ni alloy subjected to He ion irradiation at 100keV and a fluence of $6 \times 10^{16}/cm^2$.

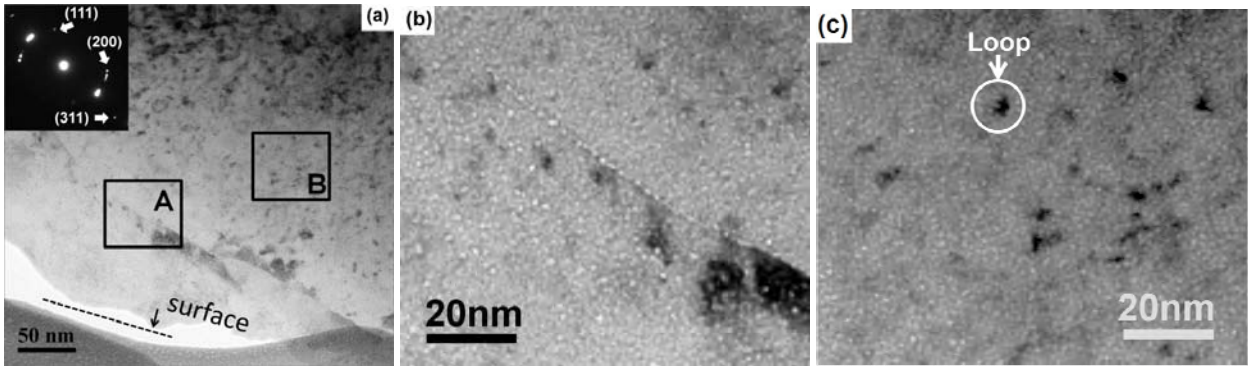

Figure 3.2. (a) Under focused XTEM micrograph of He ion irradiated CG Fe-Cr-Ni alloy. (b) The magnified image of region A shows bubbles align along grain boundaries. (c) The magnified image of region B shows dislocation loops and high density of He bubbles.

Under-focused bright field XTEM micrographs of as-received, coarse grained (CG) Fe-14Cr-16Ni alloy after He ion irradiation are shown in Fig. 3.2. Fig. 3.2 (a) presents an overview of the irradiated region, wherein He bubbles can be clearly observed. Magnified micrographs of

two regions, A and B in Fig. 3.2 (a), are shown in Fig. 3.2 (b) and Fig. 3.2 (c), respectively. Bubbles appear at a depth of ~ 100 nm from surface as shown in Fig. 3.2 (b). The maximum bubble density occurs approximately at 250 nm underneath the surface in ion irradiated Fe-Cr-Ni alloy, as shown in Fig. 3.2 (c). The black dots in Fig. 3.2(c) are dislocation loops created by displacement damage. Fig. 3.3 presents the microstructures of ultrafine grained (UFG) Fe-Cr-Ni alloy after helium ion irradiation at the same condition. Fig. 3.3 (a) shows the radiation damge region in the ion irradiated UFG Fe-Cr-Ni alloy. Grain boundaries and high density of dislocations produced by severe plastic deformations can clearly be observed. Fig. 3.3 (b) and Fig. 3.3(c) shows the magnified images of region A and B in Fig. 3.3 (a), respectively. Again in the surface region where radiation dose is low as shown in Fig. 3.3(b), He bubbles are observed. The density of He bubbles reaches a maximum in the region of peak dpa as shown in Fig. 3.3(c).

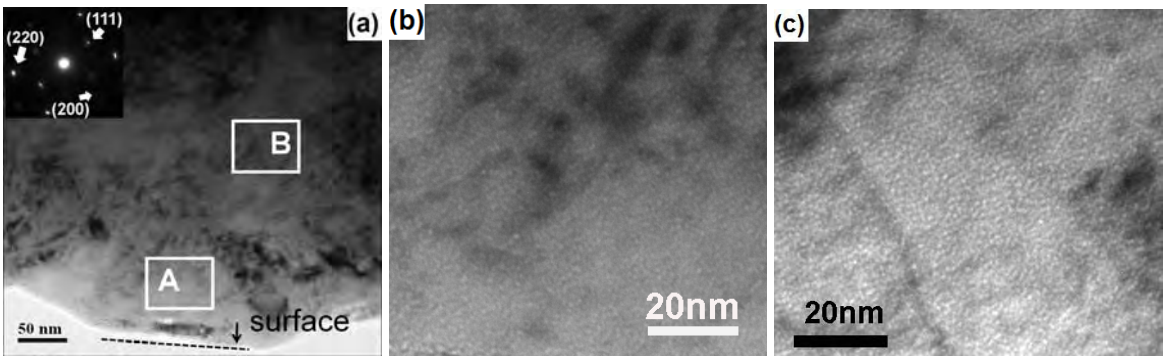

Figure 3.3. (a) Under focused XTEM micrograph of He ion irradiated UFG Fe-Cr-Ni alloy. (b) The magnified image of region A in Fig.5 (a). (c) The magnified image of region B in Fig.5 (a) shows bubbles, but dislocation loops are not detected.

He bubble density distribution at different depth is calculated from XTEM measurement, and the thickness of TEM sample is assumed to be ~ 50 nm. Fig. 3.4 compares the depth dependence of bubble density in irradiated CG and UFG Fe-Cr-Ni alloy. The peak bubble density and average bubble density of irradiated UFG Fe-Cr-Ni alloy are lower than those in irradiated CG Fe-Cr-Ni alloy. The peak bubble density appears at a depth of ~ 250 nm in CG Fe-Cr-Ni alloy, which is deeper than that in UFG alloy, ~200 nm.

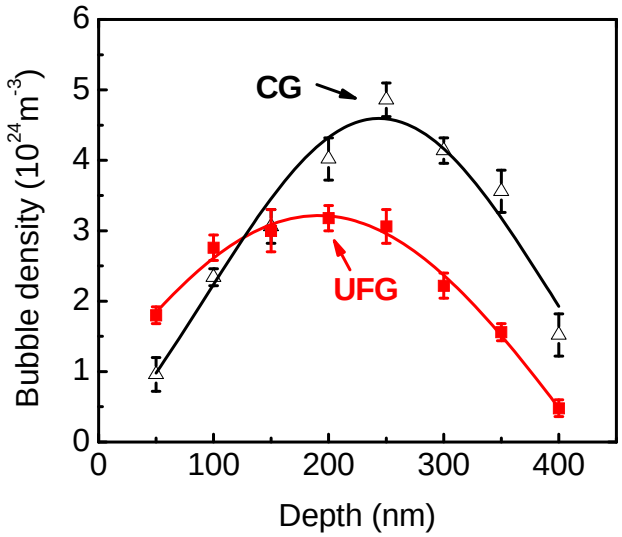

Figure 3.4. Depth dependent He bubble density in irradiated CG (open triangles) and UFG (solid squares) Fe-Cr-Ni alloy. He bubble density in the peak damage region is reduced by in UFG alloy. Also the peak bubble density in UFG alloy appears at a shallower depth with respect to film surface.

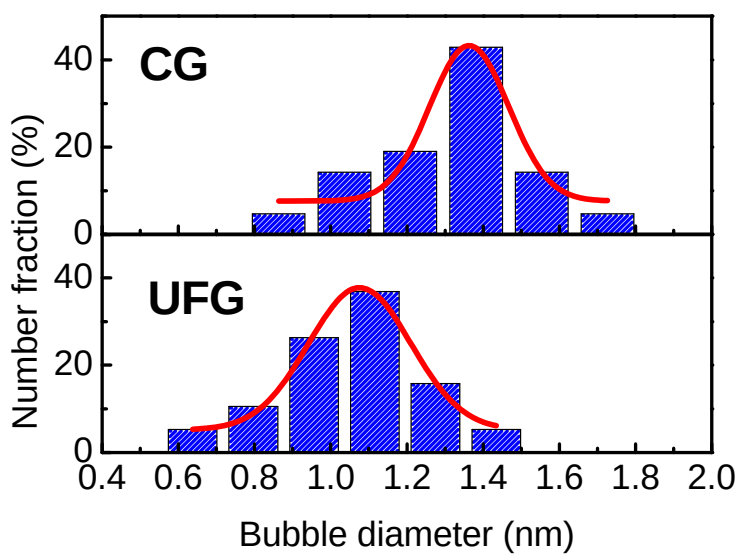

Figure 3.5. Bubble diameter distribution in the peak damage region of He irradiated CG and UFG Fe-Cr-Ni alloy. The average bubble diameter in CG and UFG Fe-Cr-Ni alloy is 1.3 nm and 1.0 nm, respectively.

Fig. 3.5 presents the bubble diameter distribution in the irradiated CG and UFG Fe-Cr-Ni alloy at the peak damage region, obtained by under-focused XTEM micrographs. The average bubble diameter in irradiated CG and UFG Fe-Cr-Ni alloy is ~1.3 nm and ~1.0 nm, respectively.

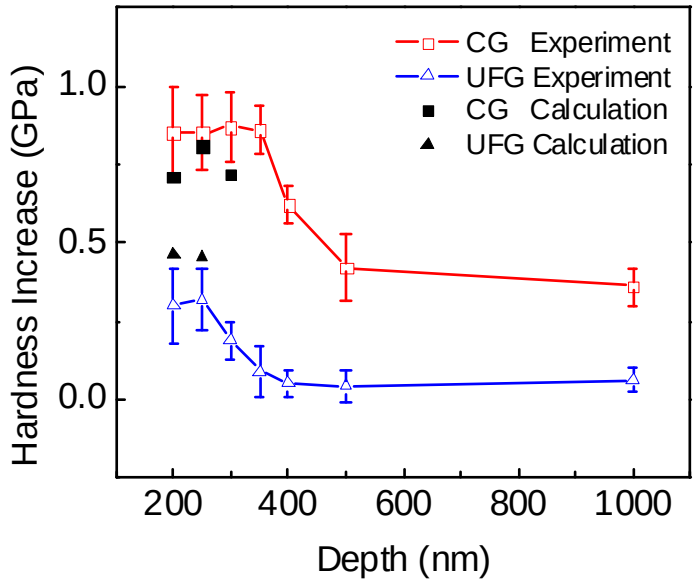

Figure 3.6. Hardness increase ($H_{\text{after ion irradiation}}$-$H_{\text{before ion irradiation}}$) of CG and UFG Fe-Cr-Ni alloy after He ion irradiation as a function of indentation depth. Radiation hardening in CG and UFG Fe-Cr-Ni alloy is indicated by open squares and open triangles, respectively. The calculated radiation hardening due to He bubbles in the peak damage region, shown by solid squares and triangles are compared with experimental values in the same figure.

The hardness evolution of CG and UFG Fe-Cr-Ni alloys after ion irradiation is examined at indentation depth of 200 nm to 1.0 µm and results are shown in Fig. 3.6. The hardness increase in CG Fe-Cr-Ni alloy is a relatively constant value, ~ 0.9 GPa, when indentation depth is between 200 and 350 nm. At greater indentation depth, the radiation hardening appears reduced and finally saturates at a level of ~ 0.35 GPa. The depth dependent radiation hardening in UFG Fe-Cr-Ni alloy follows a similar trend. But the magnitude of hardening at all depth is much lower than those in CG specimen. The maximum hardening in UFG specimen is ~ 0.32 GPa, about 65% less than that in the irradiated CG Fe-Cr-Ni alloy at a depth interval of 200-250 nm. Whereas when h > 250 nm, the magnitude of radiation hardening reduces to ~ 0.05 GPa.

The following section presents our interpretations of microstructure evolution and its correlation to radiation hardening in CG and UFG alloys.

Microstructure evolutions.

Helium bubbles have been observed in both ion irradiated CG and UFG Fe-Cr-Ni alloy. Compared to irradiated CG materials, the reduction of peak and average He bubble density in

irradiated UFG Fe-Cr-Ni alloy indicates that the overall concentration of vacancies must have been reduced. During radiation, vacancies and interstitials are generated as a result of displacement cascade. These point defects can be annihilated through direct recombination, absorbed via pre-existing defects, such as layer interfaces, dislocations, grain boundaries, cavities, etc., or aggregated into clusters, such as helium bubbles and interstitial loops. ECAP induced a very high density of high angle grain boundaries as well as dislocations which can act as effective defect sinks for the recombination of the irradiation induced point defects. And consequently ECAP specimen should possess lower density of defect clusters, as evidenced by a lower density of He bubbles and fewer interstitial loops.

The internal pressure in a pressurized helium bubble is expressed by:

$$p = \gamma / 2r$$

where p is the pressure, γ is the surface energy, $\gamma = 2N/m$ for stainless steel, and r is the average radius of the bubbles. The hard sphere equation of state (EOS), Carnahan-Starling EOS, is applied to calculate the He density in a nano-scale bubble with high pressure at 20°C:

$$\frac{pV}{NkT} = (1 + y + y^2 - y^3)(1 - y)^{-3}$$

$$y = \frac{\pi d^3}{6} \bullet \frac{N}{V}$$

where V is the volume of the bubble, N is the number of the atoms, d is the diameter of the atom , T is the temperature and k is the Boltzmann's constant. Based on the above equations, the average He density in a bubble is 0.21cm^3/mol for CG Fe-Cr-Ni alloy, and 0.19 cm^3/mol for UFG Fe-Cr-Ni alloy.

Hardening mechanisms

It is generally accepted that the irradiation induced hardening and embrittlement are caused by the interaction between dislocations and irradiation-produced obstacles such as defect clusters, loops, precipitates, void, etc. Two major mechanisms were proposed to explain the radiation hardening: source hardening, the increase in critical stress required to move a dislocation on its slip plane due to the pinning effect of the obstacles; and friction hardening, where the dislocation movement is impeded by the radiation-induced defects lying close to or on its slip plane. Compared with the friction hardening, the contribution of source hardening is

relatively small. Two types of radiation induced defects, strong obstacles such as interstitial loops, and weak obstacles like He bubbles, result in friction hardening. Two dislocation barrier models, dispersed barrier model for the strong obstacles such as interstitial loops, voids, SFT etc. and Friedel-Kroupa-Hirsch (FKH) model for weak obstacles like helium bubbles, have been proposed to describe the radiation induced friction hardening in metals.

In a low temperature range, $T \leq 0.4T_m$ (T_m is the melting temperature), the contribution of helium bubbles to the radiation hardening is very small at low helium concentration and it becomes significant only when the He concentration is above a critical value, ~ 1 at.%. SRIM simulation predicts that the helium concentration in the peak damage region is about 4 at.%. In this study, the weak obstacle model, FKH model, is used to estimate the radiation induced yield strength increase, $\Delta\sigma$,

$$\Delta\sigma = \frac{1}{8} M\mu b d (N)^{2/3}$$

where M is Taylor factor, 3.06 for FCC metals, μ is shear modulus, b is Burgers vector, d is the diameter of the bubble, N is bubble density. On the basis of the above model, the calculated radiation hardening, estimated as three times that of the calculated $\Delta\sigma$, is indicated by solid squares and triangles for the CG and UFG Fe-Cr-Ni alloy, respectively, in Fig. 3.6. The results show that the calculated radiation hardening in the peak damage region is comparable to the experimental value. Besides helium bubbles, dislocation loops may also contribute to the radiation hardening. It's difficult to distinguish the helium bubbles induced hardening and dislocation loops induced hardening. From the XTEM images, the dislocation loop density is very low and the average loop size is ~ 4 nm, and thus the contribution of dislocation loops is very small based on the dispersed barrier hardening model.

A4. In situ Kr ion irradiation of coarse grained and nanocrystalline (NC) Ni

Lead organization (Texas A&M, Xinghang Zhang)

NC Ni was synthesized by pulse electrodeposition from sulfamate electrolytes. Annealing of the as-deposited NC Ni in a vacuum furnace (10^{-7} torr) at 400°C for 2 hours was performed to obtain coarse grained (CG) Ni. Plan-view transmission electron microscopy (TEM) samples were prepared by ion milling and subsequent ion polishing. Convergent beam electron diffraction (CBED) technique was used to estimate the Ni foil thickness.

SRIM simulation was used to estimate the displacement damage profile and Kr^{++} ion distribution. Displacement energy for Ni, 40 eV, was used to calculate the displacements-per-atom (dpa). The results show that all the Kr^{++} ions with energy of 1 MeV will penetrate through the first 200 nm, whereas displacement damage will be contained primarily in the TEM foil. *In situ* Kr^{++} ion irradiation with energy of 1 MeV was conducted at room temperature in the Intermediate Voltage Electron Microscope (IVEM) at Argonne National Laboratory, where an ion accelerator is attached to a HITACHI H-9000NAR microscope. The microscope was operated at 200 kV and kept on during radiation in order to record the microstructural evolution. The average dose rate was 0.003 dpa/s.

Fig. 4.1a and b show that the average grain size of CG and NC Ni is 2.5 µm and ~ 55 nm respectively. Fig. 4.2 presents the TEM images of CG Ni after Kr^{++} ion irradiation at room temperature to a dose of 1 and 5 dpa. At 1 dpa (Fig. 2a-b) the primary radiation induced defects were the high-density dislocation loops, as revealed by black (white) dots in the corresponding bright (dark) field (BF and DF) TEM micrograph. Up to 5 dpa, dislocation loops joint together to form high density of dislocation segments and networks as shown in the corresponding BF and DF TEM micrographs in Fig. 4.2c-d. The loop density was ~ $1.76 \times 10^{23}/m^3$ at 5 dpa, and density of dislocation segments increased from ~ $2\times10^{12}/m^2$ to ~ $7\times10^{13}/m^2$. Defects appeared to accumulate along the grain boundaries as shown in Fig. 4.2d in form of large bright defect clusters. The same DF TEM micrograph also revealed high density of dislocation loops in one grain, and extremely high density of bright stripes in the other grain.

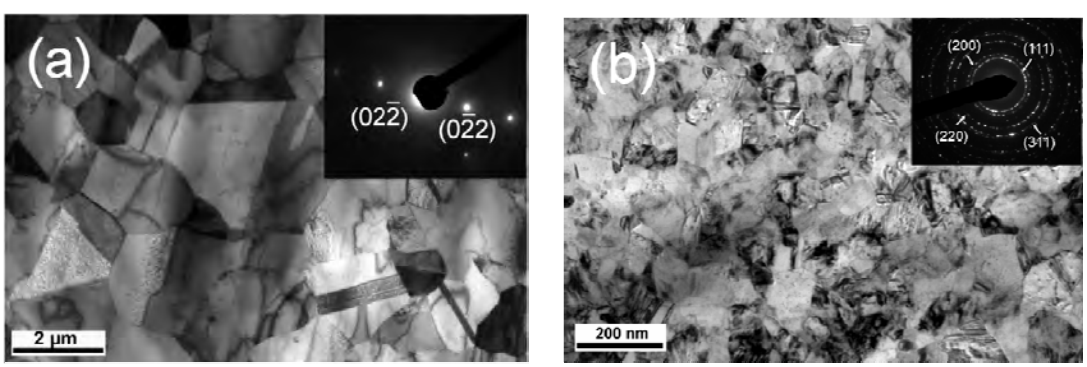

Fig. 4.1 (a) Coarse grained (CG) Ni with an average grain size of 2.5 µm. (b) Nanocrystalline (NC) Ni with an average grain size of 55 nm.

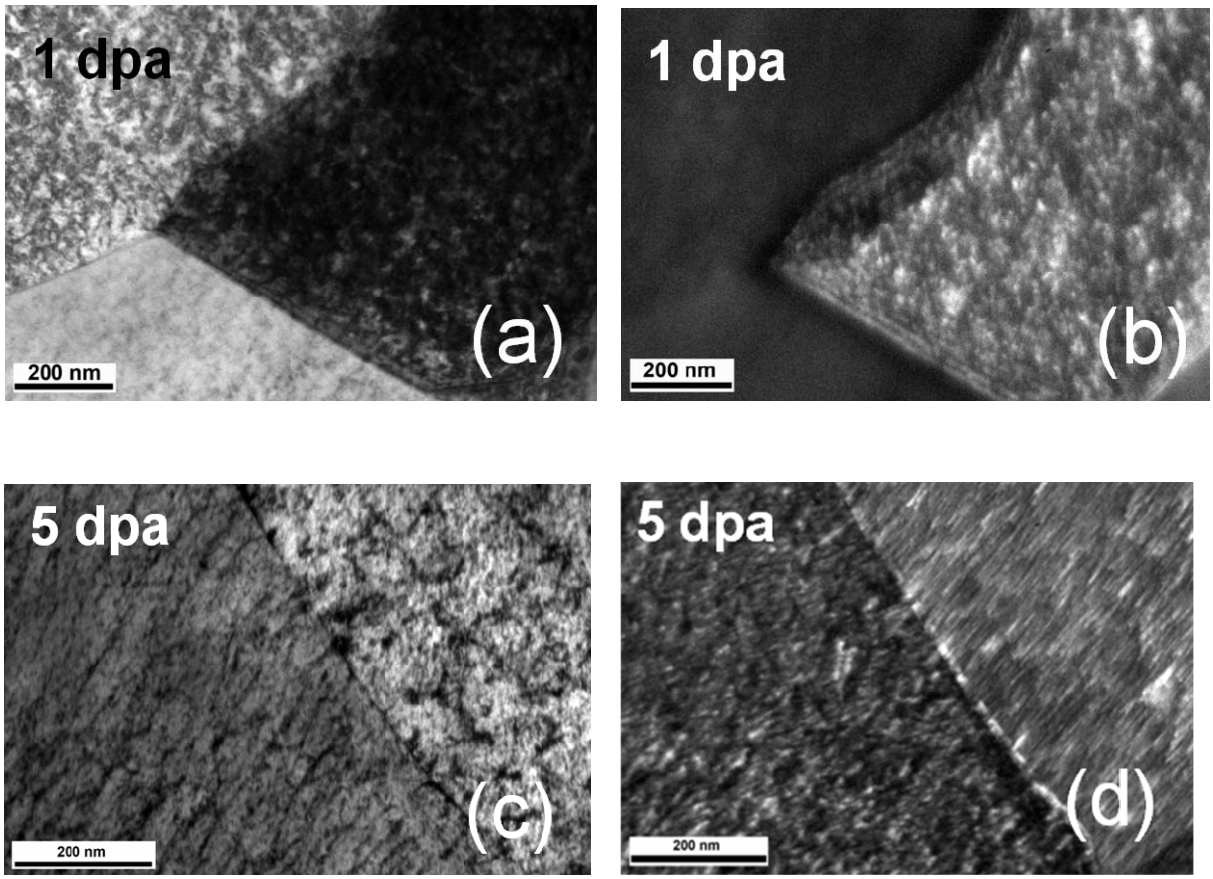

Fig. 4.2. TEM images of room-temperature, Kr^{++} ion irradiated CG Ni. (a) After irradiation up to 1 dpa, high density black dots (dislocation loops) were identified. (b) The corresponding dark field (DF) TEM image confirmed the formation of dislocation loops. (c) At 5 dpa, dislocation loops are still evident, and many of the loops joint together to form dislocation segments and networks. The density of dislocation loops and dislocation segments was ~ $1.76 \times 10^{23}/m^3$ and $7 \times 10^{13}/m^2$. (d) The corresponding DF TEM image revealed the formation of both types of defects.

Fig. 4.3 shows the BF and DF TEM images of irradiated NC Ni to a dose of 1 and 5 dpa. At 1 dpa and 5 dpa, dislocation loops were observed sporadically in NC Ni. Compared to Fig. 4.2, the defect cluster density was significantly lower in NC Ni, and no significant dislocation segments were observed.

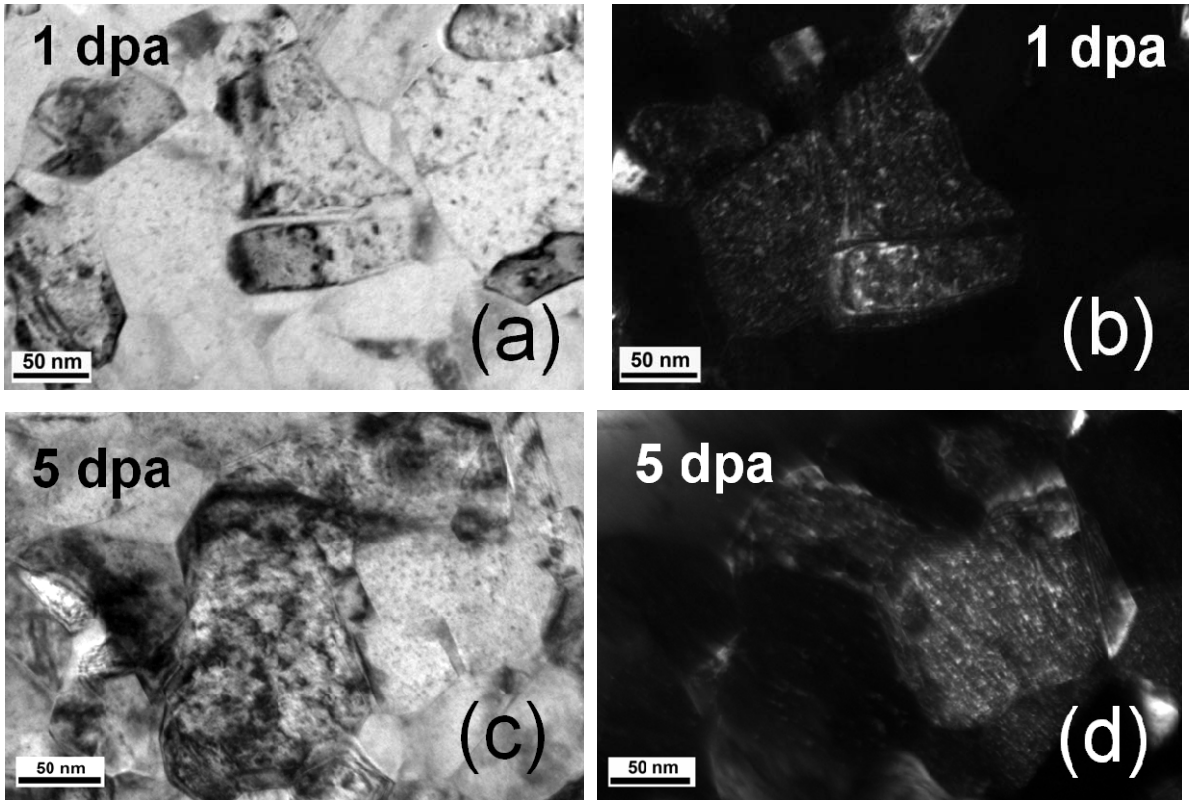

Fig. 4.3. TEM images of NC Ni subjected to Kr^{++} ion irradiation up to 1 and 5 dpa. (a) and (b) are corresponding BF and DF TEM micrographs of the specimen at 1 dpa. Dislocation loops were observed sporadically. (c) and (d) are BF and DF TEM micrograph taken at 5 dpa. More dislocation loops were observed, but no significant dislocation networks were generated. The density of dislocation loop was ~ $8.40 \times 10^{22}/m^3$.

Fig.4.4a shows the low magnification TEM image of NC Ni irradiated to 5 dpa. No significant grain growth occurred and there was no obvious change of diffraction pattern. Comparisons of the statistical distribution of grain sizes (Fig. 4.4b) show that, after radiation, the average grain size slightly increased from 55 to 62 nm.

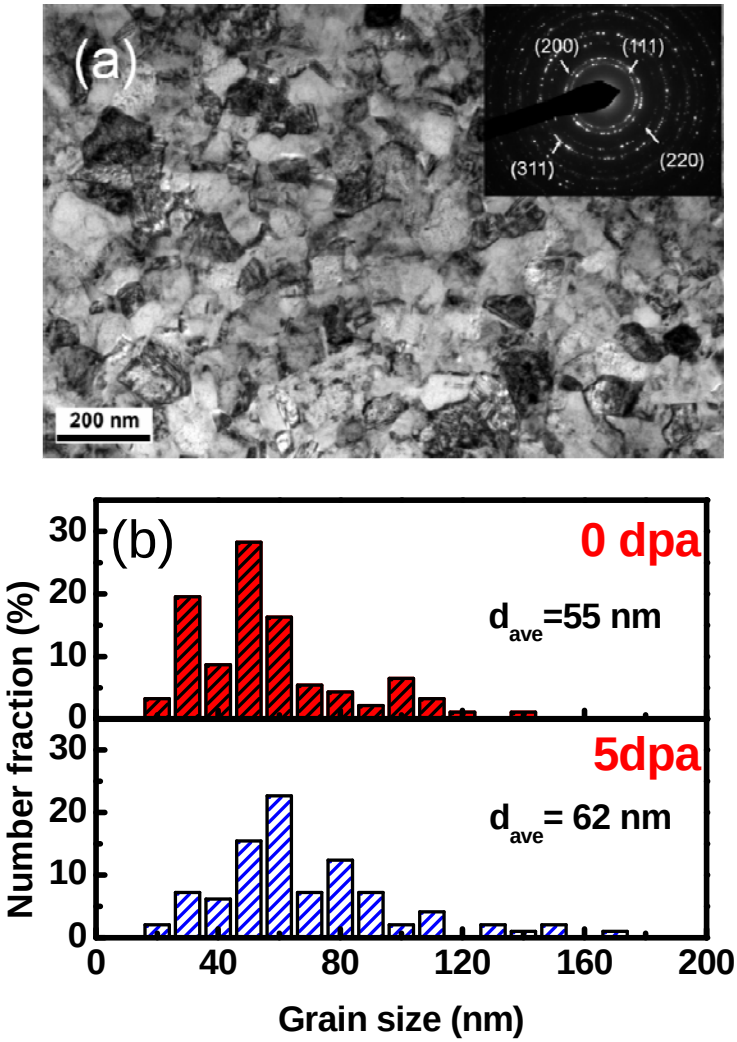

Fig. 4.4. (a) A low magnification of TEM image of NC Ni irradiated upto 5 dpa. (b) Statistic study shows that there was insignificant grain growth after radiation.

Fig. 4.5 illustrates the evolution of density of defect clusters (dislocation loops) vs. radiation dose. In irradiated CG Ni, the density increased rapidly within 0.1 dpa, and saturated thereafter. In comparison, the density of defect clusters increased moderately and gradually in NC Ni, and saturation occurred at greater dose, ~ 3-5 dpa. What is more, at 5 dpa, the density of defect clusters in NC Ni was measured to be ~ 8.4 $\times 10^{22}/m^3$, approximately 2 times lower than that in CG Ni. Fig.4.6 reveals the evolution of diameter of defect clusters during radiation. In CG Ni, the defect diameter increased linearly, from 5 to 7.5 nm by 2 dpa, and saturated afterwards;

whereas in NC Ni, the diameter of defect clusters remained ~ 3.5 nm throughout the radiation process.

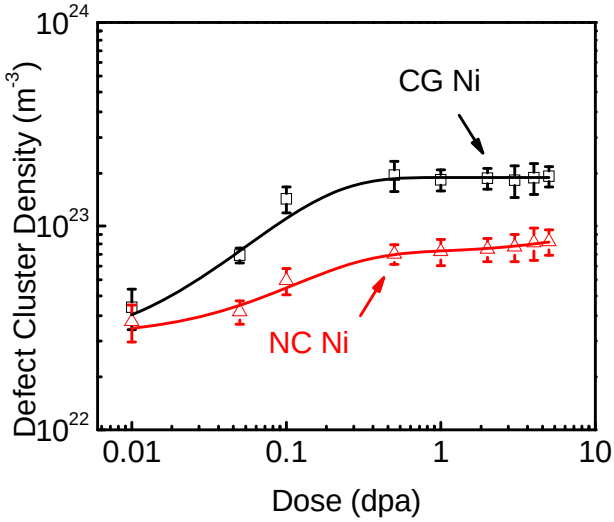

Fig. 4.5. The density of dislocation loops of CG Ni increased rapidly within 0.1 dpa and appeared to reach saturation at ~ 0.5 dpa. Meanwhile the density of loops in NC Ni increased slowly and gradually throughout the radiation up to 5 dpa. Dislocation loop density of CG and NC Ni increases with dose in the beginning stage and then saturates to certain level. At 5 dpa, the average loop density of CG Ni is 2 times greater than that of NC Ni.

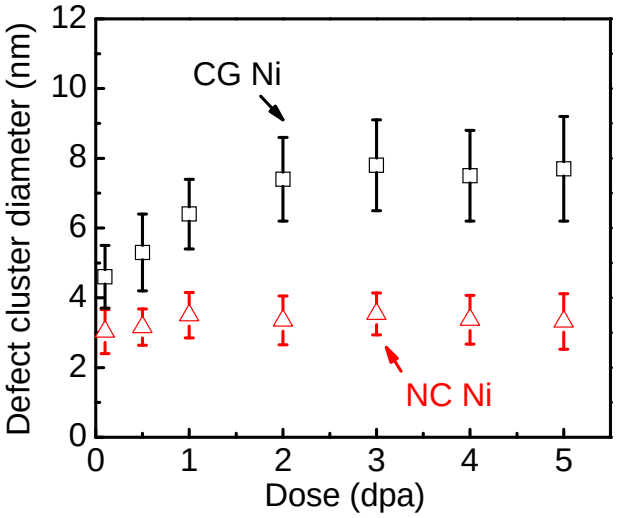

Fig. 4.6. Dose dependent evolution of loop diameters. The diameter of loops in CG Ni increased promptly from 5 to ~ 7.5 nm by 2 dpa, and reached a plateau thereafter. In parallel, the loop diameter of NC Ni remained ~ 3.5 nm over the dose of 5 dpa.

The absorption of dislocation loops by GB was frequently observed during the *in situ* Kr^{++} ion irradiation of NC Ni. Fig.4.7 shows a typical example of microstructural evolution of NC Ni irradiated over a dose of 1.67 - 1.72 dpa at room temperature, during which the absorption of individual interstitial loops by GBs was observed. As shown in Fig. 4.7a, an interstitial loop, ~ 4.5 nm in diameter, was observed next to GB. With 49 seconds (Fig. 4.7b), the loop diffused towards the GB and the diameter of the loops shrank to ~ 3.8 nm. After 49.1 s, the loop was immediately sucked into the GB, and by 49.3 s, a majority of the loop was removed by the GB. Fig. 4.8 shows an example of frequently observed absorption of dislocation segments by GBs at a dose spanning over 0.56-0.79 dpa at room temperature in 78 seconds. The arrows identify several interstitial loops of interest. Initially (Fig. 4.8a) there were three interstitial loops adjacent to the grain boundary. The closest separation distance between the grains is 8.6 nm. After 13 seconds (Fig. 4.8b), these individual loops combined together into one dislocation segment. By 28 s (Fig. 4.8c) the leading dislocation segment was absorbed by GB. In 78 s (Fig. 4.8d), the remaining dislocation segment was absorbed by the GB. After radiation, the closest separation between the two grains reduced to 6.9 nm.

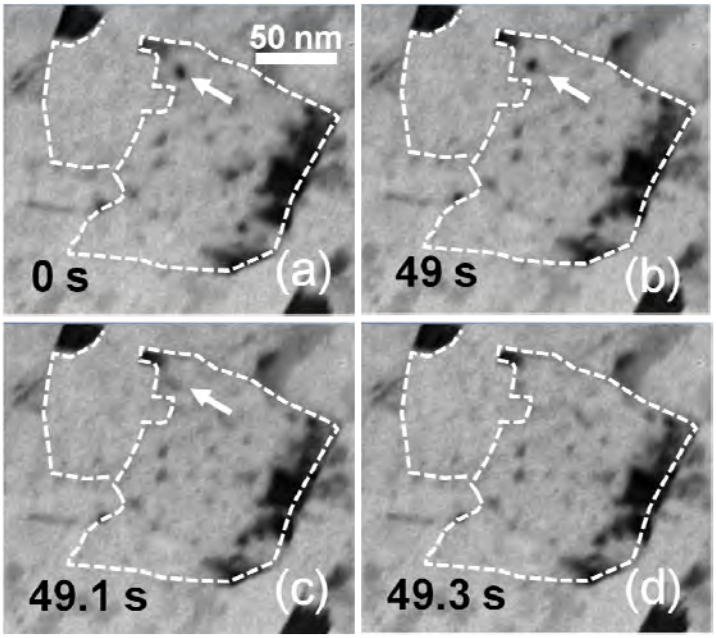

Fig. 4.7. *In situ* evidence of absorption of individual loops by grain boundaries of NC Ni. The radiation dose increased from 1.67 to 1.72 dpa within 49.3 seconds. (a) The loop, pointed by an arrow, was revealed near grain boundaries. (b) In 49 s, the loop diffused towards the grain boundary accompanied by the continuous reduction of their diameters. (c) By 49.1 s, the loop rapidly migrated towards the grain boundary. (d) By 49.3 s, the loop was fully absorbed and annihilated by the grain boundaries.

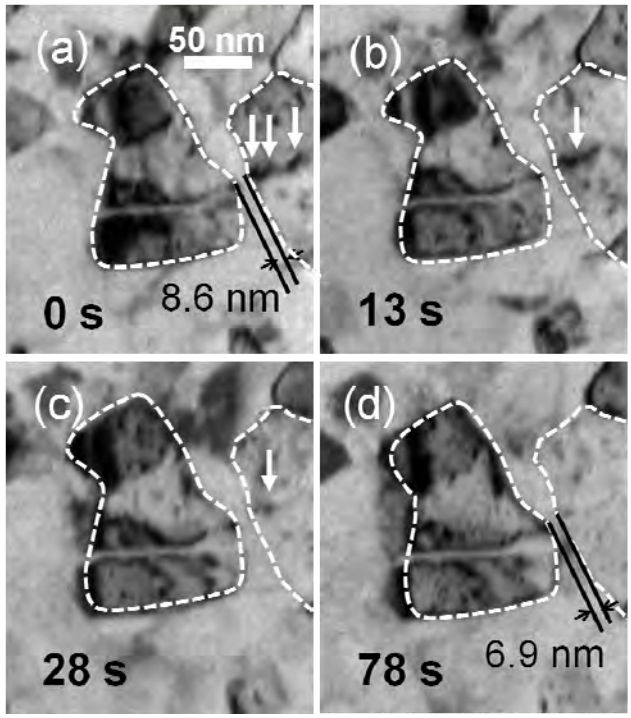

Fig. 4.8. *In situ* evidence of absorption of dislocation segment by grain boundaries of NC Ni. The radiation dose increased from 0.56 to 0.79 dpa at room temperature within 78 seconds. Interaction between grain boundary and dislocation segment is clearly observed. The arrows represent the dislocation loops. (a) Three discernible dislocation loops were located near the grain boundary, and the closet separation between the two grains is 8.6 nm. (b) With 13 seconds, the loops combine and become one dislocation segments. (c) By 28 second, the dislocation segment was absorbed continuously by the adjacent grain boundary. (d) By 78 seconds, a majority of the dislocation was absorbed except a single dislocation loop in contact with the grain boundary. Meanwhile the closet distance between the two grains is reduced to be 6.9 nm.

From the evolution of the defect density with dose, it is evident that the rate of increase of defect density in NC Ni is much less than that in CG Ni, and that the saturated density of defect clusters is also reduced by ~ 50% through grain refinement. These defect clusters were formed by the aggregation of point defects. Point defects can be removed either through the recombination of interstitials and vacancies or by the absorption by GBs (as revealed by in situ experiments), dislocations, and precipitate, etc. In monolithic NC Ni, we assume that GBs are the primary defect sinks. The concentration of point defects ($C_\theta, \theta = i$ for interstitials and $\theta = v$ for vacancies) can be expressed by a chemical rate equation as:

$$\frac{\partial C_\theta}{\partial t} = K - R_{\theta\theta'} C_\theta C_{\theta'} - S_{gb} D_\theta C_\theta \quad (1)$$

where t is time, K is the atomic displacement rate; when $\theta = i$, then $\theta' = v$; D_i and D_v are the respective diffusion coefficients for interstitials and vacancies; R_{iv} is the recombination rate of interstitial and vacancy. $R_{iv} = 4\pi(D_i + D_v) r_{i,v}$, where $r_{i,v}$ is ~ 0.72 nm. S_{gb} is the GB sink strength. For NC Ni, $S_{gb} = 24/d^2$, where d is grain size, and for CG Ni, $S_{gb} = 10^{15} m^{-2}$. D_i and D_v are calculated based on the migration energy of interstitials and vacancies, E_i and E_v, respectively. For Ni at 300K, E_i = 0.14 eV, and E_v = 1.3 eV. When the steady state concentration of interstitials and vacancies, C_i^s and C_v^s , is reached, setting $\frac{dC_i}{dt} = \frac{dC_v}{dt} = 0$, leads to:

$$C_\theta = -\frac{S_{gb} D_{\theta'}}{2R_{iv}} + [\frac{K}{R_{iv}} (\frac{D_\theta}{D_{\theta'}}) + (\frac{S_{gb} D_{\theta'}}{2R_{iv}})^2]^{1/2} \quad (2)$$

Given significant grain size difference in CG Ni (~2.5μm) and NC Ni (~ 55 nm) , we can calculate the ratio of concentration of interstitials and vacancies in CG and NC Ni at steady state: $C_i^{CG} / C_i^{NC} \approx C_v^{CG} / C_v^{NC} = 7.87$. This analysis testifies that GBs in NC Ni can effectively reduce the concentration of point defects.

In situ radiation experiments showed that the density and diameter of dislocation loops in CG Ni was ~ two times that of NC Ni. For the loops on {111} planes, we estimate the number of point defects, n, in each dislocation loop by using the relationship:

$$r_L = (\sqrt{3} a^2 n / 4\pi)^{1/2} \quad (3)$$

where r_L is the dislocation loop radius and a is the lattice parameter. Thus, we arrive that the concentration ratio of point defects in CG and NC Ni is ~ 8, close to the results from aforementioned calculation.

From *in situ* radiation experiments, Fig. 4.8, it is clear that the size of the individual dislocation loops became smaller while the loops moved towards GBs, and eventually being absorbed rapidly into the GB. In this case, the shrinkage of the dislocation loop and its absorption by the GB are diffusion-controlled processes, which is most likely to be the diffusion-controlled climb when the radiation experiments are performed at temperatures below $0.5T_m$

(where T_m is the melting temperature of the specimen). As GBs are sinks for vacancies, the concentration of the vacancies near GBs will be lower than that in the grain, which leads to a vacancy concentration gradient near GBs as shown schematically in Fig. 4.9. In the region 2, far away from the GB, there is a saturation of vacancy concentration induced by radiation. Both ends of interstitial loops can readily absorb vacancies from the bulk matrix, resulting in the reduction of loop diameters. In this region, lattice diffusion is the dominant diffusion mechanism. In region 1, there is a large vacancy concentration gradient adjacent to the GBs. The absorption of vacancies from one end (towards matrix) of interstitial loops will lead to positive climb (towards GB). Simultaneously vacancies will be emitted from the other end (facing GB) of interstitial loop and hence will induce a negative climb. Both processes (absorption and emission of vacancies) will lead to migration of dislocation loops towards GBs. Thus, the rate of migration is expedited in the region close to GBs. The climb rate depends on the emission rate (K_{em}) and absorption rate (K_{ab}) of vacancies. When $K_{em} < K_{ab}$, the loop diameter will shrink during climb. If $K_{em}=K_{ab}$, a fast conservative climb via pipe diffusion will occur. The rate of absorption of the dislocation loops by GBs depends on at least the following two factors. First, the separation distance between loops and GBs. At a large separation distance, loops perform random walk by lattice diffusion, experiencing insignificant influence of the GBs. Second, the loop diameter. More vacancies need to be absorbed and/or emitted for the loops of larger diameter, increasing the activation energy for pipe diffusion. The *in situ* studies presented here showed that individual loops are more readily absorbed by GBs than a string of loops, i.e., dislocation segments. Wirth et al. also reported that the smaller cluster is more mobile than larger ones at low temperature.

In the bulk region (region 2), where the lattice diffusion dominates, from migration distance observed during *in situ* experiments, we estimate the diffusivity D to be ~ 2.2 nm^2/s by using the Brownian diffusion model. Based on Arrhenius's law, the migration energy for dislocation loops in this region is estimated to be ~ 0.28 eV. This value is very close to the calculated activation energy for bulk diffusion in Ni, ~ 0.2 eV, in which the dislocation loops have diameters of ~ 3.5 nm. In the region near the GBs (region 1), the pipe diffusion is the dominant process for the climb of dislocation loops. The total diffusivity, D_{total}, can be explained by Hart dislocation pipe diffusion:

$$D_{total} = D_1 + gD_0 \exp(-\frac{E_p}{kT}) \quad (3)$$

where the total diffusivity near the grain boundary, D_{total} , was measured to be ~ 40.6 nm^2/s from *in situ* experiments, the lattice diffusivity D_1 =2.2 nm^2/s, g is the fraction of cross section area of the pipes per unit area of the matrix, which is estimated to be ~ 3.4×10^{-5} based on the defect cluster density. The diffusion coefficient of pipe diffusion, D_0, is considered to be the same as lattice diffusion. Therefore, the activation energy for pipe diffusion of the dislocation loops near GBs, E_P , is ~ 0.11 eV, which is ~ 40% of the activation energy for lattice diffusion in the bulk. This result is consistent to Balluffi et al.'s claim that the activation energy for the pipe diffusion is 40%-70% of the activation energy for lattice diffusion. The reduced activation energy for the diffusion of dislocation loops near GBs makes the loop more mobile than those in the bulk region. Meanwhile, these dislocation loops preferentially diffuse towards GB due to the vacancy concentration gradient. Thus fast diffusion processes of the dislocation loops are frequently observed in NC Ni near GBs and consequently loops are frequently absorbed by GBs.

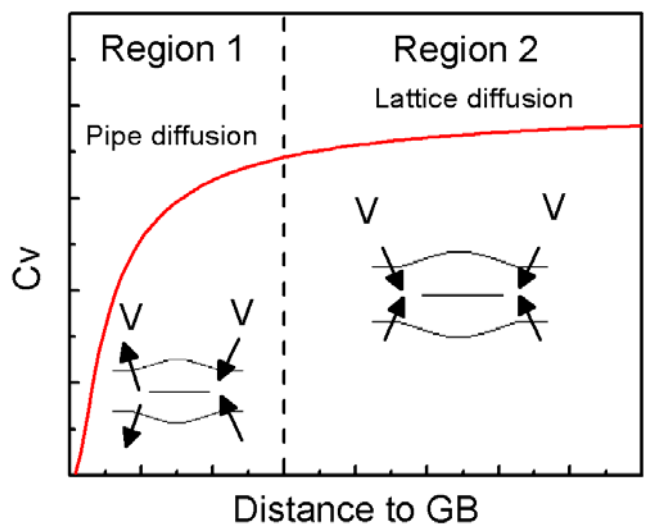

Fig. 4.9. Illustration of the shrinkage and migration of dislocation loops towards GBs. In region 2, further away from GB, the concentration of vacancy induced by radiation approaches a plateau, and the continuous absorption of vacancy leads to the gradual reduction of interstitial loop diameter. In region 1, adjacent to GB, there is a concentration gradient of vacancies. The absorption of vacancy by one end of dislocation loop and corresponding emission of vacancy from the other end (facing GB) lead to rapid migration (climb) of the loop towards GB.

A5. Microstructure Refinement of a 12Cr ODS Steel by Equal Channel Angular

Lead organization (Texas A&M, Xinghang Zhang, K. Ted Hartwig)

The ODS steel powders were prepared by mechanical alloying (MA). The elemental powders were blended with 70 micron of Fe particles, Cr, Ta, V, and W particles of less than 10 microns in diameters, and 20 nm yttrium oxide (Y_2O_3) nanoparticles. The MA processes were carried out using a planetary ball mill operated in a glove box protected by UHP Argon gas. The ball-to-powder ratio was 15:1. The milling time was typically 12 hrs. After degassing, the ball milled powders were consolidated by HIPping (hot isostatic pressing) at 1150 °C for 4 h under 100 atm pressure. The nominal chemical composition (in wt.%) of the present alloy is 12 Cr, 1.1 W, 0.2 V, 0.14 Ta, 0.002 B and 0.3 Y_2O_3 with the remainder being Fe. ECAE processes were carried out on an MTS-controlled hydraulic press with 2.22×10^3 kN force capacity. The ODS rods with diameter of ~ 12 mm were ECAE processed at 700 and 300 °C respectively.

The ECAE processing conditions are summarized in Table 5.1. Processing routes B and C involved billet rotations of 90° and 180° respectively around their long axis prior to the sequent extrusion. A sample extruded two passes at 700 ℃ following route C is designated as 2C700. The hardness was measured by an LM 300AT micro hardness tester using a 0.3 kg force for a loading time of 13 s. X-ray Diffraction (XRD) measurements were carried out on a Bruker-AXS D8 diffractometer.

Table 5.1 ECAE processing condition with sample identifiers.

Identifiers	ECAE route	ECAE temperature (°C)
As-Hipped	–	–
1A300	1	300
2C700	2C	700
2B700	2B	700

Transmission electron microscopy (TEM) was performed using a JEOL 2010 transmission electron microscope operated at 200 kV. Selected area diffraction (SAD) patterns were obtained by using an aperture with a diameter of 1.3 µm. High Resolution TEM (HRTEM) and scanning transmission electron microscopy (STEM) were performed on an FEI Tecnai F20

microscope equipped with a high angle annular dark field (HAADF) detector and an Oxford instruments EDX detector. TEM specimens were electro polished using 10% (volume fraction) perchloric acid methanol solution at −20 °C. Scanning electron microscopy (SEM) was performed on an FEI Quanta 600 microscope operated at an acceleration voltage of 20 kV with a working distance of 10 mm. The SEM samples were electrochemically etched with a KOH solution, which selectively etched the Cr rich phases.

The as-HIPped ODS sample had a bimodal structure as shown by the representative TEM micrograph in Fig.5.1a. The average size of coarse grains was about 2.5 µm and the maximum grain size was ~ 8 µm. The surrounding ultrafine grains were 400 ~ 500 nm in diameter. After 2C processing (2C700), the maximum dimension of coarse grains was effectively refined to below 2 µm and all grains became more equiaxed as shown in Fig.5.1b. When applying route B at the same temperature (2B700), although the same amount of strain was introduced into the specimen, the volume fraction of non-equilibrium grain boundaries and fine grains is greater as shown in Fig.5.1c. After processing via 1A300, a smaller grain size was achieved (Fig.5.1d) compared to that in 2B700. In the ultrafine grain zone, shown in Fig.5.2, grain refinement was not as pronounced. The density of dislocations in grains significantly increased (Fig. 5.2c-d). Also, a greater fraction of high-angle grain boundaries was observed in the 1A300 material as shown by discontinuous rings in the inserted SAD pattern. The d-spacing measurement showed that this steel had predominantly BCC structure, which was confirmed by the XRD profiles (not shown here).

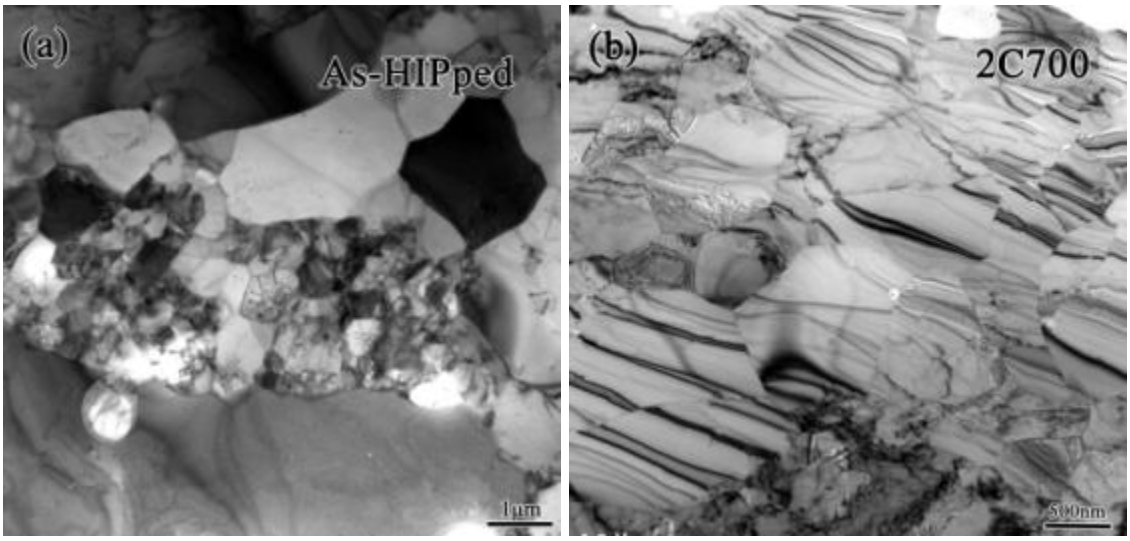

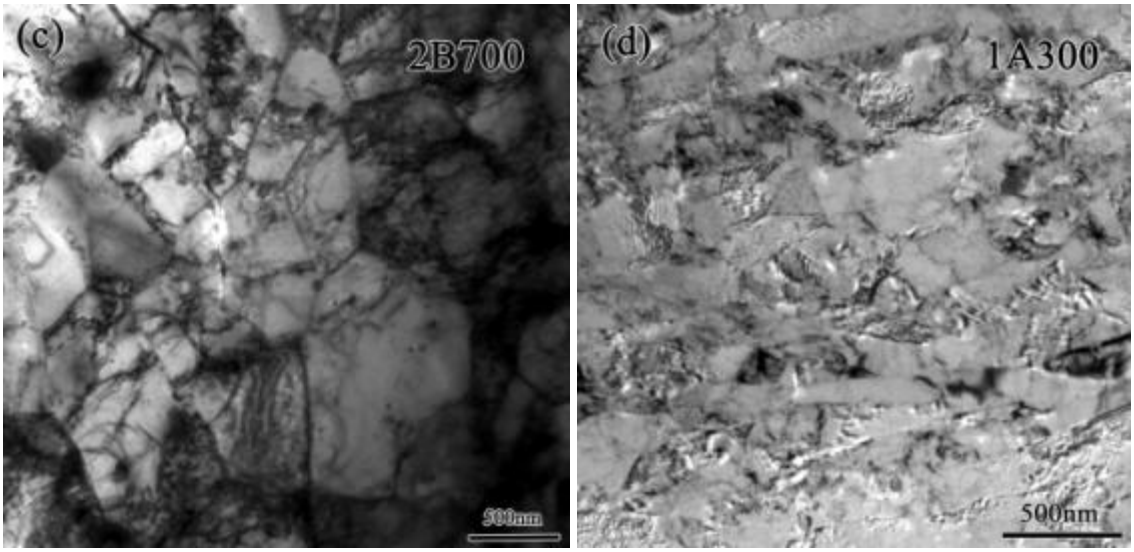

Fig. 5.1.(a) Bright field TEM micrograph of as-HIPped ODS steel having a bimodal structure with larger grains of several microns and puddles of small grains of ~ 460 nm in diameter; (b-d) are TEM micrographs of ODS steel following 2C700, 2B700 and 1A300 ECAE processes.

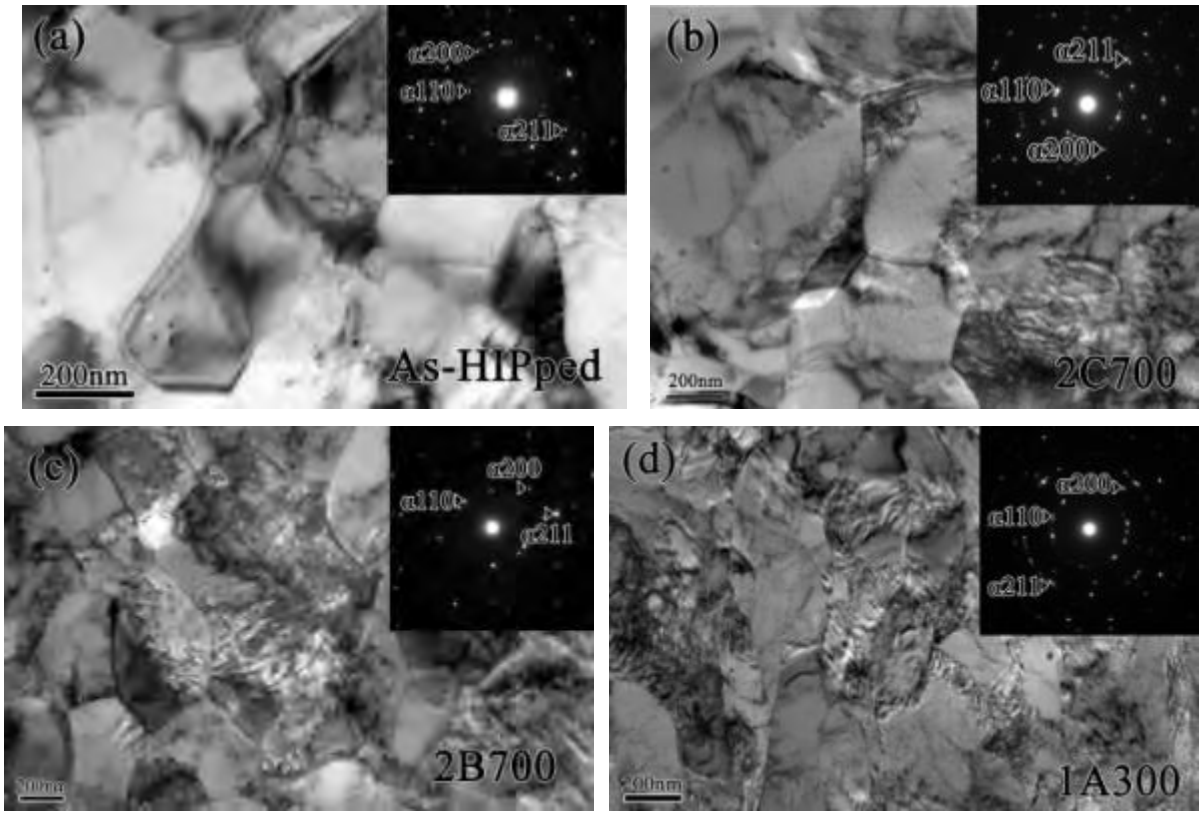

Fig. 5.2. Comparisons of ultra-fine grains in as-HIPped and ECAE processed ODS steels. (a) Ultra-fine grains in as-HIPped ODS steel exhibit interiors that are relatively free of dislocations. After ECAE processing at (b) 2C700, (c) 2B700 and (d) 1A300, the density of dislocations in

grains increases significantly. The inserted selected area diffraction (SAD) patterns show that the ODS steels subjected to ECAE processing have predominant BCC structure.

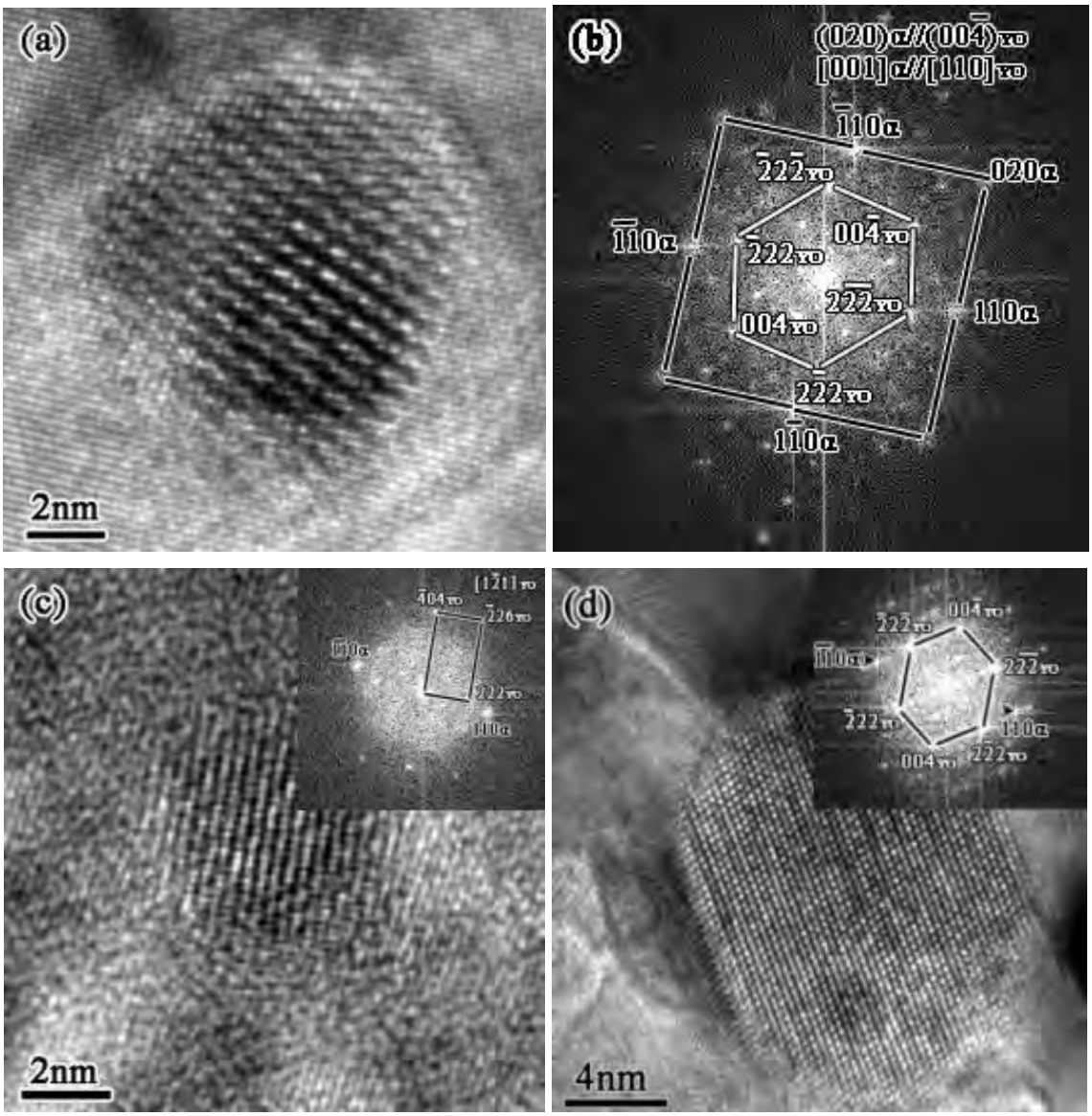

Fig. 5.3. HRTEM images of nanoscale oxide particles in the as-HIPped alloy: (a) medium-size spherical Y_2O_3 particle, about 8 nm in diameter with corresponding (b) FFT pattern shows the orientation relationship between the Y_2O_3 particle and matrix. The zone axis of the oxide particle is [110]. (c) A 4 nm oxide nanoparticle indexed as Y_2O_3 examined along its $[1\,\bar{2}\,1]$ zone axis; and (d) a larger faceted oxide particle examined along the same zone axis as the oxide particle in (a) revealed clear phase boundaries between oxide and matrix.

HRTEM examination was performed to determine the crystalline structure of the oxide particles. As shown in Fig.5.3a, many oxide nanoparticles appear spherical with diameters of ~ 8 nm. Fast Fourier transform (FFT) of the micrograph, in Fig.5.3b, shows that the oxide particle had a BCC Y_2O_3 structure with a lattice parameter of 1.06 nm. The diffraction dots near the central beam are from the secondary diffraction of the matrix spots. The orientation relationship between the crystalline oxide particles and the matrix (denoted as α phase) derived from FFT pattern was determined to be $(020)_\alpha$ // $(00\bar{4})_{Y2O3}$ and $[001]_\alpha$ //$[110]_{Y2O3}$. Smaller and larger oxide particles were also characterized. Many larger oxide particles (Fig.5.3d) had a faceted shape rather than the spherical shape of smaller particles. The corresponding FFT patterns show crystal structure similar to the medium sized particles.

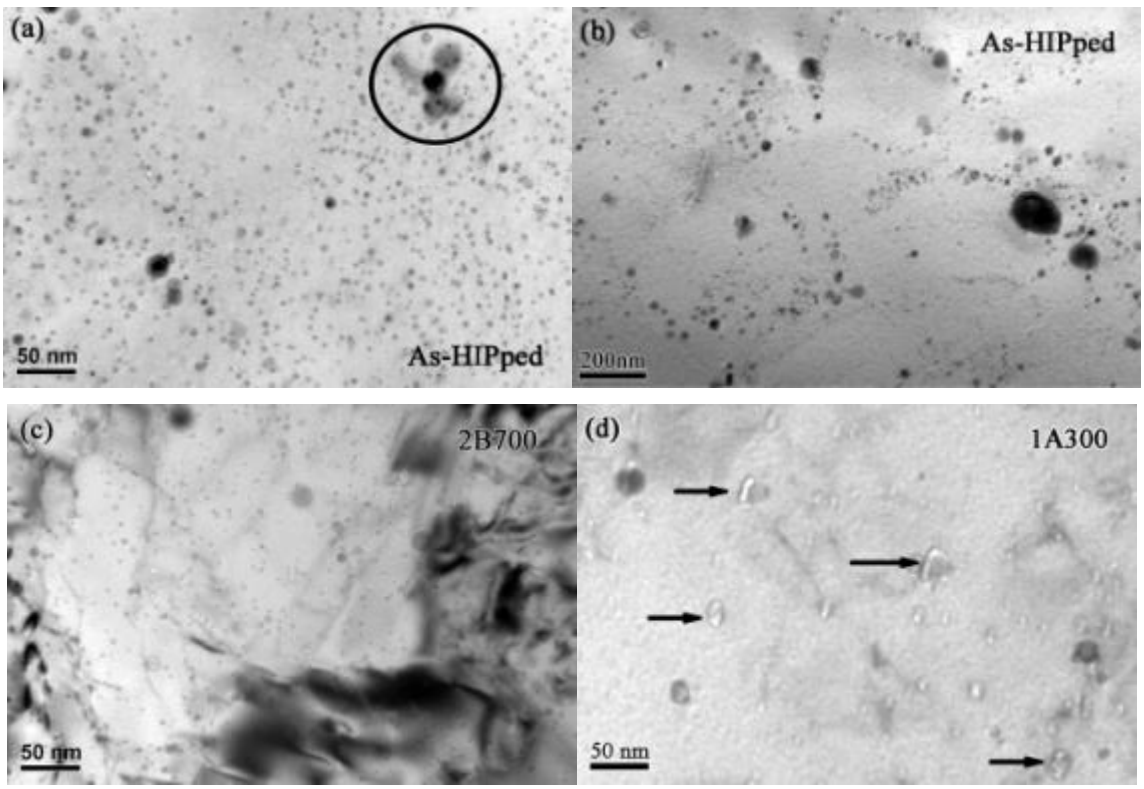

Fig 5.4. TEM micrographs show that (a) oxide particles were randomly distributed in the as –HIPped ODS steel. (b) Oxide particles decorate the grain boundaries of ultra-fine grains in as-HIPped specimen. (c) After ECAE (2B700), oxide particles were more uniformly distributed throughout grains. (d) Numerous oxide particles in ECAE processed samples (1A300) were deformed via shear.

Fig.5.4a shows that oxides particles are well distributed inside certain grains of the as-HIPped specimen. Other types of precipitates (Cr rich oxide particles) as indicated by circles were also observed. A non-uniform distribution of the oxides within other larger grains was also observed. For instance numerous oxide particles were arranged preferentially along grain boundaries in the primary ultrafine grain region (Fig.5.4b). After ECAE at 700 °C, oxide particles were more uniformly distributed inside grains as shown in Fig.5.4c. When applying single pass ECAE at a lower temperature, 300 °C, triangular or elliptic shaped oxide particles were observed as marked by arrows in Fig.5.4d. A close examination of oxide nanoparticles shows that their structure remained BCC Y_2O_3 with a lattice parameter of 1.06 nm as shown in Fig.5.5a. Some of the oxide nanoparticles tended to evolve into smaller particles (Fig.5.5b).

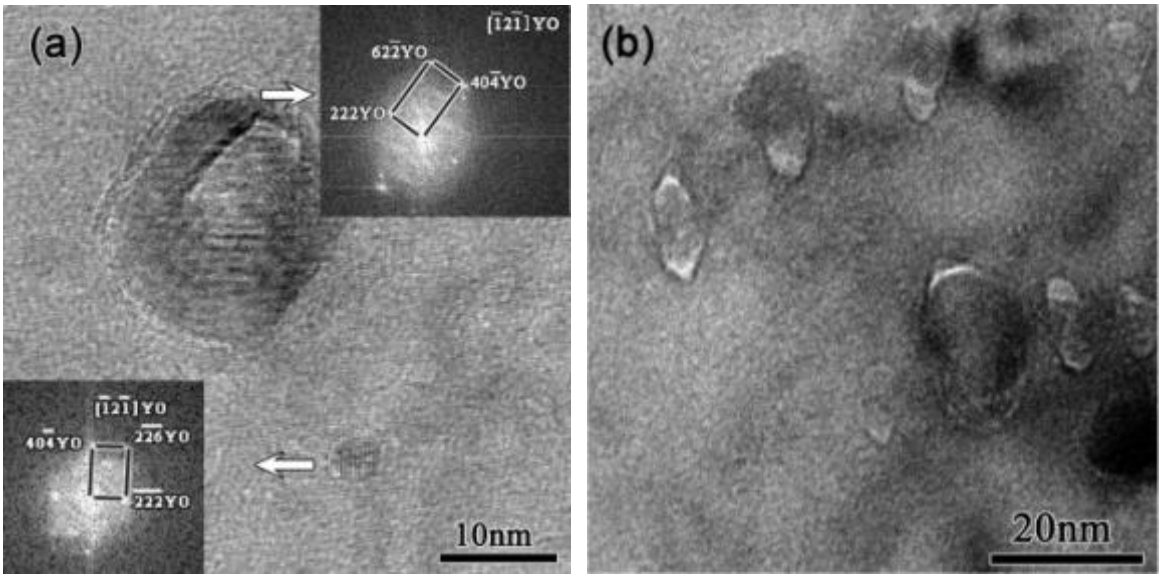

Fig 5.5. (a) HRTEM images of nanoscale oxide particles in specimen 1A300. The FTT patterns (upper-right from the 20 nm and lower-left from the 5 nm diameter Y_2O_3 oxides) show that the oxide particles remained BCC in crystal structure (zone axis along $[\bar{1}2\bar{1}]$). (b) Numerous oxide nanoparticles were deformed by shear stress.

Other types of precipitates were investigated further in as-HIPped specimens. Fig.5.6a shows a “palm like” precipitate tilted to a perfect [110] zone axis. This precipitate has an FCC structure with a lattice parameter of 1.07 nm as confirmed by the inserted SAD pattern. A STEM image of the same location is shown in Fig.5.6b. Chemical analysis (Fig.5.6c) reveals that the precipitate has the stoichiometry of $(Cr, Fe)_{23}C_6$. Other Cr rich oxide particles were also detected. As shown in Fig.5.7a (TEM) and 7b (STEM mode), a larger particle with ellipsoidal

shape was identified with the shorter dimension of ~ 500 nm. According to the EDX line scan result, Fig.5.7c, the particle was Cr rich oxide. The enrichment of Cr inside the particle led to the depletion of Cr in surrounding matrix. The same type of particles was also investigate by SEM (after selectively etching by KOH solution) as shown in Fig.5.7d in order to obtain statistical distribution of particle sizes. No pronounced geometry change was observed for the Cr oxide particles and Cr carbides after ECAE according to the SEM results (not shown here).

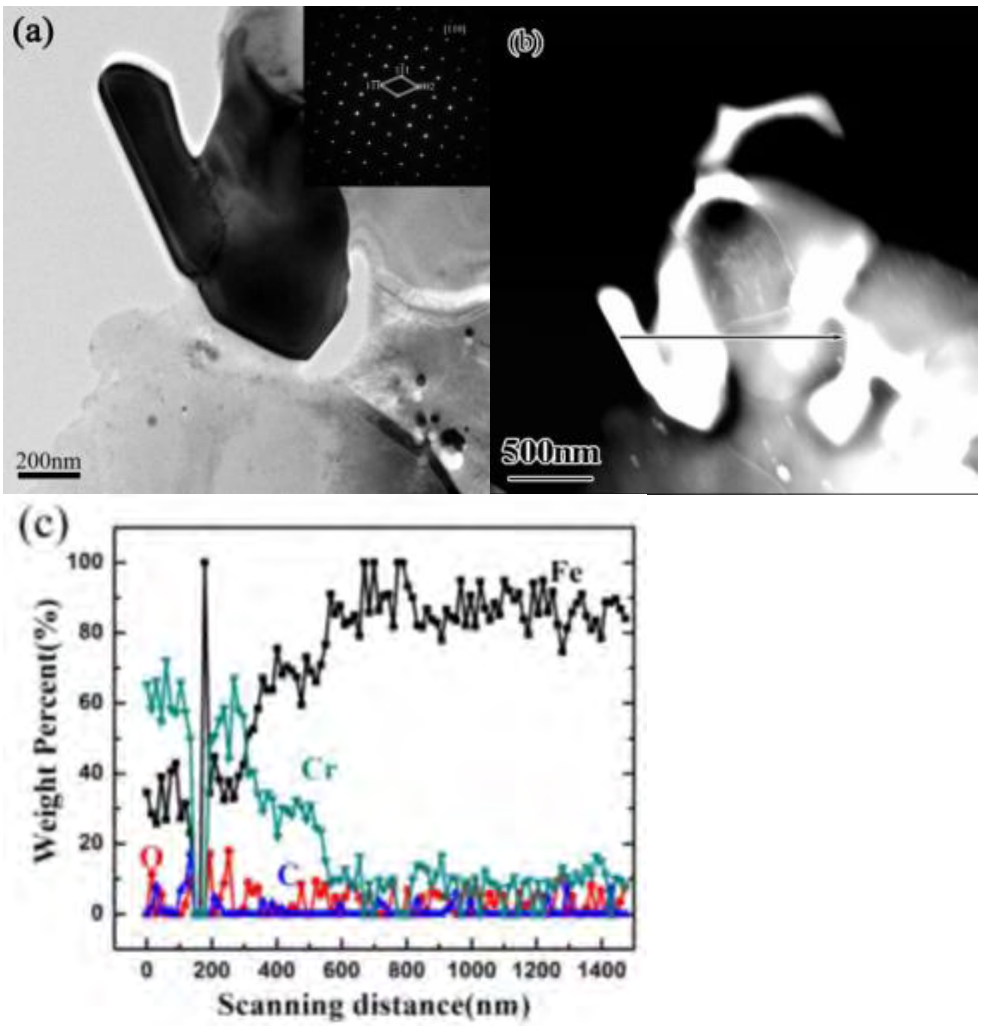

Fig 5.6. (a) Bright field TEM image and the corresponding SAD pattern of $(Cr, Fe)_{23}C_6$ particles in as-HIPped ODS steel; (b) STEM image of the same region and (c) the corresponding compositional profile along line scan (black line in (b)) showing chemical composition changes along this line.

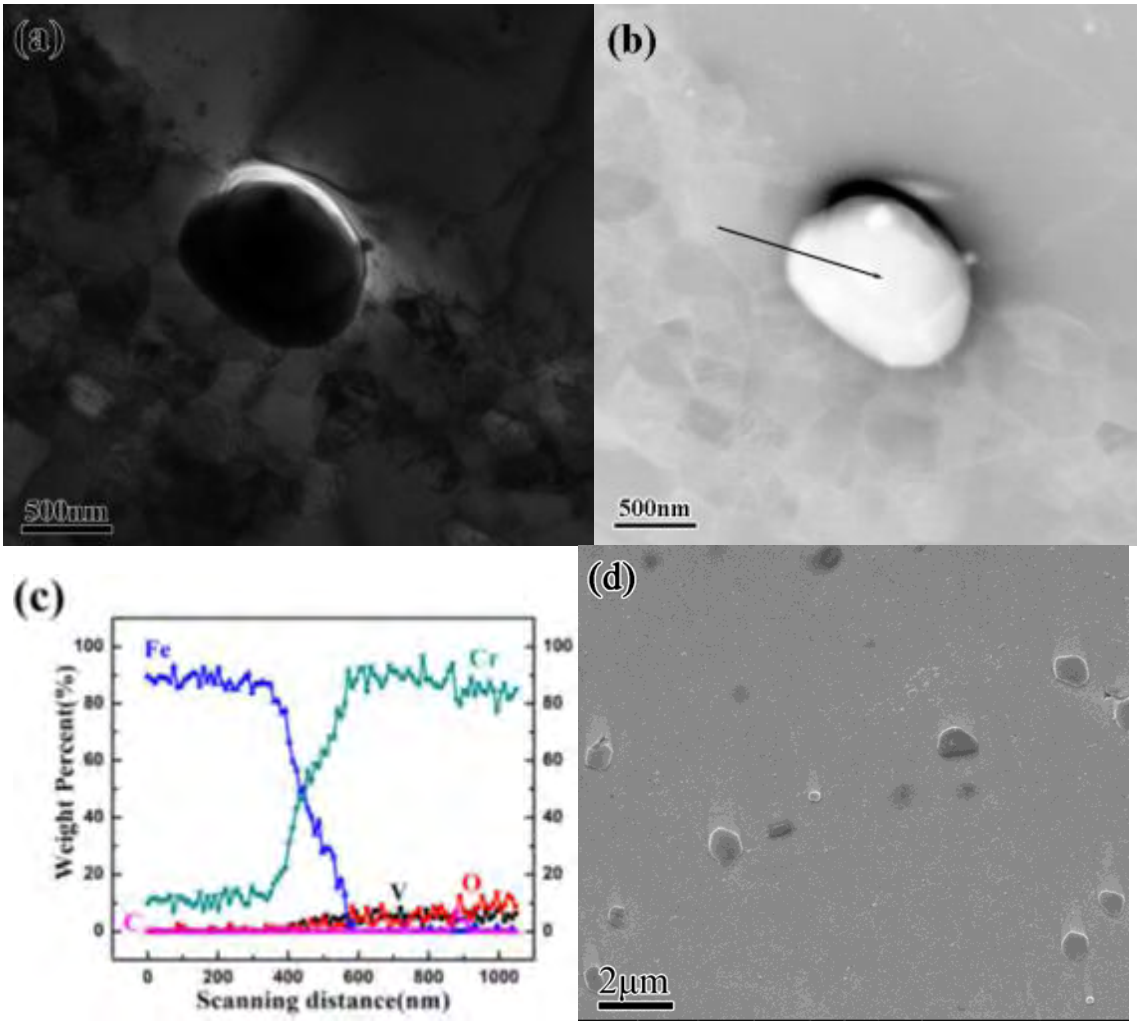

Fig. 5.7. (a) TEM micrograph of a large oxide particle in as-HIPped alloy with corresponding (b) STEM image.(c) The line scan along the black line in (b) shows that the particle was depleted in Fe, and enriched with Cr and contained V and O. (d) SEM micrograph shows that after KOH solution treatment, Cr rich particles were selectively etched.

Statistical analyses of the microstructure were carried out to determine the size distribution of grains and particles. Fig.5.8a and b show grain size distributions determined from TEM micrographs by using linear intercept method. More than 140 grains were analyzed for each case. Grains as large as 8 μm existed in the as-HIPped alloy. Processing via route 2C700 refined the maximum grain size to less than 2 μm. In the 1A300 specimen, no grains larger than 1.2 μm were observed. The refinement of larger Cr rich particles by ECAE was also noticed from Fig.5.8c which shows the statistical distribution of ~ 360 Cr rich particles based on SEM studies. Fig.5.8d shows TEM based measurements of the size distribution of ~ 320 Y_2O_3 nanoparticles in specimens processed at different conditions. The 2C700 specimen had slightly

greater Y_2O_3 particles. Details of microstructural features are given in Table 5.2. The average grain size of the matrix was reduced by a factor of two after processing via 1A300. In addition, both the size and volume fraction of Cr rich oxide particles were reduced by ECAE processing. The density of oxide particles was little affected, on the order of $10^{22}/m^3$.

Fig.5.9 shows a Hall-Petch plot, i.e. the dependence of hardness on $d^{-1/2}$, where d is the average grain size. The hardness increased from 2.4 (as-HIPped) to 3.2 GPa (~35%) after ECAE, and followed a linear relationship with $d^{-1/2}$.

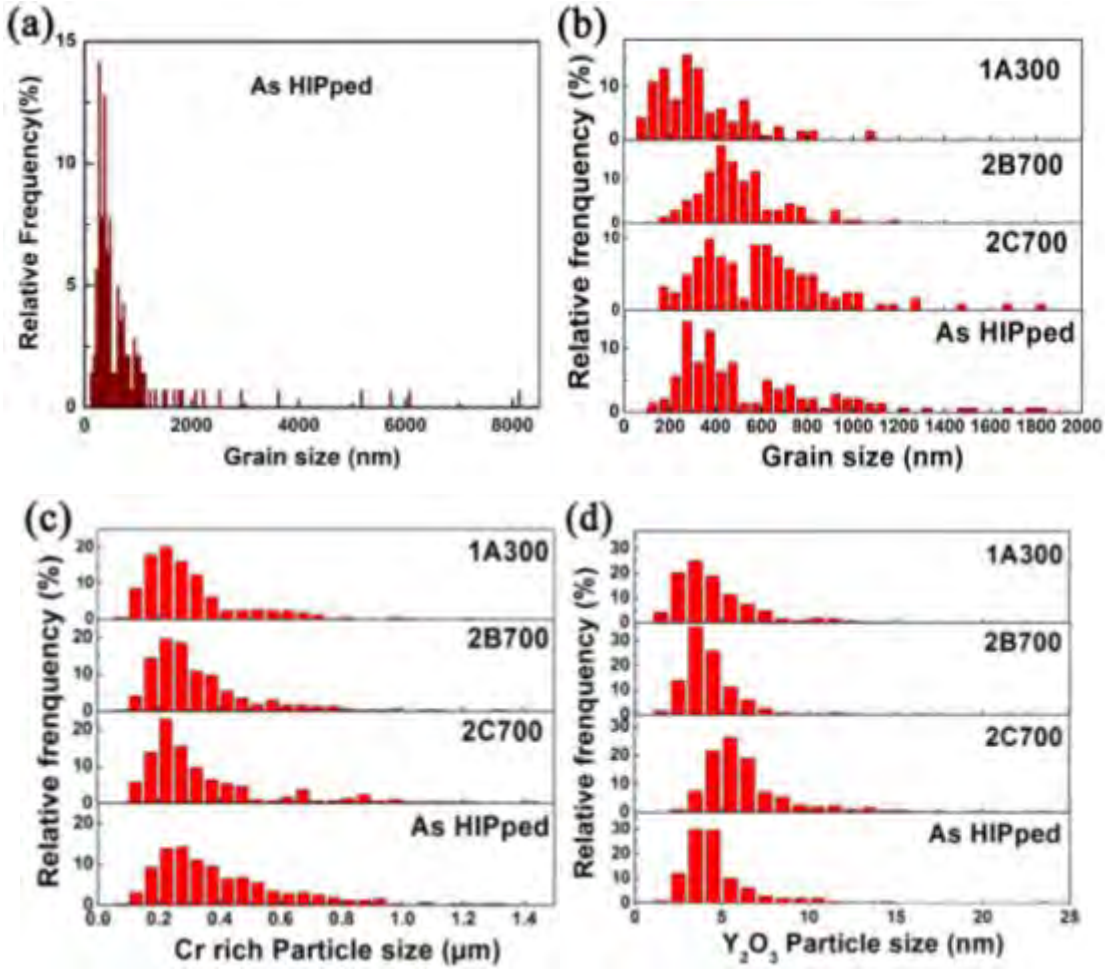

Fig. 5.8. Grain and particle distributions in as-HIPped and ECAE processed ODS alloys. (a) Grain size distribution in as-HIPped sample shows that grains as large as 8 μm existed after consolidation. (b) Grain size distributions showed grain refinement after ECAE processing. (c) Cr rich particles were also refined after ECAE. (d) Insignificant variation of distribution of Y_2O_3 oxide particles after ECAE except that the average particle size appeared to increase slightly in 2C700 specimen.

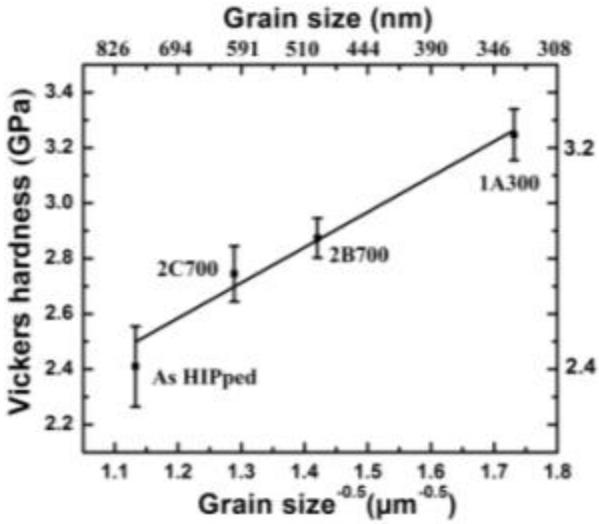

Fig. 5.9. Hall-Petch plot of ODS steels with average grain size varying from 300 to 800 nm. Grain refinement through ECAE led to strengthening of ODS steels.

Table 5.2 Evolution of microstructural features after ECAE

Alloy ID	Grain		Cr rich phase ($M_{23}C_6$ and Cr oxides)			Y_2O_3 nanoparticles	
	Average size(μm)	Maximum size(μm)	Average size (μm)	Volume fraction (%)	Density (m^{-3})	Average size(nm)	Density(m^{-3})
As-HIPed	0.77±1.09	≥8	0.40±0.22	2.31±1.31	2.8×10^{16}	4.7±2.3	3×10^{22}
2C700	0.60±0.29	2	0.35±0.23	1.53±0.68	2.5×10^{16}	6.5±2.9	
2B700	0.50±0.17	1.2	0.33±0.18	1.47±0.51	3.4×10^{16}	4.4±2.0	
1A300	0.33±0.19	1.2	0.30±0.17	1.25±0.31	3.8×10^{16}	4.6±2.4	

Microstructure of the as HIPped materials

Bimodal grain structure is commonly achieved by two methods: thermal mechanical treatment followed by annealing and blending/consolidation of mixed powders with desirable grain sizes and volume fractions. Zhao *et al* successfully fabricated bimodal ODS steels by using blended powder of different sizes. In the present study, large grains were observed probably

because of abnormal grain growth during HIPping at 1150 °C. No bimodal structure was observed in EUROFER ODS steel by Lindau *et al*. This is likely because their alloy was prepared from gas atomized master alloy, a process that may give less phase segregation. The consolidation temperature is greater than recrystallization temperature and thus lead to the bimodal structure.

The average diameter of Y_2O_3 particles in this study (~ 4.5 nm) is slightly greater than what had been observed in previous work (≤ 3 nm). This may be related to the absence of Ti in the current ODS steels. Titanium is apparently beneficial to the formation of smaller oxide nanoparticles. The orientation relationship between the matrix and Y_2O_3 particles in the present study is $(020)_\alpha$ // $(00\bar{4})_{Y2O3}$ and $[001]_\alpha$ // $[110]_{Y2O3}$. This is similar to previous studies on an FeAl based ODS alloy although the matrix (FeAl) in that system had a CsCl structure, which is different from the present BCC structure. Klimiankou *et al* showed a somewhat different orientation relationship in EUROFER97 ODS, that is $[111]_{FeCr}$//$[110]_{Y2O3}$ and $(1\bar{1}0)_{FeCr}$//$(1\bar{1}\bar{1})_{Y2O3}$. These orientation relationships were developed during the HIPping process as a means to minimize the interface energy between the oxide particles and matrix.

The formation of $M_{23}C_6$ is inevitable because of the contamination of carbon from the balls and vials used in the MA process. The $M_{23}C_6$ phase was also observed by Klimiankou *et al* [48] after heat treatment of a similar alloy. $(Fe, Cr)_{23}C_6$ can lower the ductile-to-brittle-transition-temperature (DBTT) of the alloys. Cr rich oxide particles frequently observed in the ODS steel formed because of excessive oxygen in the matrix.

Multi scale microstructural refinement achieved by ECAE

The effect of ECAE on microstructural refinement of the present ODS steels is summarized as follows. First, the maximum grain size was successfully reduced from several microns to ~ 1 μm, and a smaller average grain size with a uniform distribution was achieved. The low temperature extrusion (1A300) was more effective in grain refinement than the high temperature (2C700 and 2B700) process, even though less strain was applied. ECAE at 700 °C might have triggered dynamic recrystallization that led to concurrent grain growth during extrusion. There are two peaks in the grain size distribution chart of the 2C700 samples (Fig.5.8b). The first peak, ~ 375 nm in average grain size, may arise from the original ultrafine

grains in the as-HIPped material. The second peak, ~ 600 nm in average grain size, may be formed by refinement of the larger grains in the as HIPped samples.

Second, the average dimension of Cr rich precipitates ($M_{23}C$ and Cr oxides) was refined and their volume fraction was significantly reduced by ECAE. The refinement of precipitates strongly suggests that ECAE is an effective route to redistribute solute, remove precipitates to some extent, and achieve a more homogeneous microstructure. No fractured particles were observed in this study. In fact fractured particles induced by ECAE were rarely observed except for particular shaped particles which had a large stress concentration factor.

Third, ECAE appears to change the distribution and geometry of small Y_2O_3 nanoparticles. The oxide nanoparticles were not uniformly distributed in the as-HIPped material. Numerous oxide nanoparticles were found surrounding ultra-fine grains. This is because the oxide nanoparticles were mechanically mixed with metal powders during milling, and hence were not fully incorporated uniformly throughout the metal grains even after long duration mechanical alloying. After ECAE, however, most of the oxide particles were found to be distributed uniformly throughout the matrix. Furthermore, the shape of numerous oxide particles in the 1A300 samples was found to be ellipsoidal, implying that large shear stress induced by ECAE may lead to morphology changes of tiny oxide nanoparticles. Although the average particle size appeared intact in 1A300 specimens, in numerous cases, oxide nanoparticles appeared to be “decomposed” into smaller particles (Fig. 5.5b).

4.3 Hardening mechanism

The hardness of ODS steel may be affected by three factors: dispersion strengthening from Y_2O_3 particles, from the Cr rich phase, and dislocation pile-ups due to grain refinement (Hall-Petch relationship).

First, we will estimate dispersion strengthening based on the Orowan bowling mechanism. For simplicity we assume the system is a simplified Fe-Y_2O_3 alloy in which Y_2O_3 nanoparticles are uniformly distributed and the solid solution has negligible effect on hardening.

Dispersion hardening is then calculated by:

$$\tau = \frac{GAb}{2\pi\lambda}[\ln(\frac{D}{r_0}) + B] \quad , \qquad (1)$$

where τ is the shear stress for bowing of dislocations; b is the magnitude of Burgers vector of a full dislocation, and which in BCC Fe it can be written as 1/2<111>a (where a is the lattice

parameter); A=1 and B=0.7 for an edge dislocation; A=1/(1- ν) and B=0.6 for a screw dislocation. In BCC Fe, b = 0.274 nm, G = 59.7 GPa, and ν = 0.159. G and ν are the shear modulus and Poisson's ratio for the {110} <111> slip system, and are calculated to be $3/[4(S_{11}-S_{12})+S_{44}]$ and $(2S_{44}-4S_{11}-8S_{12})/(6S_{11}+6S_{12}+3S_{44})$, respectively, where S_{11}, S_{22} and S_{44} are the compliance factors for iron. r_0 is the inner cut-off radius of the dislocation core and is typically in the range of 1~3 b. λ is the inter particle distance on a slip plane, which is given by,

$$\lambda = 1.25 l_s - 2r_s \quad , \qquad (2)$$

where l_s is the center to center distance of particles, and r_s is the average radius of oxide particles. The factor of 1.25 is a conservation coefficient arising from the assumption that the Y_2O_3 particle is a strong barrier, and the dislocation segment would be unstable when interacting with pairs of obstacles with a separation distance above 1.25 l_s.

The parameter D is given by equation:

$$D = \frac{2r_s l_s}{2r_s + l_s} \quad , \qquad (3)$$

where l_s and r_s are estimated by using the following equations,

$$l_s = \sqrt{\frac{2\pi \overline{r^3}}{3 f \bar{r}}} \qquad (4), \text{ and}$$

$$r_s = \frac{\pi \overline{r^2}}{4\bar{r}} \quad , \qquad (5)$$

where $\bar{r}$, $\overline{r^2}$, $\overline{r^3}$ are the average value of r, r^2, r^3, where r is the diameter of a particle. f is the volume fraction of particles. For Y_2O_3, the volume fraction of particles was estimated from the weight fraction given a material density of 5.01 g/cm^3.

The hardness was estimated by,

$$H = 3\sigma_y \quad , \qquad (6)$$

where H is the Vickers hardness and σ_y is the yield strength of the material. A similar estimate of strengthening was carried out for the Cr rich precipitates. Results are given in Tables 5.3 and 5.4.

Table 5.3 Parameters for Orowan strengthening by Y_2O_3 nanoparticles.

Processing	$\bar{r}$(10^{-}	$\overline{r^2}$(10^{-}	$\overline{r^3}$ (10^{-}	l_s(10^{-}	r_s(10^{-}	f	λ(10^{-9}	τ_s	H(MPa)

condition	^{9} m)	^{18} m^{2})	^{27} m^{3})	^{9} m)	^{9} m)	(vol.%)	m)	(MPa)	
As Hiped	4.7	27.7	221	145	4.6	0.47	172	43 ~ 67	127 ~ 206
2C700	6.5	50.3	494	183	6.1	0.47	218	37 ~ 57	108 ~ 167
2B700	4.4	23.1	163	128	4.1	0.47	152	47 ~ 74	137 ~ 225
1A300	4.6	27.6	217	148	4.7	0.47	172	44 ~ 68	127 ~ 206

Table 5.4 Parameters for Orowan strengthening by Cr rich phases.

Processing condition	$\bar{r}$(10^{-6} m)	$\overline{r^2}$(10^{-12}m^2)	$\overline{r^3}$ (10^{-18} m^3)	l_s(10^{-6} m)	r_s(10^{-6} m)	f (vol.%)	λ(10^{-6} m)	τ_s (MPa)	H(MPa)
As Hiped	0.40	0.21	0.13	5.43	0.41	2.31	5.96	3.0 ~ 4.0	8.8 ~ 11.8
2C700	0.35	0.17	0.12	6.85	0.38	1.53	7.80	2.3 ~ 3.1	6.9 ~ 8.8
2B700	0.33	0.14	0.08	5.88	0.33	1.47	6.68	2.6 ~ 3.5	7.8 ~ 10.8
1A300	0.30	0.12	0.06	5.79	0.31	1.25	6.61	2.6 ~ 3.5	7.8 ~ 10.8

The magnitude of dispersion strengthening arising from both oxide particles and Cr rich precipitates is small, varying from 10 to 200 MPa. This is insufficient to explain the magnitude of strengthening observed in ECAE processed ODS steels.

A linear relationship between hardness and the square root of the grain size was observed (Fig.5.9), implying that dislocation pile-up against high angle grain boundaries is the predominant hardening mechanism, which is described by the Hall-Petch relationship. The smallest average grain size in ECAE processed material is ~ 330 nm, a range for which the abundant pile-up of dislocations remains available. The Hall-Petch type of hardening mechanism is frequently observed for metallic materials subjected to sever plastic deformation.

A6. Heterogeneous Nucleation and Growth of Oxide Particles in a 12Cr ODS Steel

Lead organization (Texas A&M, Xinghang Zhang, K. Ted Hartwig)

For the ODS alloys without Ti, single phase of Y_2O_3 particles was reported by the study of TEM (transmission electron microscope) as the main formula of the particles. However, detailed studies by FIM (field ion imaging) or EELS (electron energy loss spectrum) reveal that the particles have core-shell structures with Y, O and Mn in the cores and a V, Cr, Ta rich shell dependent on the chemical composition in different ODS steels, which is complicated as expected. The minor additional elements like V or Mn may play an important role as Ti does. Although open to question, the formation of core-shell structures of the oxide particles are explained mainly through two alternative mechanisms. The first mechanism considers shell as a means of segregation of elements to the particle/matrix interface during the sequent cooling after the particles were formed. The second mechanism explains the presence of the shell as necessary to decrease the interfacial energy.

In this study, another configuration of Yttrium oxide and Chromium oxide was observed first time instead of core-shell structure. These embedded or back to back structures of oxides particles can serve as the supplemental understanding of the nature of the core-shell structure and the nucleation and growth of the complex oxide particles. Alternative mechanisms are proposed to explain the phenomenon.

The material investigated in present study was a reduced activation ferritic ODS steel, prepared by typical processing including mechanical alloying (MA) the blended powders, degassing and subsequent HIPping (hot isostatic pressing) process. The original sizes of powders were 70μm of Fe, ≤10 μm of Cr, Ta, V, W and 20nm of yttrium oxide (Y_2O_3). MA processes were carried out using a planetary ball mill operated in a glove box protected by ultra high purity Argon gas. The ball-to-powder ratio was 15:1. The milling time was typically 12 hrs. The HIPped condition was selected to be 1150℃ for 4hrs under 100 atm pressure. The nominal chemical composition (in wt.%) of the present alloy was 12 Cr,1.1 W,0.2 V,0.14 Ta, 0.3 Y_2O_3 with the remainder being Fe. Post process heat treatments were carried out in quartz tube with the protection of high purity Argon gas. 1300 ℃ annealing was carried out in sealed quartz tube with the protection of high purity Argon gas in furnace. All the samples were furnace cooled. The TEM specimens were prepared by mechanical grinding of 3 mm disks down to 50 μm. The disks were then etched in a twinjet polisher with 10vol.% perchloric acid + 90vol.%methyl

alcohol solution with voltage 15 ~ 30 V at -40°C. The ion milling was used as a cutting-open method of the particles with applied energy of 3.5 kv for 5 min after electro polishing. The microstructure and chemical analysis were performed on FEI Tecnai F20 field emission gun TEM equipped with HAADF (high angle annular dark field) detector for STEM and Oxford instruments EDX detector. Scanning electron microscopy (SEM) was performed on an FEI Quanta 600 microscope operated at an acceleration voltage of 20 kV with a working distance of 10 mm. The SEM samples were electrochemically etched with a 10g/100ml KOH solution with a voltage of 10V, which selectively etched the Cr rich phases.

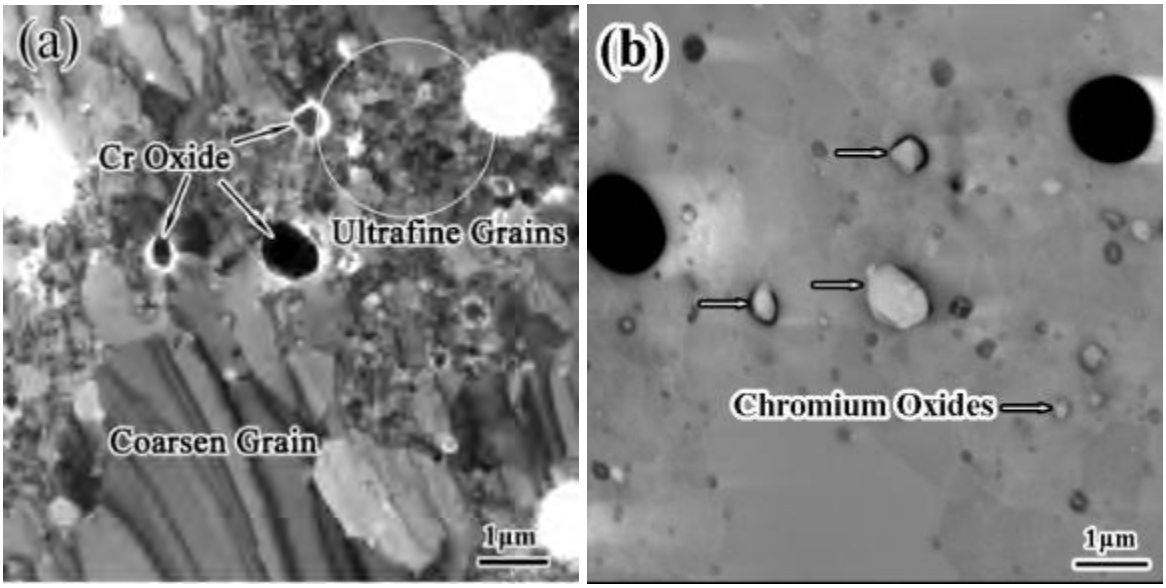

Fig. 6.1. (a) Bright field TEM micrograph of as-HIPped 12-Cr ODS steel having a bimodal structure, i. e. larger grains, ~several microns in diameters, and puddles of ultrafine grains, ~250nm, spotted with black chromium oxide particles (b) Corresponding STEM image of the same region show the chemistry and thickness contrast from chromium oxide particles with various sizes.

Fig.6.1 (a) showed the representative TEM micrograph of the as-HIPped ODS steel after electro polishing. The as-HIPped ODS steel showed a bimodal grain size structure with average sizes about 1.7 μm of coarse grains and 250 nm of ultrafine grains (based on a statistic of 230 grains totally, grain size ≥900 nm was taken as coarse grains, others as ultrafine grains). The black dots located at grain boundaries were Cr rich oxides. The grain boundaries as a high diffusion path can accelerate the growth of the particles. The enrichment of Cr in the particle led

to the depletion of Cr content near it, which deteriorated the corrosion resistance of the matrix around and thus made the corrosion property discontinuous. Holes were generated at the interfaces between the particles and matrix. Fig.6.1 (b) was the STEM image giving the chemical contrast of the same region. The Cr rich oxides should show darker contrast for the relatively low atomic number. But the higher thickness caused by the corrosive properties enhanced the elastic scattering of the electrons and also shorten the distance to the detector. These factors made the contrast of the particles brighter.

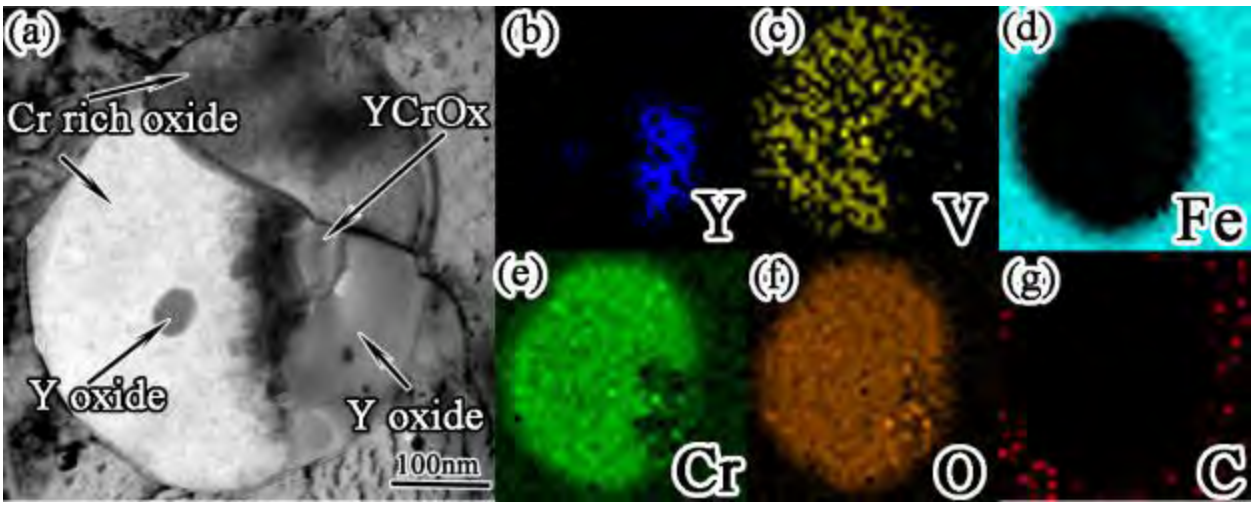

Fig. 6.2. (a) TEM micrograph of complex oxide particles in as-HIPped ODS steel with (b-g) corresponding STEM elemental mappings of Y, V , Fe, Cr, O and C.

These kind of large oxide particles existing were analysis through STEM mapping and line scanning in either as-HIPped or annealing ODS alloy after ion milling. These large particles located at both intragranularly and intergranularly. Fig.6.2 showed the bright field image of a cutting-open complex oxide particle and corresponding elemental mappings. This particle located at the grain boundaries. The center was found to be a $YCrO_x$ type particle with all of its edges were surrounded by Cr rich oxide or Y rich oxide particles. The two Cr rich particles were detected with similar chemical composition but different orientations. V was also detected within the Cr rich particles. In the Y rich oxide particles, small amount of Cr was also detected. None of elements such as C, Fe, Ta and W was detected within the particles.

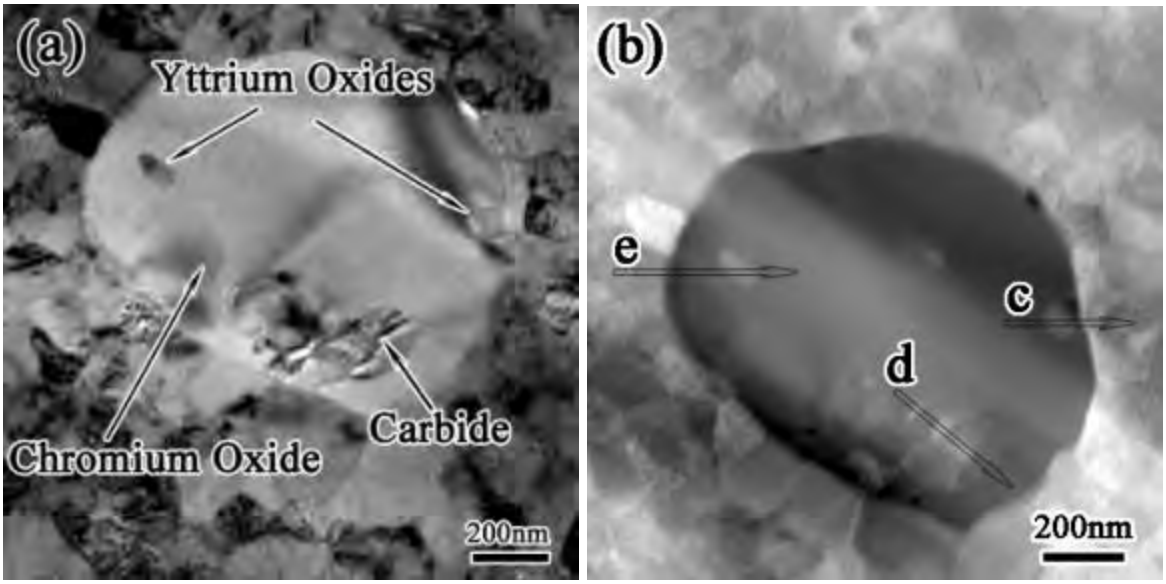

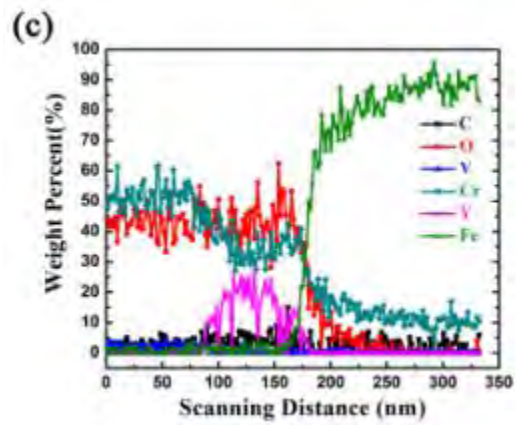

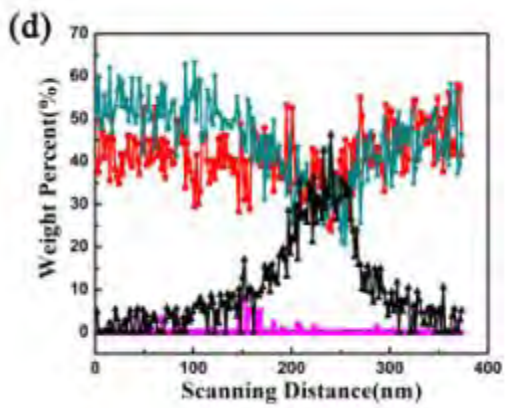

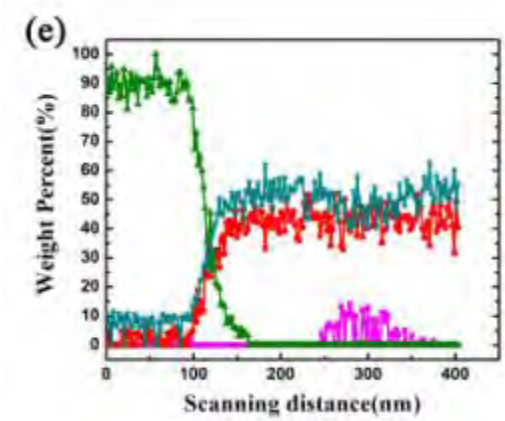

Fig. 6.3. (a) TEM micrograph of yttrium oxide nanoparticles inside of chromium oxide particle after annealing (900℃/10h) (b) Corresponding STEM image of the same particle; (c-e) The line scan along the white arrows c, d, e in (b) shows that the chemical composition change. Particles of yttrium oxide were indentified in (c) and (e), whereas complex oxidized chromium carbide was indentified in (d).

A large oxide particle after annealing at 900℃/10h was also shown in Fig.6.3a. This particle located at the grain boundaries of the ultrafine grain zone. Three smaller particles were

observed within the larger particle. Fig.6.3c-e confirmed the chemical composition of the three particles in position illustrated in Fig.6.3b. Two of them were yttrium oxides and the other was carbide. One of yttrium oxide was totally surrounded by the chromium oxide particle. The other remained half surrounded. None of small Y_2O_3 particles below 20nm was observed in the large particles. Intragrannular large oxide particles were also observed.

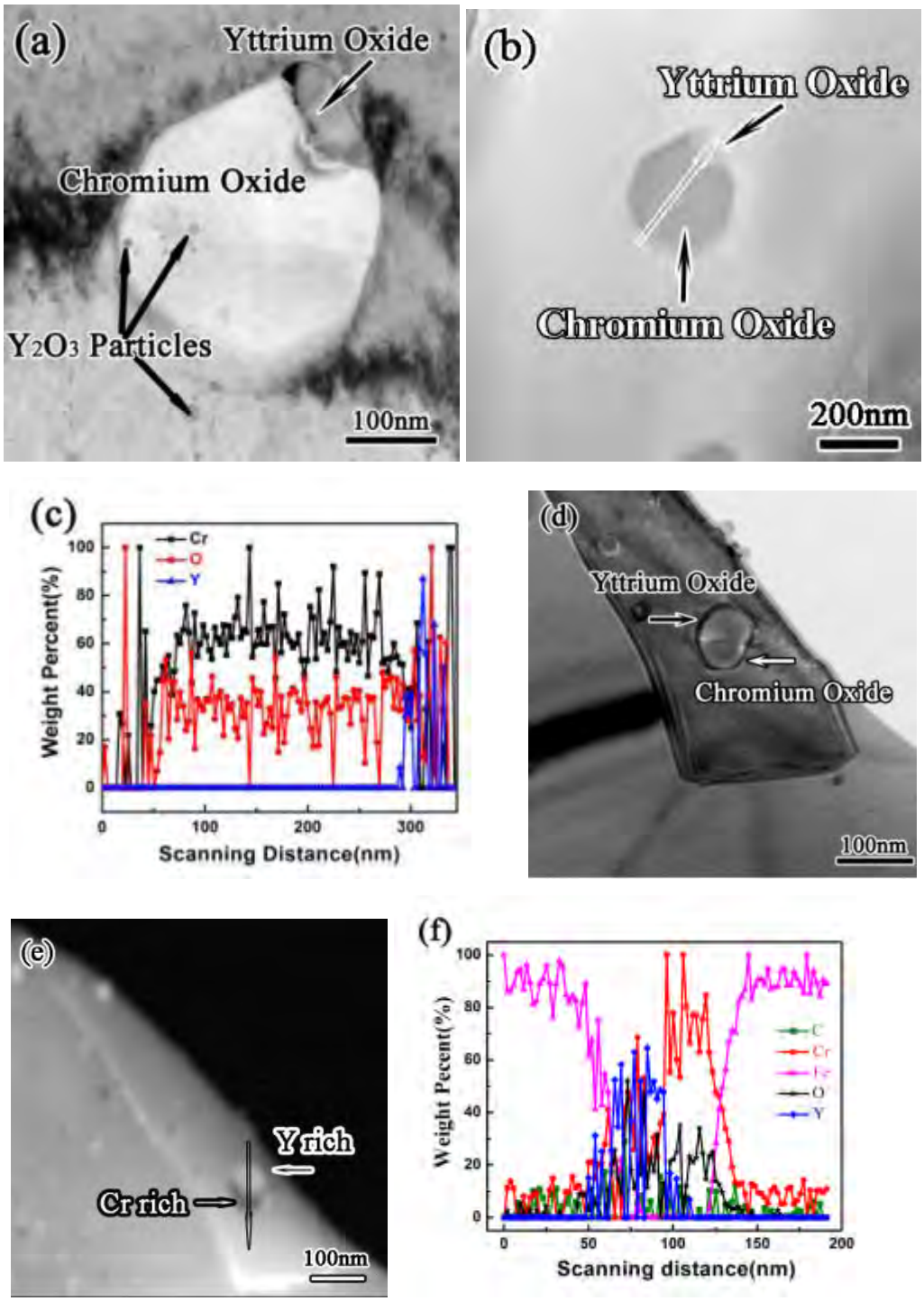

Fig. 6.4. Comparison of dual-phase intragranular oxide particles in as-HIPped and annealed alloy (a) TEM micrograph of a dual-phase oxide particle, ~200nm in diameter, in the as-HIPped 12-Cr ODS steel;(b) STEM image of the same particle;(c) The EDX line scan along the white arrow in (b)shows that the two particles are mainly chromium oxide and yttrium oxide, respectively (d) TEM micrograph of a dual phase oxide particle after annealing (1300℃/10h) (e) The corresponding STEM image of the particle (f)The line scan across the particle indicated that the two particles are mainly chromium oxide and yttrium oxide.

Fig.6.4 showed the cutting-open particles in both as-Hipped (Fig.6.4a-c) and after 1300℃/10h annealing (Fig.6.4d-f) state within the matrix. The two oxides exhibited coherence boundaries as shown in Fig.6.4a. The black particle in Fig.6.4b was chromium oxide and the white particle adjacent to it was yttrium rich oxide particle, both of which were confirmed by the EDX shown in Fig.6.4c. Small Y_2O_3 particles with size less than 20 nm were also observed within chromium oxide particle. The two oxides formed a broken line interface. Stress formed around the corner of interface within chromium oxide indicated by the change of contrast. At the corner, the lattice parameters of chromium oxide need to match those of yttrium rich oxide particle along two different crystalline directions simultaneously. This stress can play an important role in the coherence and the change of the shape of the yttrium rich oxide during annealing. Another intragranular particle was a combination of chromium oxide and yttrium oxide with similar size in Fig.6.4d. The chemical contrast was given in Fig.6.4e by the STEM image with confirmed line scanning shown in Fig. 6.4f. This kind of particles with similar size of both oxides was seldom observed in as-HIPped alloy.

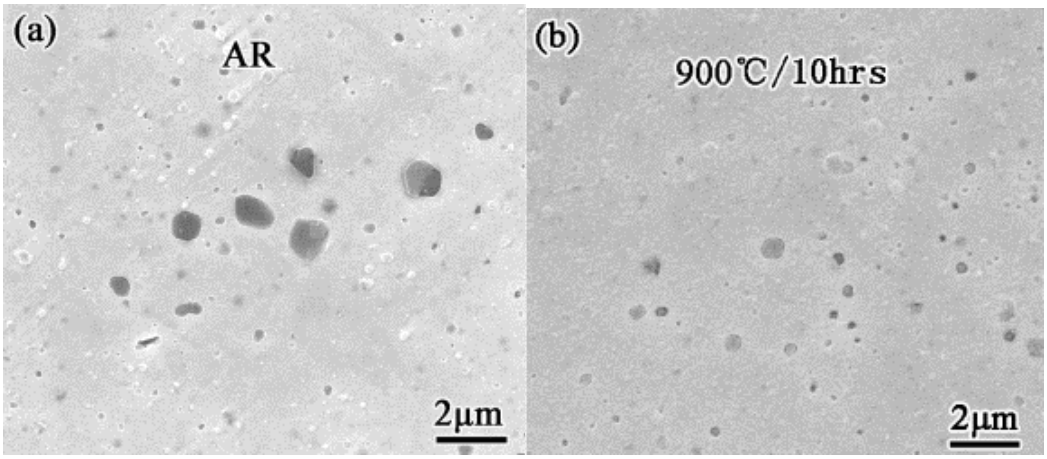

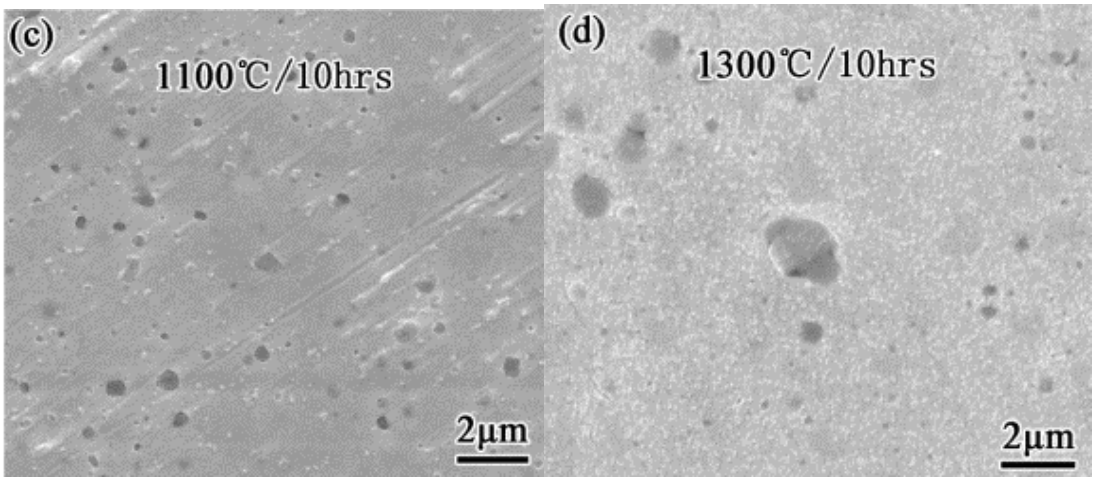

Fig. 6.5. SEM micrograph shows that after KOH solution treatment, Cr rich particles were selectively etched (a)As Hipped and after annealing (b) 900℃/10h (c)1100℃/10h and (d)1300℃/10h.

SEM micrographs were used to get the lower magnification images of the larger oxide particles in various conditions as shown in Fig.6.5. The black particles were Cr rich oxide. The particles size was up to 1 micron. Coarsening occurred 1300℃/10h.

Fig.6.6 showed the small oxide particles. In the as-HIPped state as shown by Fig.6.6a, few Janus particles were observed. As revealed by the HRTEM image shown in Fig.6.6b, the structure of oxide particles corresponded well to a BCC Y_2O_3 with lattice parameter about 1.06 nm. Annealing the sample at 900℃/10h was insufficient to cause precipitation of Janus particles at mass scale as Fig.6.6c shown. After annealing at 1300℃/10h as Fig.6.6d, Janus particles were observed at large scale. HRTEM images Fig.6e showed that these two particles formed a straight coherent boundary. The upper was $YCrO_3$ complex oxides with a tetragonal structure. The lower part should consist of mainly chromium and oxygen but not consistent with any standard value of chromium oxides (Cr_2O_5, Cr_3O_8, Cr_8O_{21}, Cr_2O_3, CrO_3, Cr_3O_4, CrO_2). This is consistent with our EDS result Fig.6.4 (f) that in the Yttrium rich part, signal of Cr was also detected, while in the Cr rich part, no signal of yttrium was detected. The signal of Fe was also absent, which indicated the influence from the matrix was negligible. Some of the chromium oxides take the monoclinic, tetragonal and triclinic structures rather than the cubic ones. If the unit cell varies a bit from the standard value, the process of indexing the diffraction pattern will become difficult.

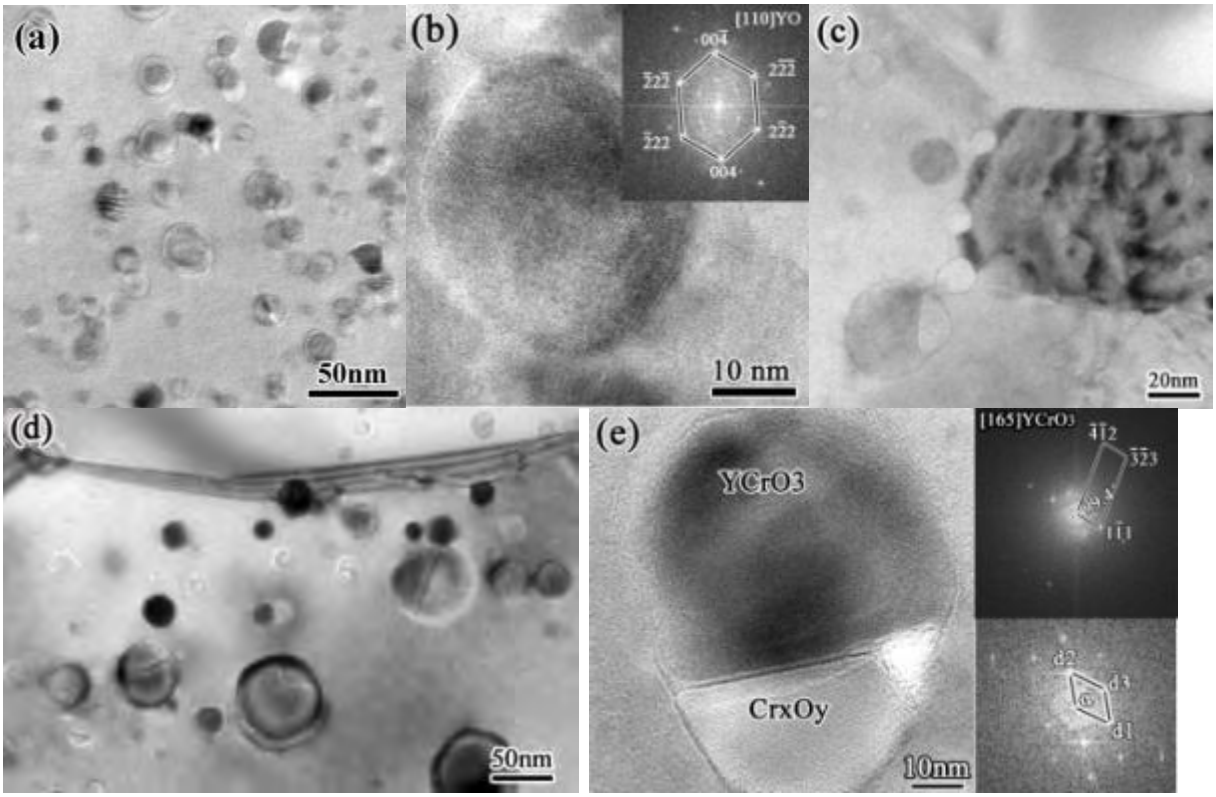

Fig. 6. 6. TEM micrographs of small oxide particles at various conditions (a) As-HIPped and (b) HRTEM images at the same condition, the particle can be index as Y_2O_3 [110]axis;(c) Annealing at 900 ℃ /10h (d) Annealing at 1300℃/10h show that the critical forming size of Junus particles decreased; (d) HRTEM image at same condition as (e) with corresponding FFT, the upper particle can be index as $YCrO_3$ [165] axis; the lower particle didn't match any standard Cr oxides, the interplanar spacings were measured to be d_1 = 0.44 nm, d_2 = 0.45 nm, d_3 = 0.51 nm and the included angle of planes α = 124.6°

Statistical analyses of the microstructure results were performed to determine the size distribution of both large and small oxide particles. The large particles were measured from SEM images (250≥ particles were analyzed for each case). The small particles were measured from TEM images (≥300 particles were analyzed for each case). The large particle was quite stable up to 1100℃. Large Particles above 1.5 μm existed in the 1300℃/10h sample. The small particles also coarsened around 1100℃. The size was general below 100nm.

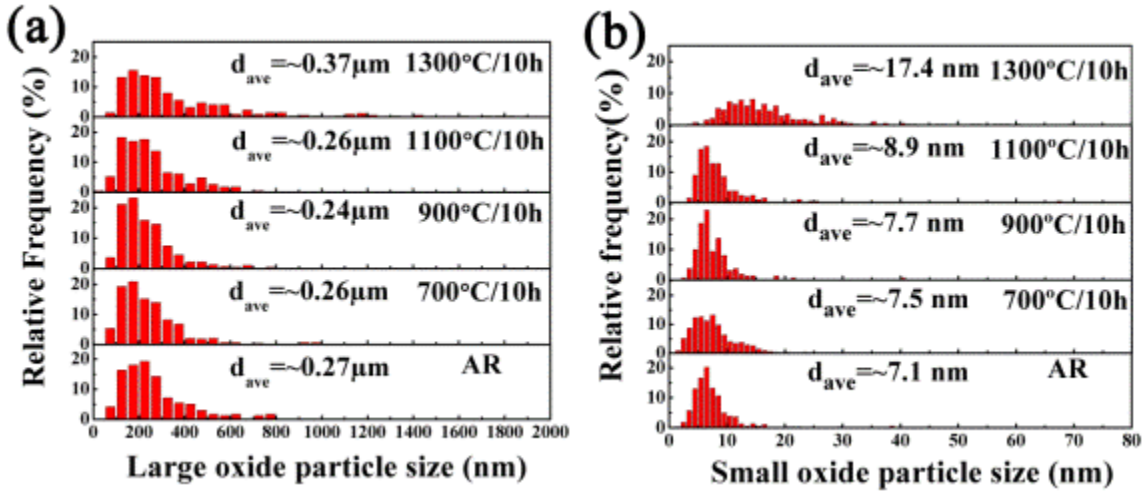

Fig. 6.7. Oxide size distribution in as-Hipped and various condition of annealing ODS alloys. No significant coarsening occurred till 1100℃ for both (a) small oxide particles and (b) large oxide particles.

To understand the nucleation and growth mechanism, the whole processing including thermal and mechanical treatments history of the ODS steels need to be clarified. The MA (mechanical alloying) was a complicate processing, the products of which can be influenced by many parameters. After MA, the dissolution or not of Y_2O_3 into matrix was a key issue for understanding the mechanism. To solve this, XRD experiment was performed using a Y_2O_3 with amplified composition (10 times higher than the real application) two decades ago, in an ODS alloy with addition of Ti. However, the absent of Y_2O_3 peak was insufficient to confirm the dissolution of Y_2O_3. For the ODS without Ti addition, some researchers claimed that the Y_2O_3 particles were observed in the as-milled powders in their TEM observation. Other cannot find such particles. The APT experiments of as-HIPped alloys support the idea that the Y_2O_3 powders at least dissolved partially into the matrix. Experiments of SANS (small angle neuron scattering) on the as milled powders provided evidence for the dissolution of most Y_2O_3 particles if not all, with and without the addition of Ti. However, recently XRD experiment using the amplified composition revealed that most of 10wt.% oxide particles became actually fragmentation or amorphization rather than solid solution.No solid solution limit of the Y_2O_3 in Fe has been determined after ball milling.

The nucleation of Cr oxides was explained through the following alternative mechanism based on the general accepted case that most of the Y_2O_3 were dissolved into the matrix. The

dissolved oxygen from Y_2O_3 would then either solute in the matrix or re-precipitate as oxides particles including Y_2O_3, $YCrO_3$, or other complex oxides during the HIPping and cooling process. The first scenario was that the oxygen re-precipitates in the form of Y_2O_3 or $YCrO_3$ oxides particles. Once the thus formed Y_2O_3 or $YCrO_3$ particles reached the critical nucleation size of chromium oxides particles, the chromium oxides would take it as a nucleation site on the certain crystalline plane where they were coherence. The second scenario was that oxygen could also first re-precipitate in the form of Y-Cr-O complex oxides particles, some of the complex oxide were described in reference. Then during cooling process, the Y-Cr-O complex oxides change to thermal stable phase as $YCrO_3$ and Cr oxides where the Cr oxides took certain precipitates plane of $YCrO_3$ as nucleation sites. $YCrO_3$ was not expected to form without the excessive oxide content because Y_2O_3 was the most thermal stable phase in the system.

The growth of the primary dual-phase particles was clearly governed by the diffusion of oxygen. The oxygen in the oxide particles was tightly bonded to Y, thus the oxygen concentration was lower near the oxide particles than far away from the particles in the matrix. So the gradient of oxygen drove the oxygen flux towards the particles, providing the oxygen for the continuous growth of chromium oxide particles. This argument was supported by the fact that the larger chromium oxides particles commonly formed at the grain boundaries of ultrafine grains as diffusion along the grain boundaries was high diffusion path compared to the matrix.

The appearance of secondary dual-phase particles after the 1300℃/10h annealing suggested that there may be some energy barrier existed for the breaking of the Y-O bond. The oxygen concentration was lower near the larger oxide particles than smaller oxide particles. The gradient of oxygen again drove the oxygen flux towards the larger particles. So the smaller oxides dissolved into the matrix, however, the larger yttrium ions diffusion slower than the oxygen. Thus the high concentration of oxygen around the particles reacted with the Chromium in the matrix near it making the growth of the Y_2O_3 particles into larger complex particles. Then after cooling, the thus formed particles changed to the thermal stable $YCrO_3$ and Cr oxides. So the core-shell structure may be understood as the original growth of the Y_2O_3 particles where transition chromium oxides were formed as a case of low oxygen content in the matrix.

A7. Enhancement of Strength and Ductility in Ultrafine-grained T91 Steel through Thermomechanical Treatments.

Lead organization (Texas A&M, Xinghang Zhang, K. Ted Hartwig)

In the present study, we investigate the effect of processing temperature on mechanical properties and microstructures including the grain refinement, precipitates refinement and redistribution, and their changes after post-processing heat treatment of ECAEed T91 alloys. Thus, high strength with good ductility was achieved through the microstructure control of ECAEed T91 during the thermomechanical treatment. The strengthening mechanisms will be discussed through a simple model combining the Taylor's equation, Hall-Petch relation and Orowan mechanism which related to the dislocation density, grain size effect and precipitates hardening.

Nuclear reactor grade T91 used in present study was provided from Los Alamos National Laboratory in plate form. The nominal composition of the alloy is listed in Table 7.1. The as-received T91 are fully tempered and predominately ferritic.

Table 7.1. The chemical composition (wt.%) of as-received T91 alloys from supplier.

Cr	Mo	V	Mn	C	Si	Cu	Ni	Al	Nb	N	P	S	Fe
9.376	0.911	0.189	0.379	0.085	0.336	0.080	0.097	0.032	0.080	0.042	0.019	0.0008	Bal.

Table 7.2. ECAE Processing condition with sample identifiers.

Identifiers	Processing Condition
AR	as received sample
AA	annealing of as-received material at 800°C/1h followed by furnace cooling
1ART	single pass ECAE at room temperature of AA samples
1A300	single pass ECAE at 300°C of AA samples
2B300	two passes ECAE at 300°C following route B of AA samples
2B625	two passes ECAE at 625°C following route B of AR samples
3Bc700	three passes ECAE at 300°C following route Bc of AR samples

ECAE processes were carried out on an MTS-controlled hydraulic press with 225 ton/2.22×10^3 kN force capacity. The extrusion rate was 0.008 cm/s for cold ECAE and 1.27 cm/s for hot ECAE. High extrusion rate at low temperature could cause shear localized. Billets were water quenched after ECAE. The high temperature extrusion was realized by preheating 1h at the desired temperature in a box furnace then extruded. The processing conditions of the samples are summarized in Table 7.2.

Processing routes A and B involve billet no rotation or a rotation of 90° respectively around their long axis prior to the subsequent extrusion. More details of processing techniques are given in reference. Post-processing heat treatments were carried out in quartz tube with the protection of high purity argon gas, then furnace cooled. Dogbone-shaped samples with gauge dimensions of 8mm×3mm×1mm were cut from the ECAE processed billets using EDM (electro discharge machining). The samples were electro polished to remove the porous oxidized layer left by the EDM, then measured with calipers before testing. TEM specimens were electro polished using a 10% (volume fraction) perchloric acid methanol solution at −40 °C with a voltage between 10 ~ 20 V. Tensile testing was performed with an MTS machine at a cross head speed of 0.008 mm/s. The hardness was measured by an LM 300AT micro hardness tester using a 0.3 kg force for a loading time of 13s. X-ray diffraction (XRD) measurements were taken on a Bruker-AXS D8 diffractometer. Transmission electron microscopy (TEM) was performed using a JEOL 2010 transmission electron microscope operated at 200 kV. Selected area diffraction (SAD) patterns were obtained by using an aperture with a diameter of 1.3 μm. Scanning transmission electron microscope (STEM) was performed using an FEI Tecnai F20 microscope equipped with a high angle annular dark field (HAADF) detector and an Oxford instruments EDX detector operated at 200kV.

7.1 The microstructure evolution of T91

Fig.7.1a showed the representative low magnification TEM micrograph of as-received (AR) T91 steel. The initial microstructure of the material includes fragmentation of the original martensitic laths in a ferritic matrix, with the grain boundaries decorated by carbides precipitates. The carbides are commonly in the formula of $(Fe, Cr)_{23}C_6$ and Nb(C, N) [26, 27]. It is a typical resulting microstructure of a two step heat treatment process for T91. The AR material in present study was fully tempered and predominately ferritic. Further heat treatment (annealing at 800 °C/1h, furnace cooling) of the AR material works as a conservative way to get fully ferritic.

Fig.7.1b was the microstructure after annealing after at 800 °C/1h. Similar microstructure as AR sample was observed. The average size of as-annealed (AA) material was about 0.63 μm and the maximum grain size was ~ 2.5 μm. High dislocation density was a common feature of cold ECAEed samples as shown by Fig. 7.1c-e. The highest density of intragranular dislocation appeared after single pass at room temperature (1ART). With one pass at 300°C (1A300), the grain size was effectively refined to below 1 μm. At the same time, the density of intragranular dislocation was not as high as the 1ART case. The grain size was further reduced to about 0.15 μm, after an additional extrusion with route B at the 300°C (2B300). The density of intragranular dislocation was increased accordingly compared with the Fig.7.1d. Intergranular carbides were commonly observed in the cold ECAEed samples using STEM not shown here. After 2B processing at higher temperature 625°C (2B625), although same amount of strain was introduced into the specimen, the average grain size was about 0.31 μm which was not as effective as 2B300. However, the density of intragranular dislocation was much lower than the cold ECAEed samples as shown in Fig.7.1f. Fine carbide particles precipitated intragranularly with a size below 100 nm were observed. After triple passes following route Bc (3Bc700) processing, the grain size was not further refined compared with 2B625 sample. More intragranular carbides were observed compared with 2B625 sample in Fig.7.1g.

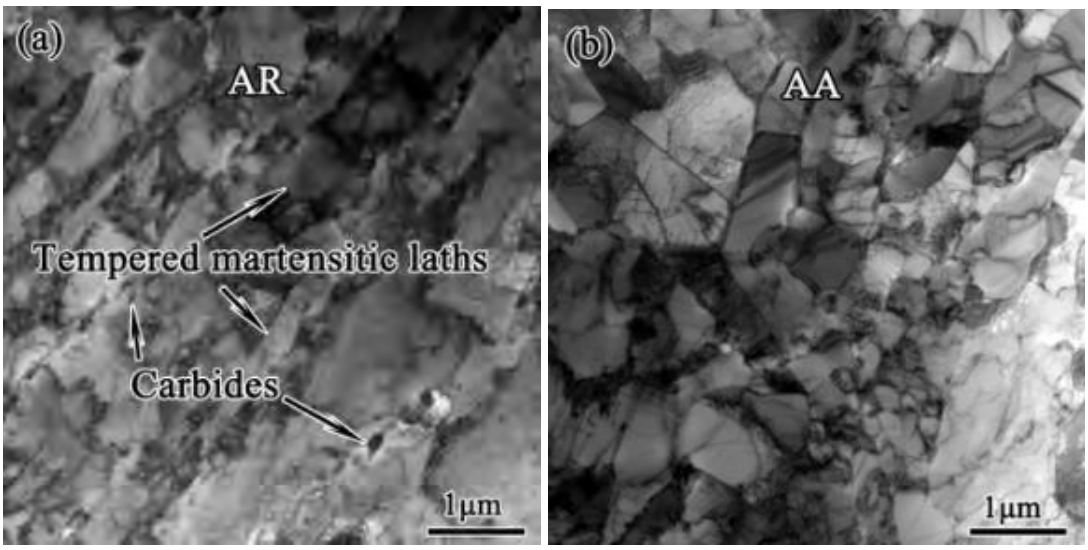

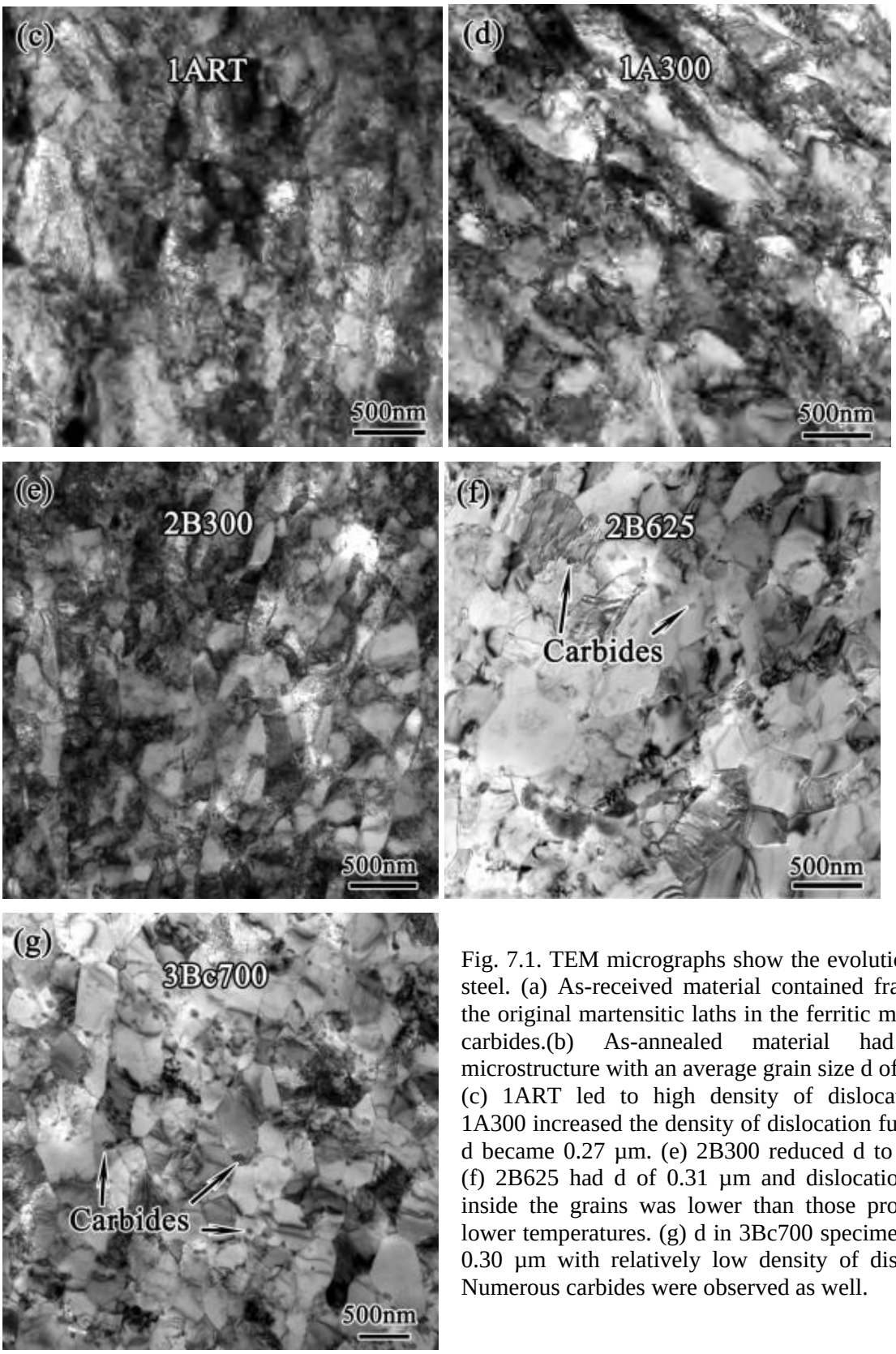

Fig. 7.1. TEM micrographs show the evolution of T91 steel. (a) As-received material contained fragment of the original martensitic laths in the ferritic matrix with carbides.(b) As-annealed material had similar microstructure with an average grain size d of 0.63 µm. (c) 1ART led to high density of dislocations. (d) 1A300 increased the density of dislocation further, and d became 0.27 µm. (e) 2B300 reduced d to 0.15 µm. (f) 2B625 had d of 0.31 µm and dislocation density inside the grains was lower than those processed at lower temperatures. (g) d in 3Bc700 specimen became 0.30 µm with relatively low density of dislocations. Numerous carbides were observed as well.

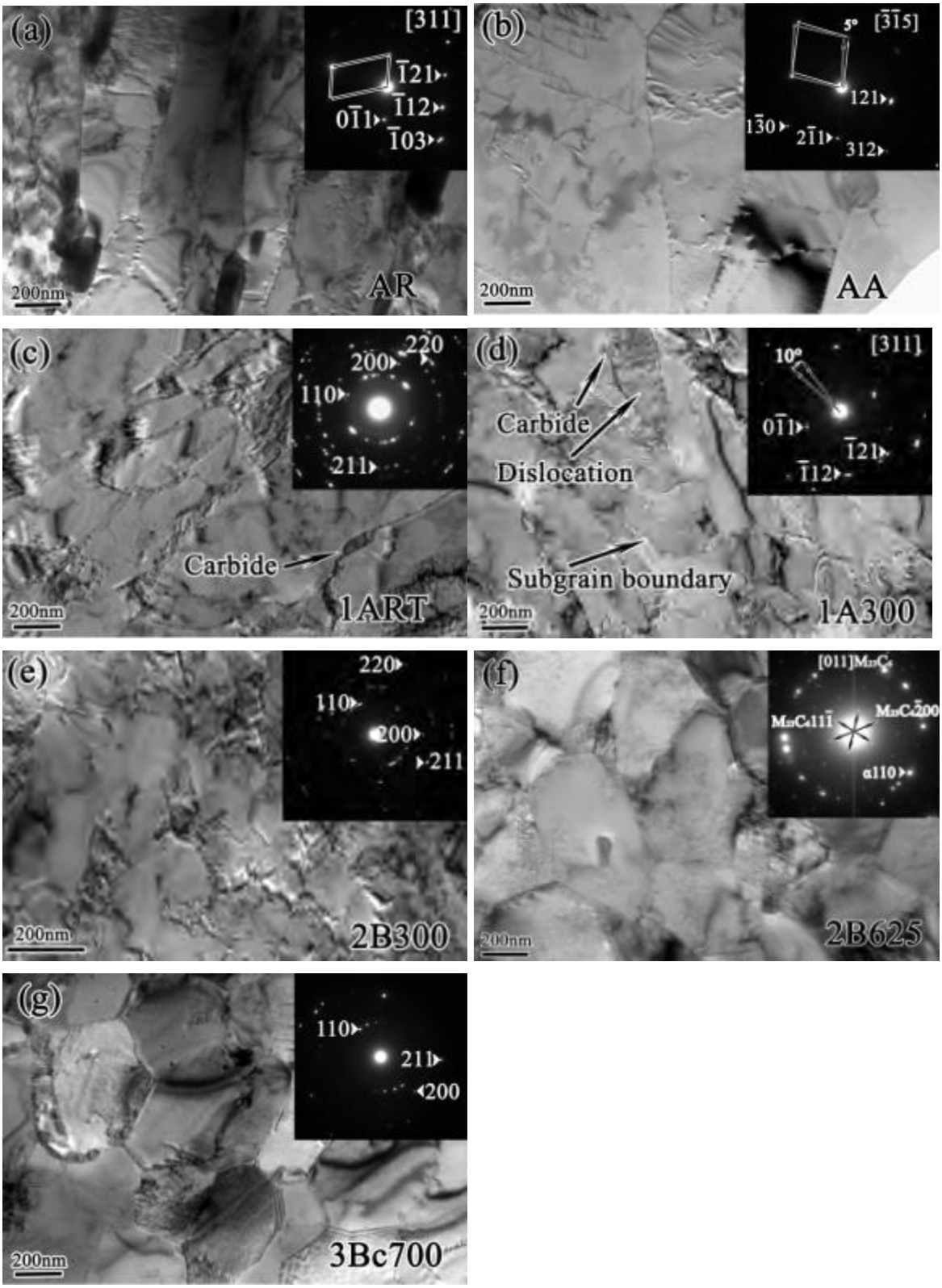

Fig. 7.2. Typical bright field TEM micrographs with the SAD patterns show the grain boundary angle information of the initial and ECAE processed T91 steels (a) AR material, the zone axis is

[311], low angle grain boundaries were detected between the four laths. (b) AA material, the zone axis is $[\bar{1}\bar{3}5]$, the grain boundary angle was about 5° as marked by arrows. (c) 1ART, the grain boundary angle was increased and some high angle grain boundaries were detected. (d) 1A300, the axis is again [311], all the grain boundaries detected were below 10°. (e) 2B300, high angle grain boundaries were detected hinted by the ring like diffraction pattern. (f) 2B625, high angle grain boundaries were observed and the small dots marked by the arrow were from the carbides at zone axis [011]. (g) 3Bc700, the grain boundaries were detected as predominately high angle grain boundaries.

The grain boundaries angle evolution is shown in Fig.7.2. Both AA and AR samples showed predominately low angle grain boundaries as indicated by the inserted SAD patterns in Fig. 7.2a-b. Grain boundary angle increased after 1A300, but still within the range of low angle grain boundary as shown in Fig.7.2d. Meanwhile, 1ART resulted in high angle grain boundaries according to Fig.7.2c. High angle grain boundaries were frequently observed after two or more passes, as shown in Fig. 7.2e-g. In addition, one carbide particle was indexed as [011] zone axis according to the diffraction pattern in Fig. 7.2f. The characteristic carbides showed an FCC structure of $M_{23}C_6$ (M=Fe, Cr, Mo) with lattice parameter around 1.06 nm.

Fig.7.3 show the representative TEM micrographs of the T91 steel after heat treatment (500°C/10h annealing). The AA samples showed more carbides precipitated along the prior austenite and lath boundaries in Fig.7.3a. The prior austenite grain size was estimated about 20μm from the AA sample before heat treatment using a SEM image (not shown here). The ECAE processed materials after heat treatment showed coarsened carbides. The density of intragranular dislocation was significantly reduced in the cold ECAEed samples (1ART, 1A300 and 2B300) as shown in Fig. 7.3b-d. 1ART sample showed the largest carbides size as the high dislocation density could accelerate the formation of carbides. The carbides in 2B625 or 3Bc700 samples also coarsened.

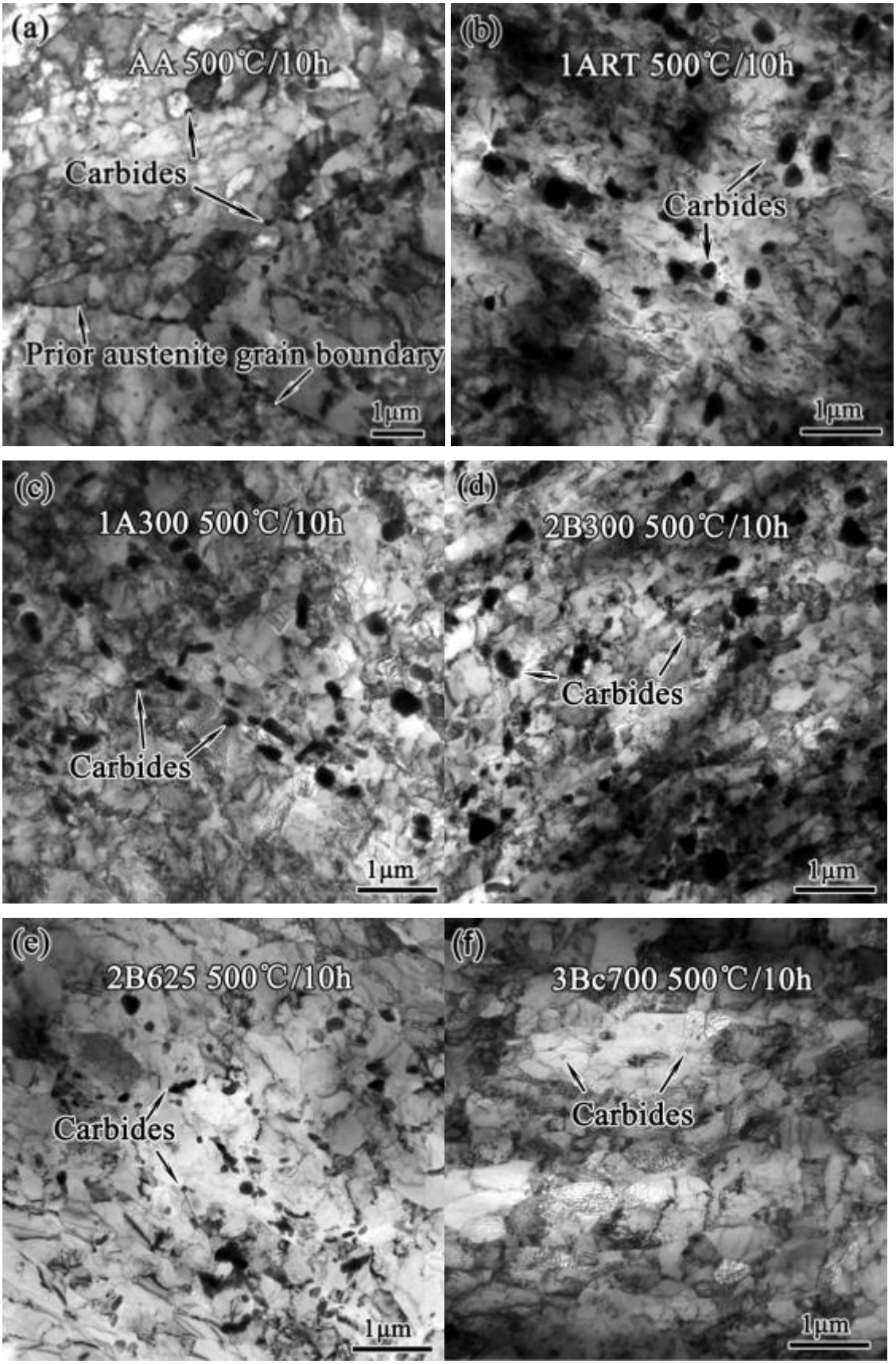
(a)
AA 500℃/10h
Carbides
Prior austenite grain boundary
1μm
(b)
1ART 500℃/10h
Carbides
1μm
(c)
1A300 500℃/10h
Carbides
1μm
(d)
2B300 500℃/10h
Carbides
1μm
(e)
2B625 500℃/10h
Carbides
1μm
(f)
3Bc700 500℃/10h
Carbides
1μm

Fig. 7.3. TEM micrographs of T91 after heat treatment, 500°C/10h followed by furnace cooling. For most specimens, (a-f), annealing induced an increase in the size and density of carbides and a reduction of dislocation density. The average grain size was less influenced by annealing. In AA specimen (a), more carbide particles were observed along the prior austenite grain boundaries and the lath boundaries.

Statistical analyses of the microstructure results were performed to determine the size distribution of grains and carbide particles. Fig.7.4a show the grain size distribution determined from TEM micrographs by using linear intercept method (≥400 grains were analyzed for each case). Grains as large as 2.7 µm existed in the AA alloy. Processing via route 1A300 refined the maximum grain size to less than 1 µm. 2B300 resulted in further grain refinement to 0.6 µm with high frequency of smaller grains. Hot ECAE processing (2B625 and 3B700) was less effective compared with cold ECAE processing in the terms of grain refinement. The refinement of carbides by ECAE was also noticed from Fig.7.4b (≥150 particles were analyzed for each case). The refinement of carbides was not significantly by cold ECAE (1ART, 1A300, 2B300). On the other hand, 2B625 refined the carbides size to less than 250 nm. 3Bc700 can further refine the carbides to less than 100 nm. Hot ECAE seems more effective compared with cold ECAE in the refining of carbides particles. After heat treatment (annealing at 500°C/10h), the carbides coarsened slightly according to Fig.7.4c (≥170 particles were analyzed for each case). The density of particle was also evaluated as shown in Fig.7.5. The thickness of the thin area in TEM samples was assumed to be 100nm. Both the size and density showed strong correlation with the processing temperature in Fig.7.5a. The carbides density increased six times after 3Bc700 processing compared with the AA condition. After heat treatment (500°C/10h), an increase of density was noticed in AA and cold ECAEed samples, while a slightly decrease of density occurred in the hot ECAEed samples as shown in Fig.7.5b.

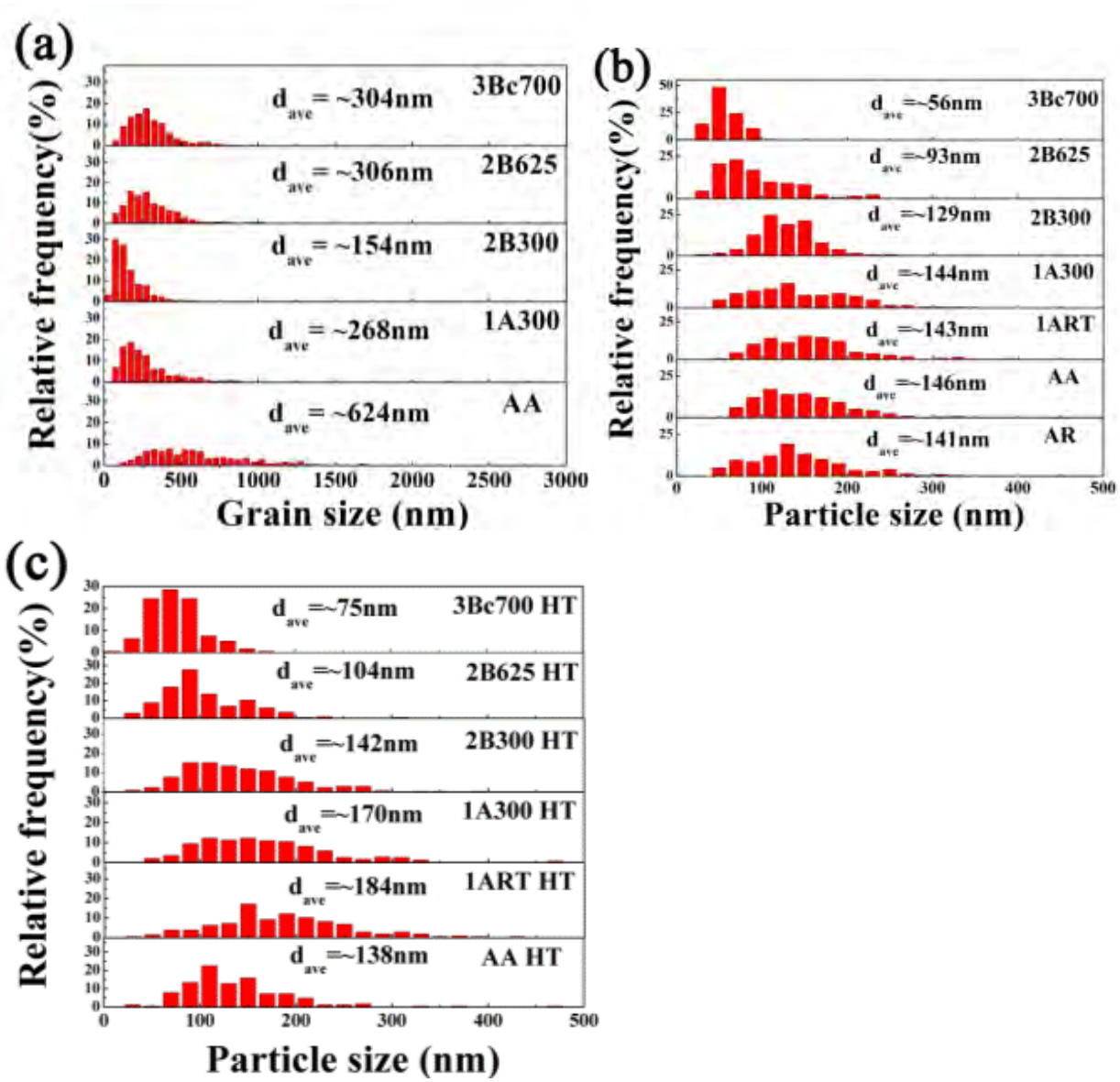

Fig. 7. 4. Grain and carbide size distributions in various T91 alloys. (a) Grain refinement occurred in all ECAE processed specimens. 2B300 specimen showed the smallest average grain size, about ~150nm. (b) 3Bc700 specimen had a large number of fine carbides with an average diameter of 50nm. No significant refinement of carbides was observed in low temperature single pass processing. 2B300 specimen showed slightly refinement of carbides. (c) After heat treatment (500°C/10h), most carbides coarsened in the ECAE processed samples. HT : 500°C annealing 10h, furnace cooling

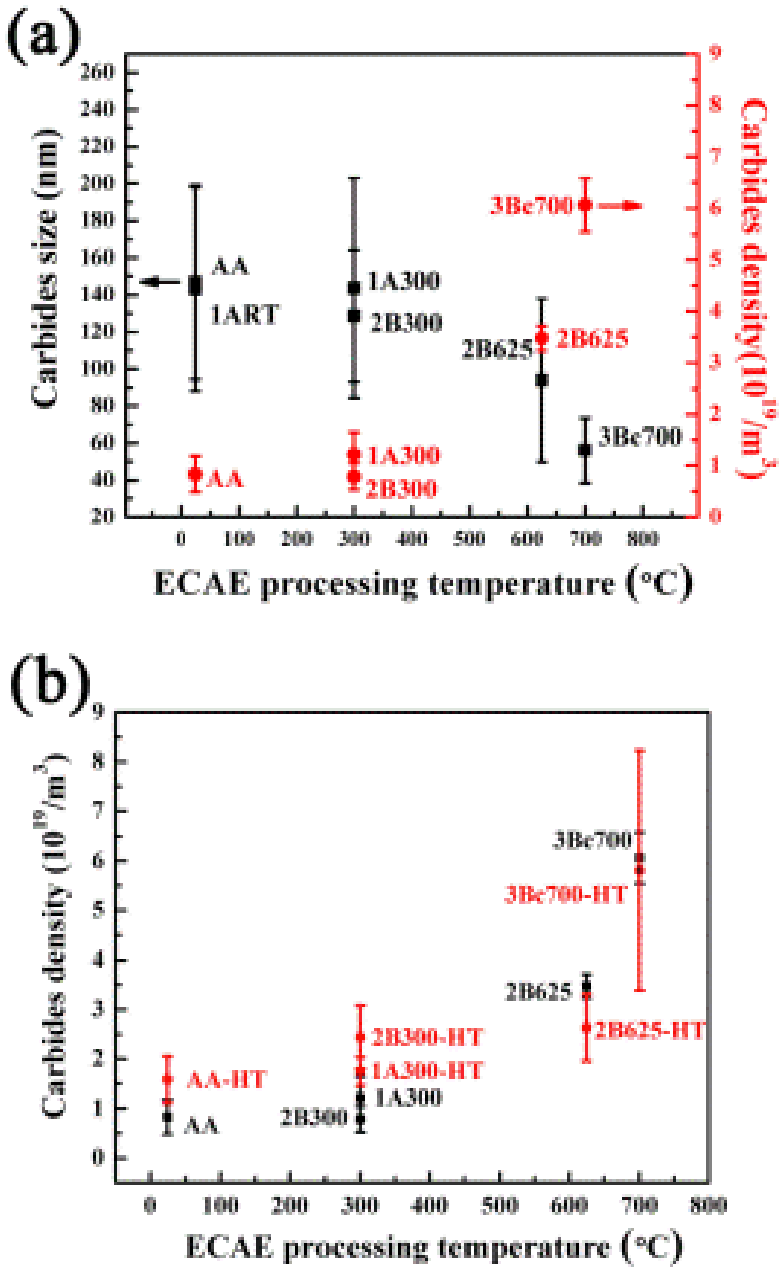

Fig. 7.5. Precipitation behavior of carbides (a) The evolution of carbides size and carbide density after different processing temperatures, the size and density were slightly changed after cold-ECAE, significant changes in carbides size and density were noticed after hot-ECAE. (b) Comparison of carbides density after post-processing heat treatment (annealing at 500°C/10h).

7.2 Thermal stability and mechanical properties of ECAEed T91

Fig.7.6a and b show the hardness of the AA and ECAEed T91 alloys after 1h annealing and 10h annealing at various temperatures up to 800°C. The AA sample showed good thermal stability up to 700°C. For ECAE processed samples, the general grain coarsening started above 500°C, and significant softening occurred thereafter. The cold ECAEed samples soften after 300°C. After annealing at 700 or 800°C, the ECAE processed materials was even softer than the AA material. After 10h annealing, the hardness of 2B625 sample slightly increased.

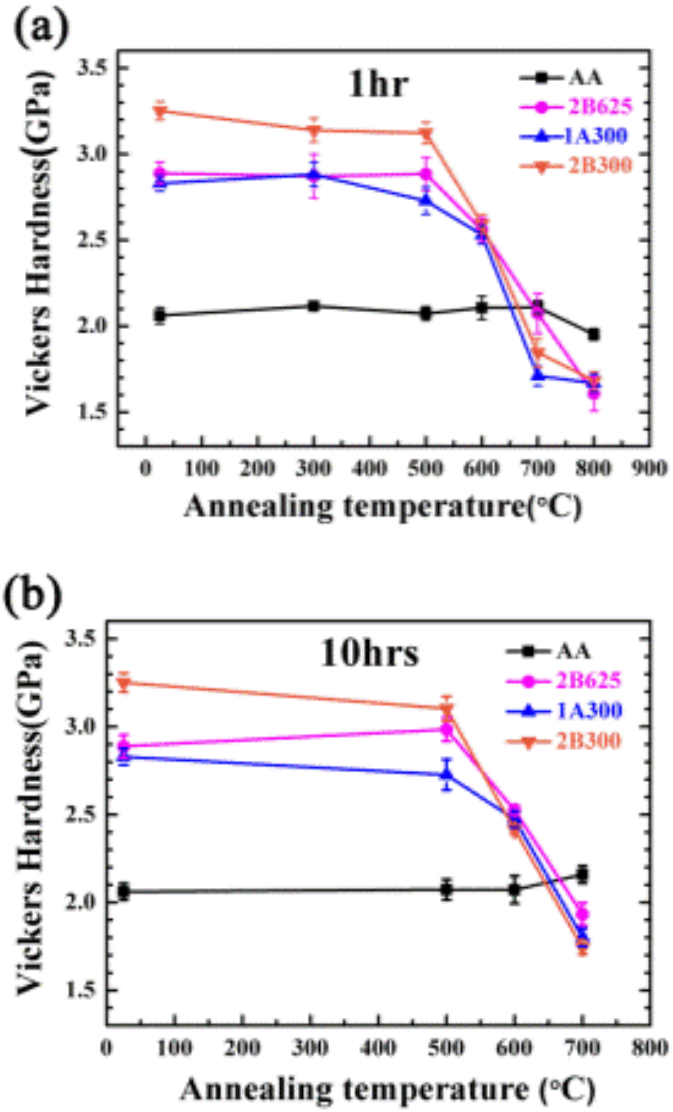

Fig. 7.6. Evolution of Vickers hardness after annealing for (a) 1 h and (b) 10 h. The recrystallization temperature is ~ 500°C. The ECAE processed samples were thermal stable up to 500°C/10h. Significant softening occurred above 500°C.

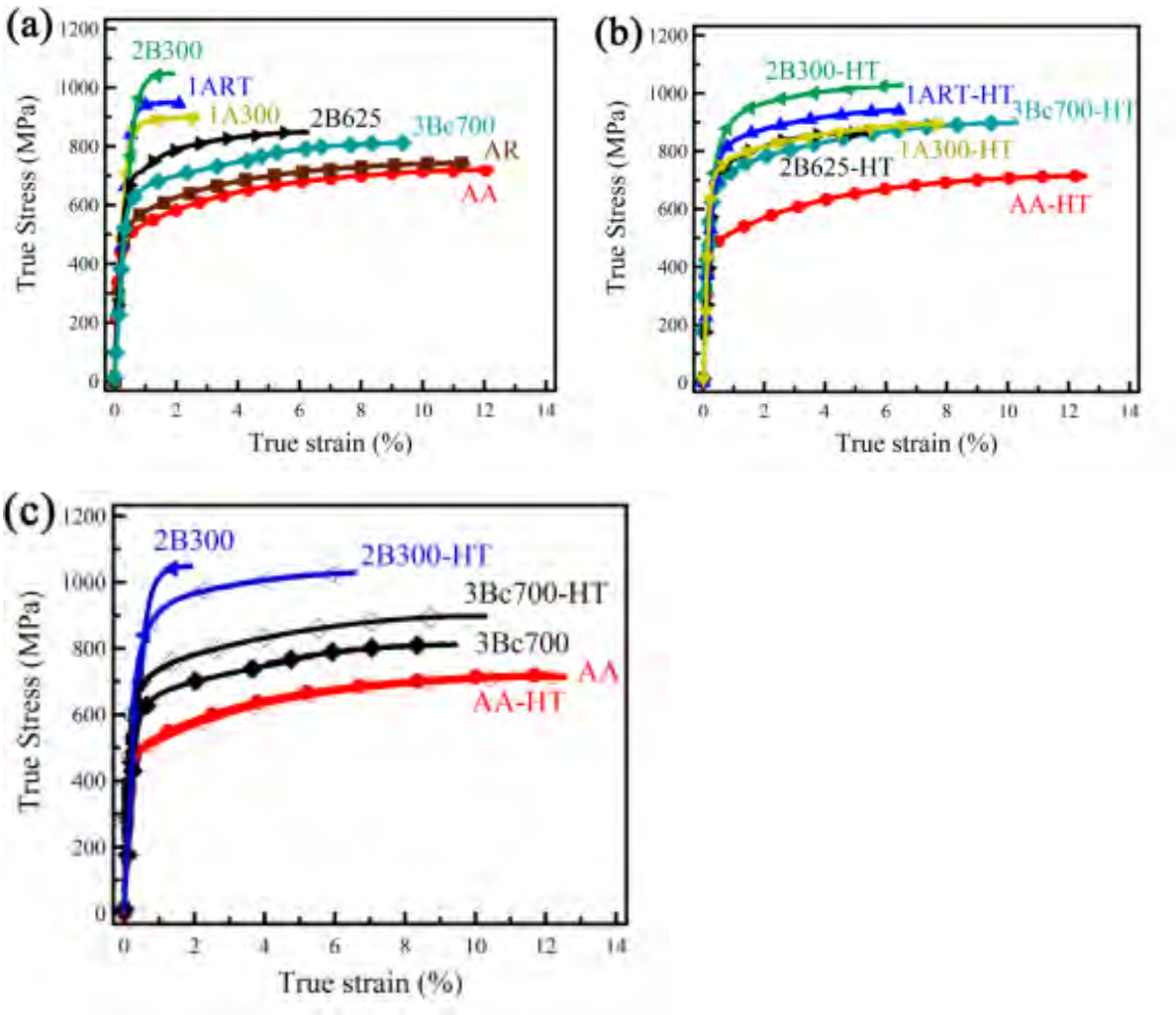

Fig. 7.7. True stress-strain curves of T91 alloys. (a) After cold ECAE, specimens showed significant increase in yield strength but considerable reduction of uniform elongation. Specimens after hot ECAE exhibited moderate increase of yield strength but a retention of ductility. (b) After annealing at 500°C/10h, specimens after cold ECAE showed significant recovery of uniform elongation with insignificant loss of mechanical strength. Whereas the increase of ductility for hot ECAE samples was less pronounced and an increase of tensile strength was noticed. (c) Comparison of annealing effect on the tensile properties of cold ECAE and hot ECAE samples.

HT：500°C annealing for 10h, furnace cooling

Fig.7.7a provided a comparison of the tensile curves (true stress and true strain) of T91 alloys before and after ECAE. AA samples showed a slightly lower ultimate tensile strength (σ_{UTS}) and yielding strength (σ_y) than AR samples with similar ductility. The 2B300 samples showed the highest strength with σ_{UTS} and σ_y about 1031 and 982 MPa, respectively. The 3Bc700 samples exhibited the largest total elongation (ε_t=22%) and uniform strain (e=11%) among the ECAEed samples. Fig.7.7b summarized the tensile curves of AA and ECAEed T91 steels after annealing at 500°C for 10h. The ductility of cold ECAEed conditions (i.e.1ART, 1A300, and 2B300) improved significantly with slightly a little sacrifice of strength. By contrast, the ductility of hot ECAEed cases (2B625, 3Bc700) remained the same, while a slight increase of strength could be observed. After annealing, the 2B300 samples exhibit the highest strength (σ_{UTS}=968MPa, σ_y=845MPa) with good ductility (ε_t=16%, e=6.5%). The 3Bc700 samples exhibited the best ductility (ε_t=22%, e=11%) with good strength (σ_{UTS}=797MPa, σ_y=650MPa). Fig.7.7c showed the typical annealing effect on the AA, cold ECAEed and hot ECAEed samples. All the tensile test data have been collected in Table 3.

Table 7.3. Summary of the mechanical properties of the T91 steel subjected to various thermo-mechanical treatment conditions. The standard deviations are obtained from multiple independent experiments.

Sample ID	UTS(MPa)		Yield strength (MPa)		Elongation to failure (%)		True uniform strain (%)	
	Before HT	After HT	Before HT	After HT	Before HT	After HT	Before HT	After HT
AR	681±4	-	508±1	-	20±2	-	10.6±1	-
AA	646±3	645±3	482±1	445±23	21±1	24±1	11.5±0.7	13.9±1.4
1ART	935±1	885±3	900±1	775±1	7.9±0.9	13±1	1.8±0.1	6.5±0.1
1A300	886±5	828±7	838±1	709±18	9.2±0.5	16±2	3±0.3	8.4±0.8
2B300	1031±1	968±3	982±1	845±15	8.5±0.1	16±2	1.8±0.1	6.5±0.7
2B625	805±2	848±22	681±16	719±13	10.9±1	13±1	5.3±0.8	5.2±0.2
3Bc700	763±15	797±23	615±3	650±3	22±2	22±1	11.1±1.6	11.1±0.8

HT：500°C annealing 10h, furnace cooling

The microstructure evolution of ECAEed T91 steels

The grain refinement and evolution of grain boundary angle during ECAE was a dislocation related process. The dislocation entangled and dislocation cells formed during deformation. The size of the cell walls decreased with the increasing amount of strain. The cell walls become sharper as the misorientation between two neighbor cells increased. Then the subgrain boundaries formed through polygonization process.

The initial structure of tempered martensite laths within the same prior austenite grain showed low angle grain boundaries in AA and AR samples. Similar results about grain boundaries were observed by EBSD mapping of grade T91 during long time aging in early observation. The grain size was about 3 μm. During ECAE, the density and distribution of dislocation was strongly dependent on the temperature of deformation. Though same amount of strain was applied, smaller grain size (~150nm) was formed during cold ECAE compared with that of hot ECAE (~300nm), because the dislocation proliferated with slow recovery speed, so the mean free path for dislocation interaction decreased. The 1ART sample showed higher density of dislocation than the 1A300 sample, which can be also explained by the dynamic recovery process during the deformation. The formation of low angle grain boundaries after single pass was consistent with early observation in pure Al and Al alloys, because it was during the beginning stage of dislocation interaction and the cell walls just formed, which was actually a low angle grain boundary. After two passes, high angle grain boundaries begin to form. Three passes following route Bc allowed the grain boundaries turned into predominated high angle grain boundaries. Actually, route Bc was the most effective route to generate high angle grain boundaries. The grain size of hot ECAE reached its refinement limited during 2B625 process, because similar grain size was achieved through 3Bc700 process. The refining limited was frequently observed in other metal and alloy systems during ECAE. The grain size and grain angle evolution was estimated based on the transverse plane of the ECAE billets. Other directions (such as flow plane and longitude plane) of observation may give total different configuration. Because all the samples after ECAE processed were examined in the same plane, the results were still comparable in the present case.

The precipitates behavior during ECAE and post-processing heat treatment

The processing of ECAE on grain refinement was well understood, but the behavior of precipitates during ECAE was still open to question and less studied. No general conclusion was

drawn from the existing results, because the precipitates behavior could be influenced by all the thermomechanical history before or during ECAE, which was varied from case to case in different systems. Previous results about precipitates hardening Al alloy showed the fracture of precipitates, and a redistribution of the precipitates occurred, where the precipitates commonly had a long plate or rod shape which exhibited a large stress concentrator. Study about Al based metal matrix composites showed no or limited broken Al_2O_3 particles were observed. The high processing temperature was supposed to be the drawback for breaking the particles. However, there is a difference between the two kind of materials during ECAE deformation, because the ceramic particles in metal matrix composites commonly show little solid solution into the matrix, while precipitate hardening phases which were from the matrix can be resolved at elevated temperature. The carbides precipitated behavior during ECAE in the present T91 alloy was strongly dependent on the ECEA temperature. During the cold ECAE, the particles were almost the same size and density as the AA condition. The carbide particles mostly belong to the intergranular precipitates which located at the grain boundaries where the atoms were loosely packed. During the hot ECAE, the carbide particles exhibited a small size with high density, most of which belonged to the intragranular precipitates. Neither case showed broken particles.

The mechanism of the particles refinement was proposed in Fig.7.8 (Use 300°C and 700°C as examples for cold and hot ECAE). As the Fig. 7.8a-d illustrated, during the cold ECAE, little solid solubility change to the elements consisted of carbides particles and prior austenite grain boundaries during the temperature range of processing. During the deformation, the particles have additional freedom at the grain boundaries, and the compression stress from the soft matrix could not break the hard particles. Rotation of the particles could happen due to the discontinuous of elastic and plastic properties at the interface between particles and matrix. Finally, the prior austenite grain boundaries were mechanically broken but chemically (segregation) and topologically (total length) conserved shown in Fig.7.8c. Actually, in Fig.7.2c, the grain boundaries beside a carbide particle were curved by it during the deformation. Based on the above explanation, no significant change of size or density should be expected at the beginning stage of deformation (at least first pass). This property allowed the use of the carbides as markers to observe the deformation behavior of prior-austenite grain boundaries. An example of using precipitates as a marker to observe the material flow during ECAE was reported in the reference. After annealing (500°C/10h), the size and distribution of carbide particles were

changed again. The prior austenite grain boundaries were chemically and energetically favored for the nucleation and growth of carbides. The coarsening of the precipitates could explain as the pipe diffusion of alloying elements along dislocation cores during the aging process. The 1ART showed the largest carbides after annealing because the highest dislocation density it possessed. The newly formed grain boundaries could also serve as a nucleation sites for carbides particles. Therefore, the density of carbides slightly increased.

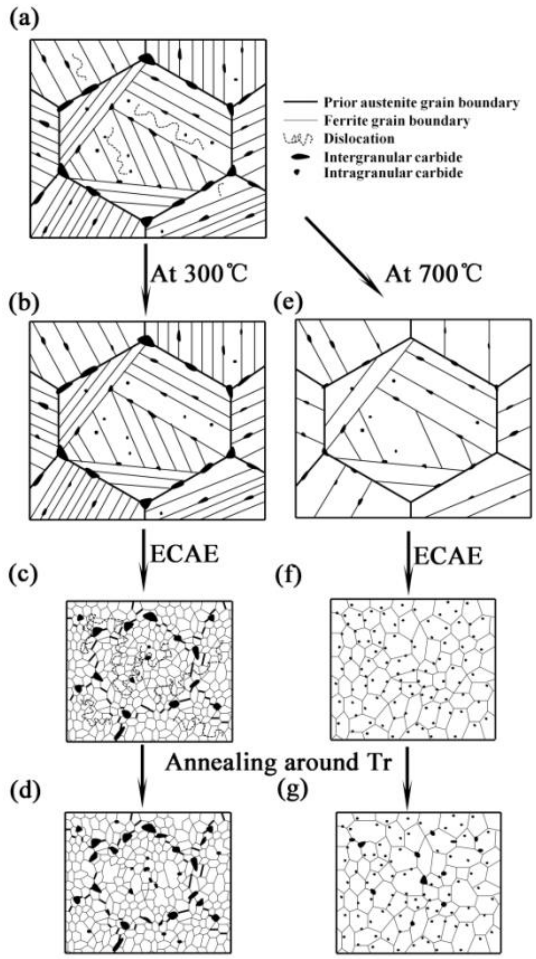

Fig. 7.8. Illustration of precipitates behavior during cold ECAE (a-b-c-d) and hot ECAE (a-e-f-g). Prior austenite grain boundary was the preference nucleation sites for carbides. The prior austenite grain boundaries were topologically and chemical conserved during cold ECAE (total length or composition was not significantly changed). The prior austenite grain boundaries were chemically eliminated during hot ECAE, so the carbides begin to precipitates randomly around the grain boundaries where the carbon concentration was slightly higher. After annealing around Tr (recrystallizaiton temperature), the dislocation density decreased and new carbides precipitates around prior austenite grain boundaries for cold ECAEed samples as shown in (d). Existing carbides begin to coarsen. For hot ECAEed samples, the carbides grew toward grain boundaries (g).

During the hot ECAE as shown in Fig. 7.8a and e-g, solid solution process happened to the element consisting the carbon particles and prior austenite grain boundaries. So the carbides at triple junction or grain boundaries became smaller because they are high diffusion path shown in Fig.7.8d. The segregation of elements at prior austenite grain boundaries begin to decrease (shown in Fig.7.8d expressed as the thickness of the line decreased). The extrusion broke the prior austenite grain boundaries. Repeated two or three times, the prior austenite grain

boundaries were chemically eliminated, where commonly served as a preference nucleation sites for carbides. New carbides could be precipitated in the random place due to the lost of preference nucleation sites, commonly near the grain boundaries because the carbides dissolved there and the carbon concentration was higher. So the carbides included the intragranular carbides which was not dissolved and newly formed carbides during cooling process. The size of both particles was influenced by the solid solubility of the alloying elements which was influence by the processing temperature. The high temperature led to high solid solution, thus smaller intragranular particles undissolved. This could explain the smaller size of particles was achieved during hot ECAE. After annealing (500°C/10h), some of the carbides grew toward grain boundaries during the annealing. Some intergranular particles also grew. The coherence was lost during the annealing process. Some small particles probably dissolved due to Ostwald coarsening process. A slightly decrease in density was observed in hot ECAE samples. If the annealing time was long enough, both precipitates in hot ECAE and cold ECAE would reach the equilibrium amount of precipitates.

Our discussion was based on the transverse plan of the billet processed by route B (with three passes). The texture was not considered in the schematic. However, different route could have different efficiency to break the prior austenite grain boundaries, thus the behavior of precipitates probably show slightly difference. For more passes during cold ECAE, the size and density of precipitates could also decreased because further deformation may lead to stress assisted solid solution, which was frequently observed in mechanical alloying process. The size was slightly refined and density decrease in 2B300 samples showed the trend consistent with this argument.

The strengthening mechanism

The increase of the strength of ECAEed T91 alloys could come from the grain refinement, the increasing density of dislocation and precipitates hardening. An established strengthening model for grain refinement of pure metals or consolidated bulk metals (which considered the strengthening from dislocation density and grain refinement) was proposed as following[36]:

$$\sigma_y = \sigma_0 + \alpha\sqrt{\rho} + \beta/\sqrt{d} \qquad (1),$$

where σ_y is the yielding strength, σ_0 is the lattice friction, the second term are due to the Taylor's equation, and the third term arises from the Hall-Petch relationship.

Considering the Orowan mechanism,

$$\sigma = \alpha Gb / L \qquad (2),$$

where σ is the additional strength needed due to the dislocation bypass an obstacle, L is the inter particle distance on the slipping plane, which could relate to the particle density,

$$L \propto 1 / \sqrt[3]{n} \qquad (3),$$

where n is the density of the particles.

The strengthening in the present study could be written as:

$$\sigma_y = \sigma_0 + k_1 Gb\sqrt{\rho} + k_2 / \sqrt{d} + k_3 Gb\sqrt[3]{n} \qquad (4),$$

where σ_y is the yielding strength, σ_0 is the lattice friction, ρ is the dislocation density, d is the average grain size, b is the burger's vector, G is the shear modulus, n is the density of particles. k_1, k_2, k_3 are dependent on the material properties. k_1 describes an average interaction strength between dislocation. k_2 is the grain boundary strengthen which was a function of grain boundaries properties such as grain boundaries angles. k_3 is related to the efficiency of precipitates as an obstacle to block dislocations. The above equation is the simplest scenario where simple rule of mixture is applied. A more accurate description of Taylor's equation and strain hardening was described in the literature.

The AA samples showed the lowest yielding strength, because the grain size was large and dislocation density was low. The precipitates located at grain boundaries which showed low efficiency to block the mobile dislocation. After cold ECAE, the dislocation density ρ was significantly increased and the grain size d decreased, thus an enhancement in strength should be expected. However, due to the low dislocation accumulation capability, the samples after cold ECAE commonly showed low or no work hardening rate. Although some research showed that after more passes the ductility could increase a few percent, that probably due to the increase fraction of high angle grain boundaries, which change the dislocation movement mechanism to grain boundaries sliding or rotation. The samples after hot ECAE exhibited a small dislocation density ρ with decreased grain size d. The precipitates were located within the grain with a very

high density. The strengthening also occurred. The samples after hot ECAE commonly exhibited good work hardening rate due to the low density of dislocation after processing.

After annealing, cold ECAE samples showed decreased of strengthen and increase of ductility due to decrease of dislocation density during recovery process. The ductility of hot ECAE samples remained the same while a slightly increase of strength were noticed. Just like the beginning stage of aging hardening Al alloys, the rearrange of solute atoms in the matrix should have some influence in the friction strength σ_0. Moreover, the grain boundaries angle change (related to the k_2 term in the equation) could influence the strengthen. The low angle grain boundary was proved to be lower efficiency in the dislocation pile-ups mechanism than the high angle grain boundaries.

A8. Grain boundary engineering on ECAP processed specimen

Lead organization: University of Florida (Yong Yang) and
University of Wisconsin, Madison (Todd Allen)

8.1 Overview

The grain structures of ECAPed model alloy, 304L and 316L Stainless steels were characterized using Electron Backscatter Diffraction (EBSD) technology, the average grain size, grain size distribution, and phases were fully studied. Moreover, the nanoMegas was used to study the nano-sized grains under TEM, and the system is equipped on JEOL 2010F TEM. Figure 3.2.1 shows a basic set up of the system, which consists of beam scanning unit, high speed external optical CCD camera and image processing, and automated indexing module. The acquired diffraction patterns are matched again pre-calculated solutions of crystal orientation. The selected materials were also studied using Transmission Electron Microscopy (TEM), and the samples were prepared using an electro-polishing method (Single Jet Polish, Southbay Technology, CA).

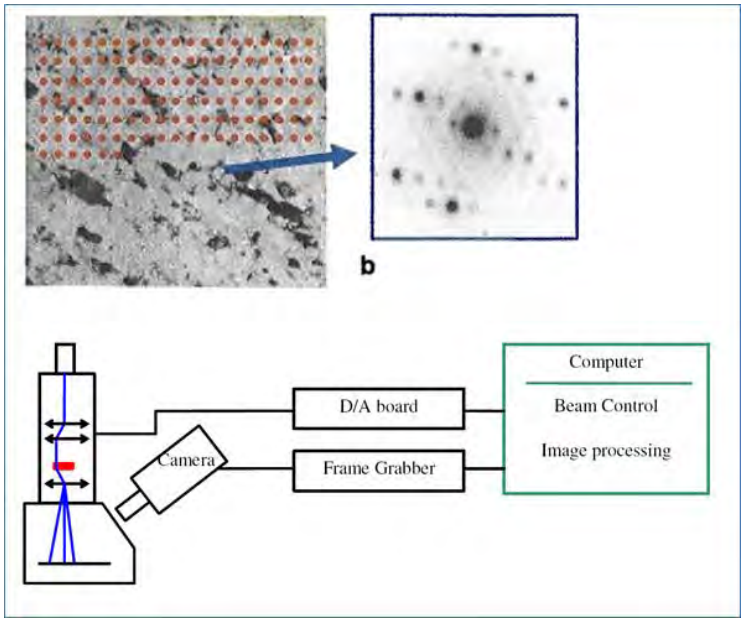

Fig. 8.1 Setup of nanoMegas on transmission electron microscope.

8.2 Grain structure characterizations:

Model alloy Fe-14Cr-16Ni (wt%):

For comparison, the as-received (AR) model alloy was also examined using EBSD, as shown in Fig 8.2, the grain size of AR model alloy is in the order of millimeter, and material is fully austenitic. Figure 8.3 shows the grain structure of 8 passes processed model alloy in the transverse plane and flow plane, respectively. The grains in transverse plane display as equiaxed and no texture was observed. However, the grain structure in the flow plane shows texture to some extent and the grains are slightly elongated and aligned along one direction. The grain size distribution in the transverse plane is shown in the Fig. 8.4 and it has an average grain size of ~360 nm, which agrees well with the value from SEM examination performed by the researchers at TAMU.

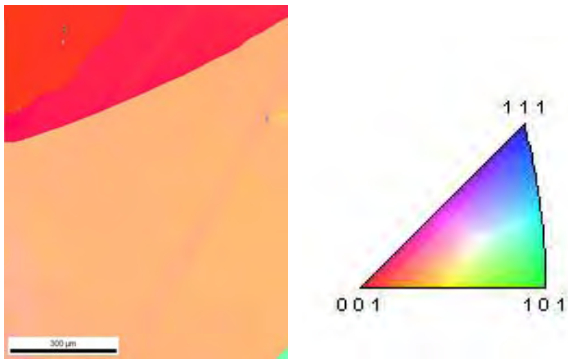

Fig 8.2 Inverse Pole Figure (IPF) of as-received model alloy.

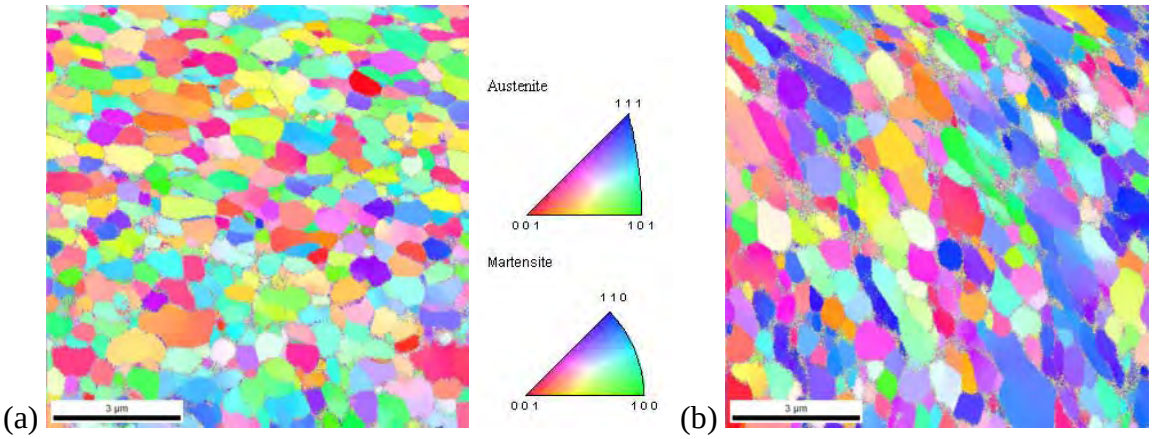

Fig 8.3 IPF image of ECAPed Model Alloy (8 passes, 500 ºC): (a) transverse plane; (b) flow plane.

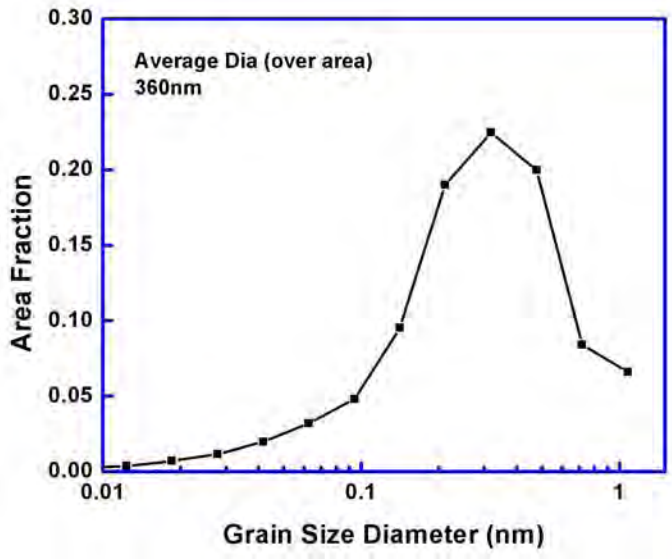

Fig. 8.4 Grain size distribution in the transverse plane of ECAPed Model alloy (8 passes, 500 ºC)

The phase distribution in Fig. 8.5 clearly shows the existence of martensitic phase which was induced by severe deformation during the ECAP process, and the grain boundaries of austenite are decorated with α' martensite as identified using diffractions in TEM (Fig. 8.7).

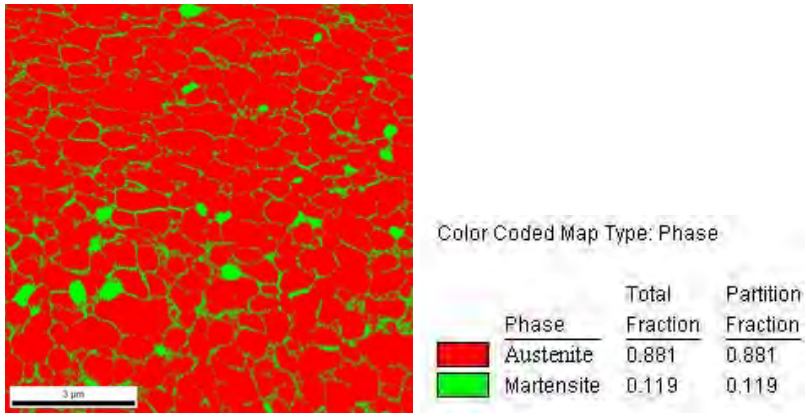

Fig. 8.5 Phase distribution in transverse plane of ECAPed Model Alloy (8 passes, 500 ºC).

The grain boundary character distribution (GBCD) of austenitic phase in the ECAPed model alloy is shown in Fig. 8.6, and the grain structure has a relatively low population of low Σ grain boundaries and the percentage of low angle grain boundary (Σ 1, 5º <θ<15º) is nearly zero. In order to optimize the GBCD of ECAPed alloy, the grain boundary engineering process is needed.

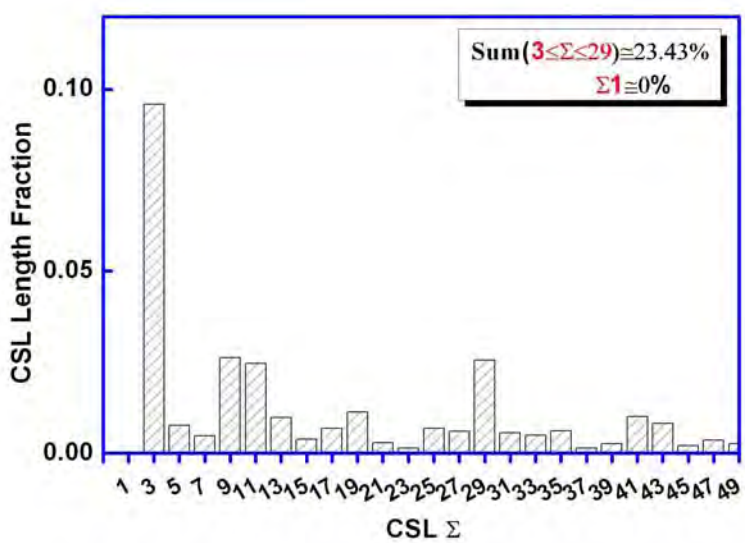

Fig. 8.6 CSL (Coincident Site Lattice) boundary length fraction

The TEM image of Fig. 8.7 clearly displays that the ECAP processed model alloy has an ultrafine grain structure and the grains are nearly equiaxed and the grain boundaries are well defined. TEM image of fig. 8.8 shows an identified α' martensite nano-grain using diffraction pattern, and this grain contains a high density of dislocations which serve as the nucleation site for α' martensite.

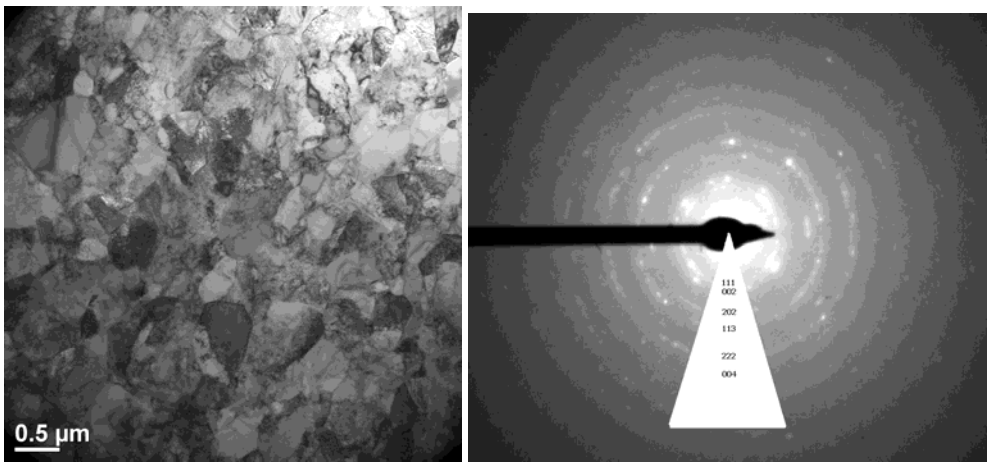

Fig. 8.7 Grain structure of ECAPed Model alloy (8 passes, 500 ºC)

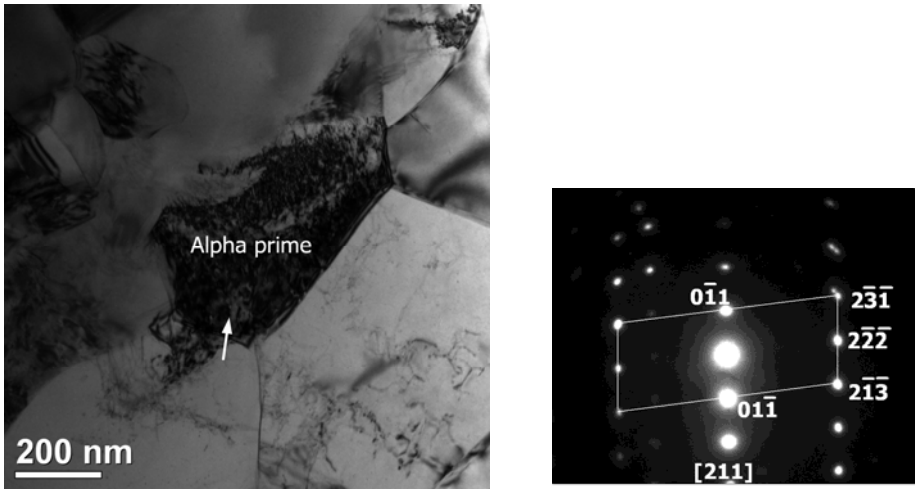

Fig. 8.8 α' martensite identified at the junction of austenitic grains

304L stainless steel:

The 304 stainless steel was ECAP processed at three different conditions: 2Bc at 300 ºC, 4Bc at 500 ºC and 6Bc at 500 ºC, and the grain structures were examined in the transverse plane. The EBSD and the TEM images are shown in Fig.8.9-11, respectively. Generally, the ECAP

processing on the 304L introduced a high density of dislocations and textures, and the materials unanimously show the banding structure after ECAP processing.

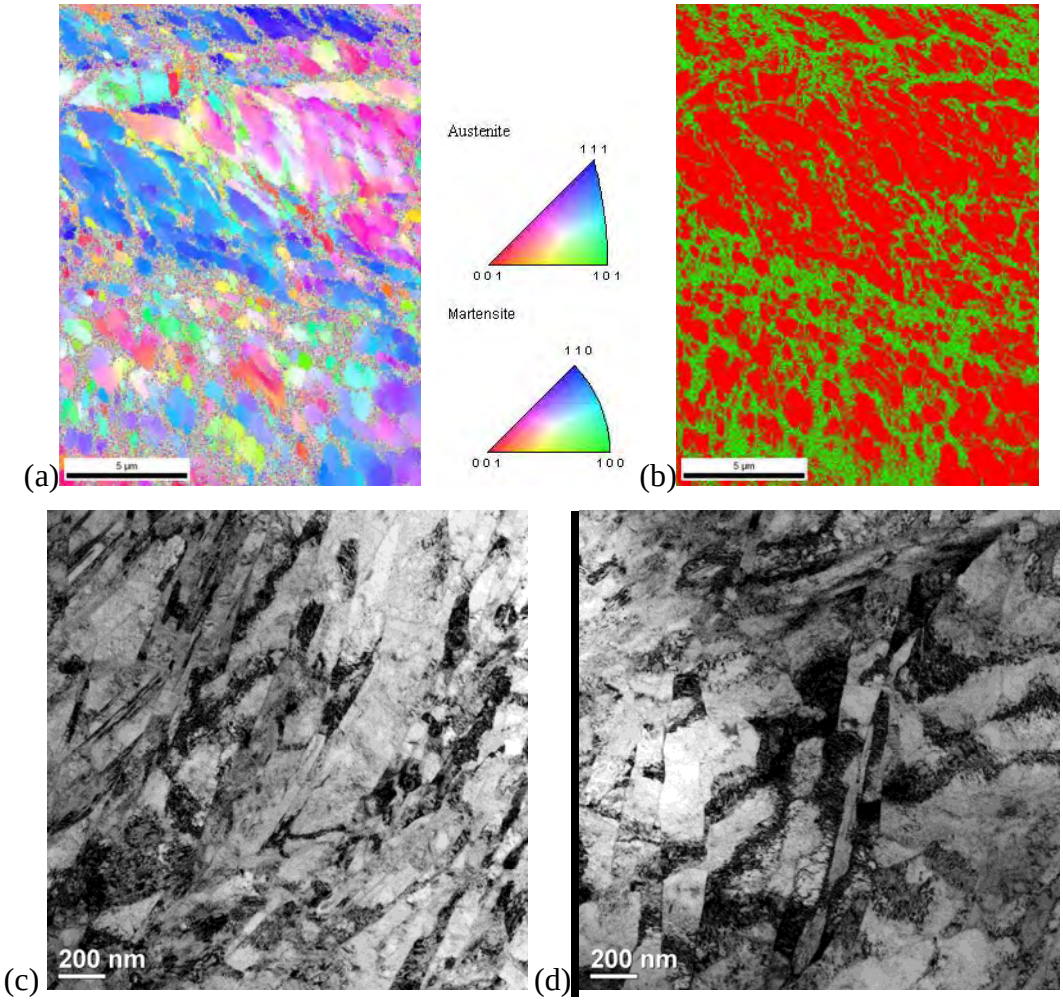

Fig.8.9. 304L 2Bc and 300 ºC: (a) IPF image, (b) Phase image: red color denotes austenite and green for martensite, (c) and (d) TEM images.

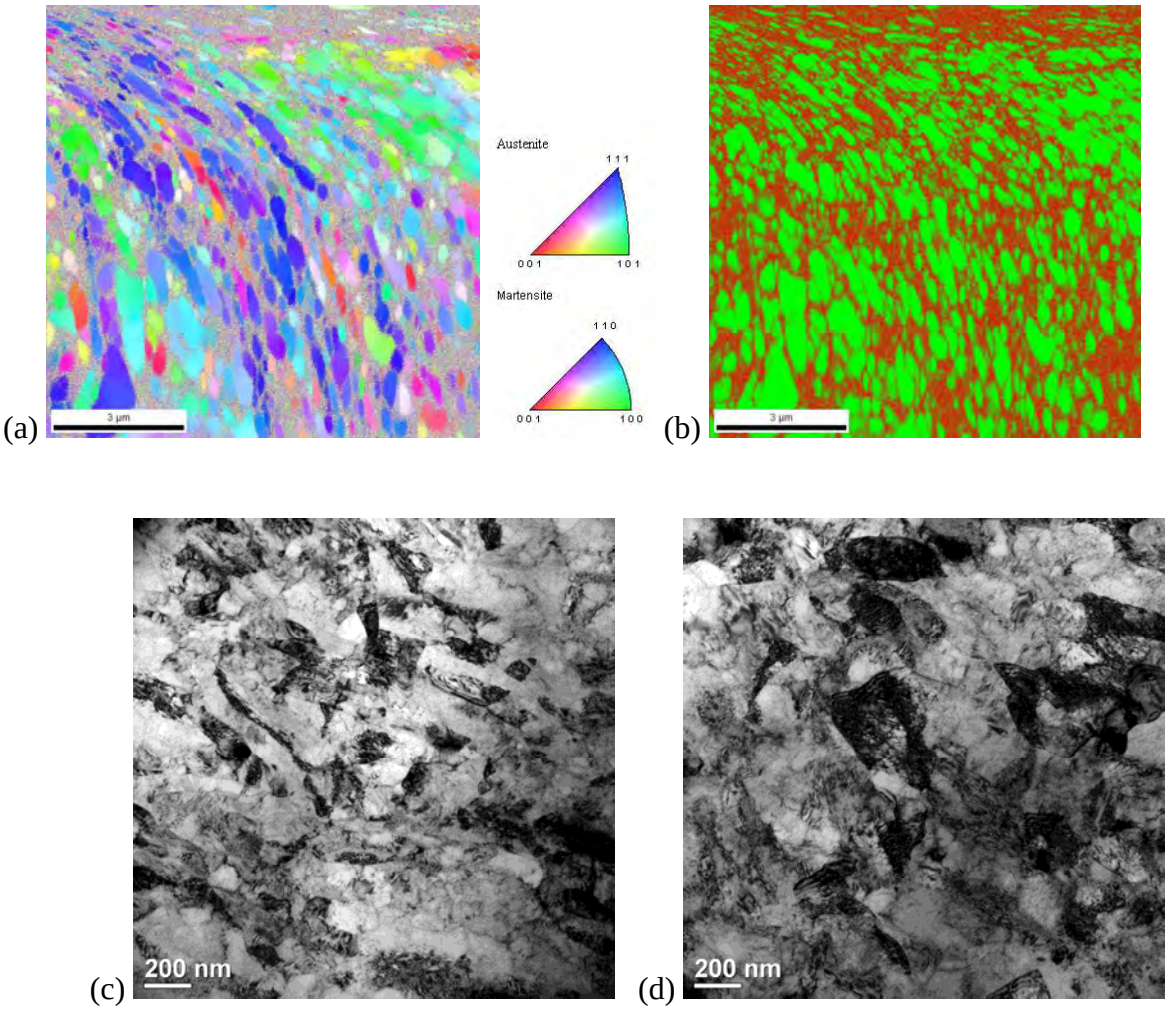

Fig.8.10. 304L 4Bc and 500 ºC: (a) IPF image, (b) Phase image: red color denotes austenite and green for martensite, (c) and (d) TEM images.

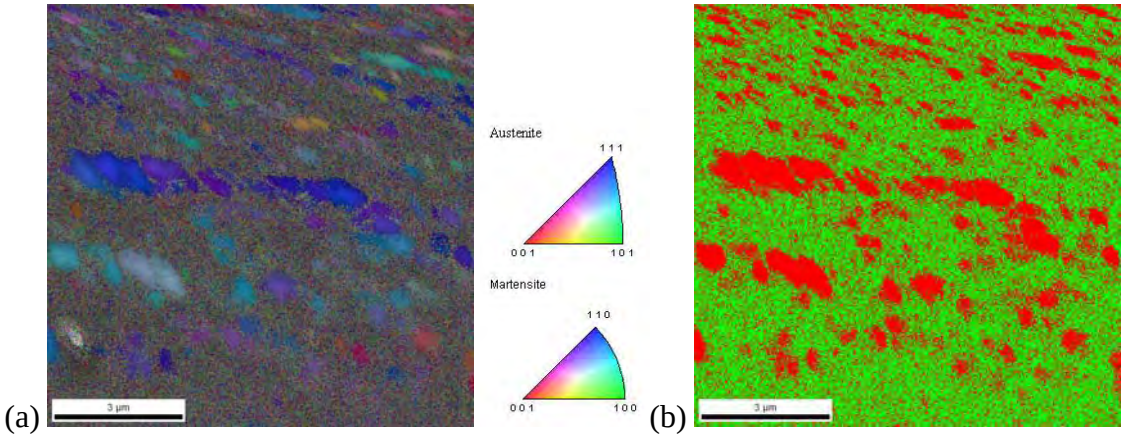

(c) 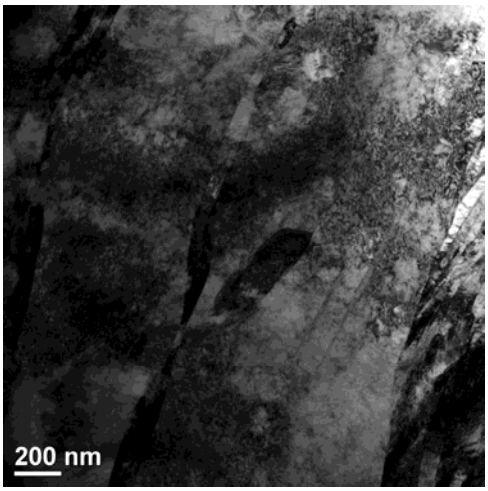

(d) 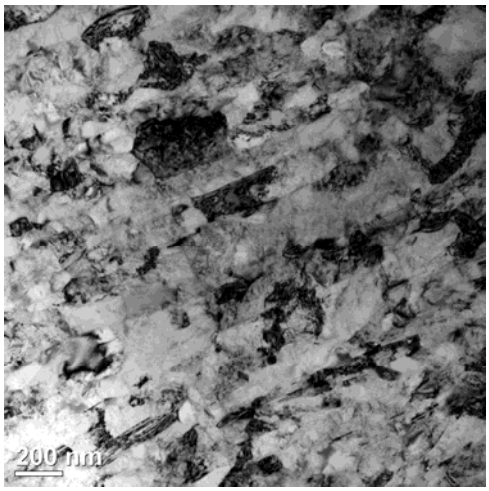

Fig. 8.11 304L 6Bc and 500 ºC: (a) IPF image, (b) Phase image: red color denotes austenite and green for martensite, (c) and (d) TEM images.

316L stainless steel:

The 316L stainless steel was also ECAP processed at conditions of 2 Bc at 300 ºC and 4 Bc at 500 ºC. And compared with 304L SS, the 316L SS shows more degraded microstructures regarding to the grain refining, uniformity of grain size, and phase transformation after ECAP processing. The microstructures of processed 316L SS are shown in Fig. 8.12-13. Due to the high density of dislocation density, the EBSD patterns were smeared and the image quality was significantly degraded. TEM images show that the shear bands are the typical microstructural features of the processed materials and the deformation twins were widely observed in the parent austenite after deformation. The martensites might be a mixture of ε phase and α' phase while more TEM studies are needed.

(a) 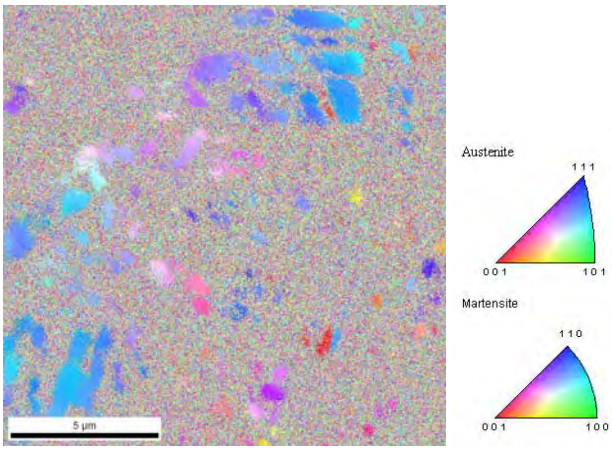

(b) 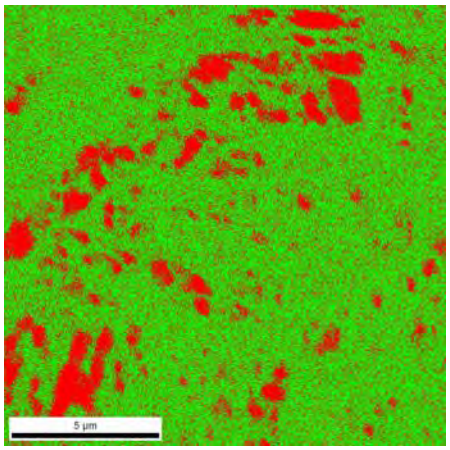

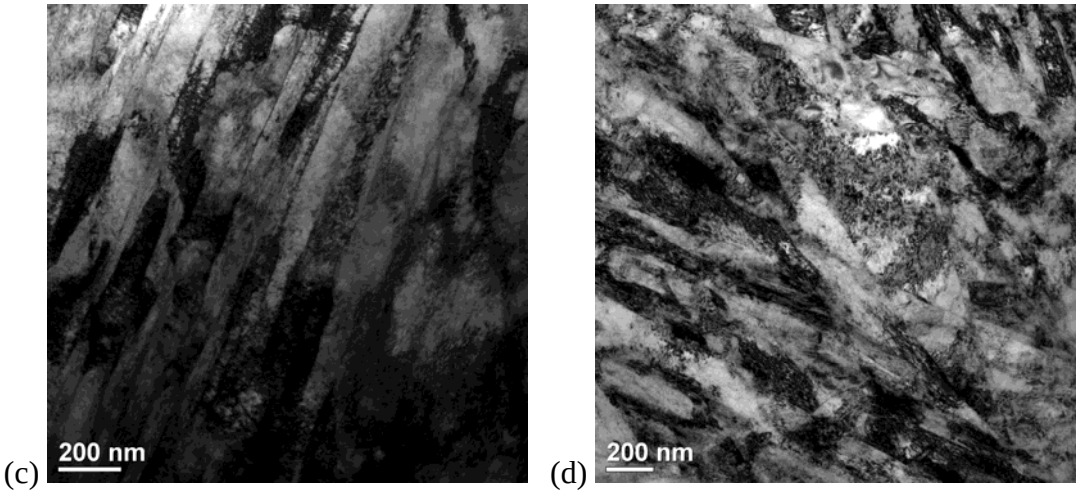

Fig. 8.12 316L 2Bc and 300 ºC: (a) IPF image, (b) Phase image: red color denotes austenite and green for martensite, (c) and (d) TEM images

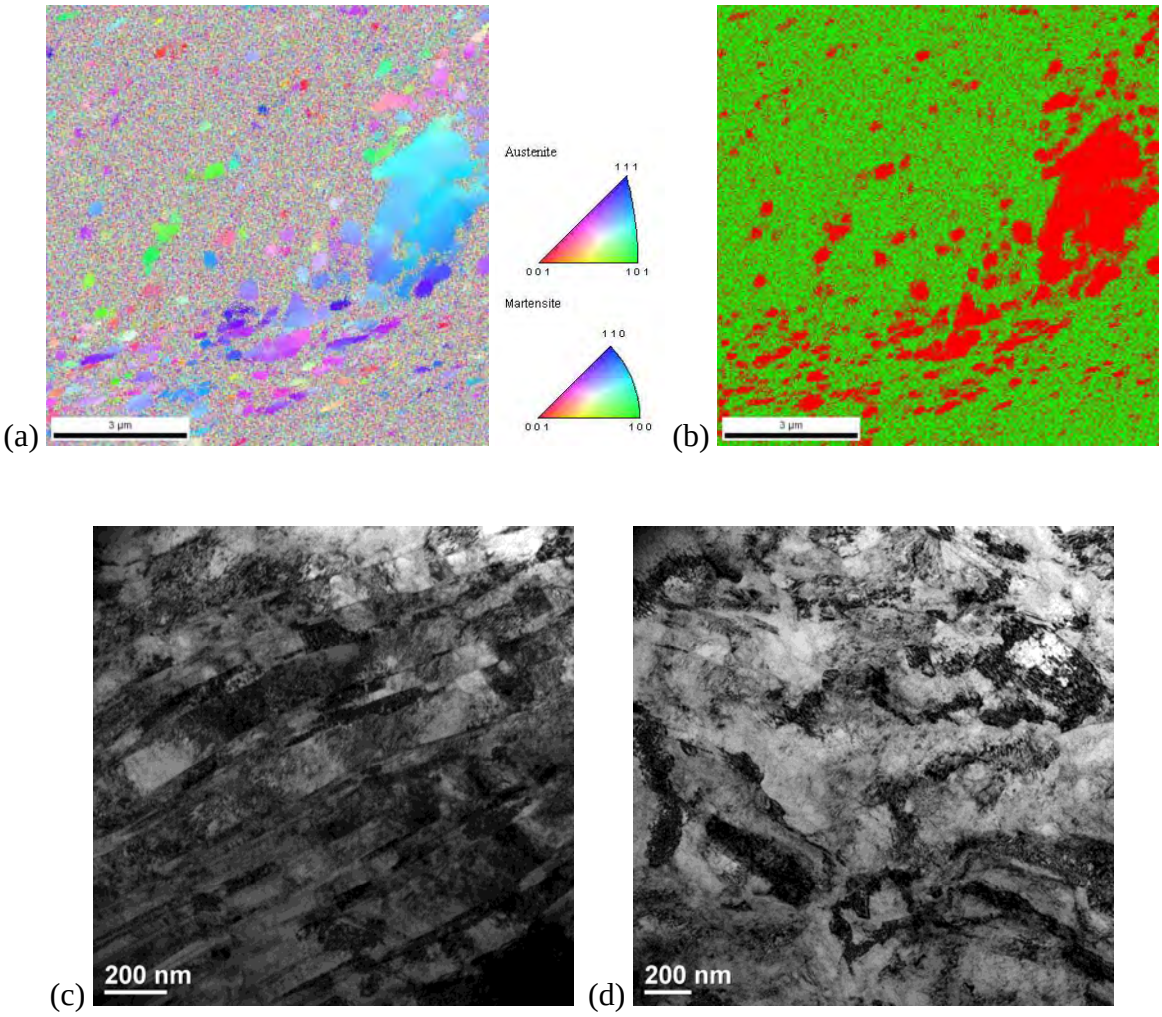

Fig. 8.13. 316L 4Bc and 500 ºC: (a) IPF image, (b) Phase image: red color denotes austenite and green for martensite, (c) and (d) TEM images

Ferrite content

EBSD, TEM and X-ray diffraction all show the existence of ferrite phase (martensite) which is derived from deformed fcc crystal structure under the high shear loading. The content of selected specimen were characterized using a ferrite scope. Figure 8.14 shows the summary of ferrite contents in the as-received, 500°C/8 passes and 300°C/4Bc processed model alloy, respectively. And for each sample, twenty measurements were performed. It clearly shows that larger number of pass will definitely introduce a higher percentage of ferritic/martensitic phase even though the processing temperature is higher.

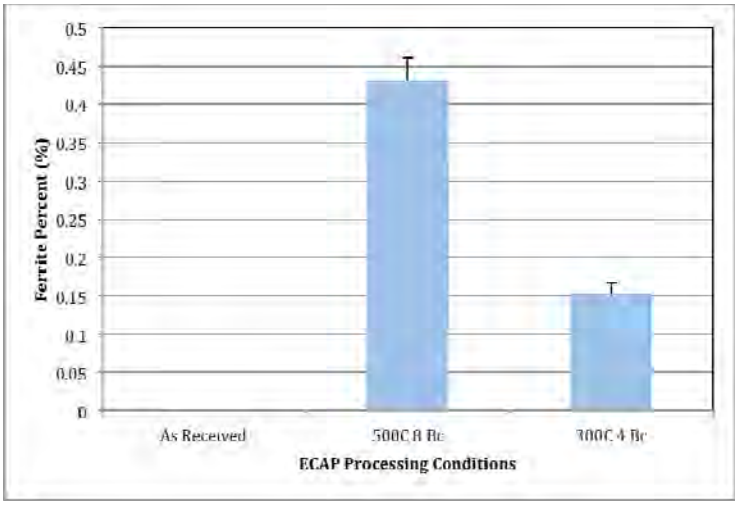

Figure 8.14. Ferrite (Martensitic) percentages measured using a ferrite scope.

Summary

As compared with 304L and 316L, the model alloy shows the most desired grain structures after ECAP processing. The refined grain structures are determined by both the composition and the grain size of parent austenite. And the transformation sequence of $\gamma \rightarrow \varepsilon \rightarrow \alpha'$ needs to be studied more systematically by examining the materials processed at a series of number of passes, which can be helpful for minimizing the volume of α' phase.

8.3 Grain boundary engineering on ECAPed model alloy

The GBE parameters were originally selected based the reported GBE research on the 316 and 304 stainless steels, and in order to screen the parameters, a test matrix was conducted as listed in the table 3.1. The cold work percentages of 0, 5 and 10% were applied on the 1.5 mm thick flat coupons and then subjected to thermal annealing at 1027 ºC for 2, 5 and 10 minutes, respectively. The grain structures were examined using EBSD, and the characterizations were firstly performed on the 5% cold rolled specimen since the 5% cold work was widely reported as an optimal thickness reduction rate for GBE on the austenitic steels.

Table 8.1. Grain boundary engineering test matrix (annealing at 1027 ºC).

Cold work (%) / Annealing time (mins)	0	5	10
2	x	x	x
5	x	x	x
10	x	x	x

However, as shown previously, the ECAPed specimen has a poor thermal stability at this annealing temperature, and a significant coarsening behavior of the grains was observed. It can be seen that for the 5% cold worked specimen, the nanocrystalline structure readily evolved into a micro-sized grain structure even after 2 mins thermal annealing. The EBSD characterization was not conducted for the other two cold work conditions since this annealing temperature was obviously too high. The significant coarsening behavior can be caused by a lowed recrystallization temperature from ECAP process, and additionally the very low carbon content and no carbide precipitates in the model alloy can further deteriorate the grain boundary stability since there is lack of a pinning mechanism at GBs and they can migrate relatively freely. The phase image of Fig.8.16 shows that all the ECAP induced martensitic phase already dissolved after 2 min annealing.

Based on previous furnace annealing experiments and the in-situ TEM heating experiments, the temperature of 700ºC tends to be better choice for the GBE processing temperature. And the ECAPed model alloy was annealed for 5, 20 and 60 minutes at 700 ºC, respectively; the annealing was conducted in a box furnace and the samples were water quenched after annealing. The annealed samples were then studied using EBSD and TEM for grain boundary character distribution, grain coarsening and the evolution of dislocation structures. Figure 8.17 shows that the fraction of CSL boundaries changes vs. the annealing time, and the 5 minutes annealing gives the highest portion of Σ3 as well as the fraction of 1≤Σ3≤29 boundaries. Figure 8.18 displays the distributions of grain size of the samples after three different annealing periods, and it can be seen that the grain size averagely increases to 2.58μm after 5 minutes, while there a very small difference in the grain size between the 20 minutes and 60 minutes annealed specimens as shown in Fig. 8.19. And it should be noted that the annealing at shorter time tends to introduce a binominal distribution of grain size while the longer time annealing promotes a normal distribution of grain size These results demonstrate that a very short time annealing at high temperature can effectively increase the fraction of Σ grain boundary while has a least coarsening effect on the grain size.

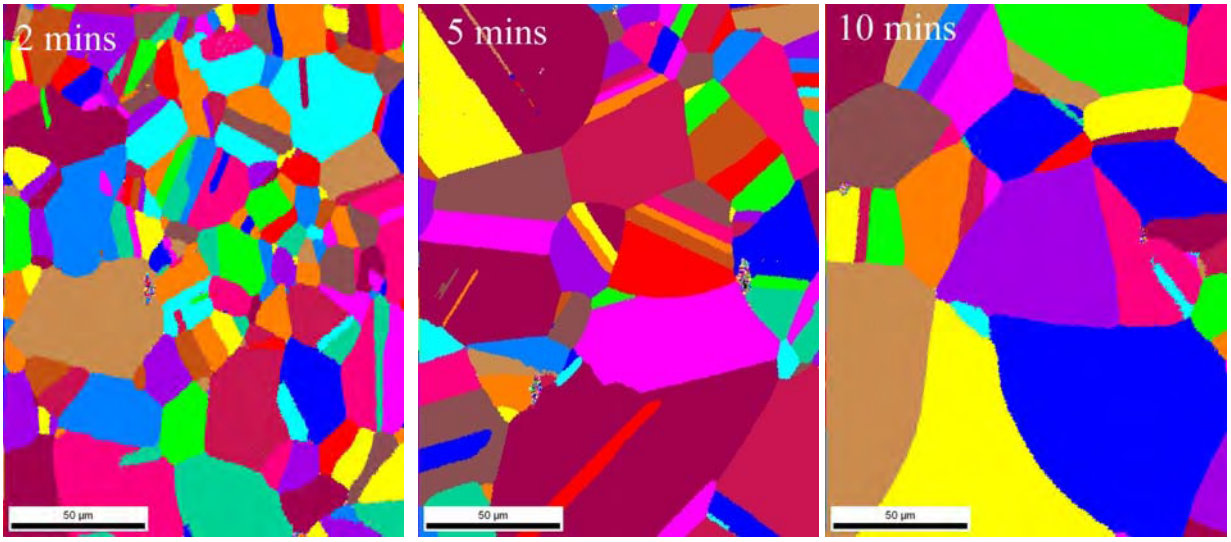

Figure 8.15 Grain coarsening after various annealing periods at 1027 ºC for 5% cold rolled ECAPed model alloy.

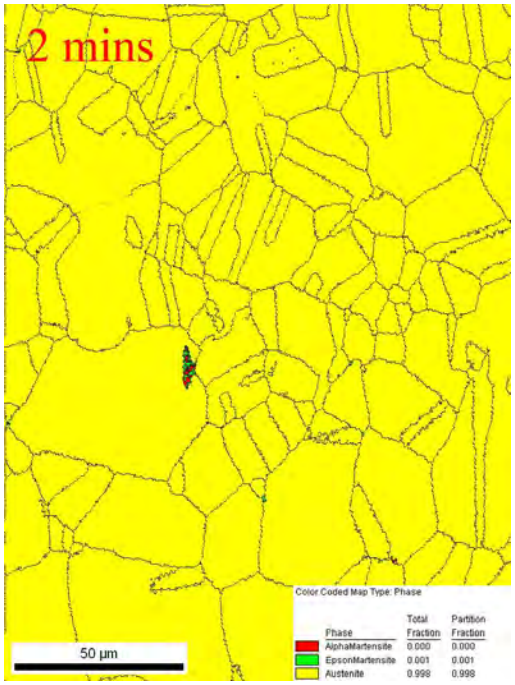

Figure 8.16. Phase image of the 2 mins annealed (1027 ºC) ECAP specimen.

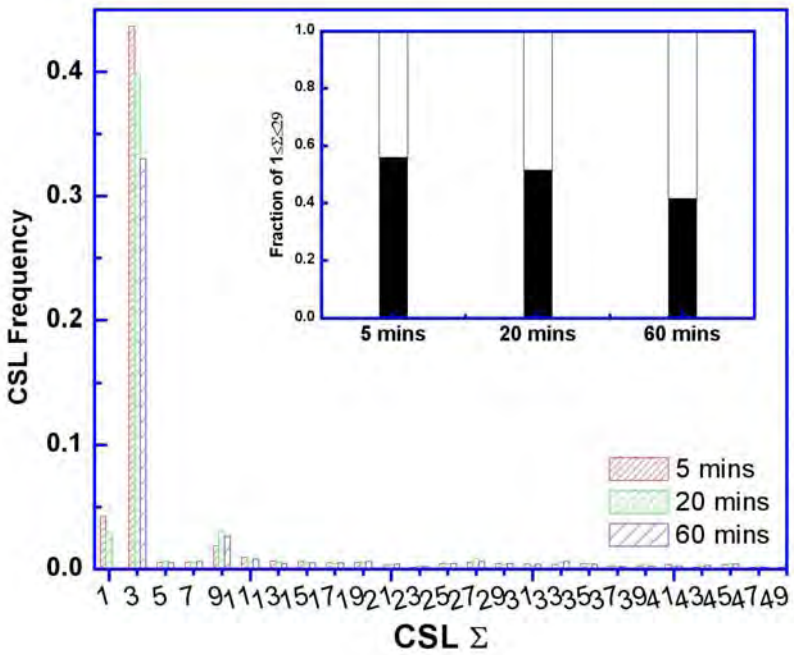

Figure 8.17 Fraction of CSL boundaries vs. the annealing time.

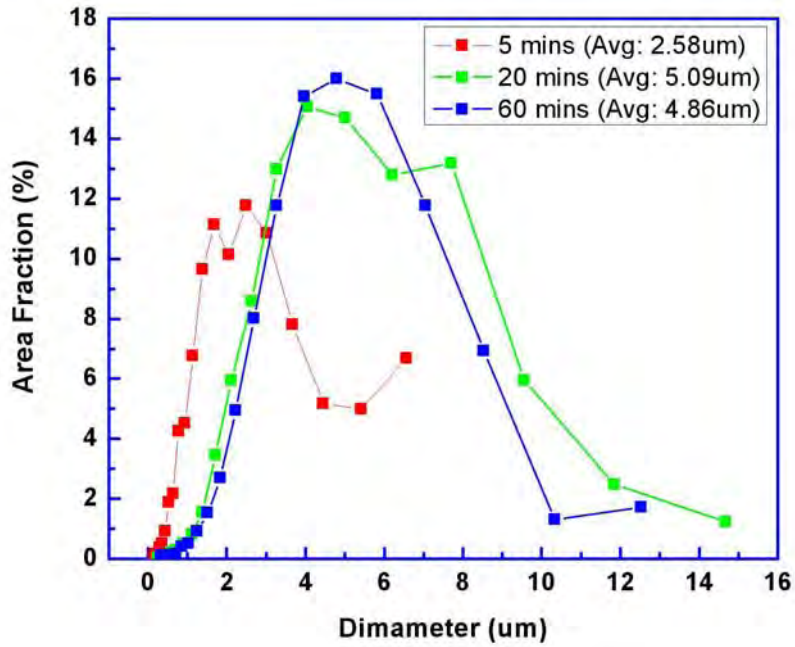

Figure 8.18 Grain size distribution vs. the annealing time.

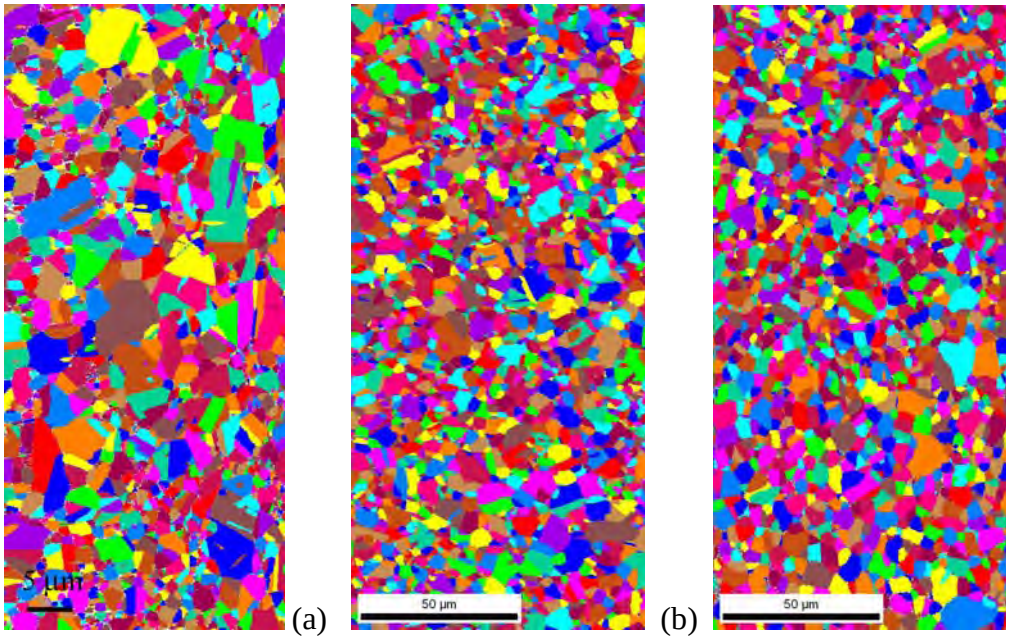

(a) (b) (c)

Figure 8.19. OIM image of the annealed (700 ºC) specimen (a) 5 min, (b) 20 min and (c) 60 min.

The TEM results in Figure 8.20 are consistent with the EBSD measurements, and the grain size is averagely around 2-3 μm after 5 minutes annealing. The TEM image at high magnification clearly shows that the 5 minutes annealing at 700 ºC can effectively removed nearly all the dislocation structures from the ECAP processing,

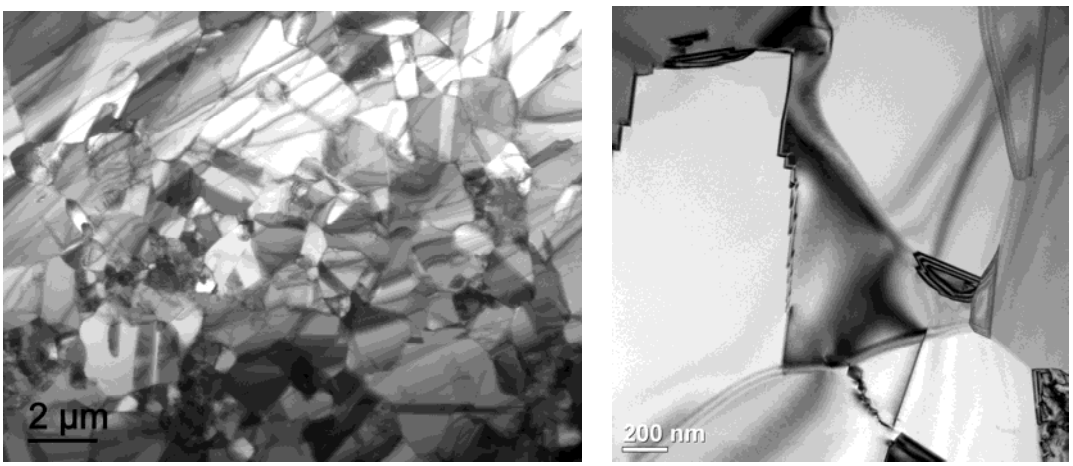

Figure 8.20 TEM images of ECAPed model alloy after annealing at 700 ºC for 5 minutes.

In order to further study the thermal stability of the ECAPed model alloy, the material was tested using a DSC, and two measurements were performed by the NETZSCH Testing Laboratory. The test parameters are listed in the Table 8.2, the system employed for this test is DSC 404 C Pegasus® differential scanning calorimeter, and it is equipped with a rhodium furnace of operation from 25 to 1650 ºC. The DSC curves are plotted in figure 3.2.21; there are no significant effects present in the two DSC curves. But a very small endothermic peak at 597.1 ºC can be identified for both the curves, which could be related with the release of lattice energy from annealing of dislocation structures, coalesce of sub-grains and migration of grains boundaries.

Table 8.2. DSC Test Parameters.

Temperature Program	Heat RT-1000ºC at 10 K/min
Purge Gas	Argon, 60 mL/min
Crucible	Pt with alumina liners and pierced lids
Sample Mass	1st run: 41.71mg 2nd run: 42.09mg

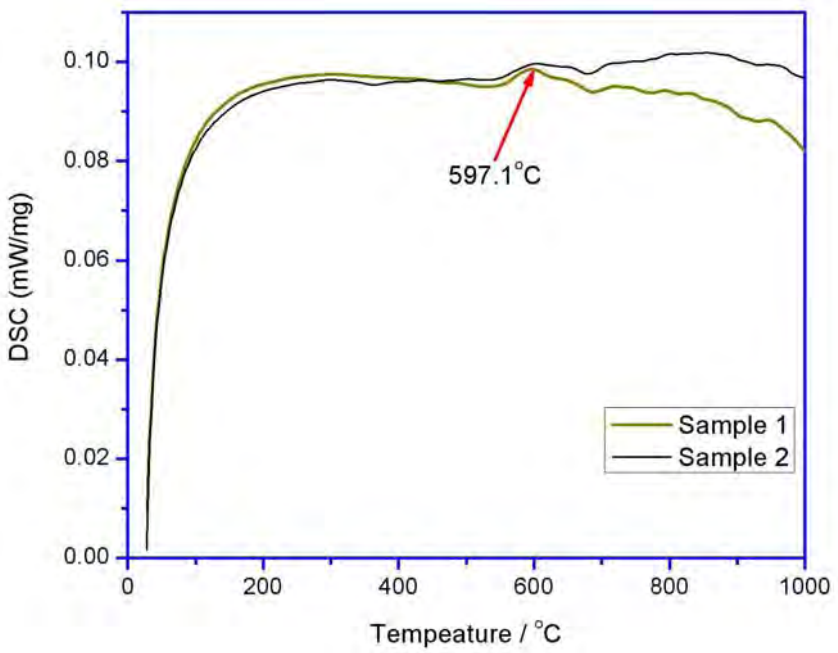

Figure 8.21 DSC curves for two ECAPed sample test from 25 to 1000 ºC.

A9. In situ Kr ion irradiation of ECAPed Fe-14Cr-16Ni

Lead organization: University of Florida (Yong Yang) and University of Wisconsin, Madison (Todd Allen)

9.1 In-situ irradiation and characterizations

The ion irradiation experiments were performed using the in-situ ion beam at the Argonne National Laboratory. And the planned irradiation conditions are listed in the Table 9.1 with the completed conditions shadowed, where the ECAP+HT denotes the heat treated ECAPped specimen, and heat treatment condition is: annealing at 700 °C for 5 min followed by water quenching. For each temperature condition, the irradiations were terminated at 2, 5 and 10 dpa, respectively, so the irradiated specimens can be re-examined after in-situ experiment. However, the irradiation at 500 °C was only performed at the dose up to 2 dpa due to the excessively receding of the electron transparent area during experiment, which can be caused by the surface diffusion at this temperature in a high vacuum. And due to a very limited access to the equipment, only partial of the experiments was completed.

Table 9.1 Conditions using in-situ ion beam (1 MeV Kr).

Materials	300 °C			400 °C			500 °C		
	2 dpa	5 dpa	10 dpa	2 dpa	5 dpa	10 dpa	2 dpa	5 dpa	10 dpa
ECAP									
ECAP+HT									
Model alloy									

During the irradiations, the grain structure of the ECAPped and ECAP + HT (heat treated) specimens remained stable at 500°C for a prolonged period of time, and no grain boundary migration was observed, which is consist with the DSC measurement. Due to the small grain size of the specimen, the in-situ TEM observations were only performed at a near bright-field kinematic condition, and it is not feasible to tilt the specimen to an exact two beam condition. Figures 9.1 only quantitatively demonstrates the evolutions of the irradiated microstructures with different doses for both ECAP ped and ECAPped+HT specimens. At higher temperature, the dislocation loops tends to grow faster.

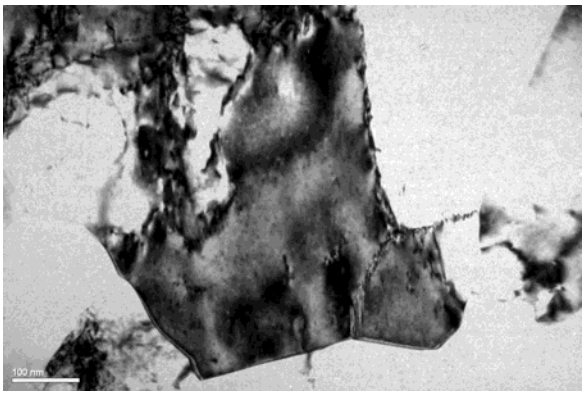

0.1 dpa

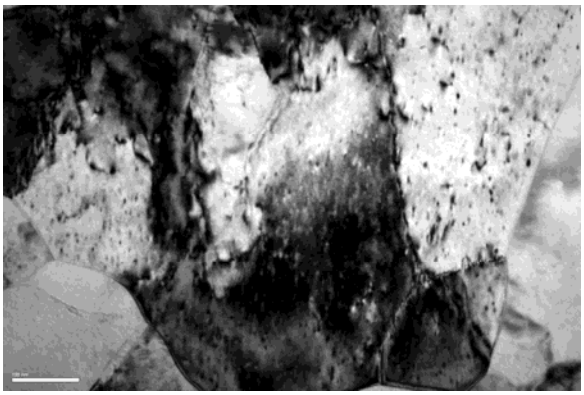

0.5 dpa

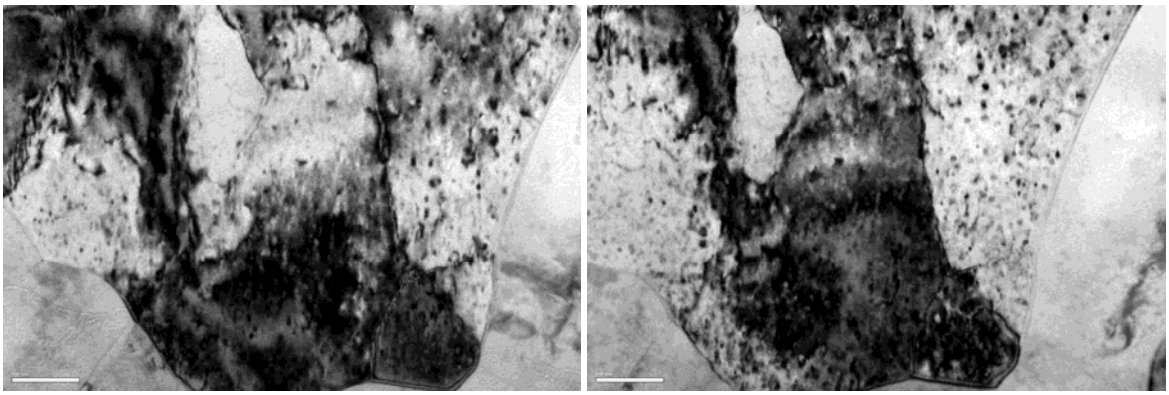

1 dpa 2 dpa

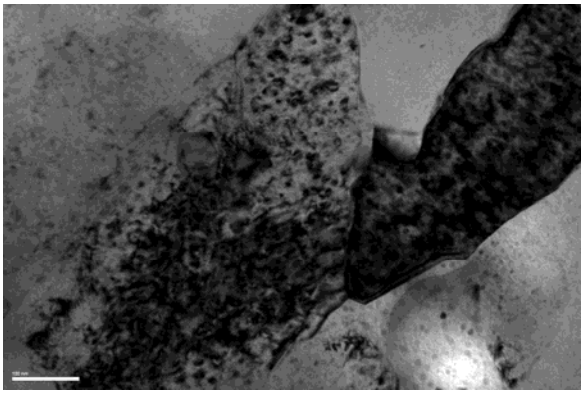

5 dpa

Fig. 9.1 Microstructural evolution in ECAP model alloy irradiated at 400 °C

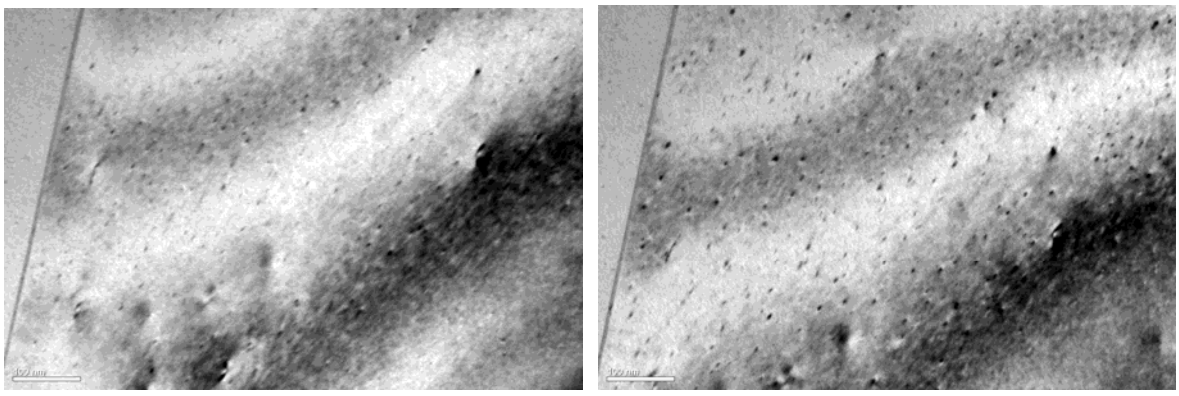

0.1 dpa 0.2 dpa

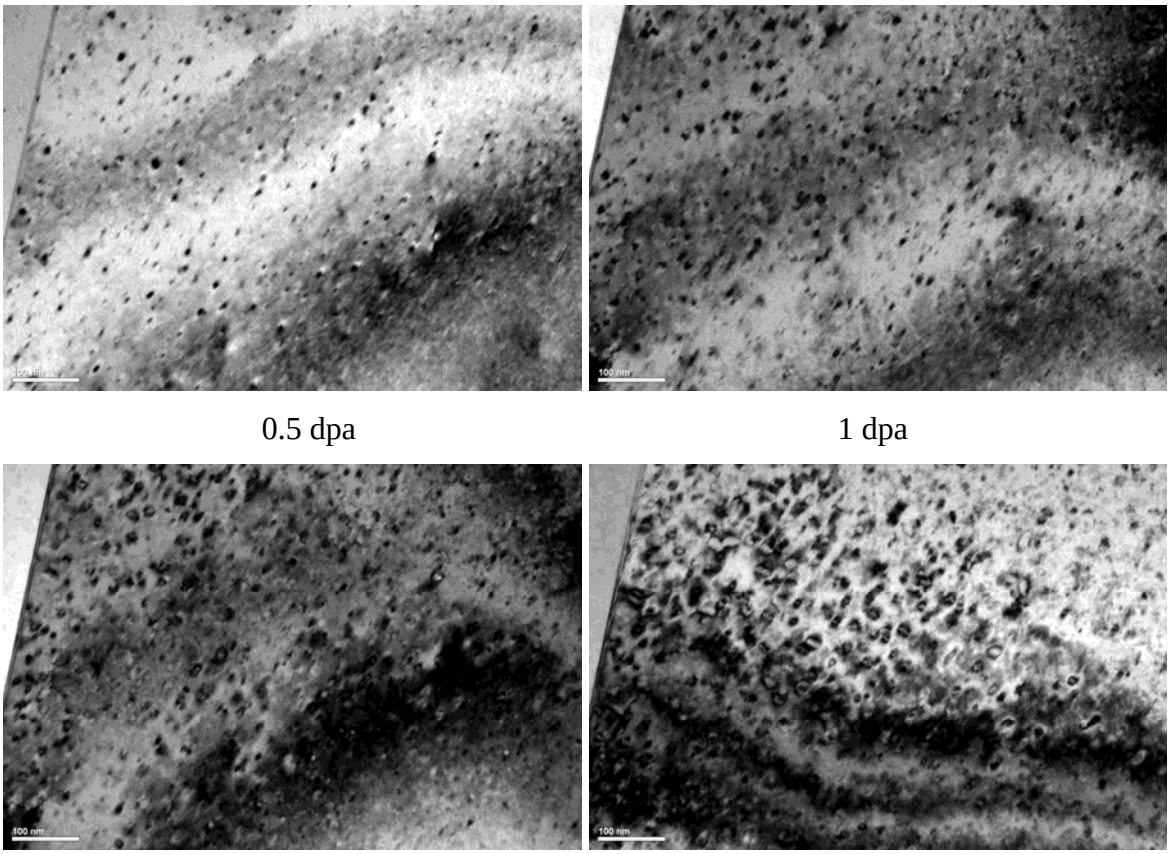

0.5 dpa 1 dpa

2 dpa 5 dpa

Fig. 9.2 Microstructural evolution in ECAP+HT model alloy irradiated at 400 °C

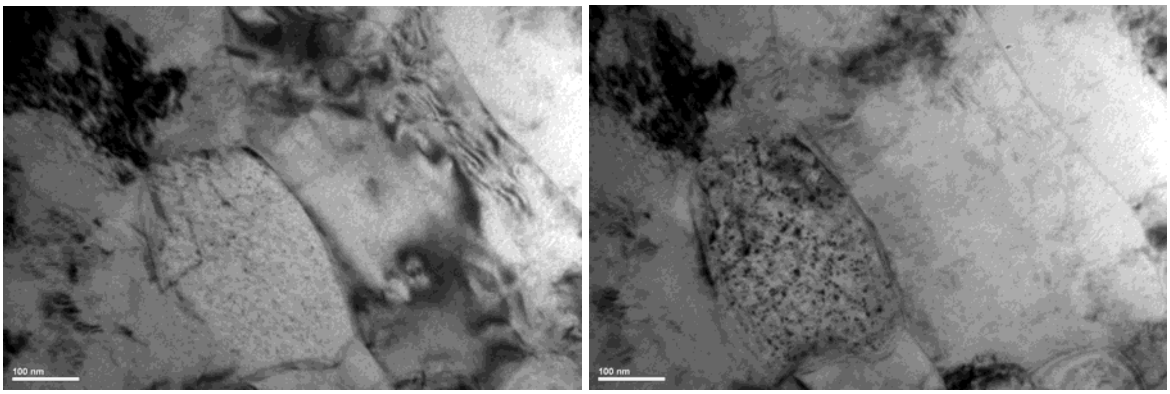

0.1 dpa 0.2 dpa

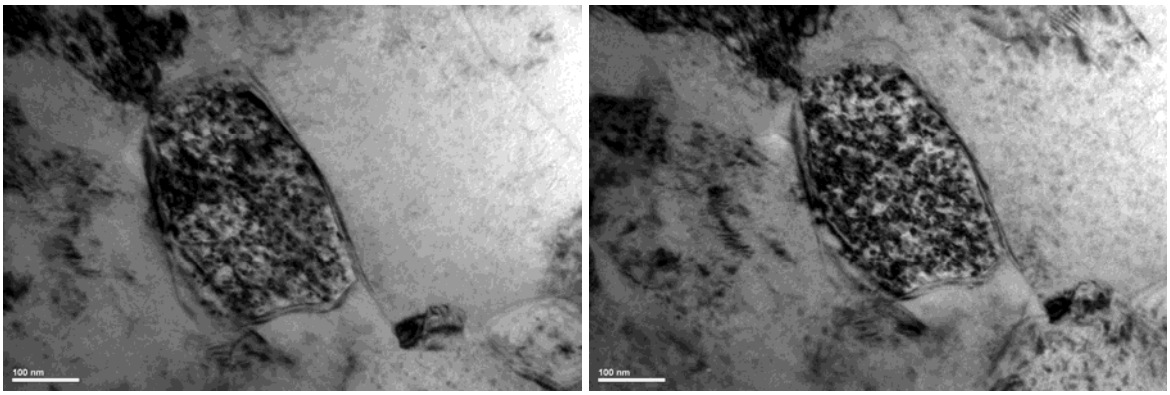

1 dpa 2 dpa

Fig. 9.3 Microstructural evolution in ECAP model alloy irradiated at 500 °C

As clearly shown in figure 9.3, the defect number tends to saturate even after only 1 dpa while the size of dislocation loops is growing with an increasing ion fluence. Unfortunately, no defect denude zones were observed near by the grain boundaries of the nano-sized grain (200nm) as shown in figure 9.3 for even 500°C irradiation. The results clearly show that ~100-200nm grain size would have a minimal effect on the point defects migration, and the spacing of grain boundaries as defect sinks is much large than the diffusion length of point defects. In order to improve the radiation damage resistance, a further refined grain structure is needed.

9.2 Fe^{2+} irradiation and characterization:

The ECAPed (8Bc, 500°C) model alloy was irradiated to 50dpa using a 5MeV F++ beam, as shown in figure 9.4, the peak of radiation damage profile is about 1.5 μm from the surface. The TEM specimens prepared using a FIB lift-out methods as shown in Figure 9.5.

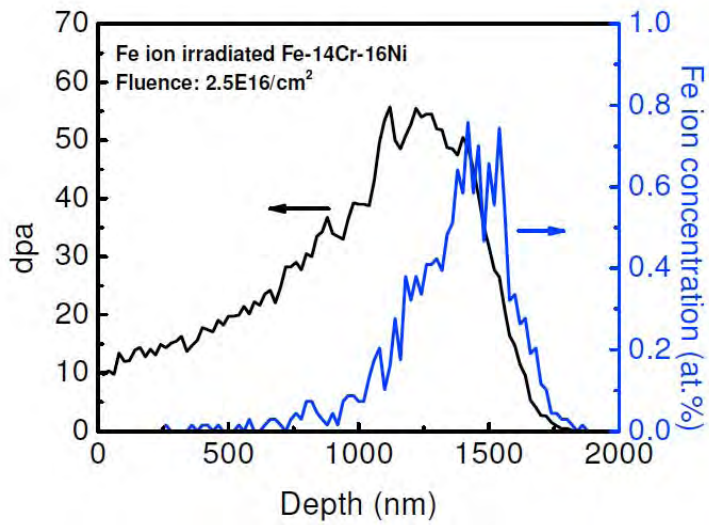

Figure 9.4 SRIM calculation of the radiation damage file and implanted Fe in the 5MeV F++ irradiated ECAPed model alloy.

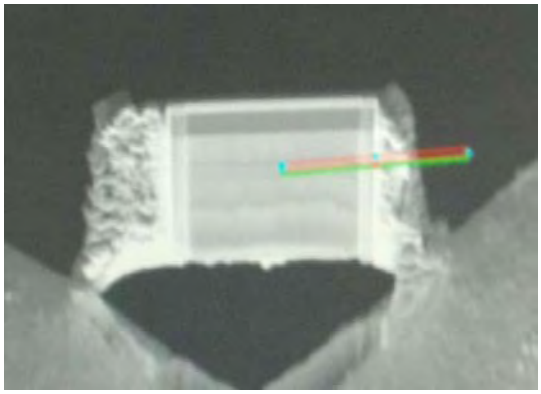

Figure 9.5 TEM specimen prepared using a FIB lift-out method

Microstructural examination:

As shown in Figure 9.6, the irradiated surface was well preserved by depositing a 100 nm thick Pt by the lift out. Base on the SRIM calculation, the peak dpa is about 1.2 μm from the surface, therefore the TEM should cover the whole irradiated zone in the irradiation direction.

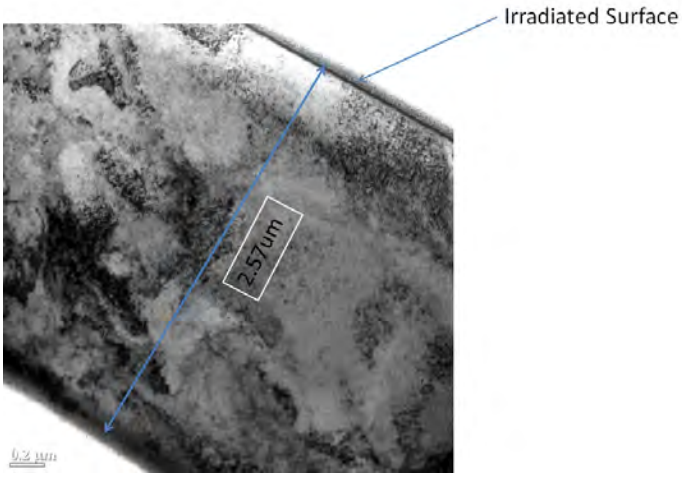

Figure 9.6 TEM image of Fe^{2+} irradiated ECAPed model alloy.

However, possible due to the saturation of defects, low irradiation temperature, and high density of pre-existing dislocations, no clear radiation damage profile can be identified in this irradiated sample. And the irradiated microstructure is generally decorated with a high density of dislocation loops, as shown in Figure 9.7. The image was taken at the position about 1μm from the irradiated surface. Additionally, no denude zones were identified nearby the grain boundary, which might be because of the low irradiation temperature as well as the migration of grain boundary during irradiation.

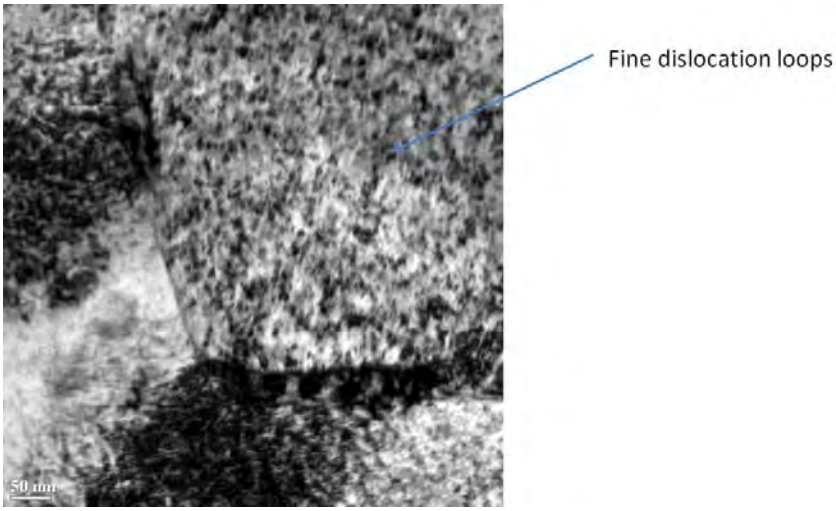

Figure 9.7. Dislocation loops and grain boundaries in Fe++ irradiated ECAPed model alloy.

Nevertheless, the grain growth in irradiated zone is observable and the growth behavior is abnormal with some large grains emerging while some very fine grains still remains intact even after irradiation of 50dpa.

NanoMegas characterization

The grain growth of 1 MeV Kr irradiated ECAPed model alloy was quantified using nanoMegas equipped on JEOL 2010F TEM. The TEM specimen was previously irradiated to 5dpa at 300°C using Kr ions, and the TEM image of figure 9.8 shows a high density of dislocation loops in the irradiated microstructure. And this high density of dislocation loops makes the measurement of grain size and boundary type impossible by using the conventional Kikuchi pattern based EBSD technique, because high density of dislocation loops severely distorts the lattices and smears out the Kikuchi pattern.

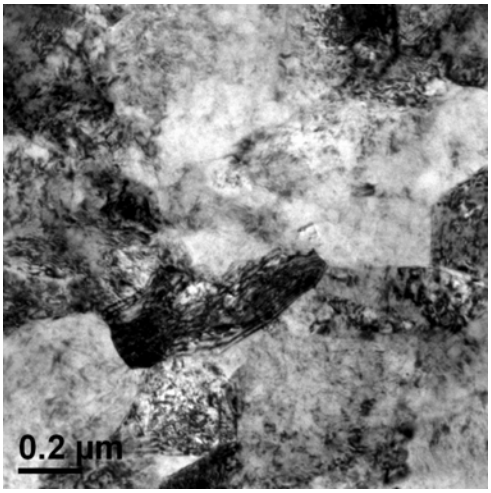

Figure 9.8 TEM image of Kr irradiated ECAPed model alloy.

By using NanoMegas system, the grain images were acquired with a step size of 10nm and scanned area of 2000×2000nm^2, the austenite and martensite phases were fitted over the acquired data. Figure 9.9 shows the inverse pole image, quality map, combined quality and orientation map and phase map, respectively. It can be seen that the size of grain slightly increased after irradiation, and similar with the response to Fe^{2+} irradiation, the growth of grain is abnormal. The martensite phase identified at the triple grain boundary junction remains

nanoscale, which might be attributed to a more stable phase boundaries as compared with the dislocation boundaries in the nanoscale austenitic phase after ECAP processing.

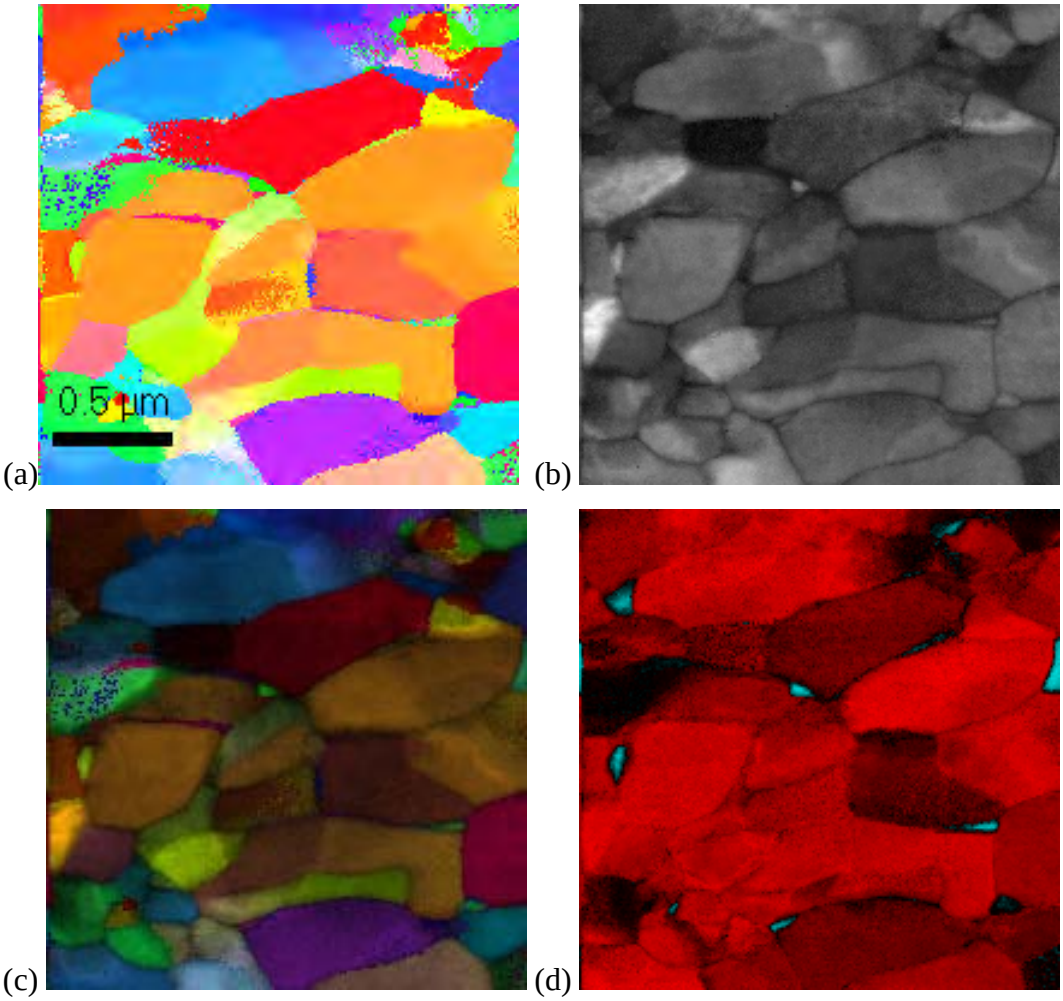

Figure 9.9. Grains of Kr irradiated ECAPed model alloy: (a) inverse pole map, (b) image quality map, (c) combined orientation and quality image and (d) phase map (red as austenite and blue as martensite).

Atom Probe Tomography

The Atom Probe Tomography (APT) was also applied on the ECAPed model alloy to reveal any elemental segregation along dislocation lines or grain boundaries as well as to identify any fine precipitates from the ECAP processing. Totally, seven APT tips were lifted out for the electropolished specimen using FIB, and the APT was run on an IMAGO Leap at CAF-UA. Figure 9.10 shows an example of the APT images of the ECAPed model alloy tip; it shows that

no elemental segregations were identified in the specimen and the concentration of C is also very low (not shown here).

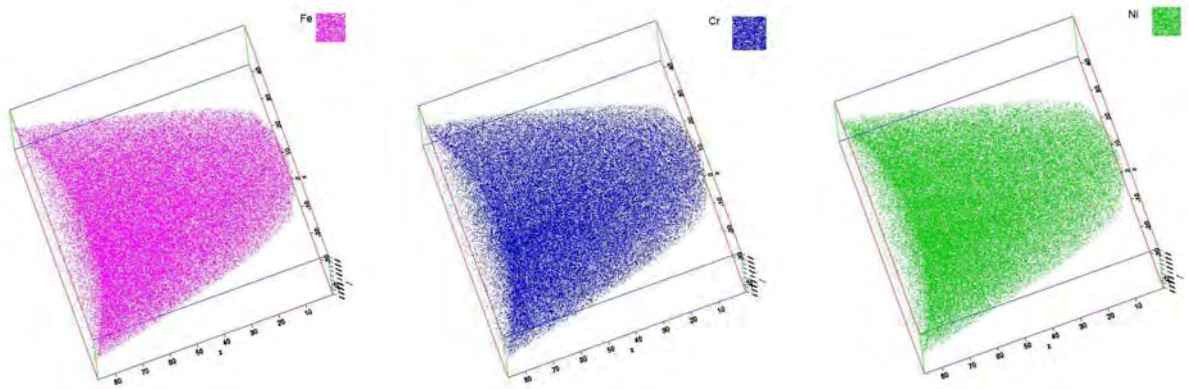

Figure 9.10. APT images of ECAPed model alloy.

Summary

Although, the short duration furnace annealing and DSC experiments show that the the ECAPed model alloy should be thermally stable at a temperature below ~600°C, the materials display a radiation induced growth behavior even at the temperature as low as 300°C possible due to the irradiation assisted grain boundary migration and coalesce of subgrains from annihilation of dislocations (grains portioned by dislocation walls). Nevertheless, the processed materials demonstrate a good radiation swelling resistance and no voids were observed up to a dose of 50 dpa.

In the future, in order to further improve the thermal stability of nano grain structure, two mechanisms should be considered: decrease the grain boundary energy by adding minor alloying elements, i.e. Zr, Y, and pin down the migration of grain boundary by introducing Y_2O_3 nano particles which has a large mismatch of atom size with that of matrix metal.

A10. Mechanical properties of nanocrystalline 304L and 316L stainless steels processed by ECAP. Lead organization (Texas A&M, Xinghang Zhang)

Processing

Commercial 304L and 316L stainless steel were used in this study. The starting material for each is a long bar (rod) of pre-extruded material of an approximately one inch square cross section from which the billets were cut. The cross-section of specimens was reduced accordingly by milling in order to accommodate for thermal expansion of material. A nominal composition for each is given in Table 10.1.

Table 10.1. Nominal composition of 304L and 316L SS.

Wt. %	304L	316L
Cr	18.19	15.94
Ni	8.04	10.13
Mn	1.68	1.38
Cu	0.55	-
Co	0.16	-
S	0.03	0.03
Si	0.3	0.47
N	0.08	0.77
P	0.026	0.028
Mo	0.12	2.01
C	0.02	0.028
Fe	Balance	Balance

There were different processing conditions for different specimens. Table 10.2 contains the key details and identifiers that will be referenced throughout this report.

Table 10.2. Processing parameters and identifiers

Specimen	**Billet Dimensions**	**Route**	**Extrusion Temperature (^{o}C)**	**Identifier**
304L	.97" × .97" × 6"	2B	300	2B 300
	.725" × .725" × 6"	4Bc	500	4Bc 500
	.725" × .725" × 6"	6Bc	500	6Bc 500
316L	.97" × .97" × 6"	2B	300	2B 300
	.725" × .725" × 6"	4Bc	500	4Bc 500

All billets were furnace annealed for up to one hour at 1150 ^{o}C and subsequently quenched in air prior to extrusion. ECAP was carried out in a sliding wall die designed by Mr. Robert Barber and Dr. K. T. Hartwig. This was done by an MTS-controlled 250 ton hydraulic press. For all extrusions, temperature was controlled by maintaining the die at the desired temperature so that extrusions could be carried out isothermally. Extrusion speed varied as a function of specimen, and pass number. The billets are then placed within the pre-heated die for approximately 30 min in order to reach extrusion temperature. Immediately after extrusion, the billet is removed quickly from the channel and quenched it in water. Maximum press load and die temperature were recorded during the extrusions and the dimensions of the extruded billet were recorded after cooling. This process was repeated for each extrusion.

Microstructure - X-Ray Diffraction (XRD) and transmission electron microscopy (TEM) studies

XRD was performed to examine the microstructure of processed specimens. Determination of γ-austenite and α'-martensite peaks were based on d spacing calculations, using γ iron as a reference for austenite and α iron as a reference for martensite, and a comparison with literature. Spectra for the as-received and as-processed 304L stainless steel (SS) normal to the transverse direction of the processed billet are shown in Figure 10.1.

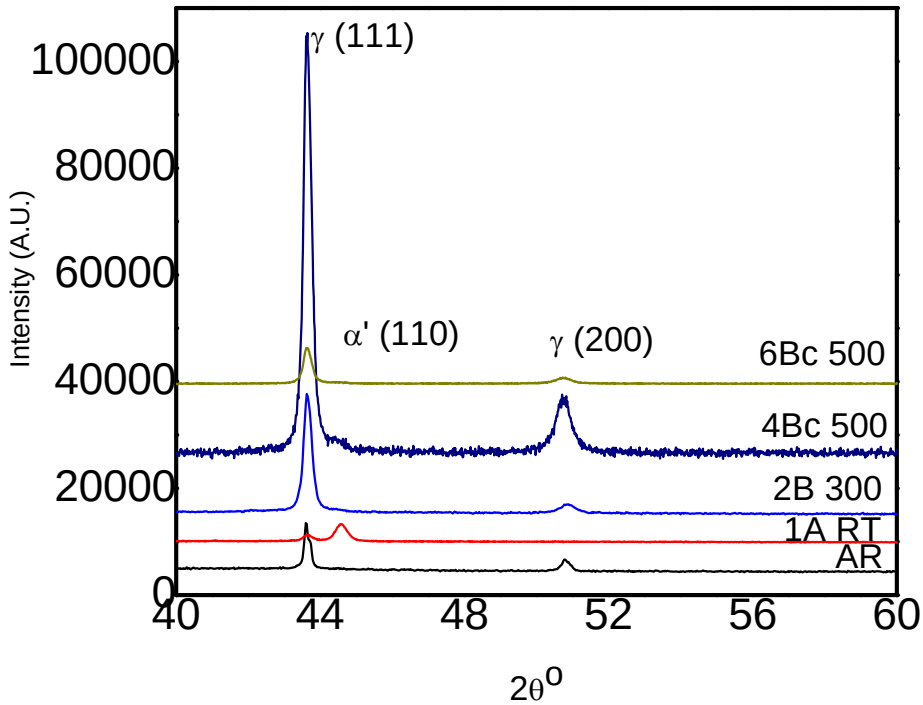

Fig. 10.1. 304L stainless steel XRD spectra for as-received and as-processed material.

The fully-annealed as-received (AR) specimen indicates a predominantly γ-austenite phase. Subsequent processing at elevated temperatures (300°C or greater) seems also to preserve the predominant γ-austenite with generation of a few stress-induced α'-martensite phases. The story is significantly different for 304L SS processed at room-temperature. The spectrum shows that α'-martensite dominates when processed at room temperature. This may explain the difficulty in achieving more than one extrusion at this condition as significant hardening occurs as shown later.

A similar situation arises in the 316L SS as shown in Fig. 10.2. Of worthy note is the fact that stress-induced martensite seems to be significantly suppressed. As shown by the 1A RT spectrum, unlike 304L 1A RT, a predominant γ-austenite is still preserved after room-temperature processing. Indeed, α'-martensite formation is still suppressed even after higher-temperature (300°C or greater) extrusions, and so does not appear in any significant quantity.

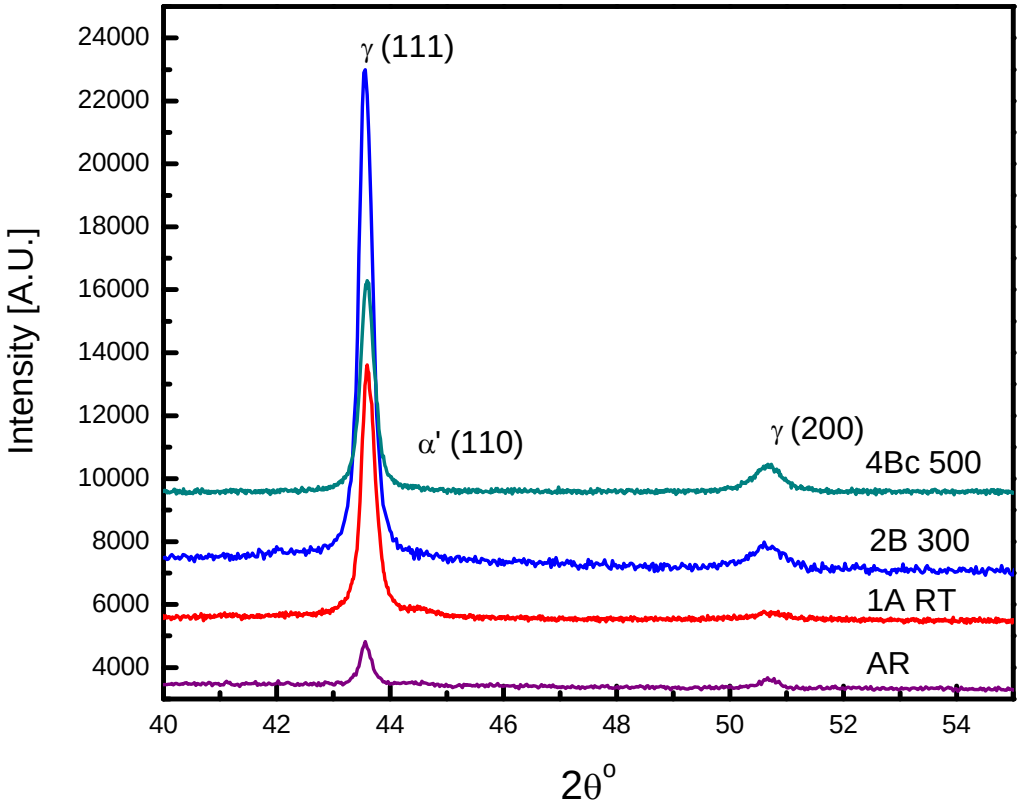

Fig. 10.2. XRD spectra of 316L SS for as-received and as-processed material.

Bright-field plane-view TEM micrographs of representative areas were taken from the transverse and flow planes of the as-processed billets. The transverse view is discussed first. The transverse view in all cases shows a mostly-laminated structure. Starting with 304L 2B300, we see that the microstructure is dominated by laminated structures which are probably plate-like, as shown in Fig. 10.3.

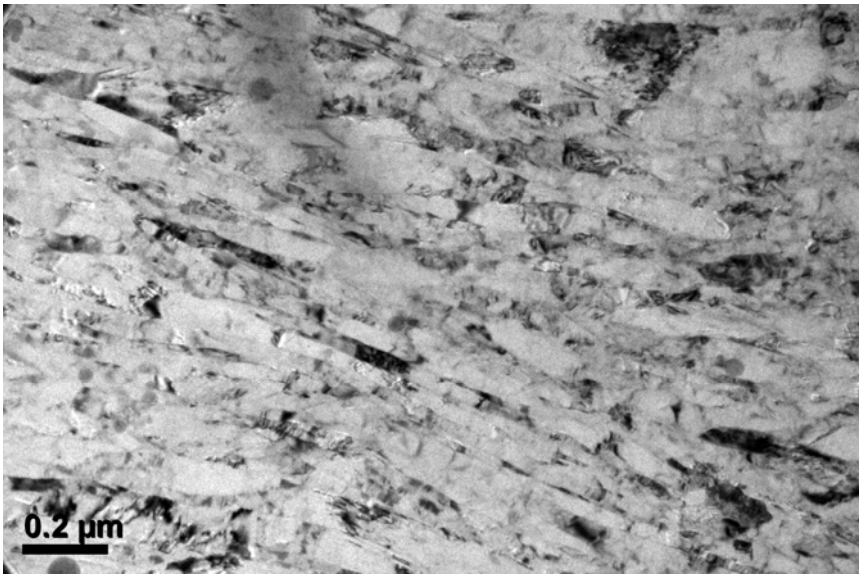

Fig. 10.3. (a) 304L 2B 300 bright field TEM micrograph showing laminated grains along the transverse direction. Selected area diffraction pattern (SAD) (not shown here) shows polycrystalline nature of grains with certain texture and predominant austenite structure.

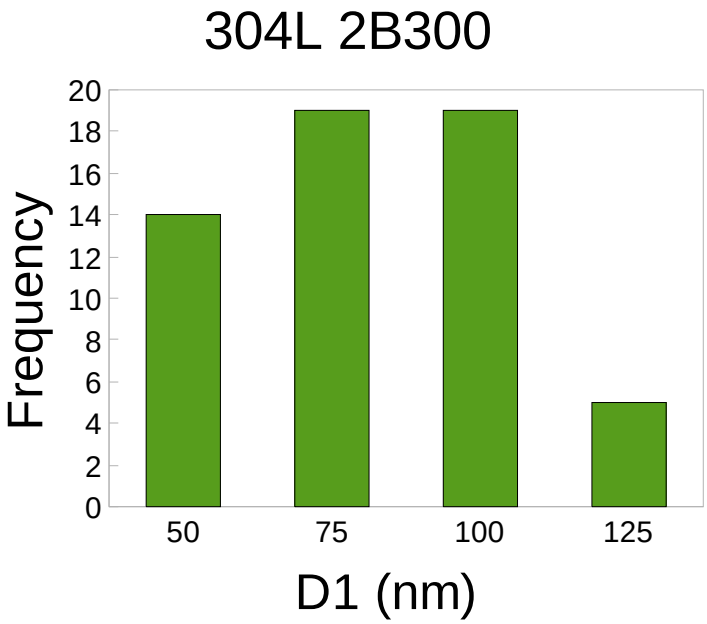

Fig. 10.4. Frequency histogram of 304L 2B 300C specimen showing the unimodal character of laminar thickness with an average laminar thickness of ~ 70 nm.

The laminar structures are highly anisotropic in dimensions indicated by the frequency distribution for the grain size of the laminar spacing which shows an effectively unimodal distribution which confirms a uniform structural refinement (Figure 10.4), with an average thickness (D1) of ~ 70 nm. The length of laminations averages at ~ 1.8 μm. The continuous ring in the selected area diffraction (SAD) pattern indicates a fine-grained polycrystalline microstructure with certain texture. All the laminations or "columns" appear to be oriented the same way as can be discerned by moving the viewing area around.

Further processing at higher temperature shows that the laminar structure remains, but the length of grains decrease significantly as shown in Fig.10.5a for the 304L 4Bc 500 specimen. The average laminar spacing increases slightly in order to accommodate the decrease in length. Average laminar spacing (D1) becomes ~ 120 nm while the longer dimension (D2) has an average length of ~250 nm with a bi-modal distribution, albeit with a noticeably smaller occurrence of larger grains. Furthermore, some equiaxed grains become apparent. The bi-modal distribution of D2 is indicative of the occurrence of grain columns being compressed as will be more apparent in the case of the six-pass material.

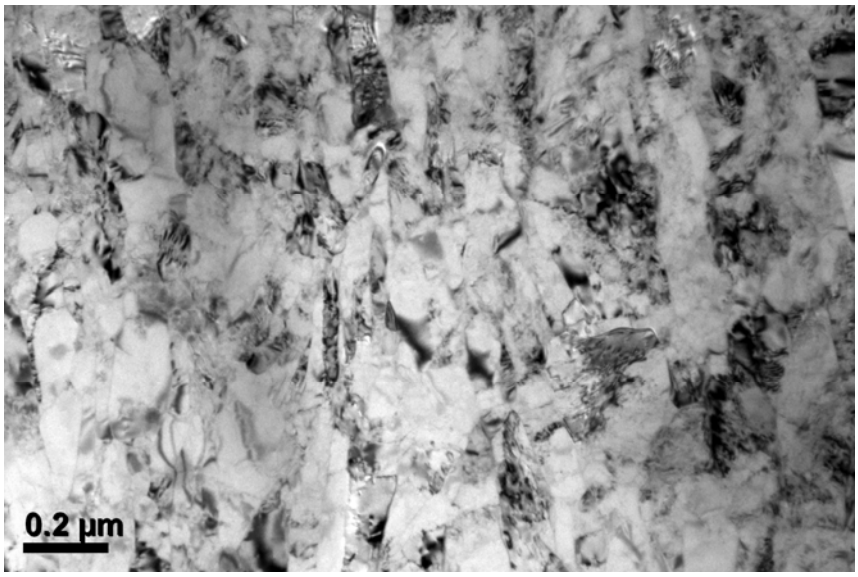

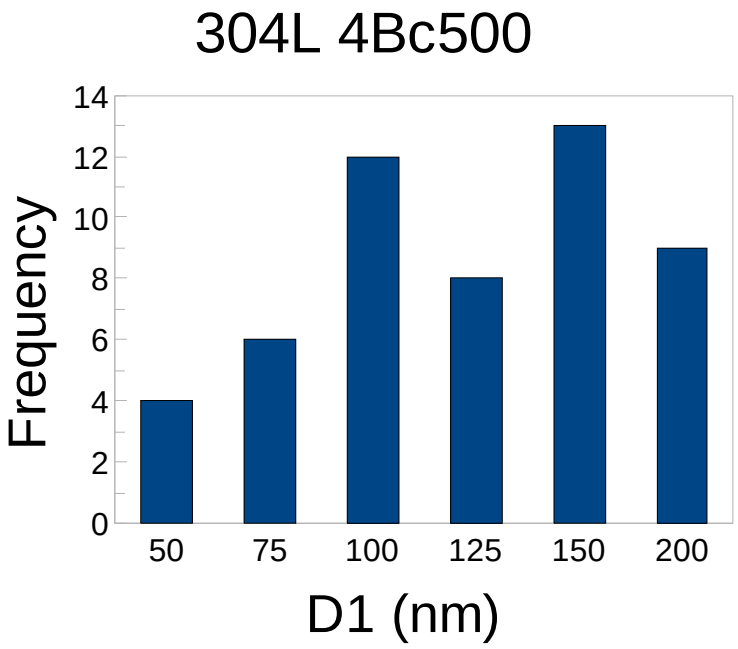

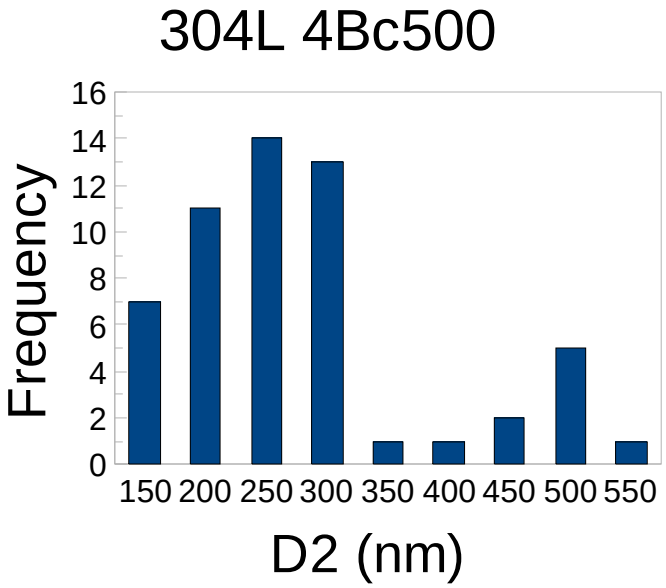

Fig. 10.5. (a) 304L SS, 4Bc 500, bright field TEM micrograph showing laminated grains and gradual formation of equiaxed grains along the transverse direction. (b) Frequency histogram of grain size showing a bimodal distribution indicative of long grains becoming smaller equiaxed grains. (c) Frequency distribution of long grain dimension indicating a decrease in laminar structure.

After six passes, the 304L 6Bc 500 sample undergoes even further grain refinement as is evident in Fig. 10.6. The average laminar spacing now decreases slightly to ~ 100 nm, as shown in Fig. 10.7a, and the size distribution takes on a more obvious unimodal characteristic which also implies that the threshold for grain refinement is being reached. Similarly, the longer dimension decreases further to an average size of ~ 260 nm, also with a unimodal type of distribution as presented in Fig. 10.7b. Upon close examination of the micrograph, more equiaxed grains can be discerned within the surrounding laminated grains. This is consistent with the original trend established in that the long grains are now being compressed in to smaller, equiaxed grains, which is also confirmed by the unimodal distribution.

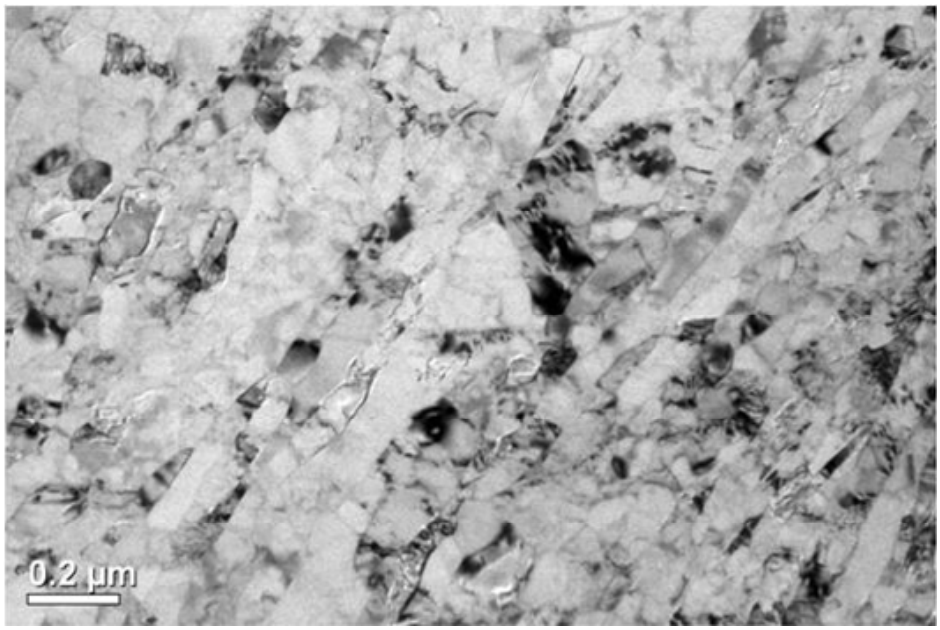

Fig. 10.6. 304L SS processed at 4Bc 500C condition. The bright field TEM micrograph shows predominantly equiaxed grains along the transverse direction.

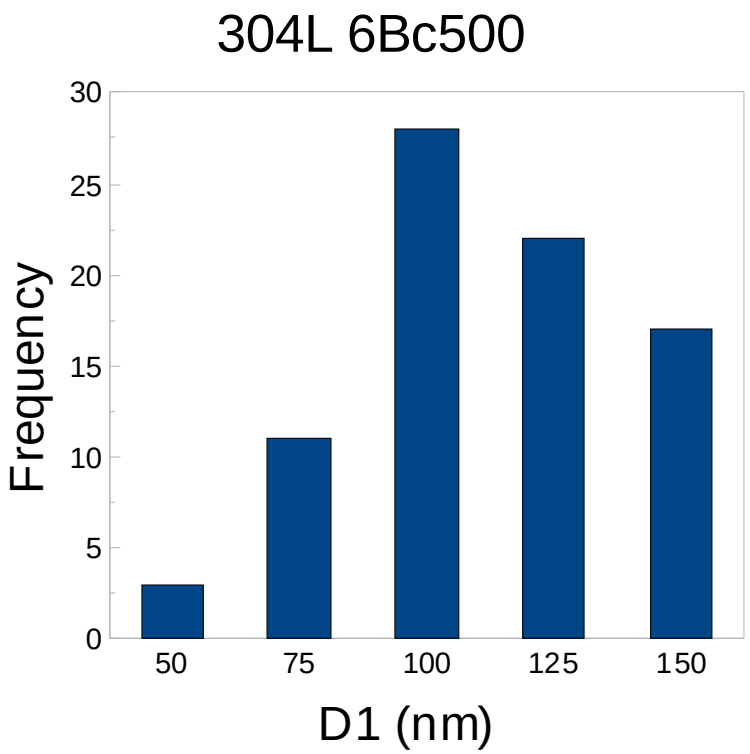
304L 6Bc500
Frequency
30
25
20
15
10
5
0
50
75
100
125
150
D1 (nm)

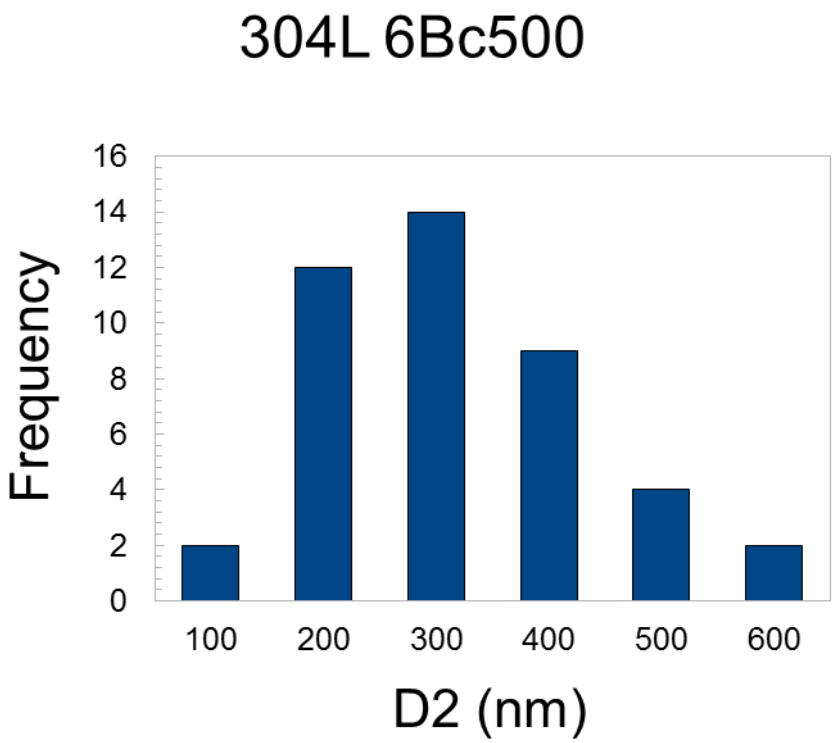
304L 6Bc500
Frequency
16
14
12
10
8
6
4
2
0
100
200
300
400
500
600
D2 (nm)

Fig. 10.7. Grain size distribution of 6Bc 500 approaching unimodal character obtained from the transverse view. The smaller dimension (a) has an average grain size of ~ 100 nm, whereas the longer dimension (b) is ~ 260 nm.

A similar situation arises in 316L stainless steel. The 316L 2B 300 specimen shows a mostly-laminated structure along the transverse direction, Fig. 10.8a, with a unimodal average laminar spacing of ~ 80 nm as shown in Fig. 10.8b. The laminations also seem a little more randomly oriented than 304L 2B 300 which may contribute to the slightly higher hardness mentioned later in this chapter. However, unlike the previous 304L 2B 300 micrograph, this TEM sample was prepared via precision ion milling and so consequently, a much smaller viewing area is visible so it is difficult to get a notion of how long the grains are and also restricts the number of grains by which to base the distribution of grain size. However, it can be inferred by inspection that the grain extends through large areas of the sample just as in 304L 2B 300.

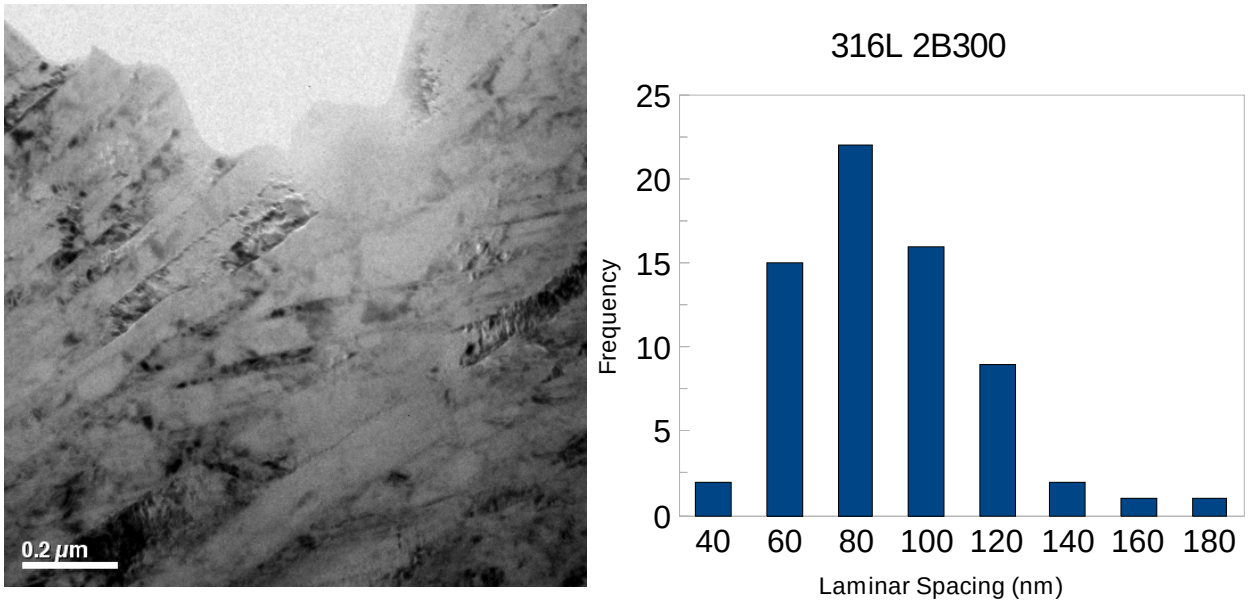

Fig. 10.8 (a) Bright field TEM micrograph of 316L 2B 300. (b) Frequency histogram of laminar thickness.

Processing at higher temperature and greater passes, 316L 4Bc 500C, leads to an average laminar thickness of 80 nm. Unlike with the previous 304L micrographs, the striations seem to

run randomly through the viewing area rather than aligning in a common direction, which may also contribute to the observed hardness. The length of laminars has been dramatically reduced compared to the 316L 2B 300C specimen. This may in fact be an evidence of a tendency to form equiaxed grains after more ECAP extrusions. Indeed, the appearance of what may be equiaxed grains is apparent from the TEM micrograph in fig 10.9 (a). This appearance persists throughout the entire viewing area and so indicates a uniformity of overall microstructural refinement.

(a) 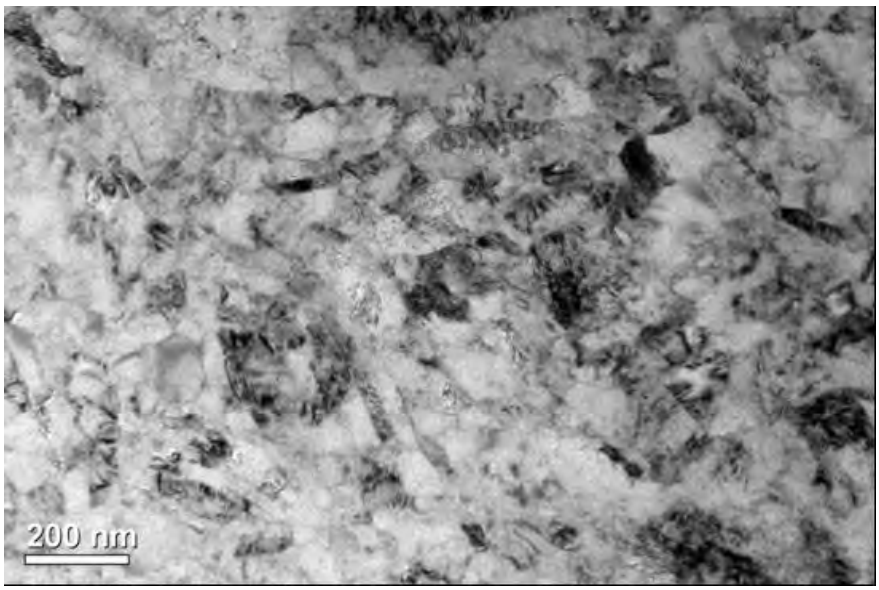

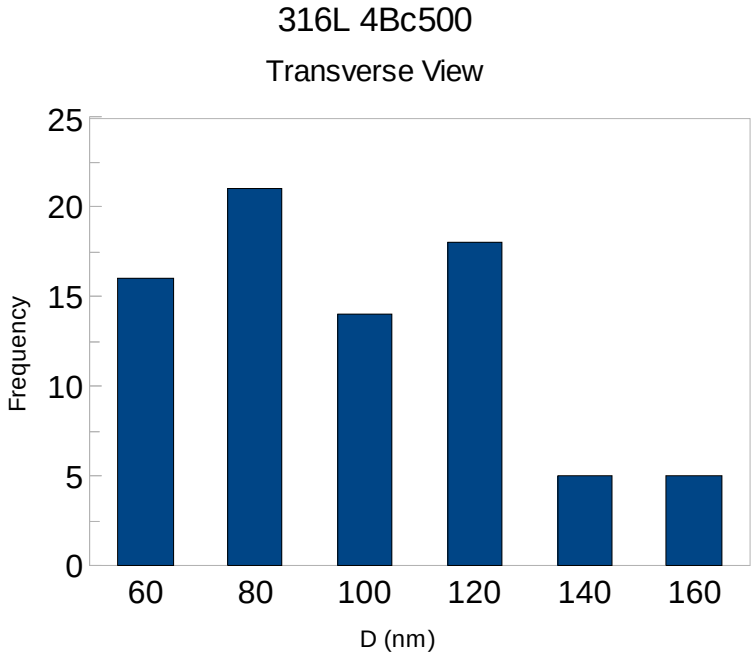

Fig. 10.9. (a) TEM micrograph of 316L 4Bc 500. (b) Frequency histogram of laminar thickness.

Mechanical Properties

The hardness evolutions of 304L and 316L before and after processing are summarized in Table 4.3. As expected, it can be seen that material hardening increases with further processing. In both 304L and 316L, significant hardening can be seen in their respective 1A RT processing. While this may be easily attributed primarily to the presence of martensite in 304L, it's slightly more difficult to account for in 316L considering the predominance of austenite with only a slight fraction of martensite. Hardness increases steadily with further processing at higher temperatures, however, which is consistent with the observed grain size refinement previously discussed. The hardness of 316L seems to increase faster than that of 304L since the hardness of 316L 4Bc 500 is comparable to that of 304L 6Bc 500. This strengthening trend will also be apparent in the results from tensile tests to be discussed later.

Table 10.3. Hardness (H_{IT}) evolution of ECAPed samples after ECAP processing.

	SS 304L	SS 316L
Annealed	2.20 ± 0.05 GPa	2.10 ± 0.03 GPa
1A RT	5.70 ± 0.09 GPa	4.90 ± 0.12 GPa
2B 300	4.30 ± 0.09 GPa	4.60 ± 0.13 GPa
4Bc 500	4.80 ± 0.14 GPa	5.10 ± 0.16 GPa
6Bc 500	5.10 ± 0.17 GPa	N/A

In collaboration with Dr. Maloy at Los Alamos National Laboratory, tensile tests have been performed on three ECAPed specimens. Overall reduction in billet dimensions after subsequent processing limited the number of tensile test samples to two. The stress-strain curves for each processed material are presented in Fig. 10.10.

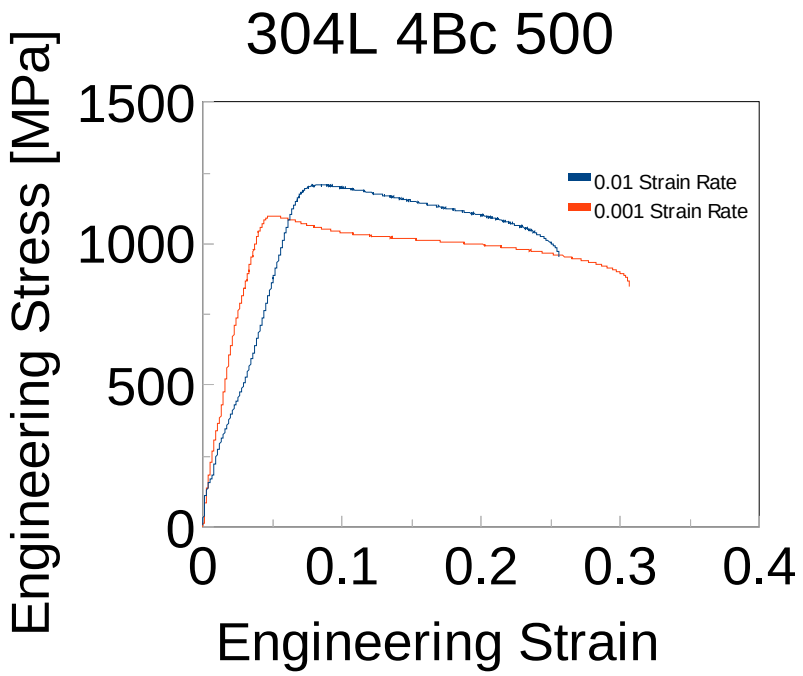
304L 4Bc 500
Engineering Stress [MPa]
1500
1000
500
0
0
0.1
0.2
0.3
0.4
Engineering Strain
0.01 Strain Rate
0.001 Strain Rate

(a)

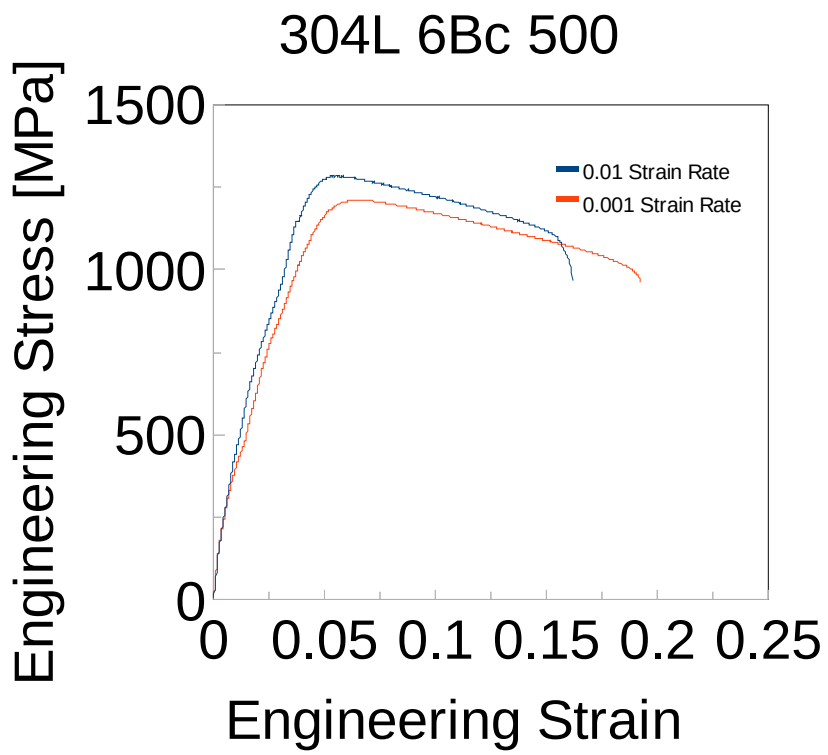
304L 6Bc 500
Engineering Stress [MPa]
1500
1000
500
0
0
0.05
0.1
0.15
0.2
0.25
Engineering Strain
0.01 Strain Rate
0.001 Strain Rate

(b)

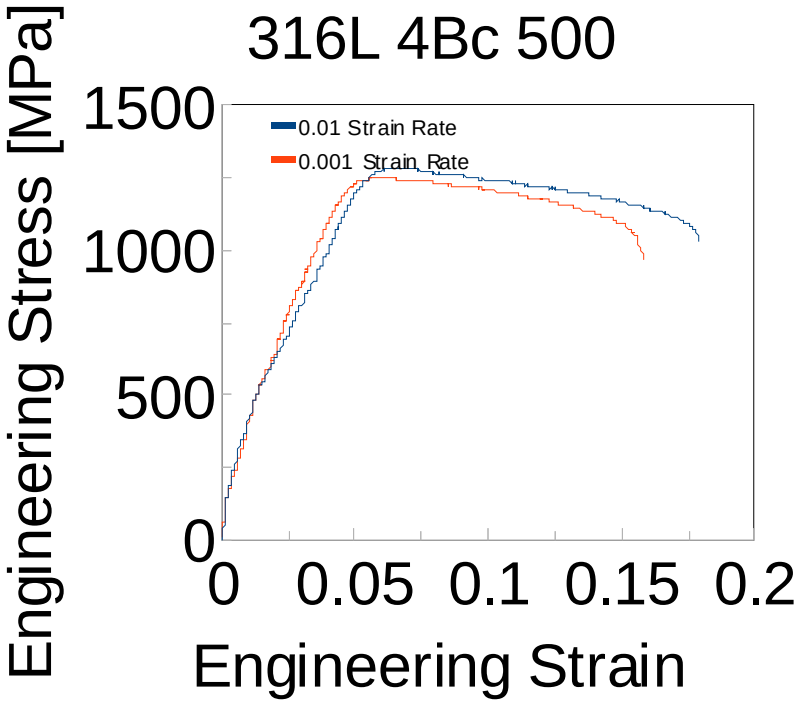

(c)

Fig. 10.10. Stress-Strain curves for (a) 304L 4Bc 500 (b) 304L 6Bc 500 and (c) 316L 4Bc 500. The two curves on each graph represent different strain rates.

It can be seen that there is an increase in yield stress from 304L 4Bc 500 to 304L 6Bc 500. 304L 4Bc 500 appears to be the most ductile of all the specimens considering the high amount of strain it is able to withstand before fracture. It also appears to have a comparable yield stress to those of 304L 6Bc 500 and 316L 4Bc 500. However, it is also important to note that there is an evident sensitivity to strain rate in 304L 4Bc500 specimen as the yield stress increases by about 200 MPa when the strain rate is increased by a factor of ten. This strain rate dependence is also apparent in 304L 6Bc 500 albeit to a lesser degree. Interestingly, 316L 4Bc 500 has a comparable yield stress and fracture strain to that of the 6-pass 304L sample indicating that similar grain refinement is achieved in 316L, but there appears to be very limited strain rate sensitivity in 316L SS.

The yield stress and strain at fracture for each specimen are summarized in Table 10.4. The comparisons show that the yield strength of 304L 4Bc500 specimen is lower than the other two specimens, but with greater strain to fracture. The yield strength and ductility of 304L 6Bc500 and 316L 4Bc 500 specimens are similar.

Table 10.4. Summary of uniaxial tensile test for as-processed 304L and 316L at various strain rates.

Specimen	Strain Rate [s^{-1}]	Yield Stress [GPa]	Strain at Fracture
304L 4Bc 500	0.001	1.099	.31
304L 4Bc 500	0.01	1.210	.26
304L 6Bc 500	0.001	1.212	.19
304L 6Bc 500	0.01	1.285	.16
316L 4Bc 500	0.001	1.253	.16
316L 4Bc 500	0.01	1.284	.18

Analysis of fracture surfaces for all specimens, Fig. 10.11 a-c, indicates a ductile fracture mode for all specimens tested at the same strain rate of $10^{-3}s^{-1}$. Ductile dimples are observed in all specimens, and they become finer in 304L specimens processed at a higher number of passes. The dimples in 316L 4Bc 500 are comparable to those of 304L 6Bc 500 confirmed by their comparable yield stresses and strain-at-fracture.

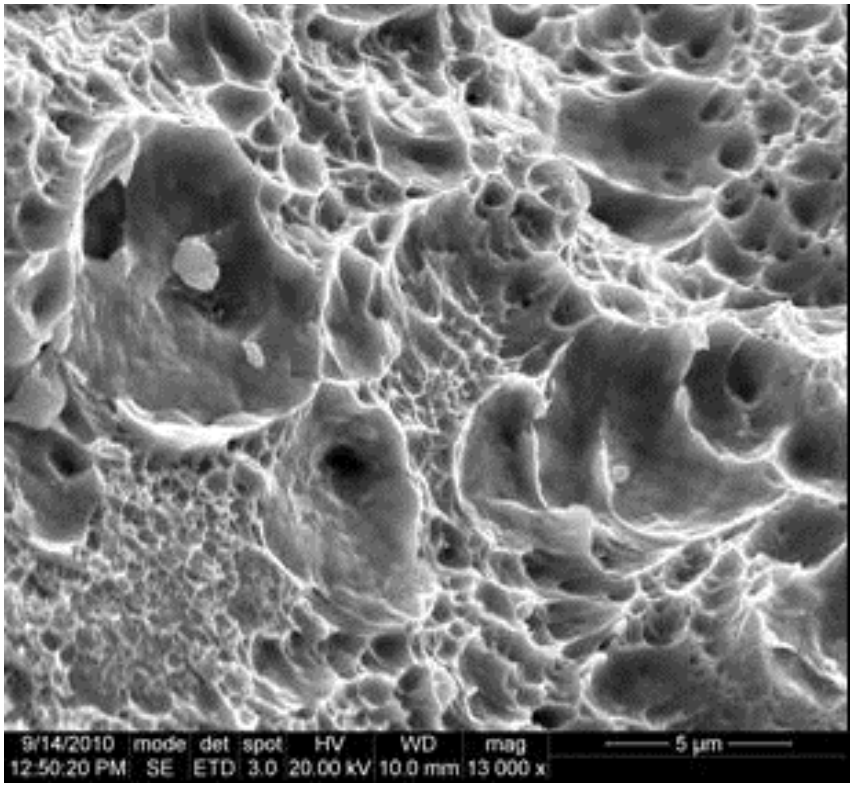
9/14/2010 mode det spot HV WD mag
12:50:20 PM SE ETD 3.0 20.00 kV 10.0 mm 13 000 x
5 µm

(a)

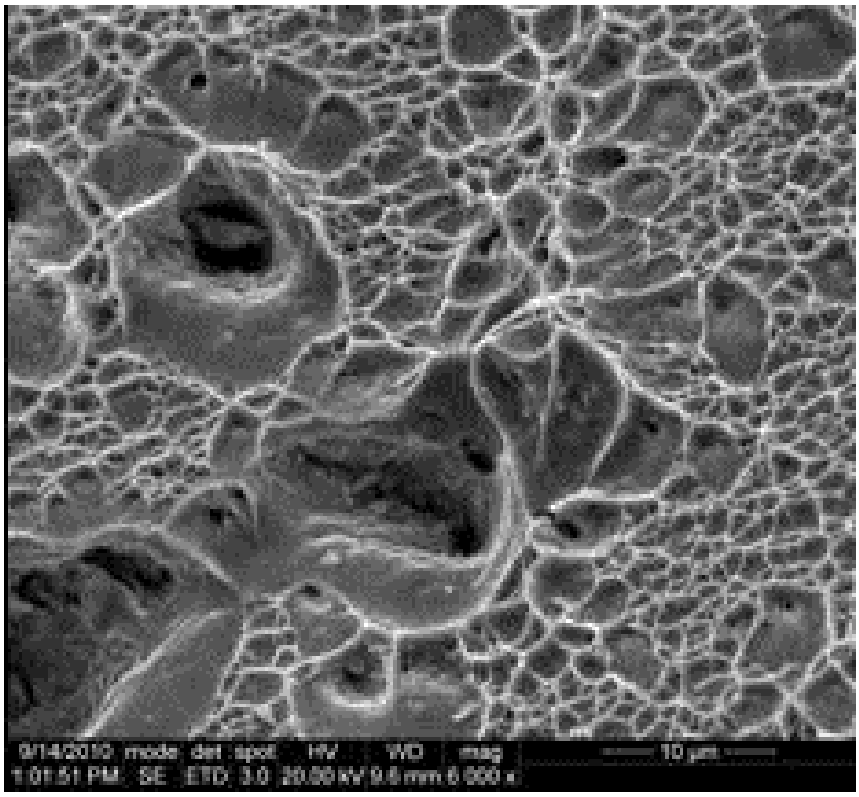
9/14/2010 mode det spot HV WD mag
1:01:51 PM SE ETD 3.0 20.00 kV 9.6 mm 6 000 x
10 µm

(b)

(c) 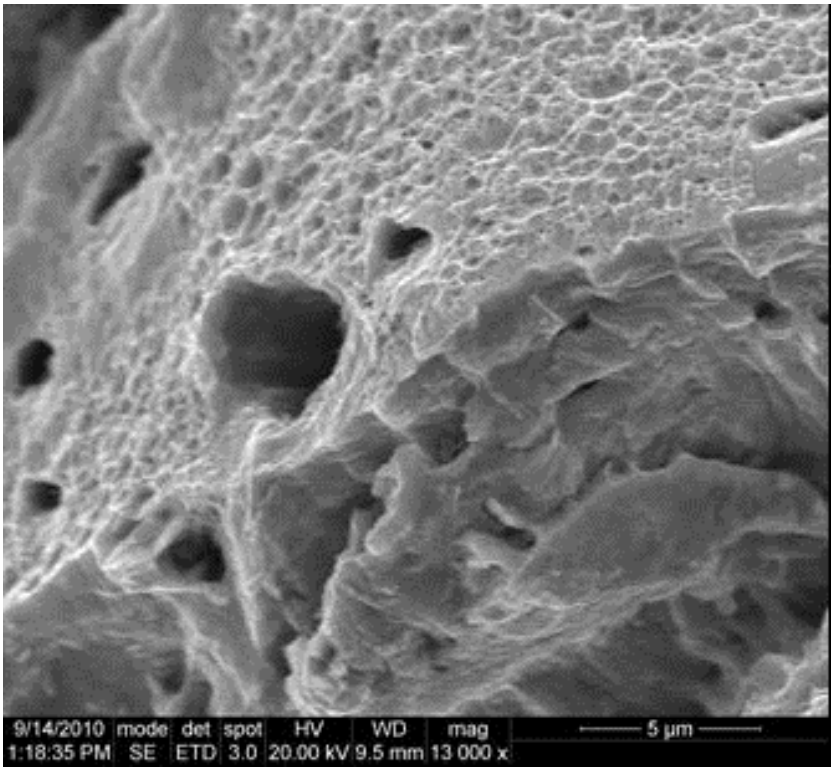

Fig. 10.11. FESEM micrographs of the fracture surfaces of (a) 304L 4Bc 500, (b) 304L 6Bc 500, and (c) 316L 4Bc500 specimens tested at a strain rate of $10^{-3}s^{-1}$.

Microstructure

The appeal of X-Ray diffraction is its versatility while remaining a non-destructive and powerful technique to analyze the microstructure of materials. Our primary interest in using this technique is to characterize the effects of ECAP on the microstructure of our stainless steels. It's been reported in the literature that austenitic steels subjected to ECAP tend to form predominantly martensite phases after numerous Bc processing at room temperature (ref: Bulk nanocrystalline stainless steel fabricated by equal channel angular pressing). Huang et. al. Report ~83% volume fraction of martensite after 8 passes following this route. It appears that there is probably a temperature dependence on this so-called deformation induced martensite transformation (DIMT) (ref: Formation mechanism of nanostructures in austenitic stainless steel during equal channel angular pressing) since, our multiple passes (4 – 6) at higher temperature did not impart such a noticable or significant quantity of martensite as can be seen from, for example, the ECAP 4-pass specimen reported by Huang et. al. in Fig. 10.12. No information of

processing temperature was made in that study by Huang et. al., however it can be inferred that it was performed at lower temperatures than our sample based on our results for 304L.

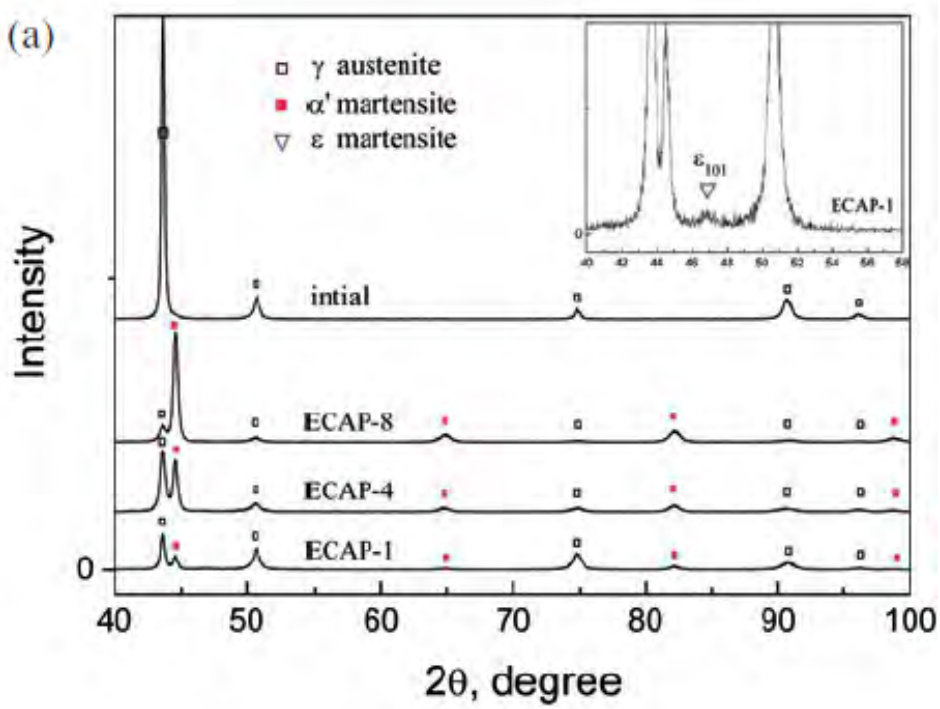

Fig. 10.12. XRD of microstructural evolution of ECAP 304L SS as produced by Huang et. al.

Formation of Fine Austenite Grains

Microstructural refinement is achieved primarily through the action of deformation twinning during severe plastic deformation. Plastic shear strain at the beginning of the ECAP process produces a high density of deformation twins. These twin boundaries subdivide the original grains in to thin plate-like grains whose thickness are in submicron regime while the length extends through much of the original coarse grains. Successive processing via ECAP further divides these grains due to shear deformation from different directions consequent of the 90° rotations between passes. This happens because large dislocation clusters are introduced into the twin grains generated from the initial passes in order to accommodate further plastic strain. These dislocations develop in to grain boundaries via the action of additional ECAP processing.

ECAP also allows for the formation of fine-grained austenite grains via the mechanism of twin fragmentation. Grain refinement mechanisms transform from that of the dislocation division previously discussed to a so-called twin fragmentation mechanism. A limiting grain size refinement is restricted by factors such as stacking fault energy. A high-enough stacking fault energy tends to a fast dynamic recovery of dislocations during deformation. This prevents the dislocations from forming in to grain boundaries. It is unclear why we would witness less recovery of dislocations with processing at higher-than-room temperature. Twin boundaries also act as obstacles to dislocation recovery. As mentioned earlier, results from TEM show the formation of these platelets which gradually evolve in to equiaxed-looking grains.

Discussion - Mechanical Properties

It is well known that nanocrystalline or fine grained materials exhibit superior mechanical properties. We see from our studies that the refined grains produce harder material with increases in yield stress and decreased sensitivity to strain rate. It is usually suspected that finer grains should also lead to increase in material ductility. Such was not the case in our study. We find that there is an overall decrease in ductility from samples of lesser processing to those of more. This is not totally unexpected since such heavy deformation due to our processing is not without artifacts such as pores and tensile instabilities [Reference: the mechanical properties of nanocrystalline materials], although this effect can be diminished by using tensile specimens of such small geometry as ours. This trade of ductility for yield stress in bulk materials should thus be expected. This may also support the notion that a high density of dislocations induced by processing may play a role in the grain refining process. The increase in hardness is also consistent with the notion that ECAP introduces such dislocations. While hardness is typically reported as Vicker's hardness, we opted to report indentation hardness instead.

Section B. South Korea contribution

As our South Korea counterpart mainly focused on ODS steels, here we only summary the projects in which US side has been actively involved.

B 11. Microstructure and mechanical properties of ECAP processed ODS steels, PM 2000, and torsion studies of 316 stainless steels.

Lead organization: KAERI (Lead by Dr. Jinsung Jiang)

11.1. ECAPed ODS steels

The microstructure of ECAPed ODS steel was also examined by TAMU as reported in the previous section. However, the goal of TAMU experiments is to investigate He and heavy ion irradiation induced defects. KAERI will focus on the evolution of microstructure and mechanical properties after ECAP processes. The following summarize the contributions from the Korean side of the team.

Fe-base oxide dispersion strengthened (ODS) alloy samples were prepared by MA (mechanical alloying) of elemental powders of Fe with about 70 micron in diameter, Cr, Ni, Mo, Ta, Ti of less than 10 micron, and yttria of about 20 nm in size. Two heats of the samples were of 17%Cr, 12%Ni austenitic steels; and the other two were 12%Cr ferritic-martensitic steels. MA processes were carried out using a planetary ball mill running in the Ar-filled atmosphere controlled glove box. Ball to powder ratio was 15:1 and the milling time was 12 hrs. For consolidation of MA powders HIP (hot isostatic pressing) process was done at 1150°C for 4 hrs under 100 atm pressure, following hydrogen reduction process by 5% hydrogen mixture gas to control the oxygen content in MA powders and degassing process. Nominal compositions of samples are shown in Table 6.1, and round rods with 12 mm in diameter and 150 mm long were cut out from the HIP processed samples. ECAP process of ODS steel samples were carried out at Texas A&M University

Table 11.1 Nominal composition of ODS samples for ECAP process

2101	Fe-17Cr-12Ni-2.5Mo-0.3Ti-0.3Y_2O_3
2102	Fe-17Cr-12Ni-2.5Mo-0.3Ti-0.3Y_2O_3-0.002B
2103	Fe-12Cr-1.1W-0.2V-0.14Ta-0.3Y_2O_3
2104	Fe-12Cr-1.1W-0.2V-0.14Ta-0.3Y_2O_3-0.002B

Microstructural characterization

Grain boundary evolution of ECAPed ODS steel sample

For EBSD analyses all ECAPed ODS samples were mechanically polished and then electrolytically polished in 10% perchloric acid with ethanol solution cooled with the liquid nitrogen at 20 V for 30 sec. EBSD analyses were done with JEOL 6500F with the accelerating voltage of 20 kV and probe current of 4 nA. The pixel step size was controlled with 0.02 micron and carried out with Package 5 of HKL.

Band contrast of ECAPed ODS steel samples are shown in Fig. 11.1. Grain sizes of all the ECAPed ODS samples reveal that significantly smaller than those of original ODS samples that are in the range of 5-10 micron in diameter. Especially ODS samples with austenitic matrix shows relatively uniform 0.5-1.0 micron in size of grains after ECAP process (Fig. 11.1 (a) and (b)). On the other hand the ODS samples with ferritic/martensitic matrix phase reveal grain size distribution somewhat differently; i.e. ODS alloy sample 2103 which showed the grain size of about 5 micron before ECAP process reveals very fine grain structure after ECAP, but the sample 2104 with the original grain size of above 10 micron shows coarser grain structure.
Therefore the grain size distribution after ECAP process seems to dependant on the initial grain size distribution (Fig. 11.1 (c) and (d)). Compared with ECAP 2C (rotation of 180° between pressings) 2B samples reveals bigger aspect ratio (more elongated) of grain morphologies due to the characteristics of 2C scheme which rotates the sample 180° between the pressings and applies reverse shear after eformation and annihilates the directionality of the deformation.

Main texture of fcc materials which go through the simple shear deformation usually shows {111} planes parallel to shear plane, and {110} planes to shear plane in case of bcc materials. Shear planes and inverse pole figures of the ECAPed ODS samples are shown in Fig. 11.2 and 11.3. In 2101 and 2102 samples which have fcc structure it is explicitly shown that {111} texture is well developed. In the sample 2104 which has bcc (ferritic/martensitic) structure reveals well developed {110} texture, while 2103 shows not very well developed texture.

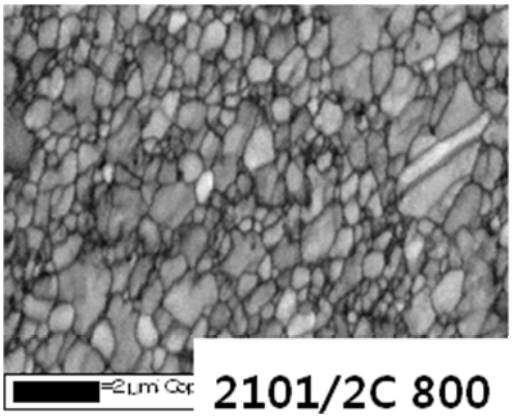

(a)

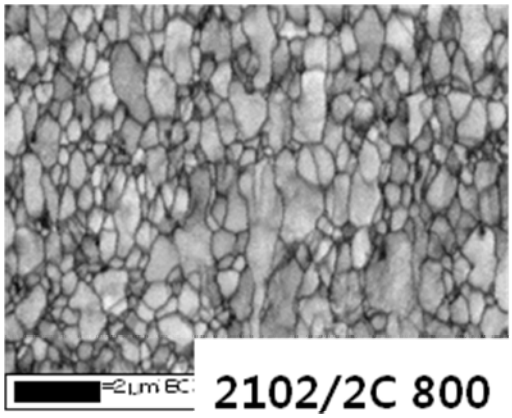

(b)

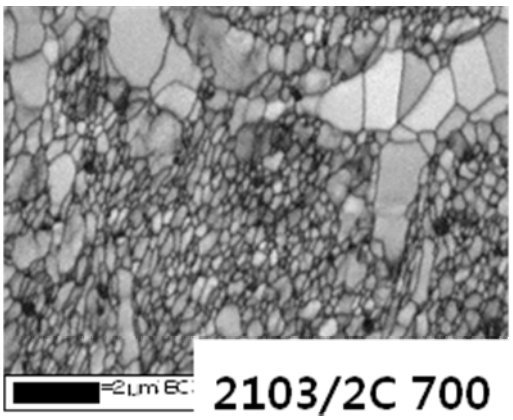

(c)

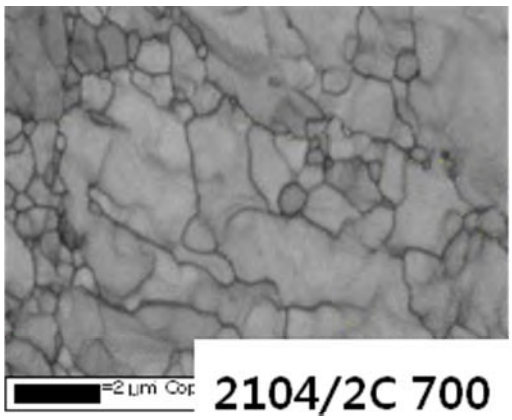

(d)

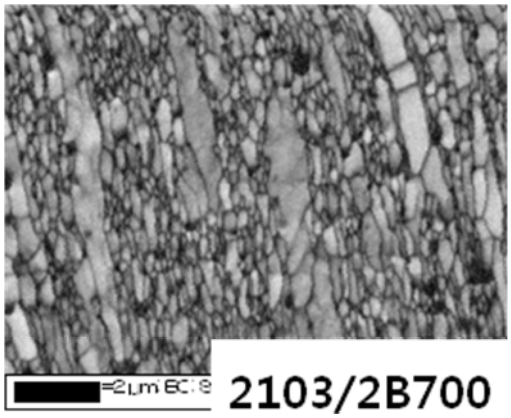

(e)

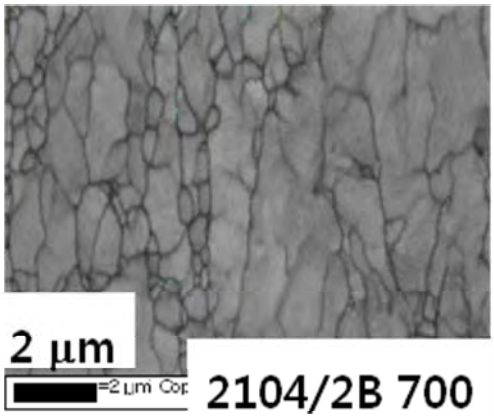

(f)

Fig. 11.1 Grain structure by EBSD band contrast map of ECAPed ODS steel samples; (a) 2101, ECAPed via 2C scheme at 800°C (b) 2102, ECAPed via 2C scheme at 800°C (c) 2103, ECAPed via 2b scheme at 800°C (d) 2101, ECAPed via 2B scheme at 800°C, (e) 2103, ECAPed via 2B scheme at 700°C, and (f) 2104, ECAPed via 2B scheme at 700°C

Low angle boundary and twin boundary distributions are illustrated in Fig. 3-4 and 3-5 respectively. Low angle boundaries here are defined as the boundaries with the misfit angle between 3 and 15°. Significant portion of the boundary contours in the band contrast maps (Fig. 3-1) appear matched with the low angle boundaries. High density of twin boundary are revealed within 2101 and 2102 ODS samples with austenite structure, while twin boundary is very rarely observed in 2104 sample of bcc structure with relatively large grain size.

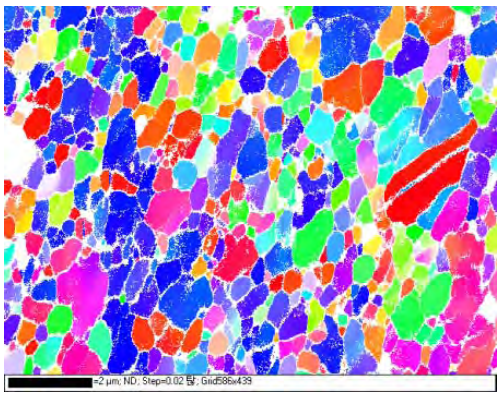

(a) 2101 2C800

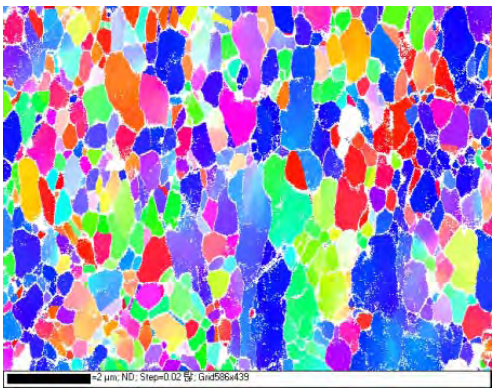

(b) 2102 2C800

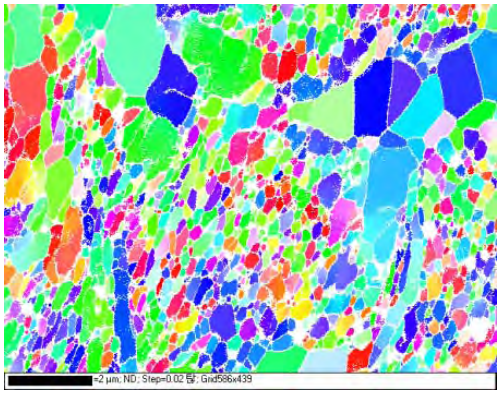

(C) 2103 2C700

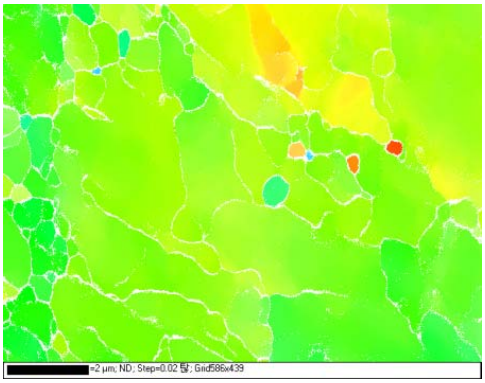

(d) 2104 2C700

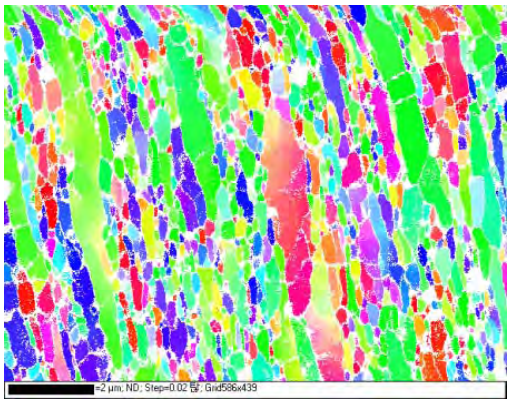

(e) 2103 2B700

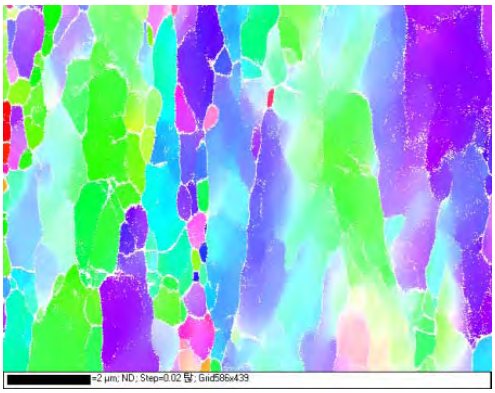

(f) 2104 2B700

Fig. 11.2 Normal direction orientation map of ECAPed ODS samples

(a) 2101 2C800

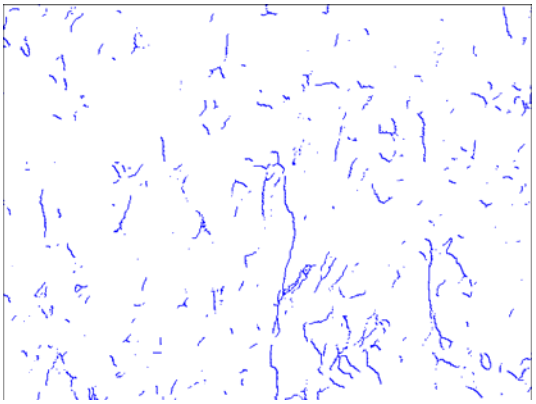

(b) 2102 2C800

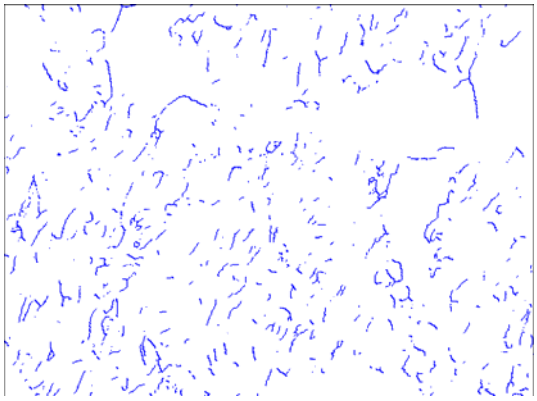

(c) 2103 2C700

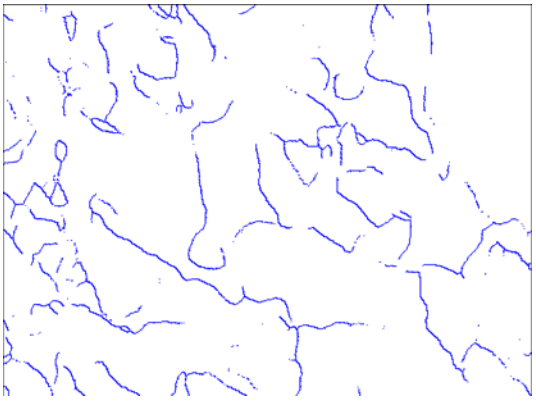

(d) 2104 2C700

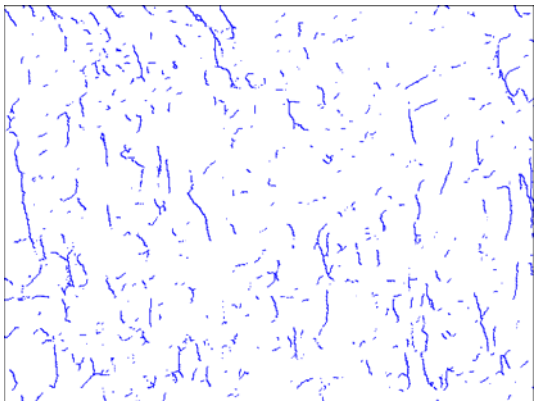

(e) 2103 2B700

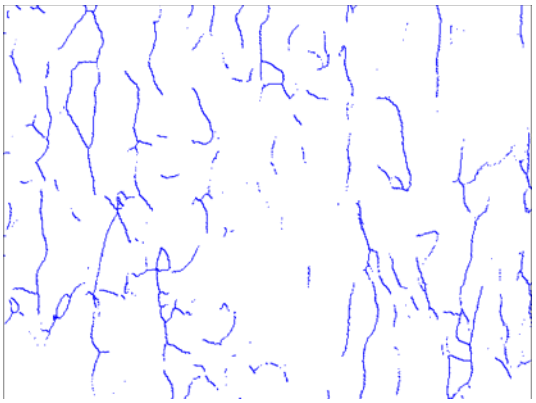

(f) 2104 2B700

Fig. 11.3 Low angle grain boundary map of ECAPed ODS samples.

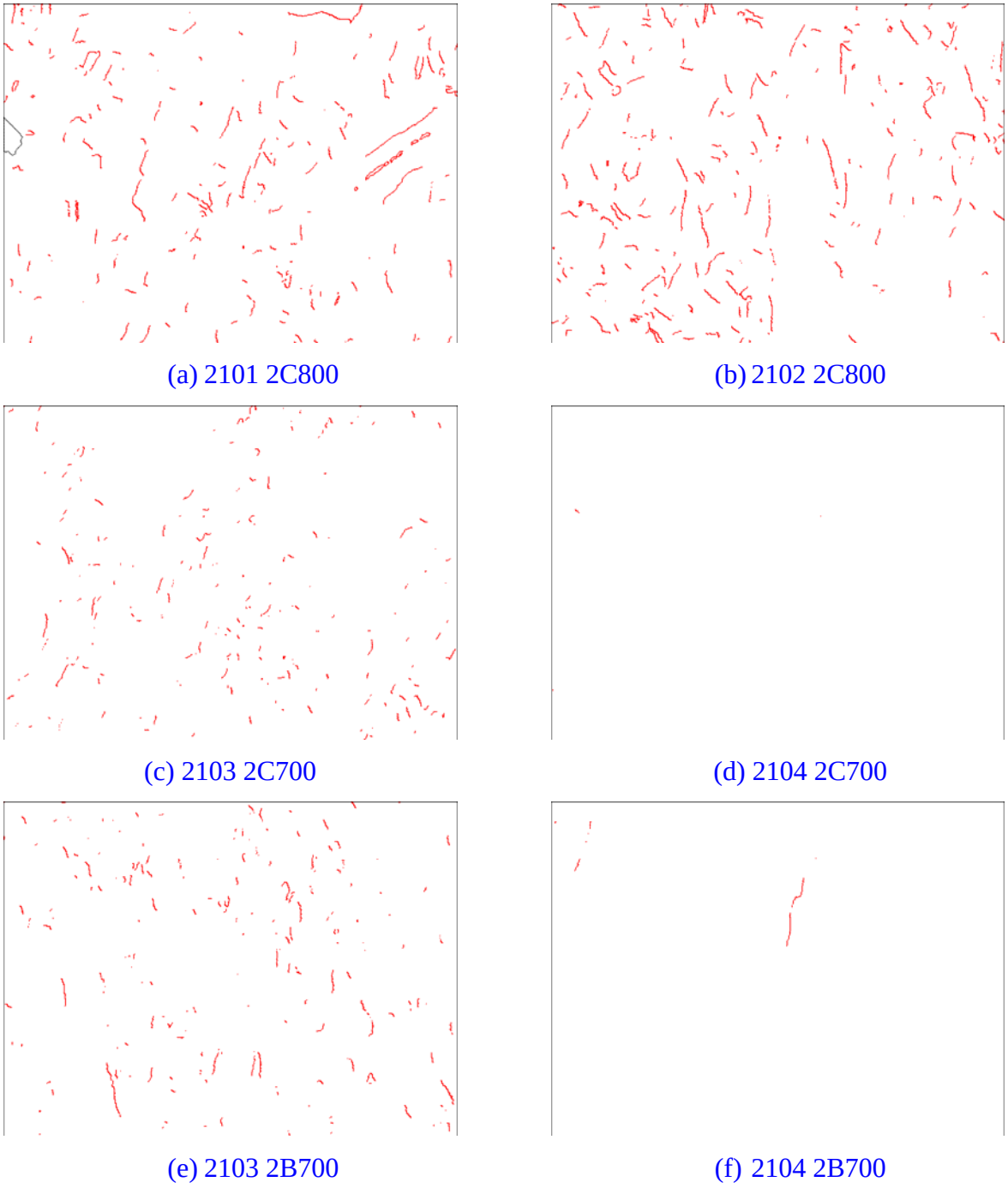

Fig. 11.4 Twin boundary map pf ECAPed ODS samples

Hardness measurement

Vickers hardness of ECAPed ODS samples were measured four times each and compared with those of the samples before the process. Hardness increased significantly by ECAP processes, except sample 2103 which showed not very big change of the grain size distribution before and after ECAP process. Different ECAP schemes (2C vs. 2B) appear not to influence the hardness change much. Further ECAP process with different temperature, schemes, and especially the number of passes would be needed to understand more comprehensively the effects of the ECAP process on the mechanical properties.

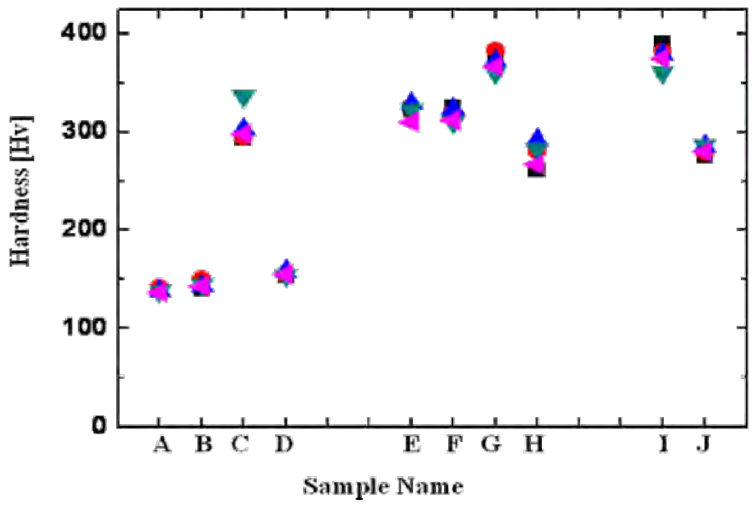

Fig. 11.5 Vickers hardness change of ECAPed ODS samples
(A: 2101; B: 2102; C: 2103; D: 2104
E : 2101 2C800; F: 2102 2C800; G: 2103 2C700; H: 2104 2C700
I: 2103 2B700; J: 2104 2B700)

11.2. In-situ microstructure analysis of PM 2000 during uniaxial deformation.

The microstructure and microtexture evolution of ODS steel during uniaxial tensile deformation was investigated. Specimens were elongated by an in-situ uniaxial deformation stage equipped with high-resolution electron backscattered diffraction (HR-EBSD) system. Microstructure and orientation rotating behaviors of individual grains were traced during the each step of the deformation process. ODS steel was found to change its crystallographic orientation on deformation, depending on its initial orientations. Further, the relationship between its mechanical properties and the distribution of dislocations was analyzed by

transmission electron microscopy (TEM) under uniaxial deformation. This result clarifies the knowledge of the relationship between the microstructure, mechanical properties and deformation of ODS steel.

The nominal chemical composition of PM 2000 is Fe-20Cr-5.5Al-0.5Ti-0.5Y_2O_3 (in wt.%). Fig. 11.6 shows the specially designed micro deformation device used to measure the crystallographic orientation change by EBSD during uniaxial tension. The uniaxial tensile sample was obtained from the edge of the extruded bar and its tensile direction was parallel to the extrusion direction. The specimen was polished mechanically down to a thickness of 300 μm. Electro polishing was carried out for 30 s at 20 V and a flow rate of 20 using a solution of 10 % perchloric acid and 90 % ethanol. To measure the strain amount and trace the microstructure of the same area during deformation, four rectangular micro indentation marks were placed on the specimen surface of length 140 μm, as shown in Fig. 11.6 (a). Macroscopic strains at each deformation step were obtained by measuring the relative displacement of the indentation marks along the tensile direction in the SEM images. The tensile strain was measured to be about 17 % along one direction. Fig. 11.6 (b) and (c) are digital images of the micro deformation device before and after the uniaxial tensile test.

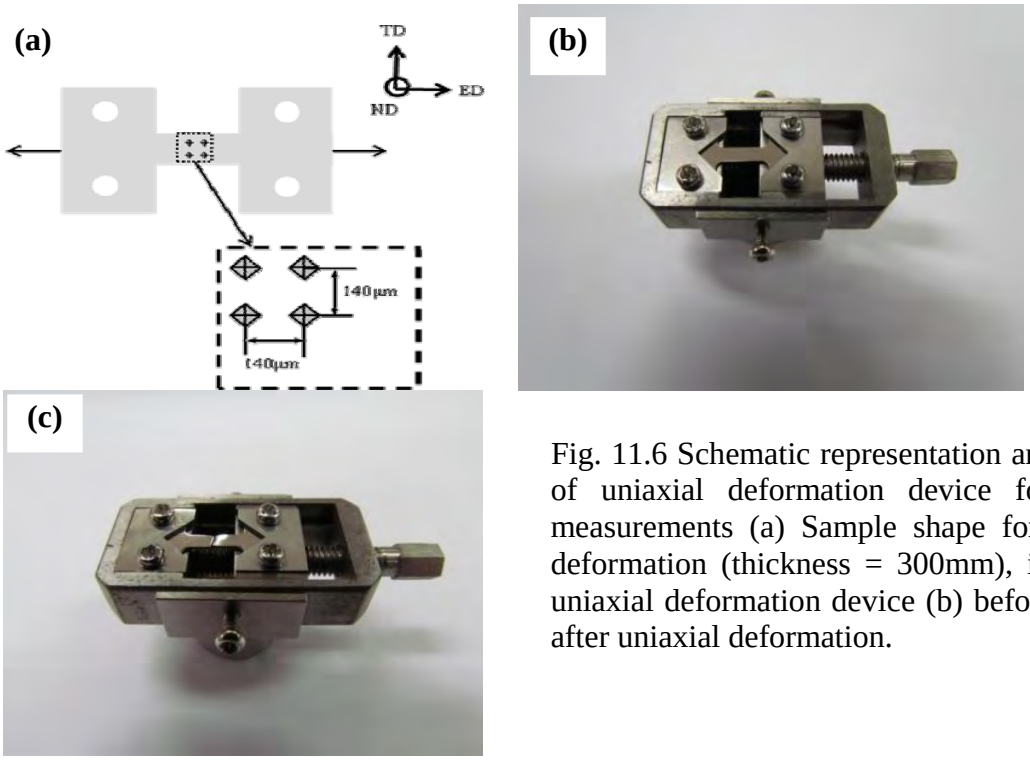

Fig. 11.6 Schematic representation and images of uniaxial deformation device for EBSD measurements (a) Sample shape for uniaxial deformation (thickness = 300mm), images of uniaxial deformation device (b) before and (c) after uniaxial deformation.

Electron backscattered diffraction (EBSD) mapping was performed using a scanning electron microscope (JEOL, JSM-6500F) with the accelerating voltage and prove current of 20 keV and 4 nA, respectively. Step size for EBSD mapping was 0.05 μm considering the initial grain size of tensile specimen. All crystallographic orientation data were collected from electron backscattered patterns and processed using the software package HKL, CHANNEL 5.

The micro hardness of PM2000 was measured at room temperature using a Vickers indenter (ITW, 432SVD). Four indentations were made before and after tensile deformation. All indentations were performed at a loading of 0.3 kgf and a dwell time of 5 sec.

Microstructural characterization of dislocations and oxide particles was performed using a transmission electron microscope (JEOL, JEM 3000F), operating at 300 keV. Specimens for TEM observation were prepared using jet polishing and using a focused ion beam (FEI, Nova nanolab 200) equipped with a schottky field emission gun column and Ga+ ion beam column.

Microtexture evolution during uniaxial tension

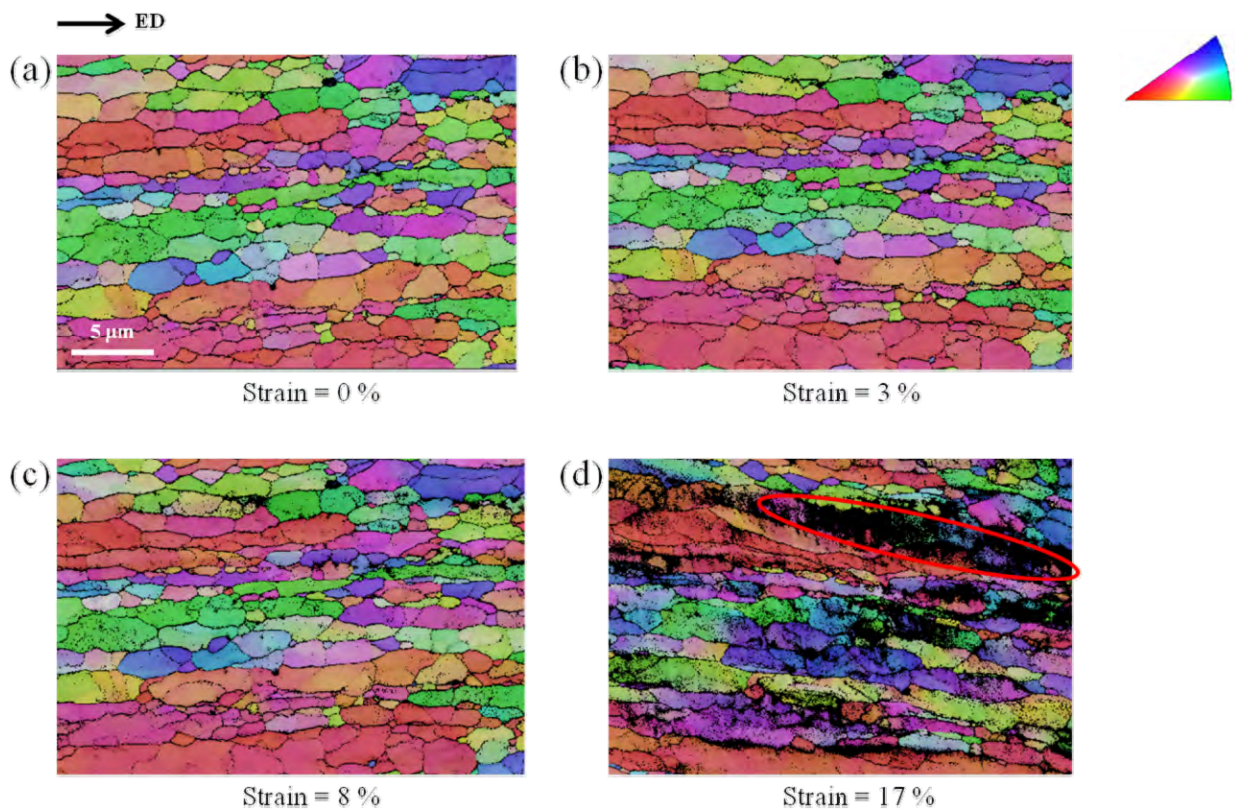

Fig. 11.7 EBSD orientation maps of PM2000 to normal direction with strain increase (a) 0%, (b) 3%, (c) 8% and (d) 17% during uniaxial tensile deformation.

Tensile deformation was discontinued at three different uniaxial strains to investigate the various characteristics before necking. Fig. 11.7 (a) exhibits elongated grains of size 1-7 µm along the ED. The aspect ratio of the grains increased with an increase in grain size because of the elongation of grains along the tensile direction. The grains rotated towards the stable orientation, and highly deformed grains increase as observed from dark contrast in the orientation map (Fig. 11.7 (d)). The area of the green region indicates that <101>//ND decreases as the uniaxial strain increases. The areas of the red and blue regions indicate that <001>//ND and <111>//ND increase with the strain, respectively. It is indicated that <101>//ND rotates towards <001>//ND or <111>//ND during uniaxial deformation.

Vickers hardness test and TEM analysis

SEM images of Vickers indentation marking indented before and after deformation are shown in Fig. 11.8 (a). Four indentation marks are clearly seen on both images, highlighted with blue and red circles. The average diagonal distance of each specimen before and after deformation is 39.7µm and 43.5µm, respectively. Fig. 11.8 (b) shows the relation between the average Vickers hardness and the indented area. The graph indicates that 17 % of the hardness increases during uniaxial deformation. That is, the increase in hardness is related to the hardening mechanism by deformation known as work hardening.

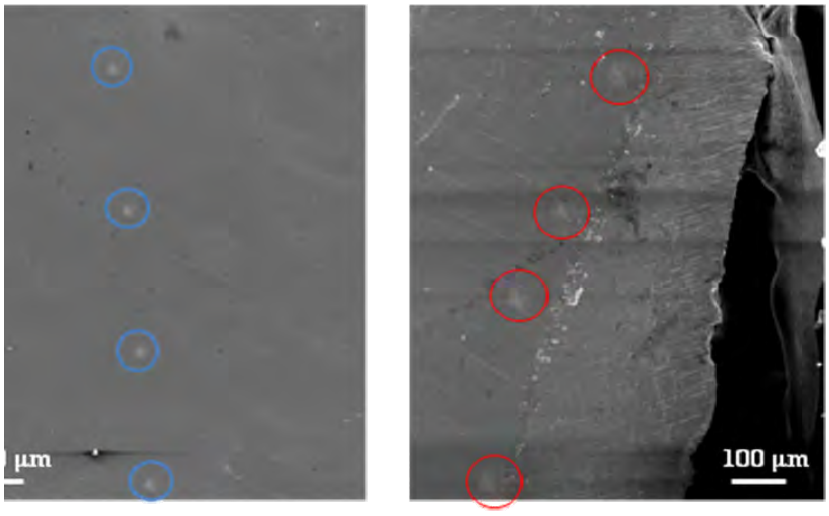

Before deformation After deformation

(a)

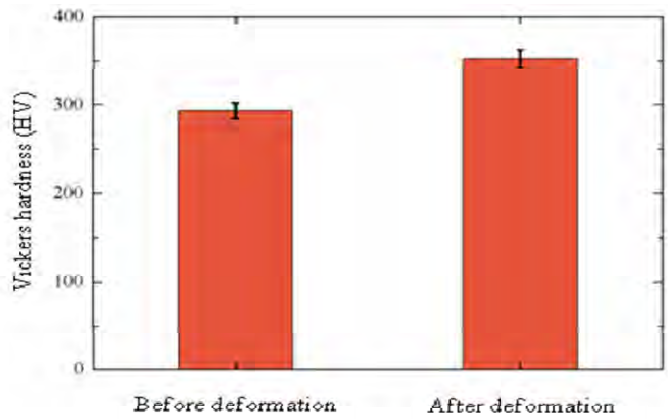

(b)

Fig. 11.8 (a) SEM images of micro Vickers indentation marking at as extruded area and deformed area, (b) average Vickers hardness related to indentation areas.

The TEM sample was prepared by jet polishing before deformation and its high resolution microstructure images are shown in Fig. 11.9. Dark field images were taken the scanning transmission electron microscopy (STEM) mode to obtain clear contrast images of oxide particles and dislocations. Oxide particles of 10-20 nm were uniformly dispersed inside the grains. A few particles over 100 nm were also observed. A number of dislocations are pinned by oxide particles because the sample is hot extruded without any heat post-treatment.

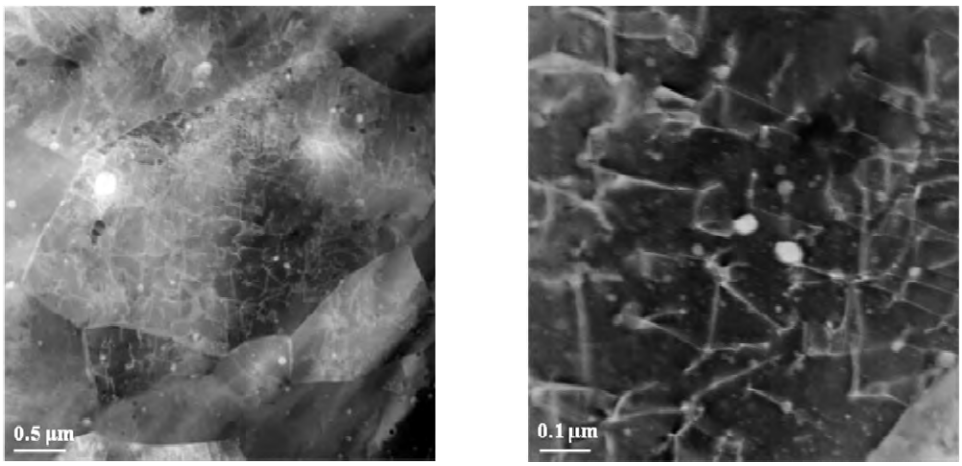

(a) (b)

Fig. 11.9. STEM dark field images of as extruded area.

To compare the microstructures between before and after deformation, TEM sample was prepared after deformation using a focused ion beam. The region of dark contrast marked by the red circle in Fig. 11.7 (d), considered to be one of the most deformed areas, was selected for comparison. The high resolution dark field STEM images of the deformed area are shown in Fig. 11.10. Particles smaller than 50 nm are covered with high density dislocations, but the large particles are clearly observed. It is hard to distinguish individual dislocation lines because planar networks are formed because of the pilling of dislocations, as shown in Fig. 11.10 (a). Several authors have shown that dislocations pile up and form subgrains during deformation. Such planar networks considered as subgrains may have different orientations with neighbors, as indicated by the contrast difference in TEM image. In addition, the intensity difference of diffraction patterns taken in the same zone axis of $[1\dot{1}\dot{1}]$ reveals the orientation difference between two subgrains, as shown in Fig. 11.10 (b).

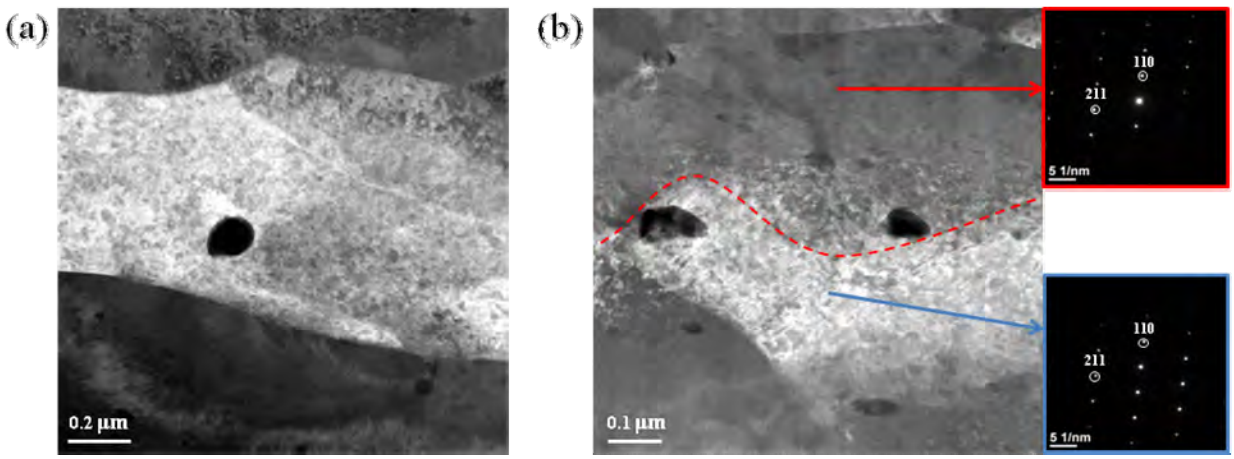

Fig. 11.10. Scanning TEM dark field images of deformed area (a) Image of subgrains formed by pilling up of dislocations, (b) Image of subgrains and diffraction patterns taken in the same zone axis of $[1\bar{1}\bar{1}]$.

In case of bright area, the intensity of the spots is uniform because the incident beam is parallel to the zone axis. Otherwise, the intensity is not uniform at dark area because the zone axis is slightly away from the incident beam direction. The misorientation between two subgrains is approximately 2° as calculated by the conversion of distance difference to angle difference.

The effect of oxide particles and dislocations on microstructures and their mechanical properties was investigated by Vickers hardness test and TEM analysis. A 17 % increase in hardness was found after deformation because the microstructure development was related to the dislocations and oxide particles. This study suggested that the finely dispersed oxide particles might contribute to form a cell structure of dislocation entanglement which increases not only the hardness of the material but also the orientation spreads in the microstructure.

11.3. Shear and inverse shear deformation by torsion of 316L stainless steel

During torsion the sample material experiences simple shear deformation without volume change. The extent of the deformation could be easily and quantitatively controlled during torsion test and the microstructural change could be observed with the deformation. Shear strain during torsion is defined by $\gamma = \tan(\theta)$, and texture is usually developed by the same amount of tensile and compression force which are perpendicularly working each other. Two deformation modes are possible; the inverse shear deformation is that the sample is deformed in the other (reverse) direction with the same amount after one simple torsion (shear) deformation. In this case total shear becomes macroscopically zero, but the deformed structure is not completely reversible and the remained deformation becomes more distinctive as the extent of shear becomes bigger.

Torsion specimen was prepared with SUS 316L. Test section was 5 mm in diameter; 10 mm in length and the grip portion was 30 mm square bar with the total sample length of 70 mm. After the torsion test the sample surface (perpendicular to the cylinder sample radius) was observed using TEM/EBSD (ASTAR).

Torsion samples before and after the test are shown in Fig. 11.11. The increasing amount of shear deformation from 0 to 0.4, 0.8, and up to 1.6 is clearly revealed in Fig. 11.11 (c).

(a)

(b)

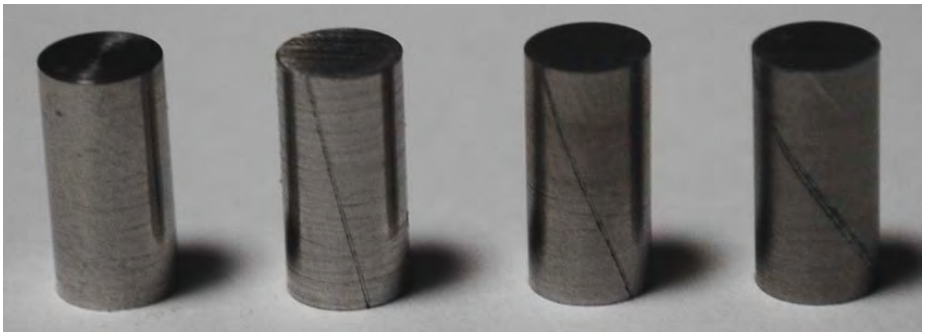

(c)

Fig. 11.11. Torsion test samples of 316L stainless steel; before and after the tests with the marks.

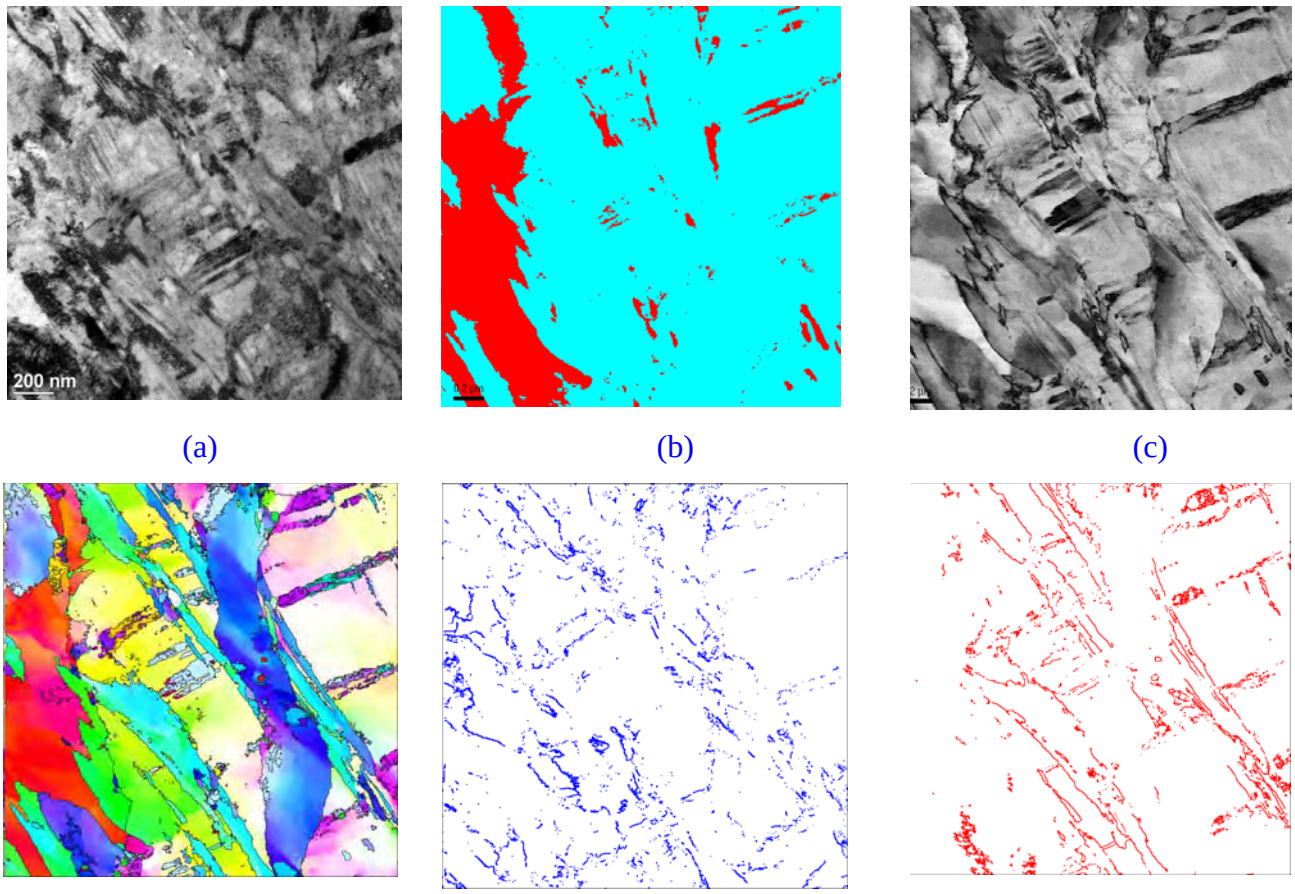

(a) (b) (c)

(d) (e) (f)

Fig. 11.12 TEM and EBSD analyses of torsion tested 316L stainless steel sample; (a) TEM BFmicrograph, (b) Phase map (blue: austenite, red: martensite), (c) Reliability, (d) Normal direction orientation map, (e) sub-grain boundary map (3° < misorientation < 15°), and (f) twin boundary (Σ3) map

B12. Microstructural Evolution of ECAPed Fe–17Cr-12Ni-2.5Mo austenitic alloys with Fe^+ and H^+ ion irradiation

Lead organization: KAERI (Lead by Dr. Jinsung Jiang)

In this study, microstructure evolutions of the Fe-17Cr-12Ni-2.5Mo and ODS alloys during Fe^+ and H^+ ion irradiations were investigated. Radiation-induced defect distributions have been examined; it was observed that the interstitials traveled further than substitutions and interacted with grain boundaries preferentially. Moreover, it was observed that crystal structure of irradiated sample surface was changed from FCC to BCC while the Fe-17Cr-12Ni-2.5Mo alloys were irradiated with Fe^+ ion. The sizes of the newly developed BCC grains were coincident with the ion irradiation depth, which could be estimated by simulation (SRIM 2012 software).

Chemical compositions of Fe-17Cr-12Ni-2.5Mo alloys are shown in table 12.1. Additional 2 wt% Mn and 1 w% Si were included in sample A, it was the contents of commercial 316 stainless steel. Excluding the Mn and Si contents, additional Ti and Y_2O_3 were added in sample B, it was the contents of 316-type ODS stainless steel. The ODS sample was fabricated by mechanical alloying and hot isostatic pressing processes. Elemental metal powders with yttria powder of 30nm in size were mechanically alloyed by using a Pulverisette-5 planetary ball mill at 200 rpm in an Ar atmosphere for 12h with a ball to powder ratio of 15:1. The MA powder was then filled into a 304 stainless steel can, followed by degassing at 500ºC under 10^{-3} Pa for 1h and sealing. The MA powder was consolidated at 1150ºC under 100MPa for 4h. The hipped bar was then pre-heated at 1200ºC for 2h and hot rolled into a 15 mm thick plate, which corresponds to a reduction ratio of 50%. Normalizing was performed at 1050ºC for 1h and tempering was carried out at 750ºC for 2h. The sample was then isothermally annealed at 1250ºC for 500 h under vacuum.

Table 12.1 Chemical composition of Fe-17Cr-12Ni-2.5Mo alloy specimens

	Fe	Cr	Ni	Mo	Mn	Si	Ti	Y_2O_3
A	Bal	17	12	2.5	2	1	-	-
B	Bal.	17	12	2.5	-	-	0.3	0.3

2.54 × 2.54 × 15.24 cm sized square bar of Fe-17Cr-12Ni-2.5Mo alloys were processed by ECAP. Two different process steps are applied; the first one is a conventional ECAP process of one pass at 25ºC (route A), the other one is a ECAP process of two passes at 800ºC, which

include one more ECAP step after 180º rotation of route A processed sample (route B). After the ECAP, samples were implanted with Fe^+ and H^+ ions at room temperature. The energy of Fe^+ ion source was 100keV, $2.0\times10^{17}cm^{-2}$, and the energy of H^+ ion source was 120 keV, $2.0\times10^{18}cm^{-2}$, respectively. The microstructure evolutions were investigated by TEM to examine the density of voids, dislocations, and radiation induced segregation. The crystal structure and misorientations in microstructures have been characterized using ASTAR, which enables orientation and phase mapping with TEM.

In Figure 12.1, TEM micrograph of sample A and B were shown after ECAP process. Sample A was ECAPed along the route 'A' at 25ºC, and Sample B was ECAPed along the route 'C' at 800ºC, respectively. The specimen was homogeneously deformed in figure 1(a); lots of defects are generated in the sample, fine planar boundaries were aligned along the shear band direction with a width of 50nm. On the other hands, an equi-axed fine grains are observed in figure 1(b), they are induced by recrystallization with an average grain size of 500nm after ECAP at 800°C. Those two different samples were subjected to ion irradiation tests.

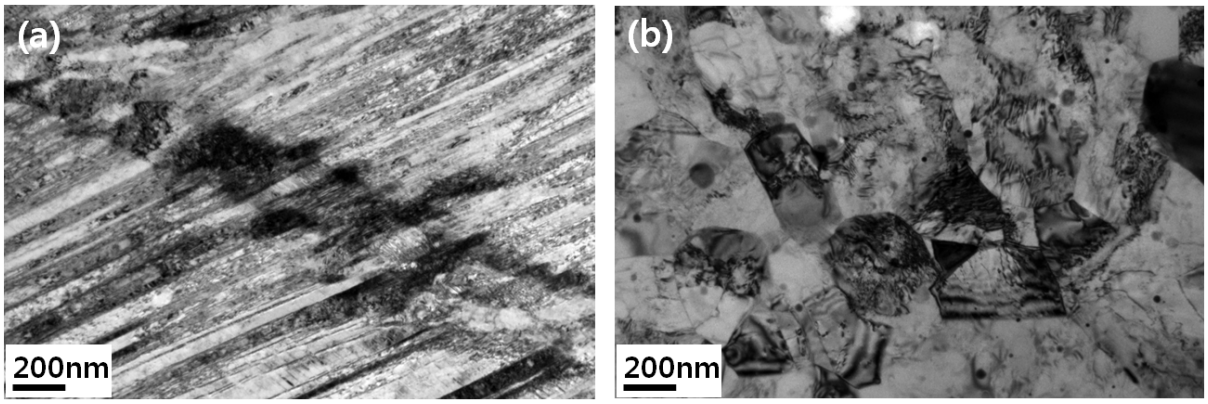

Figure 12.1. TEM micrograph of sample A and B after ECAP process. (a) Sample A was ECAPed along the route 'A' at 25ºC. (b) Sample B was ECAPed along the route 'C' at 800ºC

In figure 12.2, ion irradiation facility of KAERI is introduced. The management and operation of the machine in figure 2(a) is currently supported by Proton Engineering Frontier Project. Metal ions such as Ni, Cu, Co, Cr, Fe, etc. can be accelerated up to 100 keV, and the gas ions such as He, Kr, Xe, Ar, Ne, H, etc. can be accelerated up to 120 keV. Proton Engineering

Frontier Project recently tries to enlarge the acceleration voltage more than 100MeV. In figure 2(b), the irradiation samples are shown. The backing plate was made of copper, which is efficient for thermal conduction. Samples were attached to the backing plate within the area of 5 cm X 5 cm square. Fe^+ ions were irradiated at 100keV, and the dose was 2.0×10^{17}ions/cm^2. H^+ ions were irradiated at 120keV, and the dose was 2.0×10^{18}ions/cm^2.

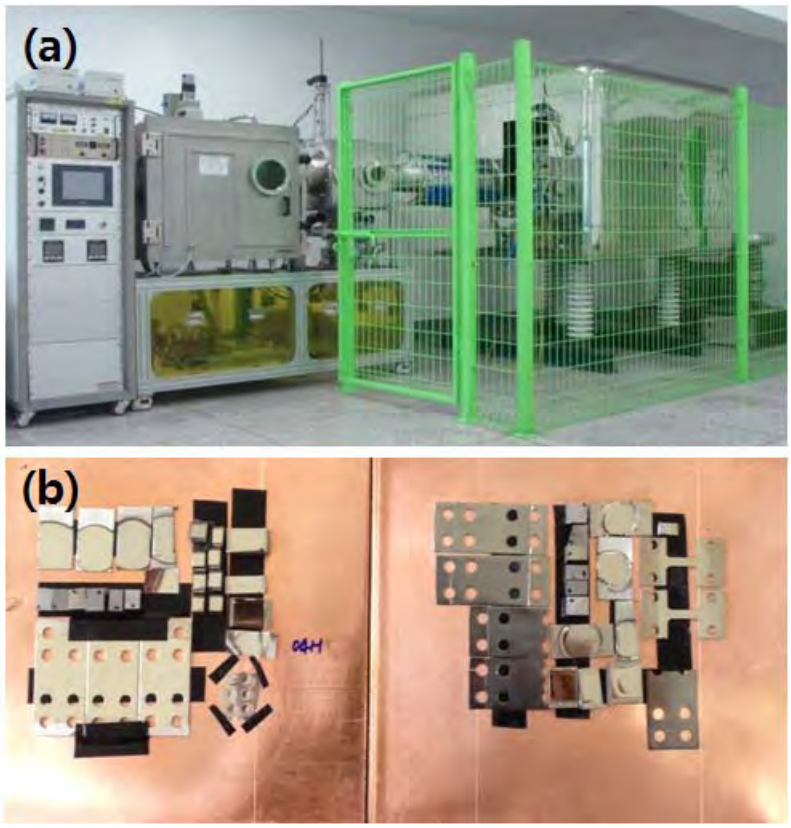

Figure 12.2 (a) Ion irradiation facility at Gyeongju site, KAERI (b) ion irradiation test samples. The facility is currently maintained and operated by Proton Engineering Frontier Project.

In figure 12.3, the penetration depths of ions on the Iron surface were estimated using a molecular dynamics simulation (The software named SRIM2012). It was also assumed that Fe^+ ions were irradiated at 100keV, 2.0×10^{17}cm^{-2}, and H^+ ions were irradiated at 120keV, 2.0×10^{18}cm^{-2}. The results showed that the peak of Fe^+ ions profile in sample would be at 30nm, and the peak of H^+ ions profile in sample would be at 500nm, respectively.

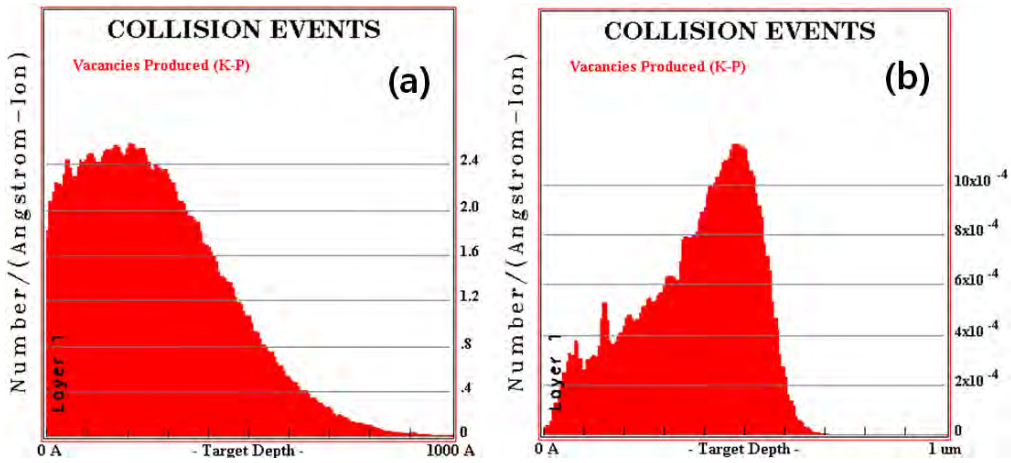

Figure 12.3 Penetration depth profile of ions was estimated using a molecular dynamics simulation (SRIM 2012). It was assumed that (a) Fe^{+}, 100keV, $2.0\times10^{17}cm^{-2}$ (b) H^{+}, 120keV, $2.0\times10^{18}cm^{-2}$ were irradiated on the iron (Fe) surface.

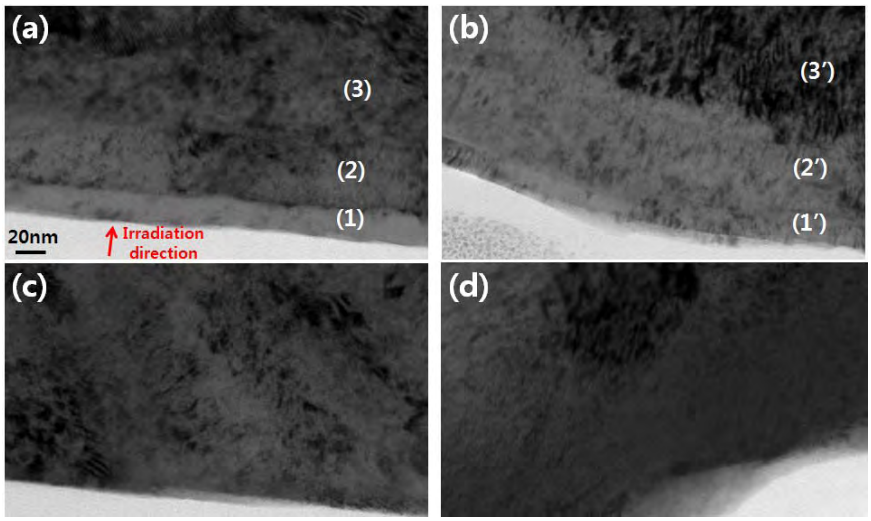

Figure 12.4 Cross-section images of irradiated samples. The samples were prepared using focus ion beam (FIB). (a) ECAPed sample A, and (b) ECAPed sample B were irradiated with Fe^{+} ion (100 keV, $2.0\times10^{17}cm^{-2}$). (c) ECAPed sample A, and (d) ECAPed sample B were irradiated with H^{+} ion (120 keV, $2.0\times10^{18}cm^{-2}$). After Fe^{+} ion irradiation, the definite layers are observed near the surfaces. Each layers are identified by numbers from (1) to (3).

Figure 12.4 Cross-section images of irradiated samples are observed. The samples were prepared using focus ion beam (FIB). ECAPed sample A, and sample B were irradiated with Fe^+ ion source (100keV, $2.0\times10^{17}cm^{-2}$), and H^+ ion source (120 keV, $2.0\times10^{18}cm^{-2}$). The damage layers were shown near the surfaces. Specially, the definite layers are observed after Fe^+ ion irradiation. In figure 4(a), each layer was identified by numbers from (1) to (3). It was suspected that the layer (1) and (2) are developed after irradiation, (3) is the base material. The depth was estimated 50nm, it was coincident with the molecular dynamics simulation results. The boundary between (1) and (2) was located in the 20nm depth, it can be the peak of ion irradiation profile. In figure 4(b), The similar layers were observed, however, the depth of (1') and (2') seemed deeper than figure 1(a). It was suspected that the grain boundaries distributions before irradiation affected damage layer construction. In figure 4(c) and 4(d) shows H^+ ion irradiation effect on the same samples, such kind of definite layers were not observed. The H^+ ions are the interstitial, the behavior would be quite different from the substitutions, Fe^+ ions.

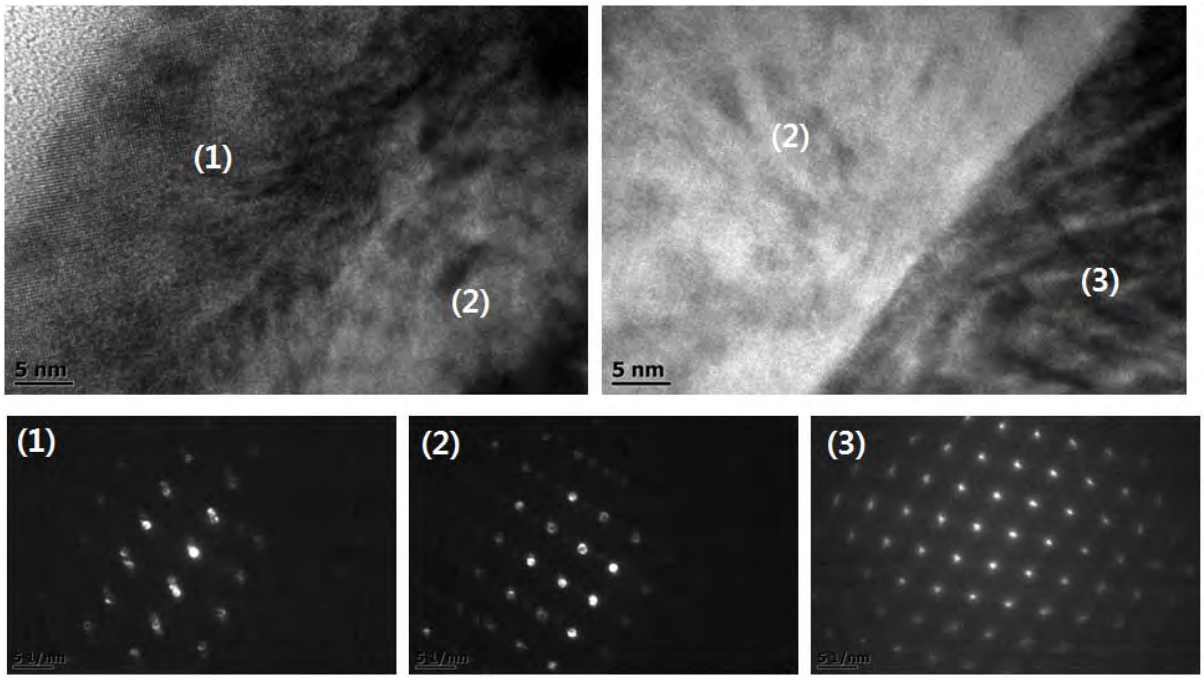

Figure 12.5 Cross-section images of ECAPed sample A after irradiation with Fe^+ ion (100 keV, $2.0\times10^{17}cm^{-2}$). Three layers which were identified in figure 4 were particularly observed from (1) to (3), and corresponding diffraction patterns were obtained.

In figure 12.5, cross-section images of ECAPed sample A after irradiated with Fe^+ ion (100keV, $2.0\times10^{17}cm^{-2}$) are suggested by magnified images. Three layers were particularly observed from (1) to (3), and corresponding diffraction patterns were obtained. It was observed that the crystal structure of damaged layer (1) was quite different from base material (3). Lattice parameters could not be match as a same crystal structure. It was suspected that some major changes were involved, such as recrystallization or phase transformation.

In figure 12.6, cross-section images of ECAPed sample B after irradiated with H^+ ion (120 keV, $2.0\times10^{18}cm^{-2}$). The definite layers were observed near the surfaces. In figure 12.6(a), nano-sized pores are finely distributted at the surface, and in figure 12.6(b), pores were gathered at the defects such as dislocations or grain boundaries. However, there were no crystallographic change even in the surface area, all irradiated part of samples seemed to be in one grain.

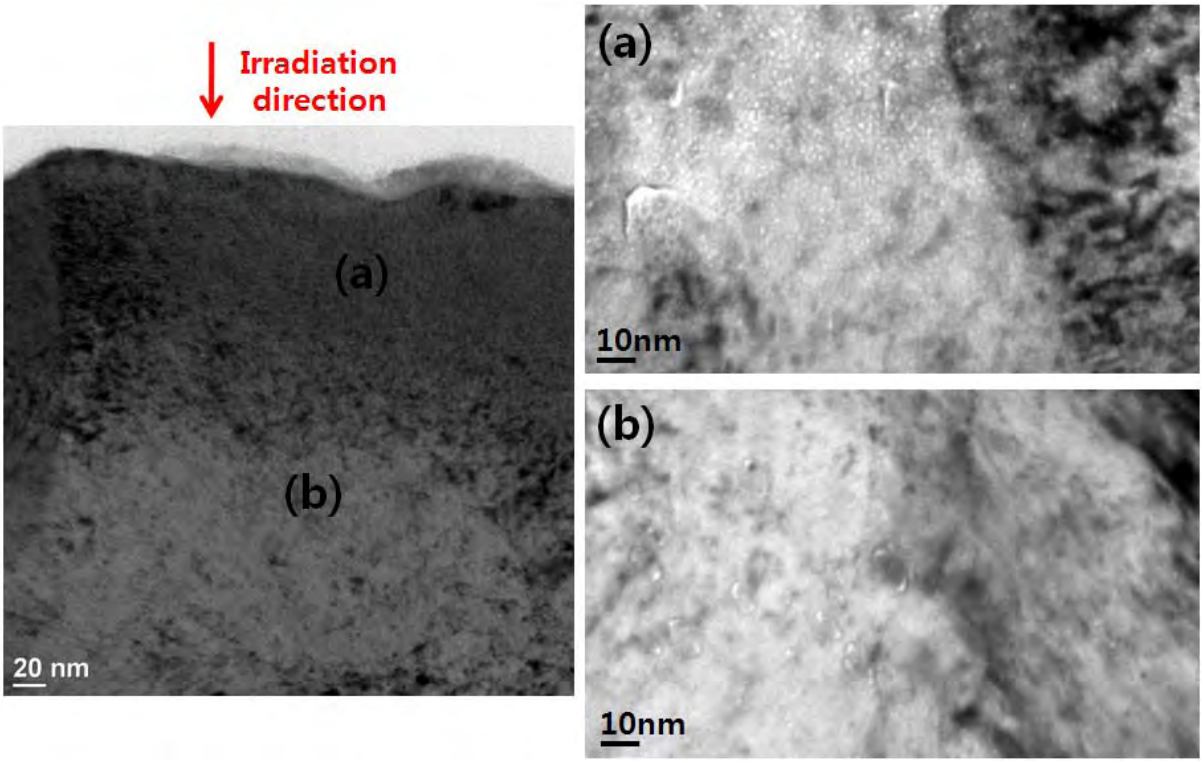

Figure 12.6 Cross-section images of ECAPed sample B after irradiation with H^+ ion (120 keV, $2.0\times10^{18}cm^{-2}$). The definite layers were observed near the surfaces. (a) Nano-sized pores are finely distributted near the surface. (b) cavities appeared to gather at the defects such as dislocations or grain boundaries.

In figure 12.7, schematic of ASTAR system is shown, basic operation concept is introduced. ASTAR is the system which enables orientation and phase mapping with transmission electron microscopes. It can be simply described that the TEM was accompanied by automated diffraction pattern analysis system. The ASTAR system is effective for visualizing crystallographic information of a sample, while it simultaneously shows the TEM micrograph.

In figure 12.8, microstructure evolutions of 17Cr-12Ni-2.5Mo alloy after Fe^+ and H^+ ion irradiation was characterized using ASTAR. A virtual bright field image and a corresponding misorientation distribution map of ECAPed sample A after irradiated with Fe^+ ion irradiation (100keV, $2.0\times10^{17}cm^{-2}$) are shown in figure 9(a) and 9(b), respectively. The same images of ECAPed sample B after irradiated with H^+ ion (120 keV, $2.0\times10^{18}cm^{-2}$) are shown in figure 12.9(c) and 9(d), respectively.

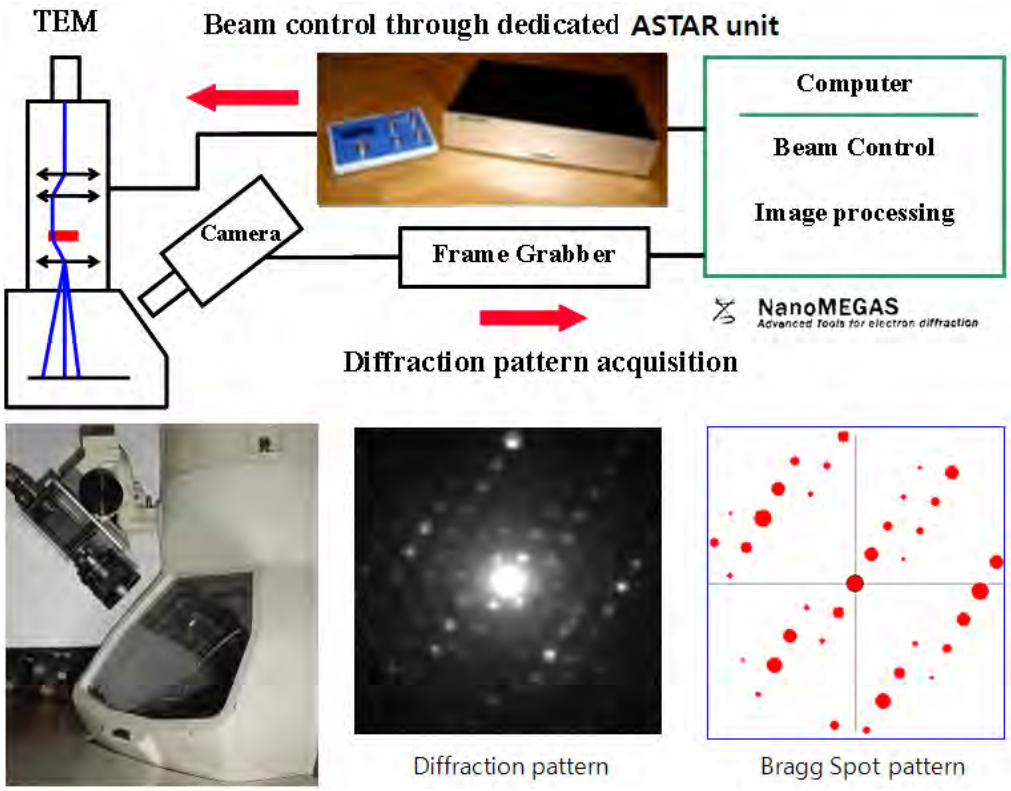

Figure 12.7 ASTAR: An orientation and phase mapping system equipped with TEM.

In figure 12.9, phase and grain orientations of 17Cr-12Ni-2.5Mo alloy after Fe^+ ion irradiation (100keV, $2.0\times10^{17}cm^{-2}$) were characterized using ASTAR. In figure 9(a), reliability factor map is shown. The reliability represents the accuracy of matching diffraction pattern data between the calculated one and experimentally obtained one. While the reliability map is white, the mismatch between them is small. Corresponding phase map, and grain map are shown in figure 12.9(b) and (c), respectively. It was observed that the ion beam damaged layers at the surface of sample A had BCC crystal structure. It means that the crystal structure of irradiated sample surface was changed from FCC to BCC while the Fe-17Cr-12Ni-2.5Mo alloys were irradiated with Fe^+ ion. The reliability map in figure 12.9(a) supports this observation, the pattern mismatch was suspected to be small because the color was white in the corresponding region of reliability map.

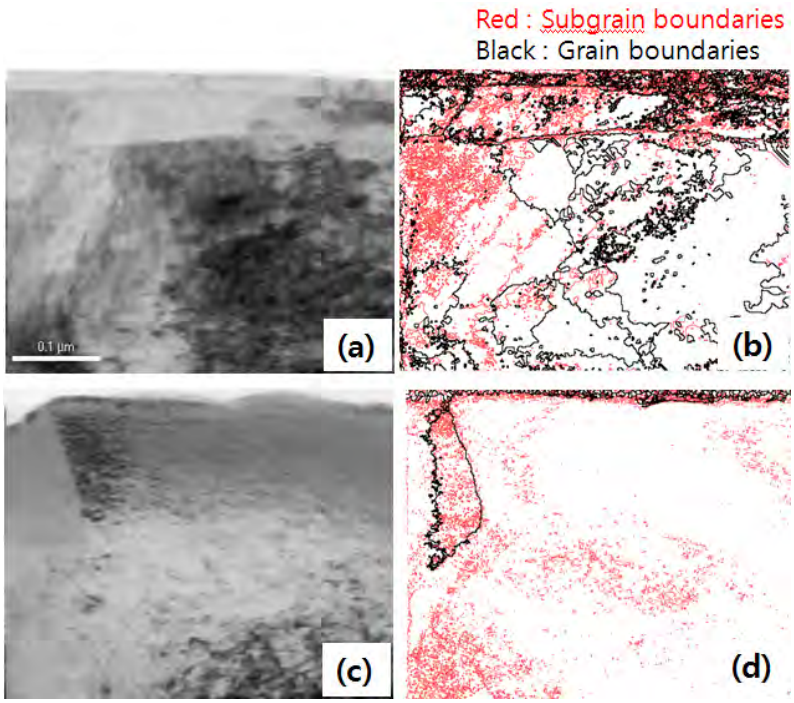

Figure 12.8 Microstructure characterization using ASTAR (a) a virtual BF image, and (b) a misorientation distribution map of ECAPed sample A after irradiation with Fe^+ ion (100 keV, $2.0\times10^{17}cm^{-2}$) (c) a virtual BF image, and (d) a misorientation distribution map of ECAPed sample B after irradiation with H^+ ion (120 keV, $2.0\times10^{18}cm^{-2}$).

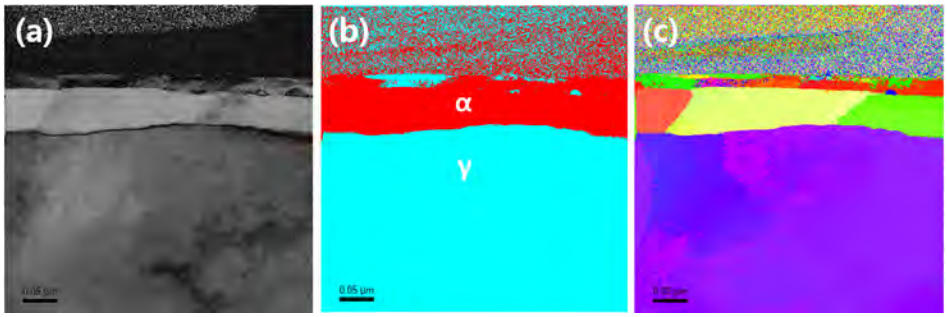

Figure 12.9. Microstructure characterization by using ASTAR (a) reliability factor map, (b) phase map, and (c) grain map of sample A after irradiation with Fe^+ ion (100 keV; $2.0\times10^{17}cm^{-2}$).

In this study, Fe-17Cr-12Ni-2.5Mo alloys were fabricated and processed by ECAP. Those ECAPed samples were implanted with Fe^+ and H^+ ions at room temperature. The energy of Fe^+ ion source was 100keV, $2.0\times10^{17}cm^{-2}$, and the energy of H^+ ion source was 120 keV, $2.0\times10^{18}cm^{-2}$, respectively. The microstructure evolutions were investigated by TEM to examine the density of voids, dislocations, and radiation induced segregation. The crystal structure and misorientations in microstructures have been characterized using ASTAR, which enables orientation and phase mapping with TEM. It was observed that the crystal structure of irradiated sample surface was changed from FCC to BCC while the Fe-17Cr-12Ni-2.5Mo alloys were irradiated with Fe^+ ion. The sizes of the newly developed BCC grains were coincident with the ion irradiation depth, which could be estimated by molecular dynamics simulation.

Project Milestone/Deliverable Summary:

Include a milestone/deliverable summary per template below.

Activities	Milestone/Deliverable Description	Planned Completion Year	Completion Year
Preparation of Fe-Cr-Ni model alloy and MA powder sample	Fe-Cr-Ni model alloy sample	2009	2009

	(1 x 1 x 6 in) MA powders of Fe-Cr-Ni		
ECAP of austenitic steel specimens	Nanocrystalline austenitic alloy sample	2009	2009
ECAP of ODS alloy specimen or Powder Consolidation of MA powders	Nanocrystalline ODS alloy sample	2010	2010
Interface/Grain boundary modification by TMT	Optimum TMT conditions	2010	2010
Analyses of Interface/Grain boundary Character & Stability	Interface/Grain boundary engineered samples (distinct increase of low Σ CSL boundary fraction)	2010	2010
Investigation of mechanical behavior (Hardness, H/T tensile, toughness)	Mechanical data of nano-grain, grain boundary engineered, and irradiated samples	2010	2010
Ion irradiation of proton & He ions	Irradiated samples	2011	2011
Characterization of ion irradiated samples (irradiation cavity size distribution, irradiation hardening)	Irradiated samples & their characters (morphology & size distribution of irradiation cavities by HR-TEM & SANS)	2012	2012
Conference presentations/Journal publications Report to DOE/US & NRF/ROK	4-5 presentation/publication per year as requested	2012	2012

List of Publications

Presentations:

1. X. Zhang, L. Shao, H. Wang and E.G. Fu, “Dose dependent radiation tolerance in Cu/V X. Zhang, L. Shao, H. Wang and E.G. Fu, “Dose dependent radiation tolerance in Cu/V multilayers”, MRS fall meeting, 2009, Boston, MA (oral presentation).
2. X. Zhang, Y. Yang, C. Sun, J. Gonzalez, T. Allen, and K.T. Hartwig, “Radiation damage in nanostructured metallic materials”, Advanced Materials Working Group Meeting, University of California, Santa Barbara, March 2010, organized by Dr. Stuart Maloy and DOE program managers.
3. X. Zhang, “Radiation tolerant metallic multilayers and bulk ultra-fine grained steels”, Engineering Conference International, “Innovative Materials Immune to Radiation”, Vail, CO, Aug. 2010.
4. X. Zhang, C. Sun, Y. Yang, T. Allen, and K.T. Hartwig, “Mechanical properties and radiation tolerance of ultra-fine grained FeCrNi alloy”, MRS fall meeting, Boston, MA, Nov. 30-Dec. 2, 2010.
5. C. Sun, J. Gonzalez, Y. Yang, T.R. Allen, S. A. Maloy, K.T. Hartwig, and X. Zhang, E.G. Fu, “Deformation mechanisms of ultra-fine grained Fe-Cr-Ni alloys”, TMS annual, 2011.
6. Yong Yang, Cheng Sun, Xinghang Zhang and Todd Allen, “Effect of Grain Size and Grain Boundaries on the Proton Irradiation Response of Nanostructured Austenitic Model Alloy”, TMS annual 2011, San Diego, CA.
7. Xinghang Zhang, L. Shao, H. Wang, E.G. Fu, Nan Li, A. Misra, Y-Q Wang, “Radiation Tolerant Metallic Multilayers”, TMS annual 2012, Orlando, FL.
8. C. Sun, J. Ma, K.Y. Yu, K. T Hartwig, L. Shao, S.A. Maloy , X Zhang, “Mechanical Properties and Radiation Response of Ultrafine Grained Fe-Cr-Ni Alloy”, TMS annual 2012, Orlando, FL.
9. Yong Yang, Cheng Sun, Xinghang Zhang, Todd Allen, Irradiation Response of Nanostructured Austenitic Model Alloy, TMS annual 2012, Orlando, FL.
10. Suk Hoon Kang, Hyung-Ha Jin, Jinsung Jang, Do Hyun Kim, Kyu Hwan Oh, Xinghang Zhang, David C. Foley, and Karl Hartwig, “Microstructural evolution of 316L stainless steel during ECAP process” TMS 2011 Annual Meeting, San Diego, CA, USA, Mar 2011

11. Suk Hoon Kang, Jinsung Jang, Hyung-Ha Jin, Kyu Hwan Oh, "Microstructure evolution and EBSD Band Contrast" International Union of Microbeam Analysis Society–V, Seoul, Korea, May 2011
12. Kyu Hwan Oh, Heung Nam Han, Jun Hyun Han, Suk Hoon Kang, Do Hyun Kim, Se Jong Kim, Yong Seok Choi "In-situ Observation of Multi-axial Deformation Behavior of Steels using EBSD" International Union of Microbeam Analysis Society–V , Seoul, Korea, May 2011
13. D.H. KIM, EBSD measurement of deformation behavior and orientation change in dual phase steel sheet during equi-biaxial tension, TMS 2011. (Poster)
14. Y.S. CHOI, In-situ microstructure evolution of oxide dispersion strengthened ferritic steel under uniaxial deformation, DIANA I 2011. (Poster), Apr. 2011, Aussois, France
15. K.H. OH, In-situ Observation of Multi-axial Deformation Behavior of Steels using EBSD Technique, IUMAS 2011. (Invited)
16. Y.S. CHOI, In-situ microstructure evolution of pure aluminum under plane strain tension, TMS 2012. (Oral)
17. J.H. HAN, In-situ observation of dynamic recrystallization in aluminum at room temperature, ReX GG 2013. (Oral, Abstract accepted)

Invited talks

18. "Microstructure and deformation mechanisms of ECAP processed FeCrNi alloys", Thermec 2011, Quebec, Canada, 2011.

19. "Radiation tolerant metallic multilayers and bulk ultra-fine grained steels", The 5th Annual Asia-Pacific Nuclear Energy Forum on Materials for Nuclear Applications, June 2011, Berkeley, CA.

Publications:

1. X. Zhang, E.G. Fug, A. Misra, M. J. Demkowicz, and R. G. Hoagland, "Interfaceenabled defect reduction in He ion irradiated metallic multilayers", **JOM**, Volume 62, Number 12, 75-78, DOI: 10.1007/s11837-010-0185-5, 2010 **(review article).**

2. C. Sun, K. Y. Yu, J. H. Lee, Y. Liu, H.Wang, L. Shao, S. A. Maloy, K.T. Hartwig, and X. Zhang, "Enhanced radiation tolerance of ultrafine grained Fe-Cr-Ni alloy", **J. Nuclear Materials**, 420 (2012) 235.
3. X. Zhang, "Radiation damage in nanostructured multilayers" (**invited review article) J. Engineering Science and Technology**, under review.
4. K. Y. Yu, Y. Liu, C. Sun, E. Fu, H. Wang, L. Shao, X. Zhang, Radiation damage in helium ion irradiated nanocrystalline Fe, **Journal of Nuclear Materials**, 425 (2012):140-146.
5. C. Sun, Y. Yang, Y. Liu, K.T. Hartwig, H. Wang, S. A. Maloy, T.R. Allen, X. Zhang , Thermal stability of ultrafine grained Fe-Cr-Ni alloy, **Materials Science and Engineering, A**, 542 (2012):64-70.
6. Hoon-Hwe Cho, Suk Hoon Kang, Sung-Hwan Kim, Kyu Hwan Oh, Heung Ju Kim, Woong-Seong Chang, Heung Nam Han, "Microstructural evolution in friction stir welding of high-strength line pipe steel", Materials and Design, Volume 34, February 2012, 258–267
7. Y.S. Choi, D.H. Kim, S.-H. Kim, S.H. Kang, J. Jang, H.N. Han, and K.H. Oh, "In situ microstructure evolution of oxide dispersion strengthened ferritic steel under uniaxial deformation", Journal of Nuclear Materials 428 (2012) 98–102
8. Suk Hun Kang, Hyung Ha Jin, Jinsung Jang, Yong Seok Choi, and Kyu Hwan Oh, "A quantitative approach of microstructure evolutions by EBSD pattern quality variations", Microscopy and Microanalysis, submitted
9. C. Sun, M. Song, K. Y. Yu, Y. Chen, M. A. Kirk, M. Li, H. Wang, X. Zhang, *In situ* evidence of defect cluster absorption by grain boundaries in irradiated nanocrystalline Ni, **Metallurgical and Materials Transactions A**, submitted.
10. M. Song, C. Sun, J. Jang, C. H. Han, T. K. Kim, K. T. Hartwig, and X. Zhang, Microstructure Refinement of a 12Cr ODS Steel by Equal Channel Angular Extrusion, submitted.

<u>Manuscript in preparation: N/A</u>

11. C. Sun, S. A. Maloy, K.T. Hartwig, Y. Yang, T.R. Allen, and X. Zhang, "Deformation mechanisms of ECAP processed Fe-Cr-Ni alloys", in preparation.

12. C. Sun, M. Kirk, M. Li, K. T. Hartwig and X.Zhang,"in situ radiation of nanocrystalline 304 stainless steel", in preparation.
13. C. Sun, S. A. Maloy, K. T. Hartwig, L. Shao, and X. Zhang, "Heavy ion irradiation of 304 stainless steel at elevated temperature to a dose of 300dpa", in preparation.
14. Y. Yang, T.R. Allen, C. Sun, S.A. Maloy, K.T. Hartwig, and X. Zhang, "Grain boundary engineering of ECAPed Fe-Cr-Ni alloys", in preparation.
15. Y. Yang, T.R. Allen, C. Sun, S.A. Maloy, K.T. Hartwig, and X. Zhang, "In situ radiation studies of ultra fine grained Fe-Cr-Ni alloys", in preparation.

Summary and Benefit statement

This is a very successful project that falls right under the current theme of NanoNuclear. Significant amount of work has been performed to refine the microstructure of austenitic stainless steels. Studies show that these nanograined steels have extraordinary radiation tolerance against He, Kr and Fe ion irradiation compared with their coarse grained counterparts. Meanwhile the nanograined steels have high strength and maintained reasonable ductility. Nanocrystalline 304 and 316L stainless steels are thermally stable up to 600°C. The next step (phase 2) of the project shall be 1) investigation of the neutron radiation tolerance of these nanograined steels; and 2) radiation resistance up to 300 dpa.

Furthermore our collaborations with South Korea collaborators through INERI have been very fruitful. We have proved that ECAP is efficient to change the chemistry and refine the size and distribution of oxide nanoparticles. ECAP is thus a promising technique for thermo-mechanical treatment of a variety of steels and alloys.

More than a dozen research articles have been (or will be) published as a result of this project. Numerous talks (including invited talks) have been delivered at national and international conference. 5 Graduate students have been supported by this project.

We are grateful for collaborations with Dr. Stuart Maloy at Los Alamos National Laboratory on mechanical testing and Dr. Don Brown on neutron scattering studies. We acknowledge the access to Argonne-IVEM *in situ* radiation facility and collaboration with Drs. Mark Kirk and Meimei Li at Argonne National Laboratory.